buildings

Traditional and Innovative Approaches in Seismic Design

Edited by
Linda Giresini and Francesca Taddei
Printed Edition of the Special Issue Published in *Buildings*

MDPI

Traditional and Innovative Approaches in Seismic Design

Special Issue Editors

Linda Giresini
Francesca Taddei

MDPI

Special Issue Editors

Linda Giresini
University of Pisa
Italy

Francesca Taddei
Technical University of Munich
Germany

For citation purposes, cite each article independently as indicated on the article page online and as indicated below:

Lastname, F.M.; Lastname, F.M. Article title. *Journal Name*. **Year**. *Article number*, page range.

Table of Contents

About the Special Issue Editors

Linda Giresini is Assistant Professor at the School of Engineering in the University of Pisa. She is author and co-author of over 50 publications in the field of earthquake and structural engineering, with emphasis on masonry and reinforced concrete structures. In particular, her research interests include mitigation of risk in existing structures, experimental tests on masonry and r.c. structures, sustainable and resilient infrastructures, low-cost structural solutions for developing countries and rehabilitation of archaeological sites. Since 2013, she has been collaborating with research groups from the Universities of Aachen, Munich (Germany), Minho (Portugal) and Bath (UK).

Francesca Taddei obtained her doctorate from the civil engineering faculty of the RWTH Aachen University and she is currently a postdoctoral fellow at the Chair of Structural Mechanics of the Technical University of Munich. Her current research focuses on structural dynamics, soil dynamics, soil-structure interaction, site-city interaction, vibration estimation and mitigation and numerical modeling of wave propagation in buildings (finite element method, boundary element method, ITM). She is involved in several worldwide collaborations, such as with the Beijing University of Technology, RWTH Aachen, Braunschweig University of Technology and the University of Pisa.

Experimental Tests on a Dowel-Type Timber Connection and Validation of Numerical Models

Fabio Solarino [1] [iD]**, Linda Giresini** [1,***] [iD]**, Wen-Shao Chang** [2] [iD] **and Haoyu Huang** [3]

[1] Department of Energy, Systems, Territory and Constructions Engineering, University of Pisa,
     Largo Lucio Lazzarino, 56122 Pisa, Italy; solarino.fabio@gmail.com
[2] Sheffield School of Architecture, The University of Sheffield, Sheffield S10 2TN, UK; w.chang@sheffield.ac.uk
[3] College of Architecture and Civil Engineering, Beijing University of Technology,
     100 Pingleyuan, Beijing 100124, China; huanghaoyu@bjut.edu.cn
* Correspondence: linda.giresini@unipi.it

Abstract: This paper examines the dynamic behaviour of timber framed buildings under wind and dynamic loads, focusing on the role of connections being experimentally tested. The main aim of this manuscript is to analyze the in-service dynamic behaviour of a semi-rigid moment-resisting dowel-type connection between timber beam and column. For this purpose, two laboratory tests have been performed, the first on a connection and another one on a portal frame. The results are used to validate a numerical model of the simple portal frame, analyzed in *OpenSees*. The obtained relationships are also discussed and compared with Eurocode rules. The main result is that the joint stiffness is calculated through the Eurocode (EC) formulation underestimates the experimental one. A mutual agreement is obtained between the numerical model, validated from the experimental stiffness value for the connections, and the experimental results on the portal frame.

Keywords: timber; dowel-type connection; rotational stiffness; curve fitting; damping; *OpenSees*

1. Introduction

Wind-induced vibrations reveal to be an important design aspect when dealing with timber structures due to their low mass. A deeper knowledge about the connection behaviour is necessary to face this issue. Connections play a significant role on structural stiffness and damping, and the lack of information about their in-service dynamic vibrations challenges designers. The connections in timber structures are often designed by using dowel-type connections and they make a significant contribution to the overall structural stiffness.

Many researchers have experimentally studied dowel type connections, focusing their attention on single dowel connection axially loaded (parallel to the grain direction) [1,2]. Beam-to-column moment resisting dowel type connections have also been tested to achieve a better knowledge about the rotational stiffness of the joint [3–5]. Dynamic properties of dowelled connections have been investigated through cyclic load tests [6,7], showing their contribution to damping in a complete structure. Analytical models can be used to predict in-service stiffness as well as the frictional energy dissipation in embedment [8–12]. Eurocode 5 [13] provides rules for calculating the slip modulus (k_{ser}), which can be used to assess the connection stiffness appropriate to static loading under serviceability limit state. Incidentally, the importance of dissipation due to friction has also been analytically and experimentally demonstrated for the collapse failures of masonry structures, by means of a rigid-plastic orthotropic damage model [14–17]. For such structures in a dynamic perspective, the dissipation due to the impact between rigid surfaces also plays an important role [18,19].

Moreover, the semi-rigid connection stiffness required for modelling and predicting the in-service dynamic behaviour of dowel-type connections is different from the stiffness required for static loading [7]. Furthermore, k_{ser} is empirically determined, independent of the geometry of the connection, relying only on the diameter of the connector and the timber density. The nonlinearity resulting from ductile connections makes their modelling difficult. Many numerical models have been developed to simulate such a behaviour [20–22] based on the mechanical parameters that play significant roles in the connection. Validation of the model through experimental campaign can be done in order to compare test data to model prediction [23].

This study aims at the evaluation of the in-service stiffness of a beam-to-column moment-resisting 4×4 dowel-type connection through experimental tests and numerical analysis.

Figure 1 shows the connection that is analyzed in this work. This connection is then included in a 1500 mm × 1500 mm symmetric portal frame. Localized phenomena (at connection level) are then investigated through a full scale specimen, whereas the global elastic response is simulated at a model scale of 1:2. Indeed, at reduced scales, the prototype response cannot be properly reproduced [24]. For that reason, and to avoid the potentially inaccurate scaling of results, the connection to test have been designed with medium-large connectors (full scale specimen).
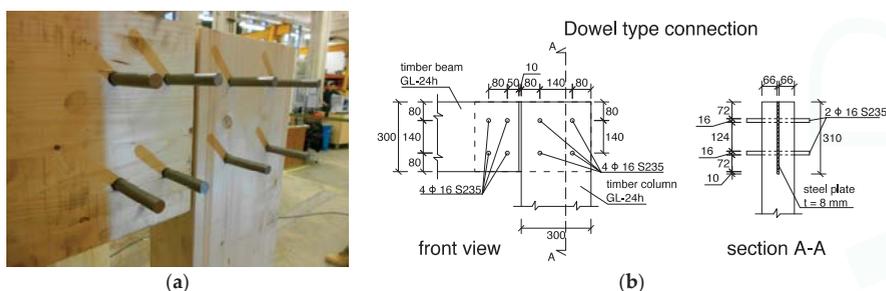
Figure 1. Dowel type connection: (**a**) beam-column joint; (**b**) joint layout (all lengths are in mm).

The single connection is firstly statically tested (Section 2), and its influence on a simple portal frame is estimated with a vibration test (Section 3). Here, the dynamic characteristics of the structure are obtained by means of a MATLAB [25] script based on the Matrix Pencil Algorithm (MP Algorithm) [26]. Experimental results are applied in Section 4 on a three-dimensional (3D) portal frame modelled in *OpenSees* [27]. Both modal and time-history analysis are performed and results are compared to the experimental outcomes.

2. Connection Test

2.1. Experimental Test Set-Up

Two experiments were performed in the laboratory at the University of Bath: a static test on a typical steel-timber connection with 4 + 4 dowels (Figure 2a) and a non-destructive vibration test on a symmetric portal frame 1500 mm × 1500 mm (Figure 2b). The joint was cut off from the frame once the vibration test had been performed.

Each member has cross section of 140 mm × 300 mm (Figure 2b) and the material is whitewood glulam of grade GL-24h, as defined in EN 1408 [28]. The steel plate slotted in the timber elements links two different connections: a four-dowel connection on the column and a four-dowel connection on the beam. The steel grade is S235, with 8 mm-thick plates and 16 mm diameter holes accommodating the steel dowels. 16 mm diameter holes have been drilled into the timber members. The fasteners are of S235 grade and have a diameter of 16 mm so to fit tight into the holes. Beams and columns were cut with an angle of 45° and the specimen was vertically loaded so to induce a bending moment in the joint

(Figure 3a,b). The connection was statically loaded through *Instron 2000 kN Universal Testing Machine* in displacement-control ($\Delta u = 3$ mm/min). Two transducers fixed at the column measured the relative column-beam displacement of the joint in two points spanned 140 mm, placed symmetrically to the beam axes (Figure 2a). The corresponding angular deformation can be easily found through the following equation:

$$\varphi[\text{rad}] = \tan^{-1}\left(\frac{\delta_1 - \delta_2}{p}\right), \tag{1}$$

where δ_1 and δ_2 are the relative displacements from the two sensors in the direction of the beam axes (Figure 3c) and p is the distance between the two reference points (240 mm). The corresponding moment is evaluated as:

$$M = F_y \cdot H, \tag{2}$$

where $F_y = F/\sqrt{2}$ is the component of the force that is applied by the loading machine orthogonal to the axes of the beam and $H = 610$ mm is the distance between the loading point and the centroid of the group of dowels of the column side, which is considered as the rotation center of the joint (Figure 3c).
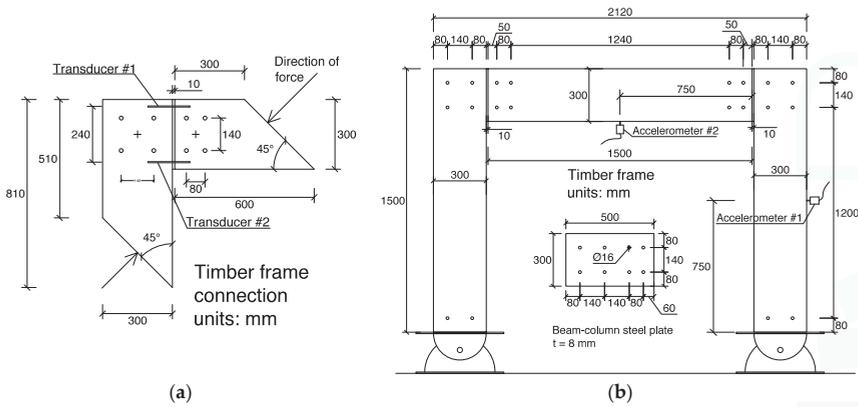
Figure 2. Laboratory specimens: (**a**) steel-timber connection; (**b**) 1500 mm × 1500 mm portal frame—all lengths in mm.
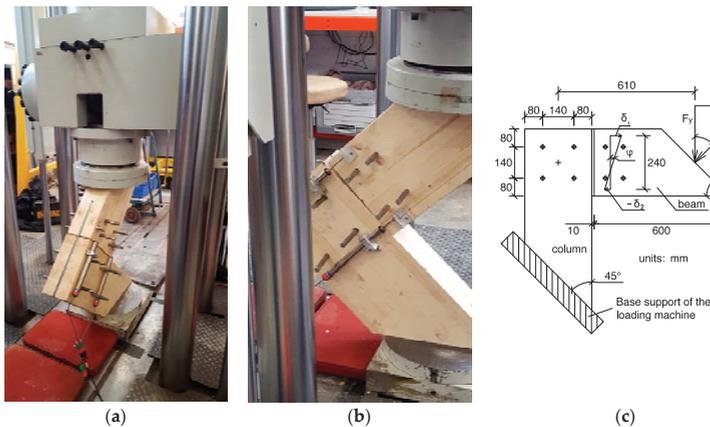
Figure 3. Experimental set-up: (**a**) machinery used for connection test; (**b**) joint under static monotonic test; and (**c**) graphic display of angular deformation.

2.2. Static Behaviour of the Joint

The static test performed on the joint allowed to obtain the moment-rotation diagram shown in Figure 4a.
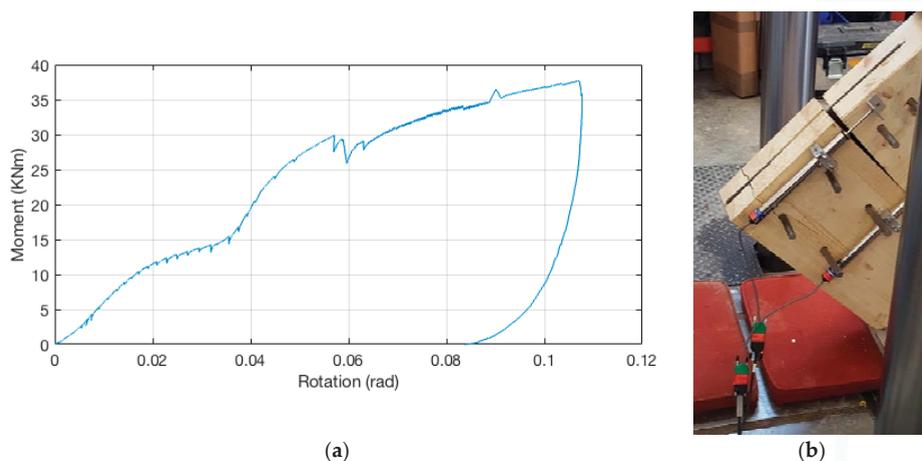
Figure 4. Connection test results: (**a**) moment-rotation diagram of the dowelled connection; (**b**) connection specimen at failure.

The examined diagram (Figure 4a) displays the whole failure load path from the beginning up to the maximum load when the cracks on the timber member become clearly visible and the test is interrupted (Figure 4b). The connection shows lower stiffness at the beginning of the loading process. Higher stiffness was not attained up to a load of 2.5 kNm. Dorn [1] argues that this initial consolidation is probably caused by imperfect contact between dowel and wood, which results from geometric roughness of the specimen in the contact zone as well as from imperfections of the contact surfaces. During the phase that directly follows the consolidation process at about 0.005 rad (Figure 4a), the maximum stiffness of the connection is attained. Even though perfect linearity is not observed, an approximation by a straight line is possible over a short section to obtain an approximate stiffness value.

The approximate stiffness value is later used to validate the numerical model in Section 4. A 'sawtooth' path is visible since the first stages of loading path. This is supposed to be caused by invisible cracks that are occurring inside the connection since low load. When the load increases (about 11 kNm), the stiffness dramatically decreases and a softening behaviour is observed in the load-displacement curve. Once the moment attains a value of 15 kNm, a steep increasing of the stiffness can be seen. This atypical behaviour is because of the contact that occurred between member surfaces at bottom-side (Figure 3b). The center of rotation of both connections shifts resulting in different angles to the grain. Another non-linear path can be shown until the bending moment arrives to about 30 kNm. Here, cracking strongly occurs in part of the wood matrix that reaches the compression strength and plastic deformations. The stiffness sensitively decreases until the maximum load is attained (37.68 kNm). A yield plateau is visible at the final stage and a maximum rotation of 0.107 rad (6.13°) is obtained. At the end of the test, final failure occurred, resulting in a sudden load reduction (Figure 4a). Brittle failure is reached because maximum tension forces are attained perpendicular to the grain in the column member.

2.3. Estimation of the Rotational Stiffness of the Joint and Comparison with Eurocode Indications

By the analysis of the first three stages of the moment-rotation relationship (Section 2.2), a linearization of the curve allows for calculating the rotational stiffness of the connection. Reynolds [7] shows that the range of loads imposed on a connection in service is of 20% and 40% of the predicted characteristic capacity. According to CEN (European Committee for Standardisation) [28] the initial stiffness is calculated from 10 to 40% of the peak load. The latter is used in this study to evaluate the rotational stiffness of the joint.

A linear regression of data in the range of $0.1\,M_{\max} < M < 0.4\,M_{\max}$ gives the rotational stiffness,

$$K_{\theta,\mathrm{ser}} = 696\ \mathrm{kNm/rad}. \tag{3}$$

The linear fit is shown in Figure 5, where the root mean squared error is 0.191 and the correlation coefficient (R^2) is 0.976, suggesting a significant variation of data. This was probably due to the 'sawtooth' shape of the diagram.
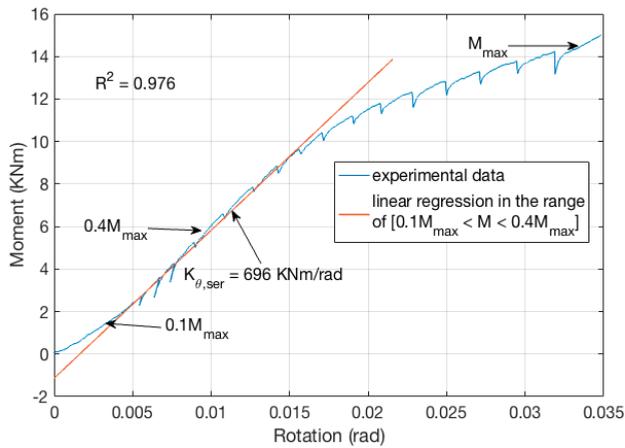
Figure 5. Linear interpolation of the moment-rotation diagram between 10% $M_{\max}$ and 40% $M_{\max}$.

Analytical prediction of the rotational stiffness of the connection can be done in order to compare the experimental value. Gelfi [29] evaluated the stiffness of the connection on the basis of the classical approach of the beam on elastic foundation, whereas Eurocode 5 [13] provides the analytical calculation of the slip modulus k_{ser}, per shear plane, per fastener under service load, through the expression:

$$k_{\mathrm{ser}} = 2 \cdot \rho_m^{1.5} \cdot \frac{d}{23} \quad ([13]\ \mathrm{Table}\ 7.1) \tag{4}$$

where d is the diameter of the fastener and ρ_m is the mean density of timber. The stiffness can be multiplied by 2 because of the steel connector [13] (§7.1(3)). It is straightforward to calculate the stiffness of the individual fastener as:

$$k_{\mathrm{fas,EC}} = n_{sp} \cdot k_{\mathrm{ser}}, \tag{5}$$

where n_{sp} is the number of shear plane. In this specific case,

$$k_{\mathrm{fas,EC}} = 23951.1\ \mathrm{kN/m}. \tag{6}$$

Even if $k_{fas,EC}$ is the serviceability limit state design value that is provided from the Eurocode, it could be of interest to extrapolate the individual fastener stiffness, $k_{fas,exp}$ from the connection rotational stiffness experimentally evaluated ($K_{\theta,ser}$) and compare it with Eurocode design value. Because only one experiment is not enough to characterize the stiffness, comparison should be done with caution. If one assumes the joint made by two separate connections linked in series, therefore the inverse of the equivalent rotational stiffness of the connection is:

$$\frac{1}{K_{\theta,eq}} = \frac{1}{K_{\theta,col}} + \frac{1}{K_{\theta,beam}}. \tag{7}$$

where $K_{\theta,col}$ refers to the column stiffness and $K_{\theta,beam}$ to the beam one. Furthermore, each rotational stiffness can be expressed in function of the single fastener stiffness:

$$K_\theta = k_{fas} \sum r_i^2, \tag{8}$$

where k_{fas} is the stiffness value of the individual fastener (force per unit length) and r_i is the ith radius vector, namely the distance from the center of the group to the ith fastener (Figure 6). By making simple calculations, in the case under examination it is:

$$K_{\theta,col} = 1.508 \cdot K_{\theta,beam}, \tag{9}$$

therefore,

$$K_{\theta,col} = 1745.35 \text{ kNm/rad} \tag{10}$$

and finally,

$$k_{fas,exp} = \frac{K_{\theta,col}}{4r^2} = 44524.30 \text{ kN/m.} \tag{11}$$

The comparison of the experimentally determined stiffness with corresponding design values from EC5 leads to a ratio:

$$\frac{k_{fas,EC}}{k_{fas,exp}} = 0.54, \tag{12}$$

graphically displayed in Figure 6.
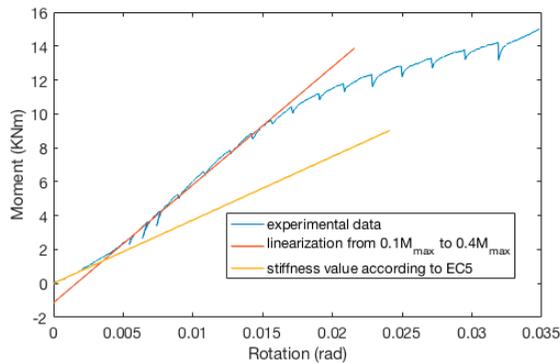
Figure 6. Comparison of experimental rotational stiffness to the Eurocode (EC) value.

The EC5 formula underestimates the stiffness, probably because it does not cover the influence of all the involved parameters, such as connection width, length of the dowel, and its consequent deformed shape. Moreover, it does not take into account the influence of the angle to grain direction and the foundation modulus. Dorn [1] compared results from dowel-type connections to the current

generation of European standards with respect to stiffness. Results clearly show that for 200 mm wide specimens, the stiffness specified by EC5 underestimates the observed stiffness. Even though the first branch of the curve was assumed, the EC5 expression would have strongly underestimated the stiffness value of the joint as well.

3. Portal Vibration Test

3.1. Experimental Test Set-Up

A non-destructive vibration test was carried out to evaluate the dynamic properties (i.e., frequency and modal damping) of the timber portal frame, as shown schematically in Figure 2b. The portal frame is made by two identical frames with four columns and two beams all 1.5 m long. Description of materials, cross sections, and geometry of the joints can be found in Section 2.1. Columns are pinned at the ground through hinge-type steel-timber connections (Figure 7a,b).

| (**a**) | (**b**) |
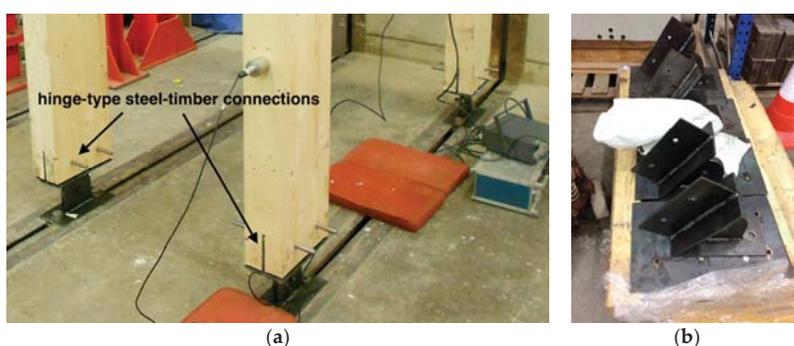
Figure 7. Details of the base connections: (**a**) detail of connections at the ground; (**b**) steel hinges.

The portal frames are connected at the top by two whitewood plywood panels, which are useful to transfer the load from the shaker to the structure, with dimensions of 1150 mm × 600 mm × 18 mm.

Table 1 summarizes the main characteristics of the performed experiments. The excitation method was a slow sine sweep, in which a sinusoidal force, gradually increasing in frequency, was applied by the shaker and the rate of increase of frequency was sufficiently slow that the steady-state response at each frequency had time to develop. The shaker (APS 113 ELECTRO-SEIS®, APS Dynamics, Inc., San Juan Capistrano, CA, USA) had a mass of 30 kg and a frequency range from 0.01 to 200 Hz. Two piezoelectric accelerometers having a lower frequency limit of 0.1 Hz and a nominal sensitivity of 10 V/g were fixed to the mid-height column (#1, Figure 2b) and at the mid-span of the beam (#2) to read the vertical and horizontal response (Figure 8). The data logger was connected to a laptop and the records were processed with the software LabVIEW (National Instruments, Austin, TX, USA) [30]. For all of the tests performed, a sampling rate of 500 Hz was used and frequency was manually tuned from 0.1 Hz to 100 Hz to cover a considerable range of frequency spectrum.

Table 1. Summary of the experimental tests performed in laboratory.

Test No.	Type of Specimen	Type of Test	Machine	Signal Recorded
#1	timber portal frame	dynamic	shaker: APS 113 ELECTRO-SEIS®	accelerometer
#2	steel-timber dowelled connection	static (displacement-control)	Instron 2000 kN Universal	displacement transducers

Figure 8. Portal frame under vibration test.

3.2. Dynamic Response of the Portal Frame

Four vibration tests (from #1 to #4) performed through the shaker on the portal frame provided acceleration time-histories variable with the excitation frequency. Figure 9 shows the acceleration time-histories read from both of the accelerometers during the experiments. For test #1 and #2, the frequency was tuned from 0.1 Hz to 100 Hz, whereas, the start frequency for test #3 and #4 was set to 0.3 Hz, as lower values were not significant for this case. To develop the steady-state response at each step, the frequency was manually shifted approximately every $15 \div 20$ s. Test #2 was clearly affected from peak accelerations that were caused by instruments acting at the same time in the laboratory. Impulse-type responses were useful to evaluate free vibrations of the structure. For the third test, the rate of frequency-turning was set to 20 s and no relevant noise affected the signal. Finally, for the last test, a higher amplitude of the shaker was set and an accurate and clear signal was obtained.

Few seconds of free swinging of the signal were trimmed and filtered by using a bandpass filter to reduce the noise that was caused by the shaker and to extract the fundamental frequency and evaluate the damping ratio. Modal analysis of a two-dimensional (2D) numerical model of the timber frame with beam-column semi-rigid connection stiffness set at $K_\theta = 374.4$ kNm/rad (based on the slip modulus, k_{ser} from EC5 [13]) was performed to evaluate the natural frequency of the structure corresponding to the interesting mode of vibration (i.e., horizontal swinging):

$$f_{\text{mod}} = 14.23 \text{ Hz} \tag{13}$$

Thus, the natural frequency of the portal frame is assumed to be included in the range 6 Hz $\div$ 30 Hz.
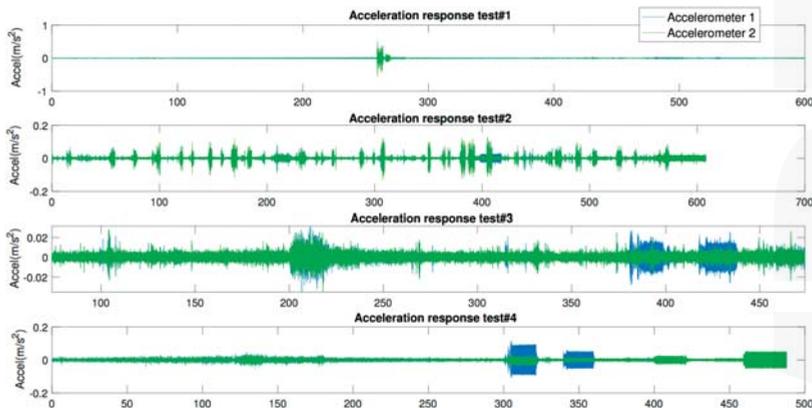
Figure 9. Registered acceleration time-histories of the four tests (time in s).

A 9th-order Butterworth filter was chosen to eliminate frequencies outside the interesting range. Figure 10 shows the filtered time history record of one of the trimmed signal ($106.80 < T < 107.70$) from test #2 displayed in Figure 11.
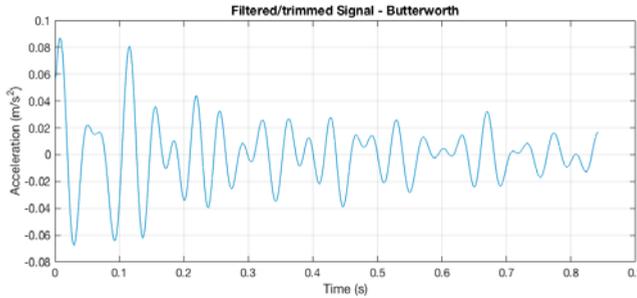
Figure 10. Filtered signal using a 9th-order Butterworth filter.
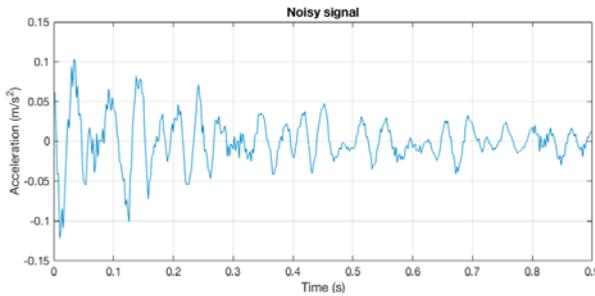
Figure 11. Trimmed signal, $T = 0.9$ s, test #2, accelerometer #1 (column mid-height).

3.3. Signal Curve Fitting Process

The acceleration time histories data (obtained as illustrated in Section 3.2) are processed in time domain by using the Matrix Pencil Algorithm (MP Algorithm) [4] through a specifically developed MATLAB script, where the number of modes contributing to vibration signal has to be assumed. A wrong assumption could lead to misleading results of the damping ratios. The algorithm derives fundamental frequencies and associated damping ratios, and performs a procedure to compare fitted signal to the measured signal visually, as shown in Figure 12. A very good agreement is obtained.
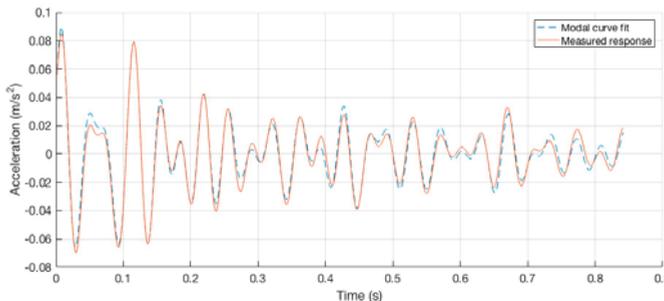
Figure 12. Modal curvefitting of the signal.

Table 2 collects all of the analysis results and shows for each analyzed segment the relative frequency and the corresponding damping ratio of the whole structure, as found from curve fitting. T_1 and T_2 are the lower and the upper limits of the segment analyzed. Most of the segments are chosen from the second test (#2, Figure 9) where free vibrations are visible. Many analyses are performed in the range of 405–409 s where resonance is clear. The average frequency is calculated with the following:

$$f_{\text{mean}} = \frac{1}{10} \sum_i f_i = 19.48 \text{ Hz.} \tag{14}$$

To evaluate the precision of the observed data, the standard deviation is evaluated:

$$\sigma = \sqrt{\frac{1}{10} \sum_i (f_i - f_{\text{mean}})^2} = 0.6734, \tag{15}$$

showing an acceptable accuracy of the analysis. The dispersion is shown in Figure 13.

Table 2. Curvefitting experimental signal.

Analysis	Test	$T_1 < T < T_2$	f	ξ
No.	#	(s)	(Hz)	(%)
1	2	$52.54 < T < 53.50$	19.08	0.82
2	2	$106.80 < T < 107.70$	19.44	1.45
3	1	$264.40 < T < 265.40$	19.22	4.18
4	2	$309.70 < T < 310.00$	18.29	2.86
5	2	$409.30 < T < 409.50$	19.90	1.40
6	2	$416.85 < T < 417.10$	20.27	3.83
7	2	$405.00 < T < 405.14$	20.71	0.50
8	2	$406.20 < T < 406.50$	19.23	0.62
9	2	$407.40 < T < 407.80$	19.28	1.12
10	2	$409.30 < T < 409.50$	19.34	0.32
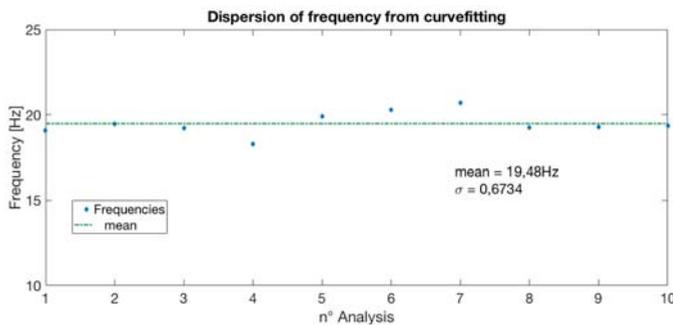
Figure 13. Dispersion of data.

4. Numerical Model of the Portal Frame

Modelling and Analysis

The 3D portal frame is modelled in *OpenSees* [27]; it includes 156 nodes and 148 elements, of frame-type elastic and isotropic (Figure 14a). The material used for modelling glulam timber is graded GL-24h according to EN 14080 [28], whose mechanical properties are listed in Table 3. Density was experimentally measured and a value of $\rho = 352 \frac{\text{kg}}{\text{m}^3}$ was obtained.

(**a**)   (**b**)

Figure 14. (**a**) *OpenSees* numerical model; (**b**) portal frame under vertical vibration.

Table 3. Properties of GL 24h according to EN 14080:2013 [28] assumed in the numerical simulation.

	$E_{0,g,mean}$	$G_{0,g,mean}$
Class	**(N/mm²)**	**(N/mm²)**
GL 24h	$11,500$	600

The horizontal panels that are placed at the top of the frame are modelled as shells, meshed with elastic orthotropic *nDmaterial* 18 mm-thick. The beam length is set to 1.32 m to take into account the dimension of the connections in both sides. Columns are 1.35 m long and the distance between the two frames is 1.10 m. All of the support nodes are pinned at the base. Rotational springs simulate the connection between beam and column and between slab panel and beam. The numerical simulation neglects the strengthening effect of the panel with respect to the beams as nailed at the top of the elements. Modal analysis has been done to evaluate eigenmodes and corresponding eigenfrequencies. The response of the portal frame model is validated by assuming the value of rotational stiffness resulted from experimental test ($K_{\theta,ser}$). Moreover, the stiffness value of the connections $K_{\theta,EC}$, based on the Eurocode 5 and evaluated in Section 2.3 is also set and results are compared. Further analytical models [6,31] can be used in order to predict the initial rotational stiffness of the joint based on the mechanical properties of the elements and on the geometry. These models are usually based on the classical approach of the beam on elastic foundation but are not considered in this work.

The modal analysis outcomes are reported in Table 4, where f is the natural frequency, corresponding to the direction along beam-column connections.

Table 4. Results from modal analysis for the three-dimensional (3D) portal frame model.

Rotational Stiffness	Value (KNm/rad)	f (Hz)
$K_{\theta,ser}$	696.0	17.84
$K_{\theta,EC}$	374.4	13.06

Figure 15 shows the third mode shape when $K_\theta = K_{\theta,ser}$, namely when the second branch of the moment-rotation relationship is assumed for the stiffness calculation (Section 2.3). The percentage difference between the experimental and numerical eigenfrequencies is 8.2%; their ratio is 1.09, value considered acceptable for the uncertainties, that, in any case, affect a numerical model.

As discussed in the Introduction, localized phenomena at the connection level have been evaluated by testing a full scale specimen, whereas the global elastic characteristics have been obtained through a scaled model (1:2). Anyway, to evaluate the scale effect, it could be worthy to vary the dimensions in

the validated FE model. By doubling the length of the structural members, the eigenfrequency of the prototype is about half of that of the model:

$$f = 8.48 \text{ Hz} \tag{16}$$

Other scale effects can be considered in further studies by varying the dimensions of the connectors and keeping their geometry constant. One of the limitations of this work is that the investigation only considers the linear-elastic behaviour of the dowel connections neglecting their cyclic hysteretic behavior, necessary to assess damping and dissipation of energy.

Further studies will be addressed to find a simple and efficient analytical model that is useful to represent a wide range of connections as a function of geometry and mechanical properties of the components. These models can be applied in numerical models of timber buildings to better evaluate the influence of connections on the building dynamic behaviour.
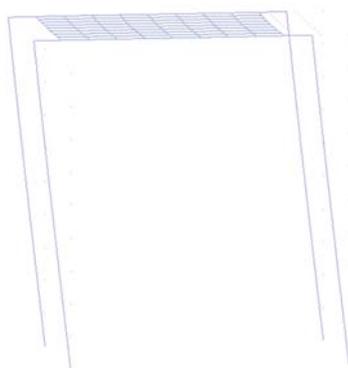
Figure 15. Third mode shape of portal frame 3D model, $f = 17.84$ Hz.

5. Conclusions

This work investigated the interaction between steel and timber in dowel-type connections, in the experimental and numerical perspective.

Laboratory tests on portal frame and connections allowed for the evaluation of the single fastener shear stiffness. The results of the experimental tests showed rotational stiffness values that were overestimated by about two times with respect to the Eurocode indications. Through a curve-fitting method, the experimental results in terms of acceleration time-histories were filtered up and the resonance condition gave the relevant frequency of vibration of the portal frame. The modal analysis was performed on a 3D portal frame by setting the rotational joint stiffness that was calculated when considering the linearization in the range of 0.1 $M_{\max} < M < 0.4$ $M_{\max}$ of the moment-rotation relationship obtained from the experimental test. The experimental frequency was seen to be less than 10% higher than the eigenfrequency obtained through the modal analysis. The results are then in good mutual agreement; the percentage difference of 8.4% is probably due to the uncertainties of the actual timber mechanical properties and on the strengthening effect of the horizontal panel nailed at the top of the frame.

This work only considers the linear-elastic behaviour of the dowel connections without taking into account the cyclic hysteretic loop of the joints, which is useful to assess the damping and dissipation of energy.

Further studies will be addressed to find a simple and efficient analytical model useful to represent a wide range of connections as a function of geometry and mechanical properties of the components.

References

1. Dorn, M.; de Borst, K.; Eberhardsteiner, J. Experiments on dowel-type timber connections. *Eng. Struct.* **2013**, *47*, 67–80. [CrossRef]

2. Sawata, K.; Sasaki, T.; Kanetaka, S. Estimation of shear strength of dowel-type timber connections with multiple slotted-in steel plates by European yield theory. *J. Wood Sci.* **2006**, *52*, 496–502. [CrossRef]

3. Polastri, A.; Tomasi, R.; Piazza, M.; Smith, I. Moment resisting dowelled joints in timber structures: Mechanical behaviour under cyclic tests. *Ing. Sismica* **2013**, *30*, 72–81.

4. Bouchaïr, A.; Racher, P.; Bocquet, J.F. Analysis of dowelled timber to timber moment-resisting joints. *Mater. Struct.* **2007**, *40*, 1127–1141. [CrossRef]

5. Chui, Y.H.; Li, Y. Modeling Timber Moment Connection under Reversed Cyclic Loading. *J. Struct. Eng.* **2005**, *131*, 1757–1763. [CrossRef]

6. Reynolds, T.; Harris, R.; Chang, W.S. Dynamic stiffness and damping of dowel-type connections for timber structures under service conditions. In *World Conference on Timber Engineering 2012 (WCTE 2012): Auckland, New Zealand, 15–19 July 2012*; New Zealand Timber Design Society: Auckland, New Zealand, 2012; Volume 1, pp. 566–573.

7. Reynolds, T.; Harris, R.; Chang, W.S. In-Service Dynamic Stiffness of Dowel-Type Connections. In Proceedings of the CIB-W18 on Timber Structures, Vancouver, BC, Canada, 26–29 August 2013.

8. De Jong, T. Stresses Around Pin-Loaded Holes in Elastically Orthotropic or Isotropic Plates. *J. Compos. Mater.* **1977**, *11*, 313–331. [CrossRef]

9. Zhang, K.-d.; Ueng, C.E.S. Stresses around a pin-loaded hole in orthotropic plates with arbitrary loading direction. *Compos. Struct.* **1985**, *3*, 119–143. [CrossRef]

10. Hyer, M.W.; Klang, E.C. Contact stresses in pin-loaded orthotropic plates. *Int. J. Solids Struct.* **1985**, *21*, 957–975. [CrossRef]

11. Echavarría, C.; Haller, P.; Salenikovich, A. Analytical study of a pin-loaded hole in elastic orthotropic plates. *Compos. Struct.* **2007**, *79*, 107–112. [CrossRef]

12. Lekhnitskii, S.G. *Anisotropic Plates*; Gordon and Breach Science Publisher: New York, NY, USA, 1968.

13. Uni En BS. EN 1995-1-1:2004—Eurocode 5: Design of timber structures—Part 1-1: General—Common rules and rules for buildings. *Eurocode 5* **2004**, *1*, 1–123.

14. Casapulla, C.; Argiento, L.U. The comparative role of friction in local out-of-plane mechanisms of masonry buildings. Pushover analysis and experimental investigation. *Eng. Struct.* **2016**, *126*, 158–173. [CrossRef]

15. Casapulla, C.; Portioli, F. Experimental tests on the limit states of dry-jointed tuff blocks. *Mater. Struct. Constr.* **2016**, *49*, 751–767. [CrossRef]

16. Casapulla, C.; Argiento, L.U. In-plane frictional resistances in dry block masonry walls and rocking-sliding failure modes revisited and experimentally validated—Under review. *Compos. Part B Eng.* **2018**, *132*, 197–213. [CrossRef]

17. Andreini, M.; De Falco, A.; Giresini, L.; Sassu, M. Structural analysis and consolidation strategy of the historic Mediceo Aqueduct in Pisa (Italy). *Appl. Mech. Mater.* **2013**, *351–352*, 1354–1357. [CrossRef]

18. Casapulla, C.; Jossa, P.; Maione, A. Rocking motion of a masonry rigid block under seismic actions: A new strategy based on the progressive correction of the resonance response | Il moto sotto sisma del blocco murario: Analisi per progressiva correzione della risposta in risonanza. *Ing. Sismica* **2010**, *27*, 35–48.

19. Casapulla, C. On the resonance conditions of rigid rocking blocks. *Int. J. Eng. Technol.* **2015**, *7*, 760–771.

20. Ceccotti, A.; Vignoli, A. A hysteretic behavioural model for semirigid joints. *Eur. Earthq. Eng.* **1989**, *3*, 3–9.

21. Foschi, R.O. Modelling the Hysteretic Response of Mechanical Connections for Wood Structures. Available online: http://timber.ce.wsu.edu/resources/papers/7-1-2.pdf (accessed on 9 August 2017).

22. Wong, E.Y. *Verification of an Analytical Hysteresis Model for Dowel-Type Timber Connections Using Shake Table Tests*; University of British Columbia: Vancouver, BC, Canada, 1999.

23. Chui, Y.H.; Ni, C.; Jiang, L. Finite-Element Model for Nailed Wood Joints under Reversed Cyclic Load. *J. Struct. Eng. ASCE* **1998**, *124*, 96–103. [CrossRef]
24. Krawinkler, H. Scale effects in static and dynamic model testing of structures. In Proceedings of the Ninth World Conference on Earthquake Engineering, Tokyo, Japan, 2–9 August 1988; pp. 865–876.
25. MathWorks. *Matlab R2016b*; MathWorks: Natick, MA, USA, 2016.
26. Sarkar, T.K.; Pereira, O. Using the Matrix Pencil Method to Estimate the Parameters of a Sum of Complex Exponentials. *IEEE Antennas Propag. Mag.* **1995**, *37*, 48–55. [CrossRef]
27. Pacific Earthquake Engineering Research Center (PEER). *OpenSees: Open System For Earthquake Engineering Simulation*; PEER: Berkeley, CA, USA, 2006.
28. Internetional Organization for Standardization (ISO). *EN 14080:2013 Timber Structures—Glued Laminated Timber (GLT) and Cross Laminated Timber (CLT)—Requirements 2013*; ISO: Geneva, Switzerland, 2013.
29. Muñoz, W.; Mohammad, M.; Salenikovich, A.; Quenneville, P. Yield point and ductility of timber assemblies: A need for a harmonised approach. *Proc. Annu. Conf. Can. Soc. Civ. Eng.* **2008**, *2*, 1146–1155.
30. National Instruments (NI). *LabVIEW*; National Instruments: Austin, TX, USA, 2012.
31. Gelfi, P.; Giuriani, E.; Marini, A. Stud Shear Connection Design for Composite Concrete Slab and Wood Beams. *J. Struct. Eng.* **2002**, *128*, 1544–1550. [CrossRef]

The TVT Glass Pavilion: Theoretical Study on a Highly Transparent Building Made with Long-Spanned TVT Portals Braced with Hybrid Glass-Steel Panels

Maurizio Froli [1], Francesco Laccone [1,*] and Dario Maesano [2]

[1] Department of Energy, Systems, Territory and Construction Engineering, University of Pisa,
    Largo Lazzarino, 56122 Pisa, Italy; m.froli@ing.unipi.it

[2] Trevi SpA, Via Dismano 5819, 47522 Cesena, Italy; dario.maesano@gmail.com

*   Correspondence: francesco.laccone@destec.unipi.it; Tel.: +39-050-2218229

Abstract: In contemporary buildings, the architectural demand for a complete dematerialisation of load bearing structures can be satisfied only in limited cases with the exclusive structural use of glass. Otherwise, for challenging applications such as long spanned or high-rise structures, the use of hybrid glass-steel systems is mandatory. Glass, fragile but highly compressive resistant, is associated with steel, ductile and tensile resistant. The present research shows the feasibility study for a fully glazed pavilion made of six TVT (Travi Vitree Tensegrity) portal frames longitudinally braced by pre-stressed hybrid glass panels. The frames are about 20 m in span and 8 m in height. Appropriate multiscalar FEM numerical analyses, calibrated on the collapse tests performed on previous TVT large-scale prototypes, stated that the structural performance would be able to withstand heavy static and dynamic loads and stated the observance of the Fail-Safe Design principles.

Keywords: structural glass; hybridism; tensegrity; pre-stressed glass; transparent bracing system; glass buckling; fail safe design

1. Introduction

1.1. Challenges with Structural Glass

In the past century, glass has become a structural material thanks to the vision of some outstanding designers. First used only in secondary building elements, such as infill window panels, glass gradually moved to the main load bearing structural elements such as columns, beams, slabs, curtain walls, facades, and roofs [1,2]. Presently, its use is suitable for many architectural purposes. For new construction, the iconic character of glazed components allows transparency, daylight, and visual lightness. The attraction of people's interest and the characterization of a site is sometimes made possible simply by means of transparent basic geometries [3] (Figure 1a). For renovation projects or in presence of artefacts of high historic and artistic value, a modern transparent skin can wrap existing buildings, consequently increasing the energetic performance and creating new spaces [4] (Figure 1b). Glass denotes a recognizable lightweight intervention, preserving visual contact with the pre-existing structure and conferring upon it a modern appearance. For high-tech components, a further advantage is the possibility offered by laminated glass panels to embed devices in the interlayer substrate. As a result, glass can host new functions such as power generation, solar shading, or image or text transmission thanks to PV cells, luminescent systems, sensors, and programmable cells. The Diamante trigenerative power station symbolizes the efficiency of such integrated design: glass-embedded PV

cells lying on the icosahedron-shaped structure are able to meet the energy demand of the public lighting system of the Parco del Pratolino in Florence, Italy [5] (Figure 1c).

Contemporary architectural needs, brittle failure modality, and scarce random tensile resistance make glass unsuitable for challenging uses for overcoming long spans. Therefore, it is necessary to mechanically connect glass panes with metallic or, in general, ductile elements in order to create hybrid components [6]. Herein, the metallic reinforcement plays a double role. First, it works as a steel bar in the cracked reinforced concrete, or rather contributes in closing the cracks. Second, it avoids the brittle sudden failure of the element (passive reinforced glass elements [7]). If the metallic component is further pre-stressed, a beneficial pre-compression is established on glass, and its apparent tensile resistance is increased (active reinforced glass elements).

Research and experimental activities emphasize the advantages of adopting hybridism. In particular, active pre-stressed beams showed excellent performance: these include beams with a single [8,9] or double [10] glass web reinforced with external tendons, beams with metallic reinforcement adhesively [11–13] or mechanically [14] bonded at the bottom side, and two-sided reinforced glass beams [15,16]. Concerning two-dimensional systems, hybrid solutions are less diffuse than hybrid beams even though glass as a shear frame restraint has been used since the nineteenth century (i.e. in greenhouses). Indeed, the performances of shear walls were extensively investigated in [17–19]. More recently, some researchers used glass panels to stiffen a steel framework [20] and as hybrid shear walls by the adhesive bonding [21] or friction connecting [22] of a glass pane to a wooden frame. A substantial lack of planar or spatial hybrid pre-stressed constructional systems is observed to date, and therefore a globally high-redundant hybrid system to tackle the challenge of transparent long spans is missing.

| (**a**) | (**b**) | (**c**) |
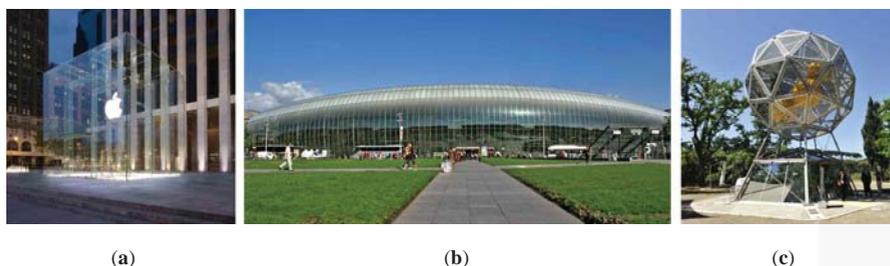
Figure 1. Use of structural glass in contemporary architectures: (**a**) Apple store entrance, New York (USA) [3]; (**b**) Train station, Strasbourg (France) [4]; (**c**) Diamante tirgenerative power station, Parco del Pratolino, Florence (Italy) [5].

1.2. Background and Scope of the Present Research

Among the research concerning hybrid glass systems, Travi Vitree Tensegrity (TVT) active reinforced beams were developed and patented at the University of Pisa. In TVT beams [23,24], the rules of Fail-Safe Design (FSD) [25] were used in the conception and design of their structural behavior. In addition to hybridism and pre-compression, TVTs adopt the principle of segmentation of the entire structural assembly. The structural integrity of the latter is guaranteed only by mutual pre-stressing. Even though radically differing from conventional monolithic beams [26], TVTs reached long spans comparable to those of competing metallic trusses.

The components in the TVTs are doubled and hierarchically calibrated both at local level and at the element level. The latter achieves a ductile behavior. At the Ultimate Limit State (ULS), a global ductile behavior is achieved through crisis by steel bars yielding to precede the buckling failure of the glass panel. At the Serviceability Limit State (SLS), once the glass panels decompression is exceeded, the detachment of the panel vertices from the nodes prevents the opening of cracks. The glass is loaded mostly by compression and shear stresses, thus matching the specific mechanics of the material.

The use of laminated panels complies with the FSD: its quasi-ductile crisis avoids a sudden accidental collapse [27,28].

The intent to extend the use of TVT system in three-dimensional space and to design an iconic, sustainable, and modular pavilion led to the design of the pilot project of the Energy Gallery [29] (Figure 2). Architectural, energetic, and comfort requirements guided the form finding process of the pavilion; consequently, an adaptive structural solution was researched to allow different roof slopes. Because of the longitudinal development of the building, a standardised adaptive TVTγ frame portal was adopted, which was able to follow variations of heights and plan shape. The TVTγ is the third constructional system and was based on TVT principles. The previous two were the TVTα (designed and experimentally validated on a 2970 mm free span) and the TVTβ (designed and experimentally validated on a 3330 mm free span). With the structural and constructional expedients of the TVTγ, a long-spanned 12 m prototype was successfully built at the Structural Laboratory of the University of Pisa. The test-observed data are collected in [23,24].

Each frame portal of the Energy Gallery is made of three or four variously inclined TVTγ beams. The connection between their end nodes is realised by an adaptive joint system, which is made of tubular rods fastened at sleeves. Since all the frame portals had a considerable in-plane strength and stiffness, telescopic hollow steel beams connect each portal with the neighbouring one to assure lateral stability. Those steel tubes support outer glass panels, which act simply as claddings. In order to meet challenging contemporary glass architecture tendencies and to cover wider spaces with a transparent system and to bridge the existing research gap, the Energy Gallery structural system was advanced by defining a new design model, consisting of the following innovations:

- The introduction of a 20 m spanned TVTγ-bis frame portal, derived from the previous TVTγ, with the substitution of the pre-stressed bars with strands. As an effect the transparency, the ULS strength and ductility are increased;
- Simplification and de-materialization of the steel connections (beam-to-column joint and column-to-base joint) in order to excel both the transparency level and the mechanical performances;
- Use of an innovative longitudinal transparent and diffuse bracing system, constituted by hybrid pre-compressed modular glass panels.

Thus, the objective of the present work is to demonstrate the architectural, the structural, and the technical feasibility of such a long-spanned glazed pavilion (TVT Pavilion). The theoretical study of mechanical behavior follows a multi-level approach, from local to global. A geometric and structural description of the pavilion and its components is provided. FEM modelling works and their relative main results are shown and commented on.

(**a**)　　　　　　　　　　　　　　　(**b**)
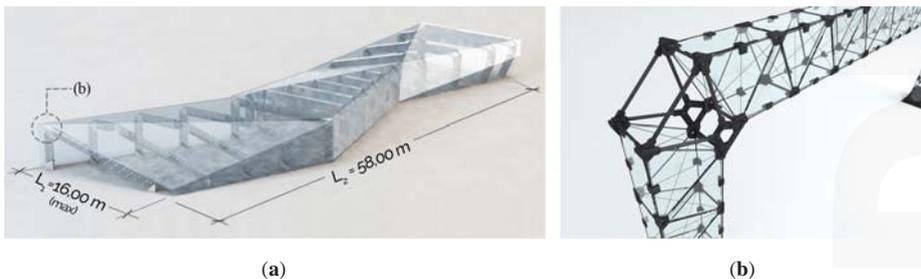
Figure 2. The Energy Gallery pilot project [29]: (**a**) overall view; (**b**) portal frame and beam-to-column connection. Main dimensions: L1 = various (16.00 m max); L2 = 58.00 m; H=various (6.50 m max).

2. Design Principles and Assembly of the TVT Pavilion

The TVT Pavilion is a parallelepiped-shaped building with a rectangular base of about 450 m^2 (21,940 mm × 20,595 mm) and 8076 mm in height. The whole glass skin is supported by six Warren-like portal frames of 20,395 mm span, longitudinally spaced by 4300 mm. Therefore, the main structural elements of the TVT Pavilion are the transversal portal frames, the hybrid bracing system (walls and roof), and the front and back façades (Figure 3). The TVT pavilion adopts the same principles of the TVTs, with advantages at the ULS and at the SLS confirmed by numerous experimental outcomes [18,19]. The installation sequence of the TVT Pavilion shall be conducted in accordance to the following steps (Figure 4):

1. Positioning of the pillars and their pre-compression. Outer, inner, and diagonal strands are pre-stressed with a different load rate to foster a quasi-isotropic compressive stress field on the glass panel. The aim is to reduce the possibility of traction force acting on glass, which arises only if its rate is higher than the compression stress value.
2. On-site assembly and pre-compression of the beams. The system is assembled on a horizontal plane in order to neglect the effect of dead loads. The purpose is to pre-stress the strands with different rates to produce a positive curvature opposite to the deflection of the structure due to its own weight and part of the live loads.
3. Installation of the beams on top of the pillars. The extremities' nodes of the beams and the top of the column are fixed through the corner joinery system.
4. Installation of the vertical panels of the bracing system. The panes are prior pre-compressed on-site.
5. Installation of the horizontal panels of the roof bracing system. The panes are first pre-compressed on-site in order to counteract the deflection due to gravitational loads.
6. Façades assembly. The aluminium mullions are fastened to the frame portals' nodes and ground connected, then the glass panels are placed.
7. All the glass panels are then equipped with waterproofing edge sealants.
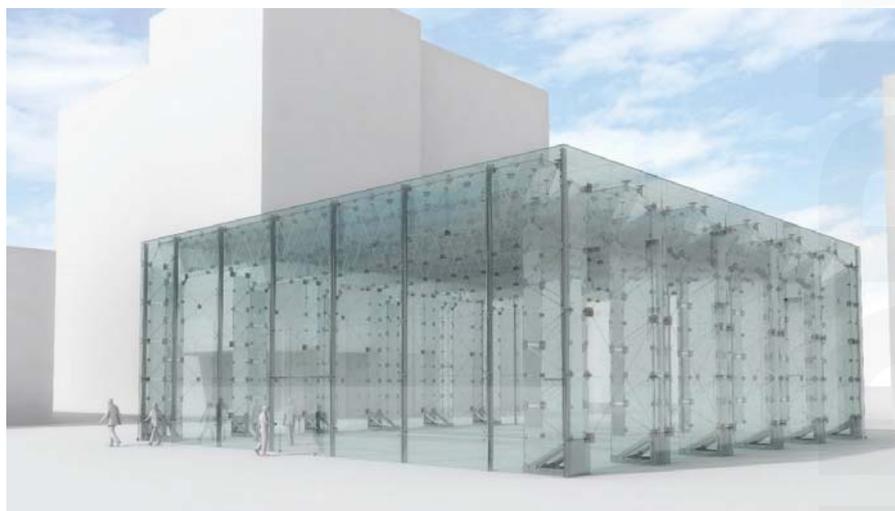
Figure 3. Rendering image of the Travi Vitree Tensegrity (TVT) Pavilion.
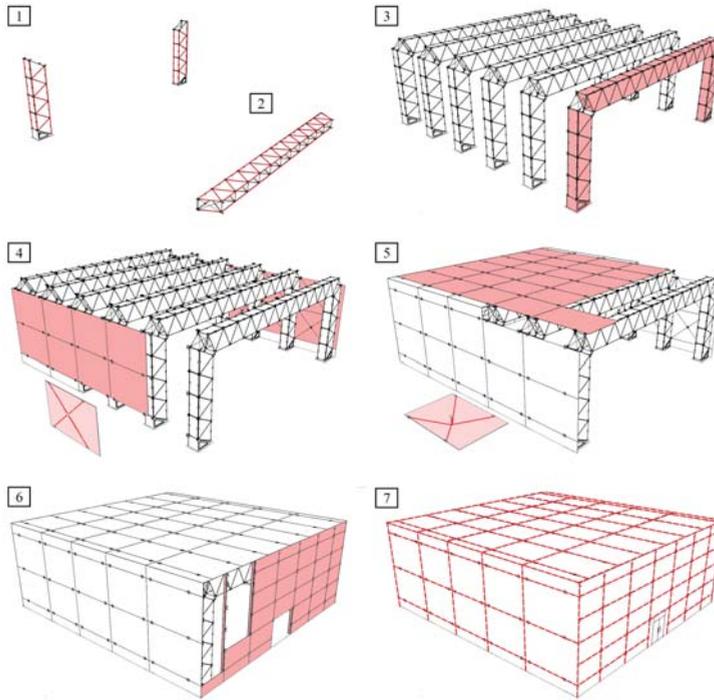
Figure 4. Installation sequence of the TVT Pavilion: **1**. Positioning and pre-stress of the columns and **2**. the beam; **3**. assembly of the TVT portals; **4**. on-site pre-stress and installation of the vertical bracing panels and **5**. the horizontal bracing panels; **6**. assembly of the façade; **7**. edge sealants.

3. Materials and Description of the Main Components of the Structural System

3.1. Materials

The selection of the materials complies with the mechanical performances expected from the building at ULS and SLS, as well as with the principles of FSD. Moreover, even non-structural functions are considered. The materials used in the design of the TVT Pavilion are shown in Table 1.

Table 1. Main materials used in the components of the TVT Pavilion.

Component	Material	Type
TVT Frame portal	Laminated HS [1] glass Steel	10 + 1.52 + 10 mm S355 J2 W P
Hybrid bracing system	Laminated HS [1] glass Steel	8 + 1.52 + 8 + 1.52 + 6 mm [2] S355 J2 W P
Façades	Laminated HS [1] glass Aluminium	10 + 0.76 + 10 Commercial product

[1] Heat strengthened (HS) glass; [2] The latter is a non-structural (outer) layer.

The design values for the strands are referred to the Pr EN 10138-3 [30]. The Young's modulus considered in the following models is E = 201,000 N/mm^2.

In the nodes of the TVTγ-bis and at the recesses of the bracing panels, connections are neither bolted nor glued. In both cases, suitable aluminium spacers were designed in order to avoid tension

peaks at the interface between steel and glass. A 2 mm thick EN AW 6060 T5 aluminium alloy was used [31] with almost the same Young's modulus of glass.

A commercial laminated PVB was designed as an interlayer for the laminated glass panels. The panes of HS glass are glued by means of a 1.52 mm thick PVB foil. In the present study, the shear resistance of the interlayer is neglected because the mechanical properties depend on the load duration and temperature. According to the [32] the strength of glass is calculated as,

$$f_{g,d} = 30.34 \text{ MPa} \tag{1}$$

3.2. TVT Frame portal

The TVTγ-bis frame is a 20 m single span and single story portal. Both the beam and the columns are designed with the TVTγ-bis technique (Figure 4), hence the use of strands as pre-stressed reinforcement prevents the reduction of the mechanically resistant section caused by the mutual connection of the bars. Moreover, thanks to the highest yielding limit of the strands, a smaller cross section is necessary, increasing the transparency of the whole assembly and its mechanical behavior.

The beam of the TVTγ-bis portal has a segmented U-upside-down glass section: spaced by 800 mm, the twin webs are each made of 23 equilateral triangular panels with 1500 mm sides organised in a Warren scheme ([A] of Figure 5. The horizontal outer flange is composed of a series of 12 quadrilateral panels ([B] of Figure 5). The two webs are horizontally connected by means of steel tubes screwed at the 25 nodes ([I] of Figure 5). The two outer extremities of the beam span of 18856 mm and its net height is 1401 mm. As confirmed by further analyses, an inner glass flange was determined to be unnecessary. Therefore, the U-upside-down section was adopted for the whole beam, benefiting from a reduced weight and technological simplicity.
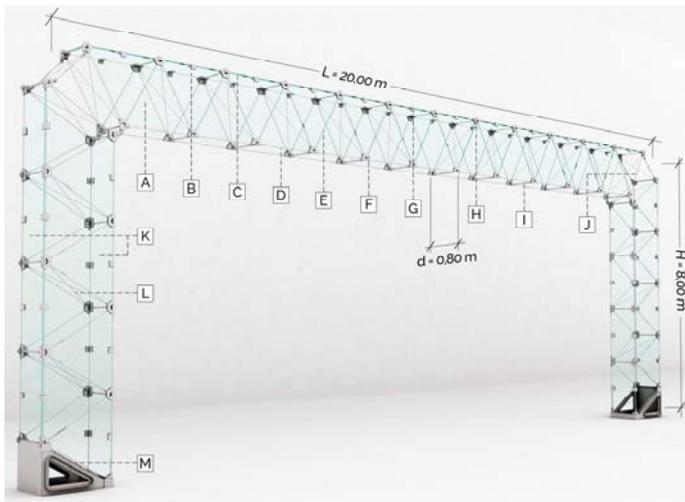
Figure 5. TVTγ-bis frame portal: A—triangular vertical glass panel of the beam (1500 mm side, 10 + 1.52 + 10 mm thickness); B—rectangular outer glass panel of the beam (724 × 1497 mm, 10 + 1.52 + 10 mm thickness); C—outer pre-stressed longitudinal strand Ø11.3 mm; D—inner pre-stressed longitudinal strand Ø11.3 mm; E—diagonal pre-stressed longitudinal strand Ø9.3 mm; F—four-way inner steel node; G—intermediate steel node; H—four-way outer steel node, connection of the bracing panels; I—transversal steel tube; J—beam-to-column joint; K—rectangular glass flange of the column (724 × 1497 mm, 10 + 1.52 + 10 mm thickness); L—pre-stressed diaphragm; M—column-to-base joint.

The 7271 mm height columns have a square TVTγ-bis glass section. Similar to the beam, the two parallel webs are made of eight triangular equilateral panels. Ten steel nodes mutually connect their vertices through the strands. The flanges ([K] of Figure 5) are both composed of four rectangular panels.

The beam-to-column joint is installed between the four end nodes of the beam and the four end nodes at the top of the column respectively (Figure 6a). On the outer side, two chains made of a two steel bars are screwed at the nodes through a fork end and an M14 bolt. An intermediate steel sleeve permits the length regulation of such chain (detail [O] of Figure 6a). A cross-bracing strand system increase the torsional stiffness of the joint. At the bottom (inner side), a finger joint connection with an M24 linchpin is located at a distance of 65 mm from the TVTγ-bis nodes (detail [Q] of Figure 6a). Finally, this joint solution achieves a greater transparency level and by conveniently graduating the lengths of the bars at the outer side. Various amplitudes of the angle between the beam and the column are possible in the range of 60°–120°, yielding an enlarged set of possible architectural solutions for the pavilion.

(**a**)   (**b**)
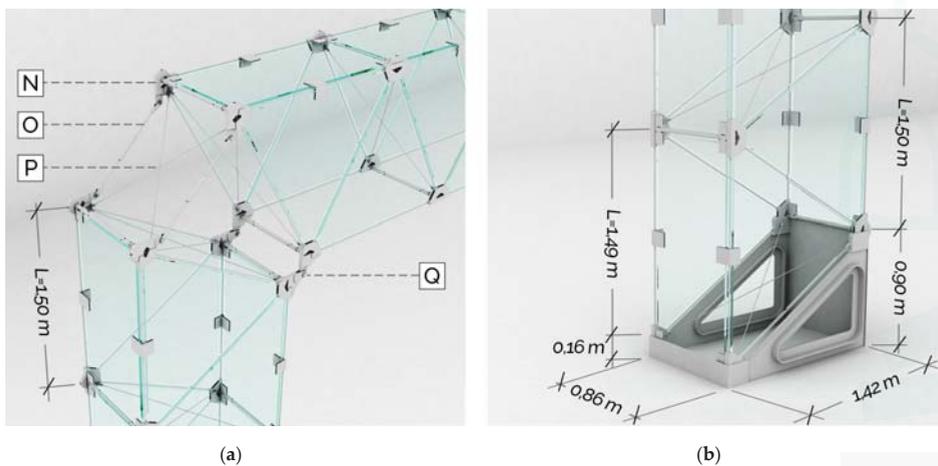
Figure 6. TVTγ-bis frame portal joints (**a**) beam-to-column joint and (**b**) column-to-base joint: N—Extreme node of the beam; O—fork-end steel bars with steel sleeve for regulation; P—cross bracing strands; Q—a finger joint connection with a M24 linchpin.

The column-to-base joint (Figure 6b) transfer the loads from the portal to the foundation while managing the geometrical transition from the horizontal base plane to the triangular segmented Warren sequence. Different heights for inner and outer steel plates re-establish the structural integrity of the flanges. Welded to those steel flanges, the webs are made of twin triangular steel plate with a central homothetic hole stiffened by a continuous transversal rib. Thus, while the ratio between voids and solid of the joint is increased, such triangular cross-section cells are highly resistant.

3.3. Diffuse Longitudinal Transparent Bracing System

The outer skin of the TVT Pavilion performs as a bracing system as well as protection from weather conditions (Figures 7 and 8), and it is made of a series of hybrid pre-compressed glass panels connected to the frame portals. The strategy of supporting the horizontal longitudinal loads is based on the diffuse bracing provided by the panels according to the redundancy and robustness principles of FSD. All the panels are activated in the presence of wind or earthquake to mechanically transfer the shear forces at the frame portal and the base. Moreover, in case of the accidental failure of one of them, the neighbouring panels are able to adsorb extra loading with an alternative path.

The rectangular glass panel is the hybrid glass-steel re-interpretation of the classic metallic cross bracing system: a three-layered HS rectangular glass panel is pre-stressed by means of two diagonal steel cables, whose extremities are at the panel vertices. Thus, the compressed zone is generated along the diagonals of the panel due to pre-stressing counterbalances for the traction forces induced by the external load. In case of glass breakage, the cables are still able to withstand a reduced amount of that horizontal force. The panel is a laminated 8 + 1.52 + 8 + 1.52 + 6 thick. The latter pane has no structural purpose: its only aim is to provide the system a higher redundancy and hierarchy, so that in case of accident, the double structural panel is protected by the 6 mm outer sacrificial panel.
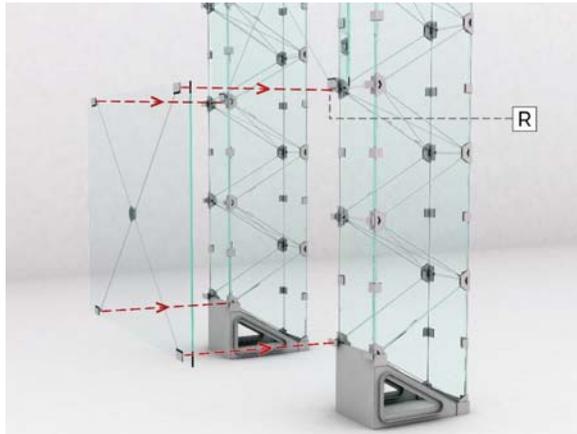
Figure 7. Hybrid longitudinal wall bracing system: R—point fixing of the panel corners to the TVTγ-bis nodes by means of pole-and-plate devices.
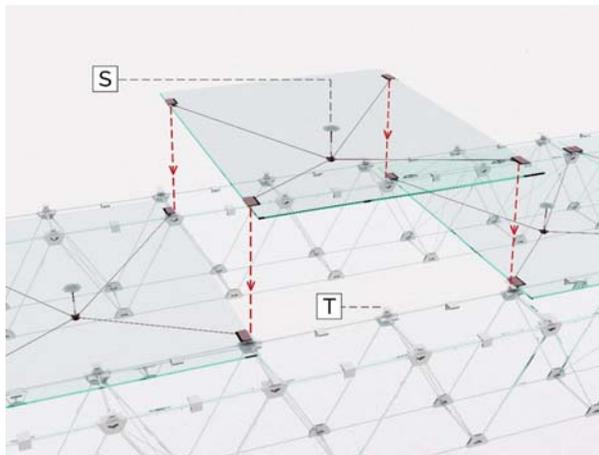
Figure 8. Hybrid longitudinal roof bracing system: S—steel tubular strut; T—intermediate midspan support of the panel out-of-plane load.

The mutual load transfer between cables and glass occurs at the interface of rounded recesses practiced in the panel, which allows the interlocking of a steel plate right inside (detail [W] of Figure 9). The extremities of the cables are connected at the inner side of the plate. The steel insert works

by unilateral contact in the transferring of the compression forces to the panel, playing the same mechanical role as the steel nodes within the TVTs. The panel is pre-stressed and then mounted at the TVTγ-bis outer nodes, where specific supports, made of a steel plate with a pole screwed on each TVT node, are arranged (detail [Y] of Figure 9).

Roof and wall panels differ in the position of the cross cables with respect to the glass, and consequently of the modality of its pre-compression. In the wall panels, the cables act in a plane parallel to the midplane of the glass (Figure 7). The cables cross within a suitable steel point fixing, adhesively bonded to glass with the aim of favouring the distribution of compression stresses.

In the roof panels, due to the vertical loads (Figure 8), the panel is pre-compressed as a reinforced plate through the cables and a central tubular strut. Therefore, the deflection caused by the weight of the panel is balanced by the pre-stressing of the cables. To avoid excessive localized stresses, a circular 200 mm plate is welded at the top of the strut and adhesively fixed at the glass panel (detail [S] of Figure 9). An additional out-of-plane-load support is located at the midspan of the shortest side of the panel (steel plate and pole, detail [T] of Figure 8).

Except for the minimal opaque presence of the cables and the central fixings, the bracing panels are fully transparent. Moreover, all of them may be equipped with integrated devices with the aim of fulfilling the insulation, shading, waterproofing, energy production and ICT requirements, besides their structural purposes. In order to standardise and reduce production costs, two sizes for the wall panels and two for the roof panels are employed.
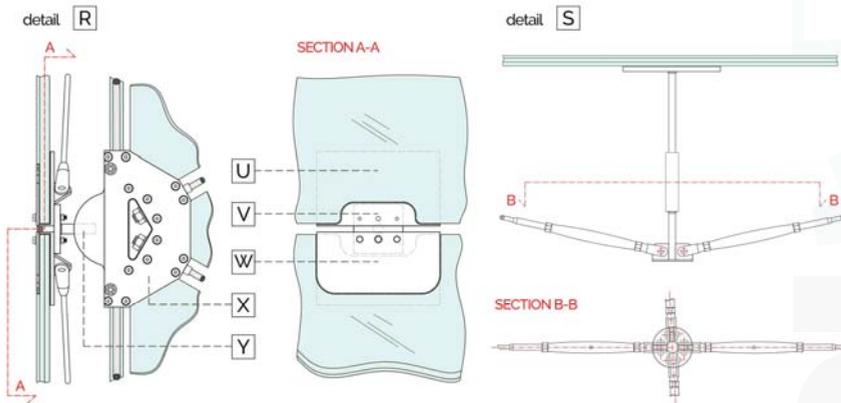
Figure 9. Details of the bracing panels: U—Glass panel with rounded recesses; V—steel plate (compression only contact with the glass); W—outer steel clamping; X—TVTγ-bis node; Y—steel pole.

3.4. Façades

The façades constitute the front and back walls of the TVT Pavilion and are installed on the first and the last TVTγ-bis portals. Each of them has a surface of 160 m^2 (20,595 × 8076 mm), which is made of 40 panels (four different types). The four point–supported panels are linked through a commercial spider system to elliptical cross sectioned aluminium mullions. A vertical slotted hole at the top of the mullion allows the transferring of the out-of-plane actions only, while the vertical load is sustained by the base-joint. The spacing of the mullions follows the position of the TVTγ-bis nodes. A 15 mm waterproofing sealant accommodates deformations and tolerances of the panels.

4. Methods

The TVT Pavilion mechanical behavior is numerically investigated by means of the software Straus7 release 2.3.3 [33]. The aim was to assess the strength and the stability of both the global system

and its components by means of FEA. Developing an accurate and consistent numerical model is always recommended, but it can lead to an excessive and time-consuming process. The strategy followed in the present research consists in realizing multi-scalar numerical manageable models from local to global. The higher order model is less accurate with respect to the lower one from a FEM viewpoint, but still suitable for its specific purpose. Development emerges from fully detailed local models, then a beam-segment model, a beam model, a frame model and finally a global model were developed, with each of them is mechanically akin to the lower one. Linear and non-linear analyses were conducted. The latter considering material, contact and geometric nonlinearities.

This paper presents the results and the discussion of the main numerical models developed for the TVT Pavilion (Figure 10), whose purposes are the followings:

- BM TVTγ-bis (Beam Model): 3D model of a quarter of beam (double half-symmetry for geometry and loads). The beam is pinned at the extreme nodes. The purpose is to assess the ULS strength and ductility and the buckling phenomena;
- FM TVTγ-bis (Frame Model): 3D model of a quarter of beam and half column (double half-symmetry with respect to the mid plane of the portal and transversal mid plane of the beam). Its purpose is to study the mechanical behavior of the portal. Special attention is paid to the corner joint which is crucial for the overall portal study;
- CFM TVTγ-bis (Complete Frame Model): Simplified 3D model of the portal frame, calibrated on the previous one to obtain the same static performances. It is used as frame in the PM TVTγ-bis;
- PM TVTγ-bis (Pavilion Model): 3D global model of the pavilion, made of 6 CFM TVTγ-bis and hybrid glass panels as bracing.

(**a**)

(**b**)

(**c**)

(**d**)
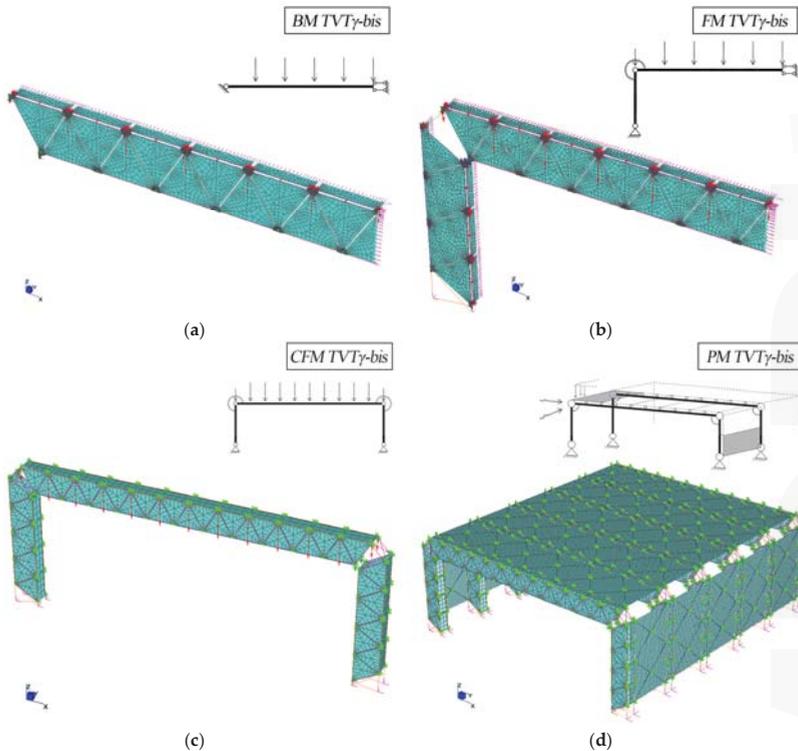
Figure 10. FE models: (**a**) BM TVTγ-bis; (**b**) FM TVTγ-bis; (**c**) CFM TVTγ-bis; (**d**) PM TVTγ-bis.

Although the equivalent geometrical imperfections are usually introduced in the models because of the slenderness of glass components, they were only considered in the sizing of the structural parts carried out with analytical calculations. Indeed, in the previous studies, TVTs FEA output was scarcely affected by the introduction of imperfections, and therefore, in this research, imperfections are not considered in FEMs.

The outer layer of the laminated panel of the bracing system has no structural role, and as a consequence it is considered only as a dead load. Leading to a conservative approach, the PVB interlayer is modelled as an out-of-plane constraint for the twin glass panes, neglecting its shear stiffness. Therefore, the laminated panel is modelled as two parallel meshed plates with an out-of-plane pin connection (Figure 11). The level of detail reached in the models is dependent on their size. The mesh refinement is scaled accordingly, as well as the accuracy in the contact of the components within the system. Figure 11 shows the node neighbourhood for a detailed model (a) and for a simplified model (b). In the first case, the aluminium spacer is introduced as a strip of (red) plate elements surrounded by special links to simulate the contact with the glass and the out-of-plane restraint. In the second case, the simplified model is calibrated on the previous one.

(**a**)   (**b**)
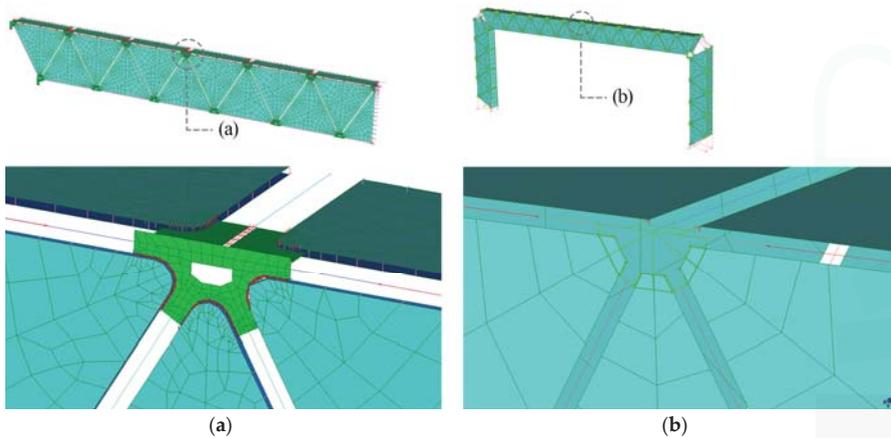
Figure 11. Details on modelling the main elements and contacts for the (**a**) BM TVTγ-bis and FM TVTγ-bis; and the (**b**) CFM TVTγ-bis and PM TVTγ-bis.

5. Multiscalar Modelling and Analyses Result

5.1. BM TVTγ-bis Model

In the preliminary phase, the components of the TVT system were designed at first with analytical calculations descending from the Warren truss scheme [34]. The aim was to localize the main tensioned and compressed areas and provide them with suitable structural load bearing capacity. The 10 + 1.52 + 10 mm thickness of glass was proved by a non-linear buckling analysis on a beam-segment model made of two triangular webs and one rectangular flange.

Then, a three-dimensional FE model was built by using beams, cables, plates, and links to simulate steel beams, strands, glass panels, and their mutual connections, respectively. The modeling phase was strongly assisted by the TVTs state of the art—or rather past experimental and numerical—outcomes. The external beam joints were pinned, while appropriate boundary conditions assured the symmetry along the transversal and the longitudinal midplanes. By setting up the material properties, the dead load is automatically affixed. For non-linear analyses, the live loads are concentrated in the steel nodes, accordingly with the load path design, and introduced step by step (Figure 10a).

With the aim of selecting the optimal solution between the TVTγ-bis with pre-stressed bars and the TVTγ-bis with pre-stressed strand, a non-linear comparative analysis was performed. Until the decompression of the SLS of glass panels, the two investigated structures manifested similar stiffness (Figure 12). Beyond that limit, for the same load, the beam with bars is stiffer than the beam with strands, but in the meantime, its behavior is less ductile. Then, the TVTγ-bis with pre-stressed strand was adopted due to its ductility. However, the deflection of both solutions accomplished the SLS requirements.

The FEA of the BM TVTγ-bis confirmed the static behavior expected from the analytical calculations, instead of the deformative behavior that could not have been predicted because it is mostly influenced by the presence of the vertical triangular glass panels. Figure 13 reports the maximum and the minimum stresses for non-linear static analysis, beyond the SLS of panels decompression. Higher values of tensile stress in glass are located along the edges of the panels close to the external supports. Regardless, they reach a value greater than 9 MPa.
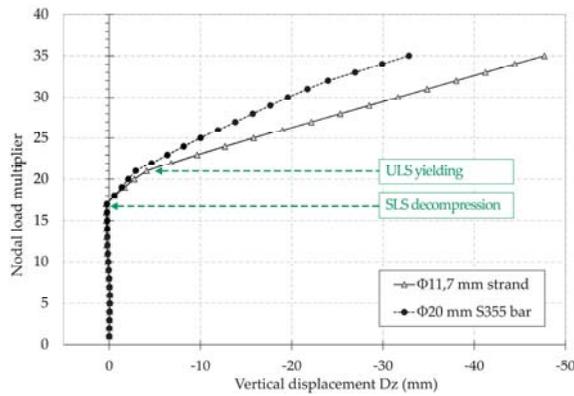
Figure 12. Comparison between the TVTγ-bis beams with pre-stressed bars and pre-stressed strands: load multiplier vs midspan deflection.
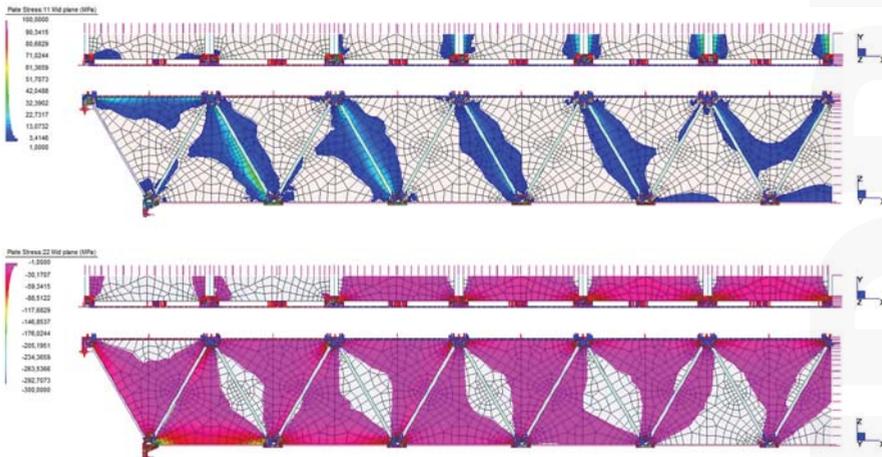
Figure 13. BM TVTγ-bis ULS non-linear static analysis: at the top, maximum principal stress; at the bottom, minimum principal stress.

5.2. FM TVTγ-bis Model and CFM TVTγ-bis Model

The FM TVTγ-bis model (Figure 10b) highlights the real expected static and deformative behavior of the beam under the influence of the column and the beam-to-column node stiffness. The finger joint connection was modelled by using plates, while the nodes and the bars by links and beams.

The lower strand of the beam reaches the ULS of yielding at the mid-span length for a nodal loading of 12 kN, showing as expected higher deformations in comparison with the BM TVTγ-bis. However, the adopted load configuration of uniform nodal loads is not matching the real design requirements because the mid-length support of the bracing panel (detail [T] of previous Figure 8) carries a three times lower load with respect to the adjacent supports (or rather where the bracing panel is fastened on the steel plate). Consequently, the structural performances are even greater than those simulated by the present model.

Besides the maximum axial force at the mid-span length, the greater displacement of the panels' lower edge from their slot appears. The deflection of the beam is limited due to an additional pre-stressing practiced on the outer strands of the columns.

The fine FE modelling detail level of the FM TVTγ-bis constituted a limit for its implementation on a global model PM TVTγ-bis. To lighten the computational task, a simplified model CFM TVTγ-bis (Figure 10c) was created. In the latter, preserving the same static outcomes of the FM TVTγ-bis, a coarse mesh was adopted, fewer links or point contacts between steel and glass were used, and the flanges of the portals were substituted by suitable equivalent beams whose stiffness was deducted from a detailed local model. The comparison between the models at the ULS shows a good agreement (Figure 14). At the increasing of the live loads, the CFM TVTγ-bis results are stiffer than the FM TVTγ-bis. However, both the SLS of glass decompression and the yielding of the strands occur for the same nodal loads, but with a 10% displacement difference (Figure 14a). The glass stresses comply in both the models if evaluated at an appropriate distance from their vertices in order to avoid peak values (Figure 15). Since the axial forces of the outer strands are conditioned by the introduction of the equivalent beam flanges, a consistent comparison is not possible, whereas the lower strands of both models are perfectly agreed, as shown in Figure 14b. This result enables the CFM TVTγ-bis to be used as a frame portal in the global PM TVTγ-bis due to its static equivalence with the FM TVTγ-bis. The maximum principal peak value is reported in Figure 16, evaluated on the more detailed FM TVTγ-bis. However, such value is below the value from Equation (1).

(a)   **(b)**
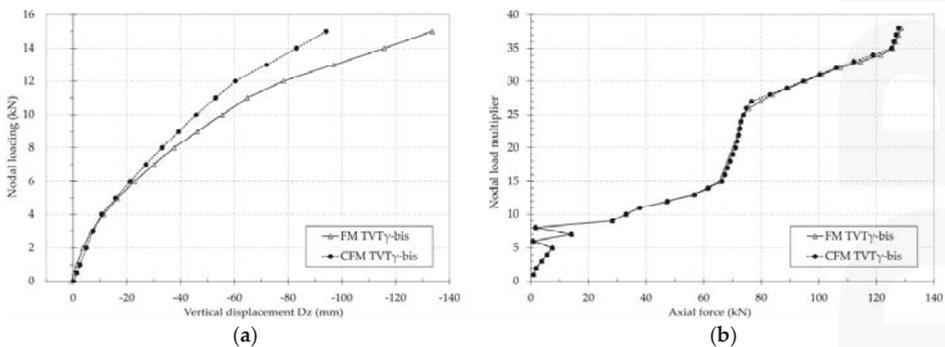
Figure 14. Comparison between the FM TVTγ-bis and the CFM TVTγ-bis: (**a**) nodal load vs. mid-span deflection; (**b**) nodal load vs. axial force in the lower strand.

(**a**)   (**b**)

(**c**)   (**d**)
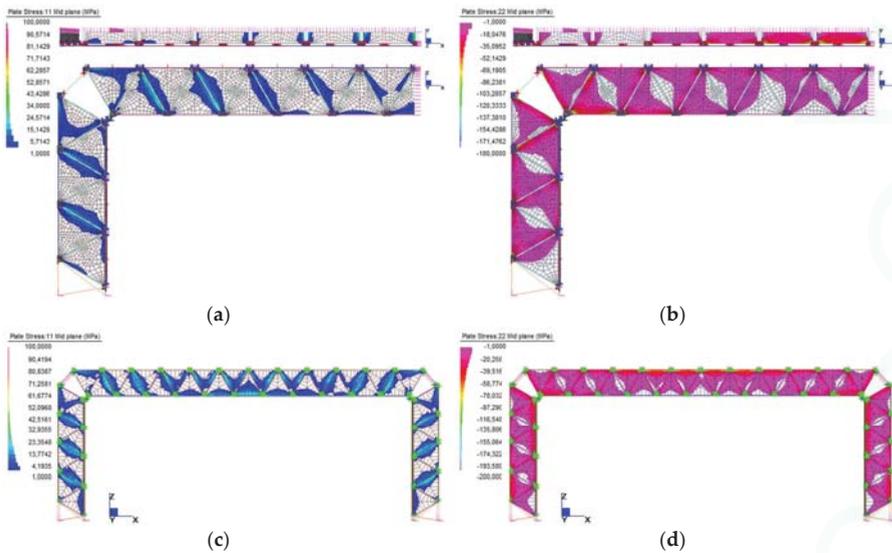
Figure 15. ULS non-linear static analysis and comparison between FM TVTγ-bis (first row) and CFM TVTγ-bis (second row): (**a, c**) maximum principal stress; (**b, d**) minimum principal stress.
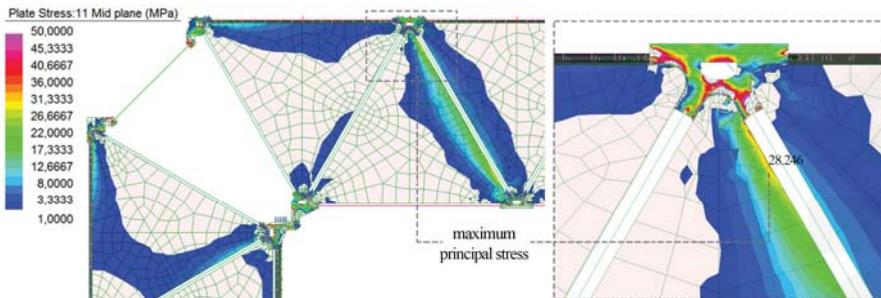
Figure 16. Details of the maximum principal stress in the FM TVTγ-bis. The peak value is below the strength of glass from Equation (1).

5.3. PM TVTγ-bis Model

The aim of the global model PM TVTγ-bis (previous Figure 10d) is to verify the overall load bearing capacity and the compliance with the hierarchy principle of the FSD. Herein, six models of CFM TVTγ-bis spaced by 4300 mm are braced by hybrid panels modelled with shell and beam elements. Suitable link elements allow the loading transmission, simulating the structural behavior of the plate-and-pole connections. The façades are excluded from the model, considering only the wind loading transferred to the nodes of the first and the last TVTγ-bis portals. Such a simplification is compatible with the conception and the designed structural behavior of the TVT Pavilion. Moreover, the analysis and the safety assessment of the façade was carried out separately based on the guidelines CNR DT 210 [23].

The stresses on the pavilion components are the results of combinations of dead, wind (transversal and longitudinal), snow, roof and earthquake loads as from [35]. In the non-linear analyses, the sequence of loading follows the assembly phases, in order to take into account the pre-stressing of the

strands. The construction site was located in Trieste to maximize the entity of the wind action, while the earthquake load combinations were lower than the wind ones because of the lightweight nature of the pavilion.

In the combinations with prevailing horizontal load, the bracing panels manifest the typical tie-strut mechanism in the midplane of both the wall and the roof panels (Figure 17). However, the glass panel is mostly affected by the presence of one main diagonal "strut" zone since the pre-stressing of glass has a favourable effect. Indeed, the opposite diagonal zone is decompressed as a compensation to the external induced tractions.

(**a**) (**b**)
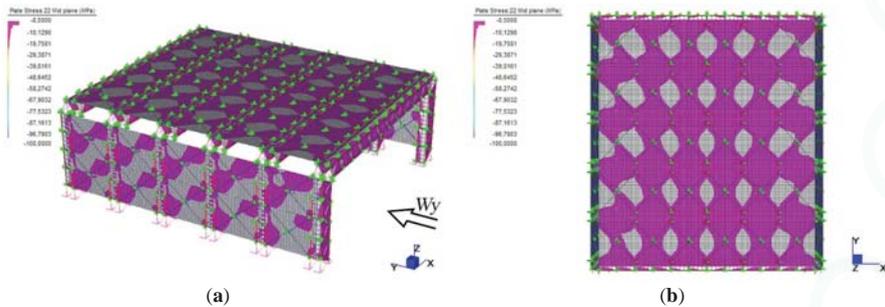
Figure 17. PM TVTγ-bis ULS non-linear static analysis, minimum principal stress: (**a**) global view; (**b**) plan view.

The maximum positive stresses in glass are located in the portal frames within the limits of technical recommendations [32] as shown by previous Figure 16. Neither local nor global failure mechanism was observed for different load configurations. The ULS of yielding of the lower strands, as much stressed structural elements, was not overstepped. In linearly growing the live loads, the yielding of the lower strands always precedes the buckling of the bracing panels for any load combination, in accordance with the structural hierarchy and ductility. Moreover, the buckling of the bracing panel is calibrated with respect to the mechanism showed in Figure 18. The first buckling factor for in-plane loading of a roof bracing panel concerns the instability of the steel strut. The panel can buckle for a much higher load. A further safety margin can be achieved by increasing the stiffness of the strut. At the SLS, the PM TVTγ-bis is not suitable for the evaluation of deflections because it was created with ULS static equivalence.

$\lambda_1 = 1.55$ $\lambda_2 = 12.6$
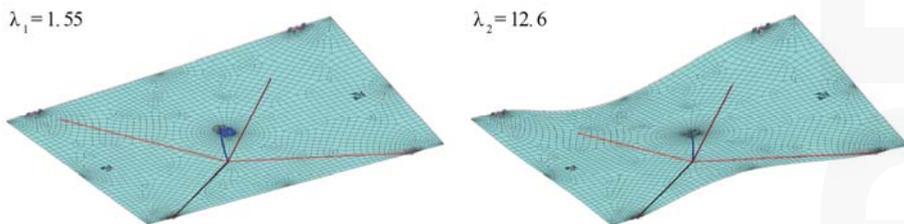
Figure 18. Buckling analysis of the hybrid roof bracing panel.

6. Discussion and Conclusions

Hybridism is a unique strategy for reaching long spans with glass components in accordance with the FSD. The TVT constructional system, based on segmentation and the mutual pre-stressing of the components, is able to maximise the mechanics of both materials with high performances both at the ULS and at SLS, guaranteeing the full transparency of the load bearing structures.

The technical and technological feasibility of a long-spanned hybrid pavilion is demonstrated in the models used here, which are calibrated on the past numerical and experimental experiences of the 12-m-spanned TVTγ beam. The TVT Pavilion is able to overcome state-of-the-art glass structures competitors thanks to its 20 m-spanned TVTγ-bis frame portal and a diffuse hybrid pre-stressed glazed bracing system. Additionally, thanks to the high standardisation of its components, the costs of fabrication and reparse are certainly reduced.

Possible uses of the TVT pavilion are as exhibition buildings, sheltering of artefacts, or advanced building envelopes. Indeed, the sacrificial layer in the bracing panels constitutes both a structural safety measure and the possibility to integrate in the interlayer thickness miniaturized devices for energy production, lighting or communicative purposes. By admitting various roof slopes, the beam-to-column joint permits wide architectural design freedom, and concurrently the use of fewer and simpler elements improves the transparency of such a connection.

The limitations of the Energy Gallery have been overcome. With the use of pre-stressed strands, the TVTγ-bis system reaches longer spans, achieving more transparency. Moreover, the higher ductility level increases the possibility of using it in presence of static and dynamic loads. By means of a calibrated design, the yielding of the most tensioned (lower) strand always precede the buckling failure of glass. The high local and global redundancy—obtained through hybridism, ductility, segmentation, and mutual pre-stressing—makes this system suitable for the intended use.

The post-breakage behavior of the TVTγ-bis is objective of further work. After the breakage of multiple components, the system is expected to maintain a sufficient load bearing capacity. Moreover, the substitution of the damaged parts gives the opportunity for a cost-saving replacement strategy. The post-breakage behavior and the replacement of components were observed for the TVTγ prototype. After the yielding of the lower bar, the prototype was unloaded and the damaged steel member was changed. In a further test, the buckling of one glass panel was observed. At the unloading, the yielded steel and the crushed panel were substituted. An undamaged new prototype was obtained. The accidental rupture of multiple panels was also experienced on the TVTγ prototype, and the damage specimen could withstand its own weight and part of the live loads. The probabilistic (accidental) failing of multiple panels and their effect on the global structural behavior can be simulated in future FEA works.

Some design recommendations are provided. The steel relaxation and the thermal effects can affect the pre-stress of strands, reducing it. This aspect has not been considered and should be tested with an experimental prototype.

The longitudinal diffuse bracing system appears to be one of the most innovative features of the TVT Pavilion because glass is efficiently used in the load transmission and not weakened by exposing it to positive stresses. The pre-stressed cables halved the apparent traction resistance of the panel and constitute an additional safety measure in case of the accidental failure of the glass. The overall conception is consistent with the glass design philosophy. The connections of the hybrid panel and the links of the panel with the structure underneath are the key design points of the system. Future study is intended to experimentally and numerically evaluate the buckling of such a promising bracing system by varying its main design parameters. Experimental validation on the connections is also needed.

The adopted multilevel methodology accomplishes time saving ULS structural checks. Hierarchy and structural redundancy are also verified. However, SLS decompression and deflections controls were not possible in the global PM TVTγ-bis due to the simplification induced by the CFM TVTγ-bis. Further work is needed to calibrate a high-resolution models or alternative models to fill this gap. In conclusion, the obtained results confirm the development of the designed controllable load paths and a good distribution of the compression stress in the glass components.

References

1. Emami, N. Glass structures, from theory to practice. In *Structures and Architecture: New concepts, Applications and Challenges*; Cruz, P.J.S., Ed.; CRC Press: Boca Raton, FL, USA, 2013; pp. 305–311.
2. Schober, H.; Schneider, J. Developments in structural glass and glass structures. *Struct. Eng. Int.* **2004**, *14*, 84–87. [CrossRef]
3. O'Callaghan, J. Adventures with Structural Glass. *Glass Perform. Days* **2012**.
4. Baldassini, N.; Raynaud, J. Free-form, form finding and anisotropic grid shell. In Proceedings of the Symposium of the International Association for Shell and Spatial Structures—Evolution and Trends in Design, Analysis and Construction of Shell and Spatial Structures, Valencia, Spain, 28 September–2 October 2009; pp. 966–976.
5. Froli, M.; Masiello, G. Una centrale solare trigenerativa alla corte del granduca di Toscana. *Inossidabile* **2010**, *180*, 16. (In Italy)
6. Kozłowski, M. Hybrid glass beams. Review of research projects and applications. *Arch. Civ. Eng. Environ.* **2012**, *5*, 53–62.
7. Louter, C.; Belis, J.; Veer, F.; Lebet, J.P. Structural response of SG-laminated reinforced glass beams; experimental investigations on the effects of glass type, reinforcement percentage and beam size. *Eng. Struct.* **2012**, *36*, 292–301. [CrossRef]
8. Jordão, S.; Pinho, M.; Martin, J.P.; Santiago, A.; Neves, L.C. Behaviour of laminated glass beams reinforced with pre-stressed cables. *Steel Constr.* **2014**, *7*, 204–207. [CrossRef]
9. Feng, R.Q.; Ji, Y.; Yao, Y. A New Type of Structure: Glass Cable Truss. *J. Bridge Eng.* **2015**, *20*, 04015024. [CrossRef]
10. Engelmann, M.; Weller, B. Post-Tensioned Glass Beams for a 9 m Spannglass Bridge. *Struct. Eng. Int.* **2016**, *26*, 103–113. [CrossRef]
11. Louter, C.; Cupać, J.; Lebet, J.P. Exploratory experimental investigations on post-tensioned structural glass beams. *J. Facade Des. Eng.* **2014**, *2*, 3–18.
12. Cupać, J.; Martens, K.; Nussbaumer, A.; Belis, J.; Louter, C. Experimental investigation of multi-span post-tensioned glass beams. *Glass Struct. Eng.* **2017**, *2*. [CrossRef]
13. Bedon, C.; Louter, C. Finite Element analysis of post-tensioned SG-laminated glass beams with adhesively bonded steel tendons. *Compos. Struct.* **2017**, *167*, 238–250. [CrossRef]
14. Bedon, C.; Louter, C. Finite-element analysis of post-tensioned SG-laminated glass beams with mechanically anchored tendons. *Glass Struct. Eng.* **2016**, *1*, 39–59. [CrossRef]
15. Martens, K.; Caspeele, R.; Belis, J. Numerical investigation of two-sided reinforced laminated glass beams in statically indeterminate systems. *Glass Struct. Eng.* **2016**, *1*, 417–431. [CrossRef]
16. Martens, K.; Caspeele, R.; Belis, J. Load-carrying behaviour of interrupted statically indeterminate reinforced laminated glass beams. *Glass Struct. Eng.* **2016**, *1*, 81–94. [CrossRef]
17. Englhardt, O. Flächentragwerke aus Glas—Tragverhalten und Stabilität. Ph.D. Thesis, University of Natural Resources and Life Sciences, Vienna, Austria, 2007.
18. Huveners, E.M.P.; van Herwijnen, F.; Soetens, F.; Hofmeyer, H. Glass panes acting as shear wall. *HERON-ENGLISH EDITION* **2007**, *52*, 5–29.
19. Wellershoff, F. Nutzung der Verglasung zur Aussteifung von Gebäudehüllen. Ph.D. Thesis, RWTH Aachen University, Aachen, Germany, 2006.
20. Haarhuis, K.; Wever, T. Glass-reinforced steel structures. *Glass Struct. Eng.* **2016**, *1*, 195–203. [CrossRef]
21. Štrukelj, A.; Ber, B.; Premrov, M. Racking resistance of timber-glass wall elements using different types of adhesives. *Constr. Build. Mater.* **2015**, *93*, 130–143. [CrossRef]
22. Antolinc, D.; Žarnić, R.; Stepinac, M.; Rajéic, V.; Krstevska, L.; Tashkov, L. Simulation of earthquake load imposed on timber—glass composite shear wall panel. In *COST Action TU0905 Mid-term Conference on Structural Glass*; CRC Press: Boca Raton, FL, USA, 2013; pp. 245–252.
23. Froli, M.; Lani, L. Glass Tensegrity Trusses. *Struct. Eng. Int.* **2010**, *20*, 436–441. [CrossRef]
24. Froli, M.; Mamone, V. A 12 m long segmented, post-tensioned steel-glass beam (TVT Gamma). In Proceedings of the Challenging Glass 4 & COST Action TU0905 Final Conference, Lausanne, Switzerland, 6–7 February 2014; pp. 243–251.
25. Haldimann, M.; Luible, A.; Overend, M. *Structural Use of Glass*; IABSE: Zürich, Switzerland, 2008.

26.   Ringli, R.; Vogel, T. Load-bearing behavior of spliced glass beams under bending action. *Glass Struct. Eng.* **2016**, *1*, 61–80. [CrossRef]

27.   Biolzi, L.; Cagnacci, E.; Orlando, M.; Piscitelli, L.; Rosati, G. Long term response of glass-PVB double-lap joints. *Compos. Part B: Eng.* **2014**, *63*, 41–49. [CrossRef]

28.   Biolzi, L.; Orlando, M.; Piscitelli, L.R.; Spinelli, P. Static and dynamic response of progressively damaged ionoplast laminated glass beams. *Compos. Struct.* **2016**, *157*, 337–347. [CrossRef]

29.   Froli, M.; Masiello, G.; Melis, A.; Mamone, V.; Giammattei, M. The Energy Gallery: A pilot project in Pisa. In Proceedings of the Engineered Transparency—International Conference at Glasstec, Düsseldorf, Germany, 21–22 October 2014; pp. 621–628.

30.   European Committee for Standardization. *Pr EN 10138–3: Prestressing Steels-Part 3: Strand*; CEN: Brussels, Belgium, 2000.

31.   Consiglio Nazionale delle Ricerche. *CNR DT 208/2011: Istruzioni per la Progettazione, l'Esecuzione ed il Controllo di Strutture di Alluminio*; CNR: Rome, Italy, 2011. (In Italy)

32.   Consiglio Nazionale delle Ricerche. *CNR DT 210: Istruzioni per la Progettazione, L'esecuzione e il Controllo di Costruzioni con Elementi Strutturali di Vetro*; CNR: Rome, Italy, 2012. (In Italy)

33.   Computing, G. *Straus7 User's Manual*; G+D Computing: Sydney, Australia, 2005.

34.   Mamone, V. Experimental, Numerical and Analytical Investigations on the Segmented Post-Tensioned Hybrid Steel-Glass Beams TVT. Ph.D. Thesis, University of Pisa, Pisa, Italy, November 2015.

35.   Italian Min. Inf. Norme Tecniche per le Costruzioni. Available online: http://www.gazzettaufficiale.it/eli/id/2008/02/04/08A00368/sg (accessed on 2 December 2016).

Effect of Material Variability and Mechanical Eccentricity on the Seismic Vulnerability Assessment of Reinforced Concrete Buildings

Mario Lucio Puppio [1],*, Martina Pellegrino [1],*, Linda Giresini [1] and Mauro Sassu [2]

[1] Department of Energy, Systems, Territory and Construction Engineering; University of Pisa, Pisa 56126, Italy; linda.giresini@unipi.it

[2] Department of Civil, Environmental Engineering and Architecture, University of Cagliari, 09123 Cagliari, Italy; msassu@unica.it

* Correspondence: mariolucio.puppio@ing.unipi.it (M.L.P.); martina.pellegrino@gmail.com (M.P.); Tel.: +39-050-2218204 (M.L.P.)

Abstract: The present paper deals with the influence of material variability on the seismic vulnerability assessment of reinforced concrete buildings. Existing r.c. buildings are affected by a strong dispersion of material strengths of both the base materials. This influences the seismic response in linear and nonlinear static analysis. For this reason, it is useful to define a geometrical parameter called "material eccentricity". As a reference model, an analysis of a two storey building is presented with a symmetrical plan but asymmetrical material distribution. Furthermore, an analysis of two real buildings with a similar issue is performed. Experimental data generate random material distributions to carry out a probabilistic analysis. By rotating the vector that defines the position of the center of strength it is possible to describe a strength domain that is characterized by equipotential lines in terms of the Risk Index. Material eccentricity is related to the Ultimate Shear of non-linear static analyses. This relevant uncertainty, referred to as the variation of the center of strength, is not considered in the current European and Italian Standards. The "material eccentricity" therefore reveals itself to be a relevant parameter to considering how material variability affects such a variation.

Keywords: material variability; strength domain; seismic assessment of r.c. buildings; nonlinear static analysis

1. Introduction

Reinforced Concrete buildings built during the 40–70s are affected by a large dispersion of mechanical properties, especially when concrete is considered. This is due to (1) the inadequate mix-design of concrete (with a huge dispersion of water-concrete ratio); (2) the use of unwashed or low quality aggregates; (3) the lack of automation and control of the concrete production; (4) ineffective procedures for the concrete casting batch and vibration [1,2]. This dispersion can be quantified through the definition of a geometrical parameter called material eccentricity [3,4]. Also, other parameters had a great relevance in the seismic evaluation of existing structures e.g., the geometry of the bearing elements, the aging of the concrete, corrosion, the type of subsoil [5–8].

The building characterization [9,10] has great relevance, in particular, to the seismic vulnerability assessment [11], in which non-structural elements also play a relevant role [12–14]. According to previous experiences on the monitoring and rehabilitation of existing buildings [4,15–17] it is possible to notice significant uncertainties in the mechanical properties of both concrete and steel bars. Innovative and traditional techniques—in particular, additional reinforcement [18,19], are not able to cover all these uncertainties. The tendency of the current Standards, e.g., [20], is to penalize the mean value

of the materials' strength with a specific "confidence factor" depending on the available information. This approach does not take into account the real distribution of the mechanical values, together with their standard deviation in material tests [21].

Nevertheless, the tendency to carry out a probabilistic analysis of existing buildings through the assessment of the uncertainties modelled with random and epistemic variables might imply analytical complications. A significant analysis can be the assessment of a material eccentricity, which induces two different effects: eccentricity of stiffness and eccentricity of strength. In the present paper both aspects are analysed.

The effects of spatial variability of concrete and steel strength are considered in this paper for typical Italian r.c. buildings. Firstly, the effect of material variability on the strength domains of the usual failure mechanisms is evaluated in Section 2, according to [22]. Those domains are related to eccentric axial force and shear for beams and columns [23]. After that, the effects of changing strength and stiffness are investigated through two simple benchmark buildings (Section 3). Section 4 then illustrates the possible failure mechanisms that can occur in r.c. buildings affecting material variability. This issue is applied to a real structure in Section 5: the school of Don Bosco in an Italian city. This structure was subjected to a set of experimental tests addressed to seismic retrofitting. The material eccentricity is evaluated in non-linear static analyses. Random distributions of strength are considered to obtain fragility curves. This method highlights the way to achieve a probabilistic estimation of the structural safety level for similar buildings.

2. Centre of Strength and Centre of Stiffness

2.1. Generalities

The European seismic code [20] generally considers in-plan irregularity throughout the eccentricities of the equivalent seismic forces. Also, non-uniform distribution of the columns material in r.c. buildings can produce torsional effects [24–27]: hence the definition of "material eccentricity" e_m. Conventional analyses on existing buildings generally consider uniform materials by assuming an average value obtained from an experimental test. Taking into account the material variability, even just for columns, produces a sensitive variation in the response of the model both in nonlinear and linear analyses. In this paragraph, the eccentricities of stiffness and of strength, deriving from the material eccentricity are illustrated.

2.2. Center of Stiffness and Eccentricity of Stiffness

In a linear elastic analysis the coordinates of the center of stiffness are [28]:

$$x_{s,j} = \frac{\sum_i^n x_i K_{yi}}{\sum_i^n K_{yi}} \tag{1}$$

$$y_{s,j} = \frac{\sum_i^n y_i K_{xi}}{\sum_i^n K_{xi}} \tag{2}$$

where:

x_i, y_i coordinates of the *i*-th column;

$K_{xi}(E), K_{yi}(E)$ stiffness of the *i*-th column in the coordinate directions, the function of the Young modulus E. Because of this definition, the center of the stiffness position is affected by material variability through E values. The elastic modulus is related to the concrete compressive strength with the following expression [20]:

$$E_c = 22,000 \left(\frac{f_c}{10} \right)^{0.3} \tag{3}$$

The stiffness eccentricity in *x* and *y* directions $e_{sx,j}$ and $e_{sx,j}$. is given by these ratios:

$$e_{sx,j} = \frac{x_{s,j} - x_{c,j}}{L_x} \tag{4}$$

$$e_{sy,j} = \frac{y_{s,j} - y_{c,j}}{L_y} \tag{5}$$

x_c, y_c coordinates of centroid of the j-th floor;
L_x, L_y building length in x and y directions.

2.3. Centre of Strength and Eccentricity of Strength

The collapse of R.C. columns depends on:

1. The strength of the concrete;
2. The strength of steel bars;
3. The position of the columns in the building;
4. The geometry (length, restraints, and inertial characteristics) of the columns.

Two possible criteria to define, in a simple way, the center of strength are here described: the first one is related to collapse caused by compression force (method 1), the second one by bending moment (method 2).

Method 1. The center of compressive strength of n columns at the j-level is calculated by a weighted average of the axial compression resistance of the columns with respect to their in plan positions.

$$x_R^C = \frac{\sum_i^n N_{u,i} x_i}{\sum_i^n N_{u,i}} \tag{6}$$

$$y_R^C = \frac{\sum_i^n N_{u,i} y_i}{\sum_i^n N_{u,i}} \tag{7}$$

$N_{u,i}$ compressive axial resistance of the i-th columns;
x_i, y_i coordinates of the i-th columns;
n number of columns at j-th level.

Method 2. The center of bending strength is calculated by a weighted average of the ultimate bending moment of the columns with respect to their in-plan positions.

$$x_{R,j} = \frac{\sum_i^n M_{u,i} x_i}{\sum_i^n M_{u,i}} \tag{8}$$

$$y_{R,j} = \frac{\sum_i^n M_{u,i} y_i}{\sum_i^n M_{u,i}} \tag{9}$$

where:
$M_{u,i}$ failure bending moment of the R.C. section of the i-th column.
The corresponding strength eccentricity is:

$$e_{Rx,j} = \frac{x_{R,j} - x_{c,j}}{L_x} \tag{10}$$

$$e_{Ry,j} = \frac{y_{R,j} - y_{c,j}}{L_y} \tag{11}$$

where:
x_{Rj}, y_{Rj} coordinates of the center of strength, computed with Method 1 or Method 2;
x_{cj}, y_{cj} coordinate of the j-th column;
L_x, L_y building length in x and y directions.

3. A Benchmark Case-Study

3.1. Description of the Benchmark Building

A simply two storey R.C. frame (Figure 1) is analyzed here as a benchmark example. The in-plan dimension of the building is 7.35 m × 6.45 m. This model is composed of six columns for each floor of cross section 40 × 40 cm^2 and n. 4 steel bars with a diameter of 20 mm for each one. The beams have a cross section of 40 × 50 cm^2. The following assumptions are made to highlight the effect of material variability:

- Uniform material distribution (u.m.d.);
- Non-uniform material distribution (n.u.m.d.);
- Flexible slab, simulated by assuming equivalent bracing of axial stiffness $K_B = 3000$ kN/cm;
- Rigid slab, obtained through kinematic restraints at the diaphragm level.

The assumed R.C. mechanical properties are listed in Table 1. Linear and nonlinear static analyses are compared to evaluate the seismic response. All the analyses are performed with FEM Software Midas GEN (ver. 2016 release 2.1, MIDAS Information Technology, Gyeonggi-do 13487, Korea).
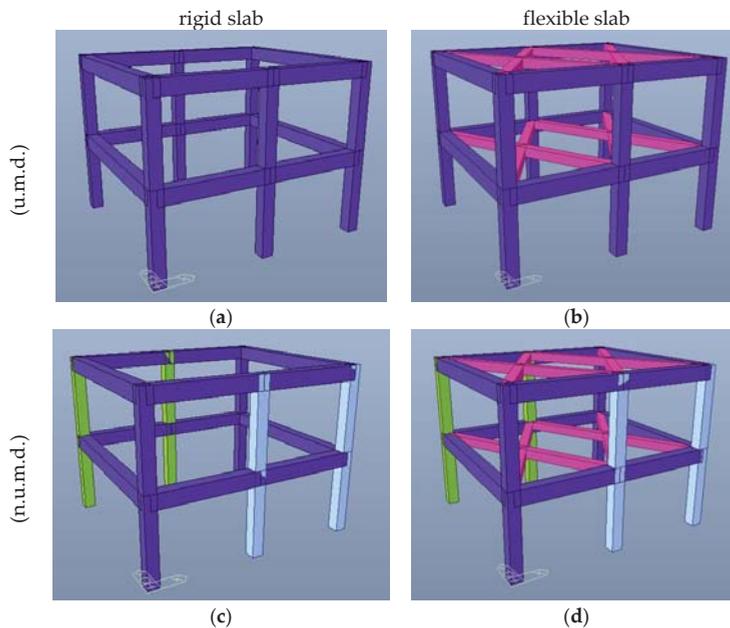
Figure 1. Main views of the benchmark finite element models: rigid slabs (**a**,**c**); flexible slabs (**b**,**d**).

Table 1. Mechanical characteristics of the benchmark model.

Material Number	f_c (MPa)	E_c (MPa)	f_y (MPa)	Color
1	10	22,000	230	Ciano
2	20	27,085	290	Blue
3	30	30,590	350	Green
4	20	13,542	290	Magenta

The assigned strength distribution causes material eccentricity.

Table 2 are calculated through the criterion of bending collapse (Equations (8) and (9)).

Table 2. Material eccentricity of the benchmark model with percentage of the total building length in the corresponding direction.

Material Eccentricity	x	y	Units
e_m	61	108	cm
	8.3	16.7	% [1]

[1] Material eccentricity ratio main dimensions of the building.

Both linear and non-linear analyses are performed by applying the seismic action in the X direction Ultimate Limit State ULS for the models of Figure 1. The results in terms of elastic displacements and rotations are reported in Table 3.

Table 3. Summary of results.

Types of Analysis		Rigid Slab				Flexible Slab			
		$D_u - D_y$	$\varphi_u - \varphi_y$	C/D	I_R	$D_u - D_y$	$\varphi_u - \varphi_y$	C/D	I_R
(uniform)	**Linear**	0.722	0.000	-	0.45	0.72	0.000	-	0.45
	n-Linear	7.840	0.000	0.82	0.76	7.96	0.000	0.82	0.76
(n-uniform)	**Linear**	0.680	0.005	-	0.40	0.71	0.030	-	0.38
	n-Linear	6.840	0.020	0.77	0.76	7.05	0.020	0.79	0.76

The symbols of Table 3 are so defined:

$D_u - D_y$ Elastic displacement ULS (Ultimate Limit State) for Linear Analysis (LA) or target displacement for Non Linear Analysis (NLA).

$\varphi_u - \varphi_y$ Elastic rotation corresponding to ULS for LA, target rotation for NLA.

C/D Max. Capacity/Demand ratio for bending mechanism. For LA it is the ratio M_{Ed}/M_{Rd}, while for NLA the ratio is θ/θ_u. θ_u is the floor rotation corresponding to the achievement of the ultimate condition. M_{Rd} is defined in Section 3.2.

3.2. Calculation of the Risk Index

The Risk Index is calculated according to [29] as:

$$I_R = \frac{PGA_C}{PGA_D} \tag{12}$$

PGA_C is the collapse capacity derived from the push-over analysis; PGA_D is the demand in terms of peak ground acceleration as mentioned in the Eurocode 8 [20]. For the models with flexible slab, displacements and rotations of the plan are evaluated as the average value at the top of each column.

It is well known that linear analysis furnishes more severe Risk Indexes I_R than the non-linear one, as also shown in the benchmark model. It is also relevant to point out that irregular material distribution in the plan also produces torsional effects also for a symmetric building such as the benchmark building; that occurs in both analyses, due to strength eccentricity. Moreover, it is important to observe that I_R and the ultimate shear strength of the columns are not influenced by the local variation of strength in LA or NLA as suggested by Eurocode 8 [20]. It is a consequence of their dependence only on the average mechanical properties of the columns. In other terms, material eccentricity involves torsional modes [27,30] as well as a geometric eccentricity but this aspect is not discussed in the current Standards [20]. The multimodal and adaptive pushover appear the most suitable methods to consider torsional effects here induced [31,32]. A comparison of the traditional model with uniform (u.m.d.) and the model with non-uniform material distributions (n.u.m.d.) in the benchmark example highlights that:

1. In-plane displacements and rotations are greater for (n.u.m.d.), inducing additional stresses on the external columns;
2. The maximum ratio between capacity and demand decreases for (n.u.m.d.);
3. The ultimate shear does not have relevant changes because it is related to the mean resistance of the structure, that does not sensitively vary in average terms;
4. The ultimate displacement decreases for (n.u.m.d.) compared to (u.m.d.).

This leads to a reduction of the risk index in linear analysis, which is more noticeable for the models with flexible slabs. The same effects are also evaluated in Section 4 on a real case-study.

4. Effects of Material Variability on Collapse Mechanisms

4.1. Input Parameters and Failure Mechanisms for Parametric Analysis

The recurring mechanical properties of the typical r.c. existing structures built in Italy in the 1960s are listed below. The yield stress of steel bars used in the present analysis are reported in Table 4 and are taken from [33].

Table 4. Yield strength of steel type AQ42, AQ50 and AQ60 [33].

Steel Strength	AQ42	AQ50	AQ60	Units
$f_{y,min}$	265.0	282.4	353.7	N/mm^2
$f_{y.med}$	325.4	369.9	432.6	N/mm^2
$f_{y.max}$	397.4	530.0	560.8	N/mm^2
σ	23.17	29.45	36.59	N/mm^2

Similarly, the concrete cubic compression strength used here is listed in Table 5.

Table 5. Concrete cubic compression strength from experimental in situ tests.

Cubic Compression Strength	Test A [1]	Test B [2]	Test C [2]	Units
$R_{c,min}$	7.0	21.9	29.6	N/mm^2
$R_{c.mean}$	26.0	37.3	38.2	N/mm^2
$R_{c.max}$	45.0	40.1	46.7	N/mm^2

[1] secondary school Don Bosco in Francavilla in Sinni (Potenza–Italy); [2] secondary school Francesco Carrara in Lucca (Lucca–Italy).

The failure mechanism, due to transverse forces, often involves collapse of the columns at the ground floor. In fact, in the common practice without considering the seismic action, as done for many existing R.C. structures built in the 1960s, the columns were loaded by axial forces due to vertical loads, together with bending and shear due to transverse wind loads. In most cases, no variation in geometric section along the height of the buildings was considered. The collapse bending moment in r.c. columns is given by Eurocode 2 (for symbols see Appendix A or BS EN 1992-1-1 2004):

$$M_{Rd,B} = N_{Ed}\left(\frac{h}{2} - \frac{k}{\beta \cdot b \cdot \alpha \cdot f_{cd}}N_{Ed}\right) + A_s(h - 2 \cdot c)f_{yd} \tag{13}$$

The corresponding shear strength is:

$$V_{Rd,c} = \left[C_{Rd,c}k(100\rho_l f_{ck})^{1/3} + k_1\sigma_{cp}\right]b_w d \tag{14}$$

$$V_{Rd,s} = \frac{A_{sw}}{s}zf_{ywd}\cot\theta \tag{15}$$

$$V_{Rd,\max} = \alpha_{cw}b_w z\nu_1 f_{cd}/(\cot\theta + \tan\theta) \tag{16}$$

The ultimate shear resistance of the section V_{Rd} is:

$$V_{Rd} = \min(V_{Rd,c}, V_{Rd,s}, V_{Rd,\max}) \tag{17}$$

From which, the collapse bending moment of a column with height h_i is:

$$M_{Rd,T} = \frac{V_{Rd} h_i}{\alpha} \tag{18}$$

where:

h_i is the height of the *i*-th column.

α is taken equal to 2 for slender elements and 1 for the squat ones (see Table 6). The slenderness is defined as:

$$\lambda = \frac{h_i}{h_s} \tag{19}$$

being h_s the height of the cross section.

The collapse occurs when the minimum value between $M_{Rd,B}$ and $M_{Rd,T}$ is attained.

In the following case, three types of columns are analysed: (a) 40×40 cm^2; (b) 40×70 cm^2; (c) 40×180 cm^2 (Figure 2) varying once the concrete and the steel strength, considering both flexural and shear failures as in Table 6. The curves are also related to different values of axial force N_{Ed} consistent with the design criteria adopted during the 1960s. A set of reasonable "historical" strength values (Table 7) for concrete and steel are then assigned to the structural elements.
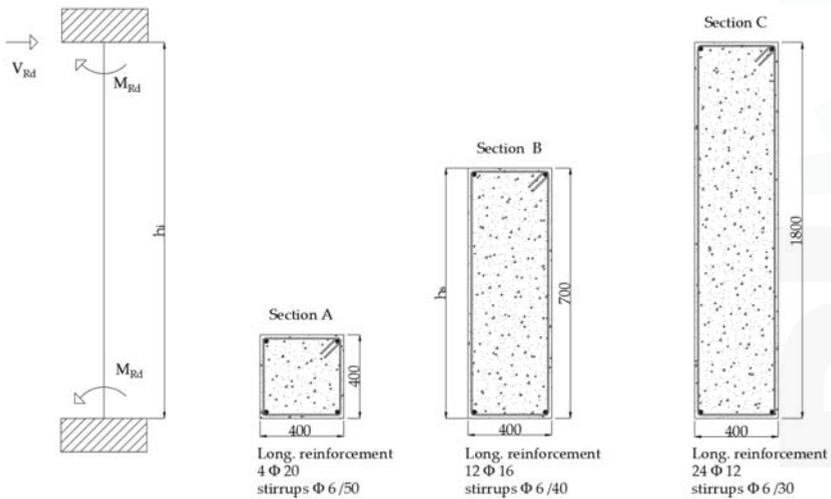
Figure 2. Considered cross sections (units in mm).

Table 6. Value of α depending on slenderness ratio.

Parameters	A	B	C
h_i/h_s	8.75	5.00	1.95
α	2.00	1.55	1.00

In case of concrete strength variation, a steel strength of 290 MPa is fixed. In case of steel strength variation, the concrete cubic compression strength of 20 MPa is assumed.

Table 7. Discretization of steel and concrete strength.

Strength	01	02	03	04	05	Unit
f_c	10	15	20	25	30	MPa
f_y	230	260	290	320	350	MPa

4.2. Results of Parametric Analysis

4.2.1. Concrete

The main results of the parametric analysis, by varying concrete strength (Table 7), are displayed in Figures 3–5. The parameters of the curves are common values of design normal force N_{ed} acting on the columns of r.c. buildings.

Figure 3a,b and Figure 4a show a nonlinear $(M_{Rd,B} - f_c)$ behavior depending on (N_{Ed}).

For the considered sections, the value of the dimensionless axial stress is variable, so the slope of the respective diagrams $(M_{Rd,B} - f_c)$ varies in the ranges of resistance. Figure 4b shows that bending and shear mechanisms depend on concrete strength and the slenderness ratio.

Because of the different slope of continuous and dashed curves, a different type of failure can occur depending on the concrete strength. Figure 5a,b illustrates how strength affects stiffness and curvature ductility.
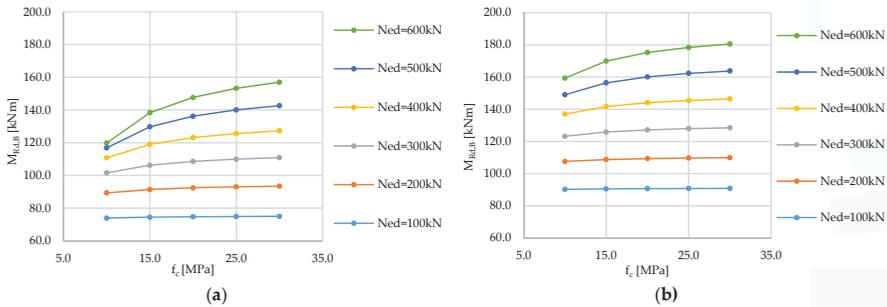
Figure 3. Bending moment of collapse ($M_{Rd,B}$) vs. concrete strength (f_c) and axial force (N_{ed}). (**a**) Cross section A (40 × 40); (**b**) Cross section B (40 × 70).
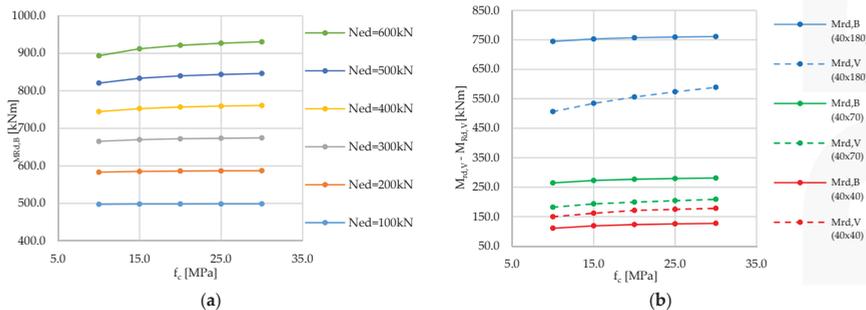
Figure 4. (**a**) Bending moment of collapse ($M_{Rd,B}$) vs. concrete strength (f_c) and axial force (N_{ed})-cross section C (40 × 180); (**b**) bending ($M_{Rd,B}$) and shear mechanism ($M_{Rd,V}$) vs. (f_c) with N_{ed} = 400 kN-cross section (A–C), with Ned = 400 kN.
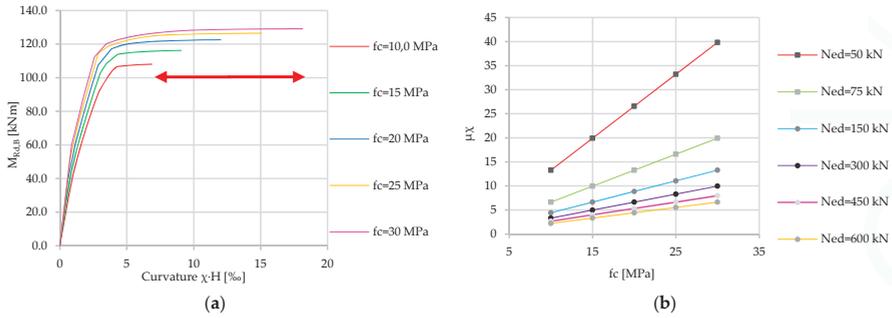
Figure 5. Bending moment ($M_{Rd,B}$) vs dimensionless curvature $\chi(h_s)$ varying concrete strength (f_c)-cross section A (40×40), N_{ed} = 400 kN (**a**); curvature ductility $\mu\chi$ vs. concrete strength (f_c) and axial force (N_{ed})-cross section A (40×40) (**b**).

4.2.2. Steel

In the second set of analyses, the steel strength is varied. The main results are reported in Figures 6 and 7. It can be observed that the variation of the collapse bending moment depends linearly on the steel strength $\left(f_y\right)$.

In case of variation of the concrete resistance, the resistant moment of the section has a nonlinear relationship with f_c, while in the case of the variation of the steel resistance, the relation is linear and the lines are parallel (Figure 6a). Therefore, in Figure 6a, only the diagram of the section 40×40 (cross sect. A) is displayed. Also, the variation of the steel resistance is shown for the graphs $\left(M_{Rd,B}; M_{Rd,V} - f_y\right)$ of Figure 6b which, in this case, assumes a linear trend with respect to the case of variable concrete. The ultimate curvature and the initial stiffness do not change by varying the steel strength, affecting only the yield values (Figure 7a) [34–36]. By contrast, in the case of the variation of the compressive strength of the concrete, there is an increase of the ductility of the curvature.

A decreasing trend of curvature ductility with steel strength also occurs by varying N_{Ed} (Figure 7b). Further parametric analyses were carried out by considering the simultaneous variation of steel and concrete strength; they did not change the main results here described, and are not reported for the sake of brevity.
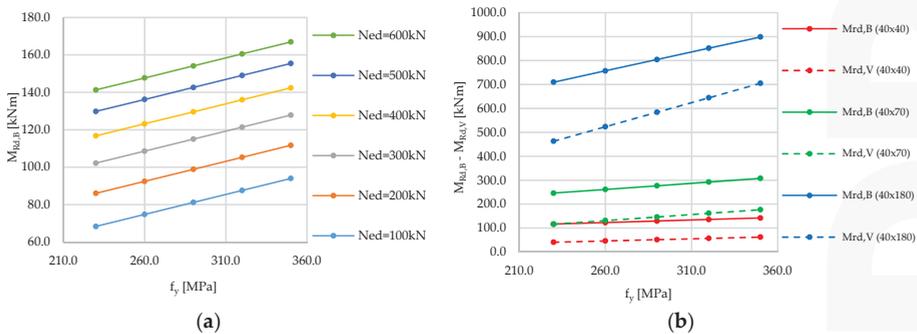
Figure 6. Bending moment of collapse (M_{Rd}) varying steel strength (f_{yd}) and axial force (N_{ed})-cross section A (40×40) (**a**); cross section (40×40) Ductile and brittle failure mechanism of the analysed cross sections (40×40, 40×70, 40×180), assuming N_{ed} = 400 kN (**b**).
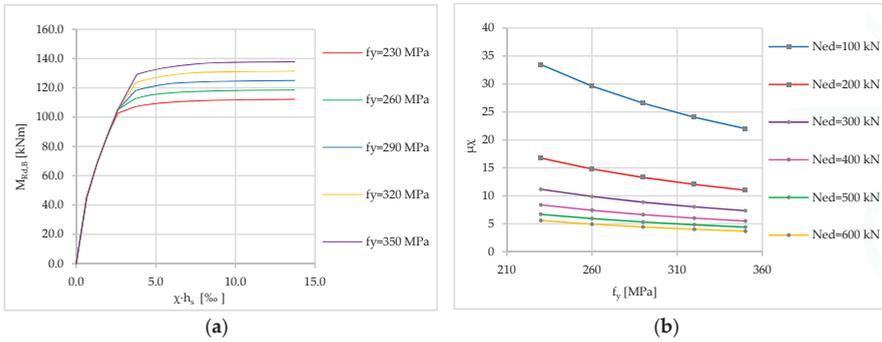
Figure 7. Bending moment (M_{Rd}) vs. dimensionless curvature $\chi(h_s)$ varying steel strength (f_{yd})-cross section A-(40 × 40), N_{Ed} = 400 kN (**a**); curvature ductility $\mu\chi$ vs. steel strength f_y and axial force (N_{Ed})-cross section A-(40 × 40) (**b**).

5. A Real Case-Study

In this Section, the effects of material variability are investigated for a real R.C. building, taking into account the failure mechanisms illustrated in Section 4.

5.1. Description of the Buildings

The secondary school "Don Bosco" in Francavilla in Sinni (Potenza, Italy) is made up of two R.C. framed buildings (A and B) built in the 1970s (Figures 8 and 9).

Figure 8. Aerial view of the school.

Figure 9. Main views of the school: Front entrance building B (**a**); building A (**b**).

Building A has a rectangular shape (45.0 m × 16.5 m), composed of two floors with an inter-storey height of 3.52 m. Column cross sections are of 40 × 40 cm^2 (72% of the total number of columns), 40 × 70 cm^2 (7%), and 40 × 180 cm^2 (21%), irregularly distributed. The structure is also irregular in elevation (with a mass reduction of 40%).

Building B has an approximately squared shape with maximum in-plan dimensions of 26.0 m × 21.0 m, composed of three floors, one semi-basement, and two completely above the ground, with an inter-storey height of 3.52 m (with the exception of a central part with taller columns (5.24 m)). The main frames are in both directions with r.c. and hollow-core concrete slabs with different heights (16 + 4 cm for the offices, 42 + 8 for the roof and the central corridor). Building B is also irregular, both in terms of its plan and height. Column cross sections are of 40 × 40 cm^2 (45%), 40 × 50 cm^2 (25%), 25 × 40 cm^2 (20%) and 40 × 70 cm^2 (10%). Each building has an independent strip foundation system placed at a different level. The two structures are divided by a separating joint with insufficient width from a seismic point of view (Figure 10). Several experimental tests were made on the concrete columns of two buildings: rebound hammer, sonreb and crushing test (made on cylindrical coring samples). In particular, the experimental data of the investigations have been 11 sclerometric tests, 12 sonreb tests, and eight crushing tests on cylindrical samples of the real structure. These tests are made on the same structural elements to have more reliable values. The resulting mean data are presented in Table 8. These data are used in two different ways: (1) extreme values (min and max) are calculated to determine the strength domain in Section 4.2.2; (2) mean value and standard deviation are used to generate random distributions of resistances (compatible with those found in situ) in order to derive fragility curves.
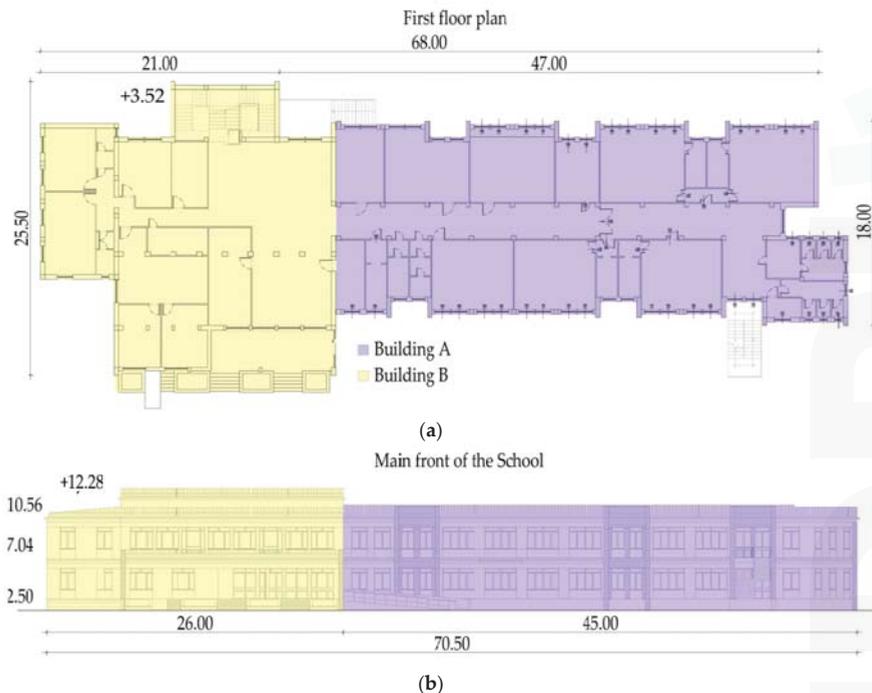
Figure 10. View of plan of the first level (**a**); front view (**b**) (units in m).

Table 8. Experimental test carried out on the school "Don Bosco".

TEST	Hammer	Sonreb	Coring	Units
1	29.0	14.9	17.2	N/mm^2
2	29.0	17.2	13.9	N/mm^2
3	22.0	9.4	10.4	N/mm^2
4	25.0	8.6	9.6	N/mm^2
5	33.0	11.7	12.3	N/mm^2
6	42.0	23.2	28.7	N/mm^2
7	45.0	28.9	31.3	N/mm^2
8	43.0	29.0	-	N/mm^2
9	38.0	27.5	-	N/mm^2
10	40.0	17.4	-	N/mm^2
11	43.0	22.8	-	N/mm^2
12	-	21.7	19.5	N/mm^2

The original drawings show an improper use of stirrups, especially in the R.C. columns, and inadequate bonded lengths and overlapping of bars. All these deficiencies in structural details may cause the local brittle shear mechanism and global collapse mechanism of "weak columns"[37,38].

5.2. Parametric Analysis

5.2.1. Extreme Strength Distribution

To obtain the in-plan limit distributions of strength (that may include all the real ones), extreme values of strength are assigned to the model, and studied analogously to the models in Section 3. A vertical plane passing through the centroid of each floor subdivides it into two parts. Each distribution is obtained by rotating a vertical plane by 45° around the centroid C (Figure 11), thus getting eight limit distributions of strength for the columns (Figure 11).
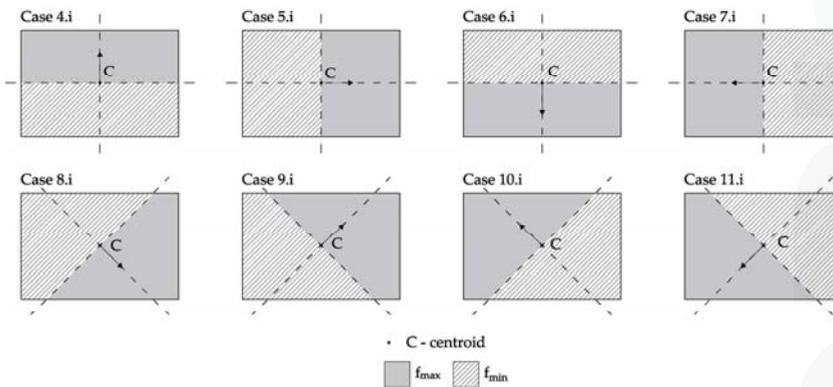
Figure 11. Extreme material distribution analysed.

The variable parameters are the concrete compression strength and the yielding strength of the steel bars. Each pair of values is assumed in both uniform and non-uniform in-plan distribution. Firstly, the two variables are considered separately. The material strengths assigned are the extreme values of Tables 4 and 5.

In Figure 11 the subscript i assumes the values 1 or 2 according to whether the variable strength is of concrete or steel, taking the other parameter constant and equal to the mean value. Cases 1.i 2.i, and 3.i are not represented in Figure 11 but are representative respectively of uniform mean, and

the minimum and maximum value of resistance. For each configuration of strength nonlinear static analyses (NLSA) are performed.

Figures 12 and 13 show the regression between ultimate shear and eccentricity of material. The two seismic directions are separately considered and the ultimate shear in x-direction (V_{Ux}) is related to the eccentricity and vice versin y-direction (e_{my}) (and vice versa).
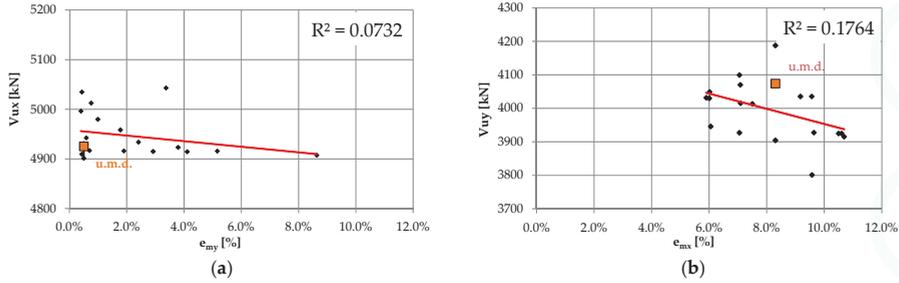
Figure 12. Linear regression $V_u - e_m$ for building A. *x* direction (**a**); *y* direction (**b**). The orange square with the label u.m.d. indicates the uniform material distribution case.
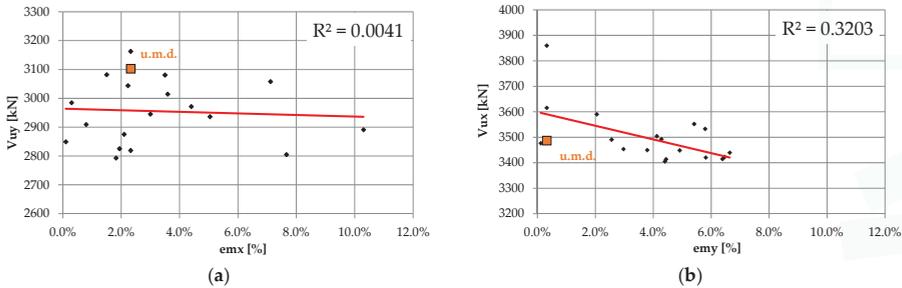
Figure 13. Linear regression V_u - e_m for building B. *x* direction (**a**); *y* direction (**b**). u.m.d. indicates the uniform material distribution case.

The elongated in-plan shape of building A produces the differences in the slope of the line that represent the relationship between $V_{Ux} - e_{my}$ and $V_{Uy} - e_{mx}$ (Figure 12). In the case of building B, characterized by a compact shape, the difference between the two-coordinate direction is less remarkable.

5.2.2. Strength Domain

With Equations (6)–(9) it is possible to calculate the position of the resistance centers referring to the limit distributions of Figure 11. For each of these points a F.E.M. model is subjected to non-linear static (pushover) analysis to determine the risk index. It is seen that the risk index does not significantly differ from one case to another so the points represent equipotential lines for parameter I_R.

Figure 14a,b shows the domains of the center of strength for each building, obtained from the set of extreme strength distributions. They represent the material eccentricity due to extreme values of concrete strength (grey domain) or steel strength (yellow domain) by rotating the vertical plan that divides the two regions in Figure 14.

In this figure, the numbers in the strength domain j.i mean the following: subscript j the eight cases of Figure 11, starting from 4 to 11. Cases 1-2-3 are referred to uniform distributions and are not reported for the sake of brevity. Subscript i assumes the values 1 or 2 according to whether the variable

strength is of concrete or steel. NLSA are carried out for both buildings. Each analysis evaluated the structural capacity relating to the border points of each domain. The main results are the variation of the index of seismic risk I_R, given by Equation (12). I_R values are reported in the histograms of Figure 14a,b.
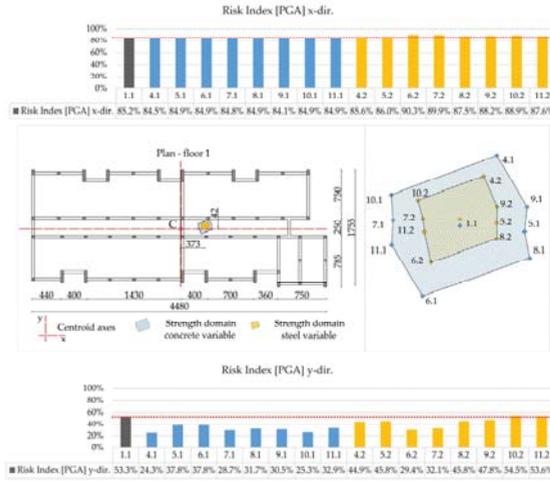
(**a**)
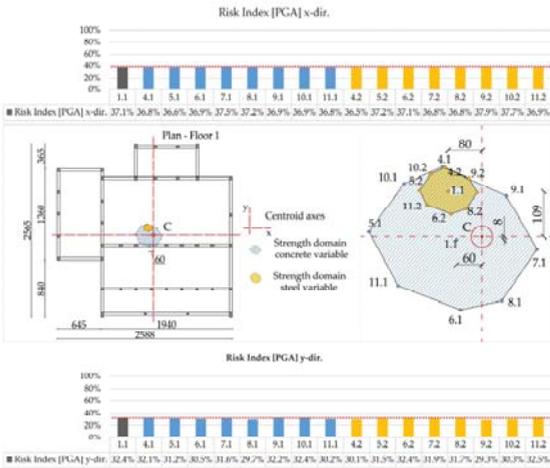
(**b**)

Figure 14. Strength domain of building A (**a**) and B (**b**). At the top and at the bottom is the change rate of the risk index I_R in x and in y directions (units in cm). C is the centre of mass of each storey.

The results show that the risk index has a sensitive change in the shorter direction of the building, which is lower in the compact in-plan building (B), whereas along the longer direction the variation is negligible. The strength domains are greater considering the variation of concrete rather than steel. The material eccentricities are much more relevant in the irregular building, for which the strength domain does not include the centre of mass of the storey C.

5.2.3. Fragility Curves

Finally, random material distributions are numerically generated to obtain fragility curves. The random distribution considers variation both in steel and in concrete strength. To ensure that material distribution could be realistic, a probability density function (PDF) is defined starting from the mean value and the standard deviation of strength. Two strength values (for concrete and steel) are obtained and randomly assigned to each column.

ULS and DLS (Damage Limit States) are examined. The ULS limit state is achieved for the value of PGA that determines the collapse of the structure while the DLS state is achieved for the maximum interstorey drift [13].

The steps to determine the fragility curves are [39,40]:

- Non-Linear static analysis for each random case;
- PGA for each random case;
- Mean value μPGA and standard deviation σPGA of all calculated PGA;
- Determination of the probability cumulative function (PCF) as:

$$(x) = \Phi \left[\frac{PGA - \mu PGA}{\sigma PGA} \right] \tag{20}$$

Table 9 contains the P(x) values for both buildings. The corresponding fragility curves are shown in Figure 15. The probability cumulative function PCF related to low damage is represented with the grey line; meanwhile, the one related to severe damage is represented with the black line.

Table 9. PGA values for building A and B.

Average Value and Standard Deviation of PGA		Low Damage (LD)		Severe Damage (SD)	
		PGAx	PGAy	PGAx	PGAy
Building A	μ_{PGA}	0.064	0.064	0.117	0.093
	σ_{PGA}	0.003	0.002	0.003	0.002
Building B	μ_{PGA}	0.062	0.006	0.133	0.093
	σ_{PGA}	0.0007	0.002	0.134	0.003

(**a**)

(**b**)
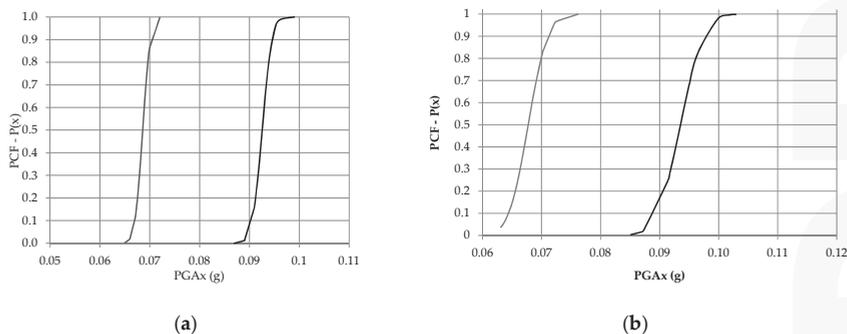
Figure 15. Fragility curves, (**a**) Building A; (**b**) Building B.

The fragility curves of Building A had a greater slope than that related to Building B. This means that Building B had a greater dispersion of the PGA values and therefore its seismic capacity is more sensitive to the material variability. The comparison of the curves (a) and (b) of Figure 15 reveals the vulnerability of building A that collapses for lower PGA values.

6. Conclusions

In this paper, a simplified method to consider material variability is proposed for the seismic vulnerability assessment of existing R.C. buildings. From the consideration that concrete and steel variability can produce additional torsional effects, a material eccentricity is defined.

The illustrated methodology is based on the idea of adding a material eccentricity to those already considered in the Standards for seismic analysis. In the structural design of rehabilitation, as shown in the examples, it is easy to take into account the variability of the mechanical parameters.

Several nonlinear analyses are performed on a benchmark example and on two real case-studies of R.C. frames. The effects on the risk indexes and on collapse mechanisms are discussed. Extreme strength distributions are considered leading to the definition of a strength domain, varying concrete and steel strength separately. These domains can be considered as contour lines of the seismic risk index.

For the benchmark model, the results showed that in the case of non-uniform material distribution the ratio of capacity to demand in terms of PGA and the ultimate displacement capacity decreased. For the real case study, the risk index was observed to have a sensitive change in the shorter direction of the building, whereas along the longer direction the variation is negligible. The strength domains are greater considering the variation of concrete rather than steel. The material eccentricities are much more relevant in the irregular building, for which the strength domain do not include the centre of mass of the storey.

Further investigations could be carried out on similar structures by considering random and/or real strength distributions, evaluating the changes in the strength domain. Further studies can be addressed to evaluating which types of buildings can be more sensitive to material variability, with the aim of properly taking this into account for the evaluation of the seismic capacity.

Author Contributions: M.L.P. conceived and wrote the paper. M.P. Performed structural analysis and managed experimental data. L.G. and M.S. contributed to write the paper and improved its structure proposing analytical tools. The Paper widely derived from the Master Thesis *Seismic vulnerability and a proposal of seismic improvement of the building Middle School "Don Bosco" in Francavilla in Sinni (PZ) - Italy* (Author: M.P.; Supervisors: M.S. and M.L.P).

Appendix A

The Symbols of the equations (13)–(16) are described below:

β coefficient equal to: 0.81;

α coefficient equal to: 0.83;

b width of the section;

A_s area of the longitudinal steel reinforcement;

h height of the section;

c filler tiles;

$C_{Rd,c}$ $\dfrac{0.15}{\gamma_c}$

k $1 + \sqrt{\dfrac{200}{d}}$;

ρ_l ratio of longitudinal steel reinforcement;

k_1 coefficient equal to: 0.15;

σ_{cp} mean compressive stress in the section due to axial force;

b_w minimum width of the section;

d	internal height of the section;
A_{sw}	transverse area of the stirrups;
s	spacing between the stirrups;
z	moment arm;
f_{ywd}	strength of the stirrups;
θ	inclination of the concrete struts;
α_{cw}	coefficient equal to: 1;
ν_1	$0.5(1 - f_{lck}/250)$.

For further details see: BS EN 1992-1-1 2004.

References

1. Marie-Victoire, E.; Cailleux, E.; Texier, A. Carbonation and historical buildings made of concrete. *J. Phys. IV Fr.* **2006**, *136*, 305–318. [CrossRef]

2. Glasser, F.P.; Marchand, J.; Samson, E. Durability of concrete—Degradation phenomena involving detrimental chemical reactions. *Cem. Concr. Res.* **2008**, *38*, 226–246. [CrossRef]

3. Parisi, F.; Augenti, N. Influence of seismic design criteria on blast resistance of RC framed buildings: A case study. *Eng. Struct.* **2012**, *44*, 78–93. [CrossRef]

4. Parisi, F.; Augenti, N. Seismic capacity of irregular unreinforced masonry walls with openings. *Earthq. Eng. Struct. Dyn.* **2013**, *42*, 101–121. [CrossRef]

5. Tubaldi, E.; Barbato, M.; Dall'Asta, A. Seismic Response and Vulnerability of Steel-Concrete Composite Bridges Accounting for Model Parameter Uncertainties. *Struct. Congr. 2010* **2010**, 1840–1851. [CrossRef]

6. Badalassi, M.; Braconi, A.; Cajot, L.G.; Caprili, S.; Herve, D.; Gundel, M.; Hjiaj, M.; Hoffmeister, B.; Karamanos, S.A.; Salvatore, W.; et al. Influence of variability of material mechanical properties on seismic performance of steel and steel–concrete composite structures. *Bull. Earthq. Eng.* **2016**. [CrossRef]

7. Zelaschi, C.; Monteiro, R.; Pinho, R. Parametric Characterization of RC Bridges for Seismic Assessment Purposes. *Structures* **2016**, *7*, 14–24. [CrossRef]

8. Giresini, L.; Sassu, M. Tests Results and Simple Structural Analysis of the Main Lighthouse in the Harbor of Livorno (Italy). *Adv. Mater. Res.* **2013**, *834–836*, 1299–1303. [CrossRef]

9. Rovero, L.; Alecci, V.; Mechelli, J.; Tonietti, U.; De Stefano, M. Masonry walls with irregular texture of L'Aquila (Italy) seismic area: validation of a method for the evaluation of masonry quality. *Mater. Struct.* **2015**, *49*. [CrossRef]

10. Muller, D.; Forster, V.; Graunbner, C.-A. Influence of Material Spatial Variability on the Reliability of Masonry Walls in Compression. In Proceedings of the 13th Canadian Masonry Symposium, Halifax, NS, Canada, 4–7 June 2017.

11. Viti, S.; Tanganelli, M.; De Stefano, M. Seismic performance sensitivity to concrete strength variability: A case-study. *Earthq. Struct.* **2015**, *9*, 321–337. [CrossRef]

12. Alecci, V.; De Stefano, M.; Luciano, R.; Rovero, L.; Stipo, G. Experimental Investigation on Bond Behavior of Cement-Matrix–Based Composites for Strengthening of Masonry Structures. *J. Compos. Constr.* **2015**, *20*. [CrossRef]

13. Alecci, V.; Focacci, F.; Rovero, L.; Stipo, G.; De Stefano, M. Extrados strengthening of brick masonry arches with PBO-FRCM composites: Experimental and analytical investigations. *Compos. Struct.* **2016**, *149*, 184–196. [CrossRef]

14. Alecci, V.; Misseri, G.; Rovero, L.; Stipo, G.; De Stefano, M.; Feo, L.; Luciano, R. Experimental investigation on masonry arches strengthened with PBO-FRCM composite. *Compos. Part B Eng.* **2016**. [CrossRef]

15. Sassu, M.; De Falco, A. Legal disputes and building defects: some data from Tuscany (Italy). *J. Perform. Constr. Facil.* **2013**, *28*, 1–32.

16. Alecci, V.; Briccoli Bati, S.; Ranocchiai, G. Study of Brick Masonry Columns Confined with CFRP Composite. *J. Compos. Constr.* **2009**, *13*, 179–187. [CrossRef]

17. De Falco, A.; Froli, M.; Giresini, L.; Puppio, M.L.; Sassu, M. A proposal for the consolidation of a r.c. social housing by means of external hybrid steel-glass frameworks. *Appl. Mech. Mater.* **2014**, *638–640*, 3–8. [CrossRef]

18. Alecci, V.; Briccoli Bati, S.; Ranocchiai, G. Numerical homogenization techniques for the evaluation of mechanical behaviour of a composite with SMA inclusions. *J. Mech. Mater. Struct.* **2009**, *4*, 1675–1688. [CrossRef]
19. Alecci, V.; Bati, S.B.; Ranocchiai, G. Concrete columns confined with CFRP wraps. *Mater. Struct.* **2014**, 1–14. [CrossRef]
20. EN 1998-1 EN 1998-1: Eurocode 8—Design of structures for earthquake resistance. Part 1: General rules, seismic actions and rules for buildings. *CEN* **2004**, *1*, 1–229.
21. Giresini, L.; Gioeli, A.; Sassu, M. Seismic Reinforcement of a r.c. Building with External Steel Frameworks: The Case of the Primary School XXV April of Arcola (Italy). *Adv. Mater. Res.* **2013**, *834–836*, 697–700. [CrossRef]
22. Lavan, O.; de Stefano, M. Geotechnical, Geological and Earthquake Engineering. *Geotech. Geol. Earthq. Eng.* **2013**, *24*. [CrossRef]
23. Biondini, F.; Bontempi, F.; Frangopol, D.M.; Malerba, P.G. Probabilistic service life assessment and maintenance planning of concrete structures. *J. Struct. Eng.* **2006**, *132*, 810–825. [CrossRef]
24. Fajfar, P.; Marusic, D.; Perus, I. Torsional Effects in the Pushover-Based Seismic Analysis of Buildings. *J. Earthq. Eng.* **2005**, *9*, 831–854. [CrossRef]
25. De-la-Colina, J.; Alberto González-Pérez, C.; Valdés-González, J. Accidental eccentricities, frame shear forces and ductility demands of buildings with uncertainties of stiffness and live load. *Eng. Struct.* **2016**, *124*, 113–127. [CrossRef]
26. De Stefano, M.; Pintucchi, B. A review of research on seismic behaviour of irregular building structures since 2002. *Bull. Earthq. Eng.* **2008**, 285–308. [CrossRef]
27. De la Llera, J.C.; Chopra, A.K. Accidental torsion in buildings due to base rotational excitation. *Earthq. Eng. Struct. Dyn.* **1994**, *23*, 1003–1021. [CrossRef]
28. De Stefano, M.; Pintuchi, B. Predicting torsion-induced lateral displacements for pushover analysis: Influence of torsional system characteristics. *Earthq. Eng. Struct. Dyn.* **2010**, *39*, 1369–1394. [CrossRef]
29. Shibin, L.; Lili, X.; Maosheng, G.; Ming, L. Performance-based methodology for assessing seismic vulnerability and capacity of buildings. *Earthq. Eng. Eng. Vib.* **2010**, *9*, 157–165. [CrossRef]
30. Chopra, A.K.; Goel, R.K. A modal pushover analysis procedure to estimate seismic demands for unsymmetric-plan buildings. *Earthq. Eng. Struct. Dyn.* **2004**, *33*, 903–927. [CrossRef]
31. Chopra, A.K.; Goel, R.K. A modal pushover analysis procedure for estimating seismic demands for buildings. *Earthq. Eng. Struct. Dyn.* **2002**, *31*, 561–582. [CrossRef]
32. Ricker, N. Further developments in the wavelet theory of seismogram structure. *Bull. Seism. Soc. Am.* **1943**, *33*, 197–228.
33. Verderame, G.M.; Stella, A.; Cosenza, E. Le proprietà meccaniche degli acciai impiegati nelle strutture in c.a. realizzate negli anni '60. In Proceedings of the X Congresso Nazionale "L'Ingegneria Sismica in Italia—ANIDIS, Potenza-Matera, Italy, 9–13 September 2001.
34. Zhou, J.; He, F.; Liu, T. Curvature ductility of columns and structural displacement ductility in RC frame structures subjected to ground motions. *Soil Dyn. Earthq. Eng.* **2014**, *63*, 174–183. [CrossRef]
35. Arslan, M.H. Estimation of curvature and displacement ductility in reinforced concrete buildings. *KSCE J. Civ. Eng.* **2012**, *16*, 759–770. [CrossRef]
36. Biondini, F.; Camnasio, E.; Titi, A. Seismic resilience of concrete structures under corrosion. *Earthq. Eng. Struct. Dyn.* **2015**, *44*, 2445–2466. [CrossRef]
37. Augenti, N.; Parisi, F. Learning from Construction Failures due to the 2009 L'Aquila, Italy, Earthquake. *J. Perform. Constr. Facil.* **2010**, *24*, 536–555. [CrossRef]
38. Andreini, M.; De Falco, A.; Giresini, L.; Sassu, M. Structural damage in the cities of Reggiolo and Carpi after the earthquake on May 2012 in Emilia Romagna. *Bull. Earthq. Eng.* **2014**. [CrossRef]
39. Vona, M. Fragility Curves of Existing RC Buildings Based on Specific Structural Performance Levels. *Open J. Civ. Eng.* **2014**, *4*, 120–134. [CrossRef]
40. Rota, M.; Penna, A.; Strobbia, C.L. Processing Italian damage data to derive typological fragility curves. *Soil Dyn. Earthq. Eng.* **2008**, *28*, 933–947. [CrossRef]

Article

Seismic Reinforcement of a R.C. School Structure with Strength Irregularities throughout External Bracing Walls

Mauro Sassu [1],* , Mario Lucio Puppio [2],* and Eleonora Mannari [2]

[1] Department of Civil, Environmental Engineering and Architecture, University of Cagliari,
    09123 Cagliari, Italy
[2] Department of Energy, Systems, Territory and Construction Engineering, University of Pisa, 56126 Pisa, Italy;
    mannari.eleonora@gmail.com
*   Correspondence: msassu@unica.it (M.S.); mariolucio.puppio@ing.unipi.it (M.L.P.);
    Tel.: +39-070-6755409 (M.S.); +39-050-2218204 (M.L.P.)

Abstract: The effect of irregularities due to the non-uniform distribution of material properties on structural elements of a significant real case is here investigated. Mechanical tests performed on a typical Italian reinforced concrete (r.c.) school building built in the 1960s showed irregularity in the distribution of compression strength in columns, even though the construction is featured by substantially symmetric distribution of the frames. Extreme scenarios in the distribution of irregularities in compression strength of concrete columns are analyzed, with the hypothesis of rigid or deformable slabs. The seismic analysis showed the influence of the response due to the irregular distributions of concrete strength. A proposal of equivalent "material eccentricity" is shown to account for the mentioned irregularity. Furthermore, the practical solution of reinforcement to mitigate the effects of irregularities is also described. It consists of couple of external r.c. walls stiffened by r.c. buttresses added to the building, connected by transverse slabs. An extensive reduction of material eccentricity is achieved, together with a relevant improvement in seismic capacity.

Keywords: seismic analysis; material eccentricity; nonlinear static analysis; r.c. framed structure; structural irregularities; external bracing walls

1. Introduction

The role of irregularities in the seismic response of buildings [1] is a critical issue in the evaluation of structural reliability, as observed in recent Italian earthquakes [2–6], mainly in those built during the 1960s.

The irregularities [6–8]—similarly to the out-of-plane rocking response [9–12] and the energy dissipation of existing constructive elements [13–15]—are not completely covered by codes such as Eurocode 8 part 3 [16]. Furthermore, the on-site tests play a fundamental role in the knowledge of an existing construction [15] that should be properly regulated. The level of maintenance of a construction is a further aspect that should be taken into account on structural codes, also for extreme climatic events [17]. Finally, the possibility of protecting the building with preventive provisory elements is a relevant issue to be evaluated in the seismic protection of cultural heritage or historic elements [18].

An issue relevant to the seismic assessment of existing buildings is related to the wide dispersion of strength values. During the 1960s, the concrete was extensively produced on-site without quality control methods. This fact induced significant differences in the strength of r.c. elements of the same building. The water/concrete ratio and the handmade compaction phases were primary factors of

inhomogeneity [19]. In the present paper, only concrete strength variation is assumed, neglecting the variation of the strength of the steel bars.

A current instrument to account for uncertainty in knowledge of the structural elements is the Confidence Factor [15], although in the current Italian code, it is related only to the number of tests provided on the structure [20]. In the present case, extreme scenarios of strength distribution are performed through non-linear static analysis. It permits the role of inhomogeneity in concrete strength to be emphasized, independently of the number of experimental tests. [6]. No differences are considered in the height distribution of mechanical properties. The results are compared considering both rigid and flexible slabs. Referring to the irregularities induced by the non-uniform distribution of strength [21] of vertical elements in r.c. structures [8], a possible helpful strategy for designers should be based in terms of "material eccentricity". The concept of eccentricity is currently used to determine the well-known center of mass and of stiffness of a building. The definition of "center of strength" as the center of the horizontal forces of collapse acting on the columns, together with its eccentricity, can then be easily implemented in numerical codes [6].

An example based on an existing r.c. building is illustrated. The school building "I.T.C. Carrara" is a complex from the early 1960s, located in Lucca (Italy) (Figures 1–3). It consists of four isolated buildings labeled A, B, C, and D, weakly joined to a one-floor structure. The pavilion B (Figure 2) is formed by three levels and a basement on an extension of about 1000 m^2/level. A large number of thin r.c. columns, together with a set of short columns at the top of the ground floor (Figure 3) are seismically vulnerable. Original drawings are available (Figures 4–6). Poor quality of the concrete is another relevant and emblematic aspect of seismic vulnerability of the building. In this sense, the considered example represents a typical situation of r.c. constructions that must be urgently enforced.

(**a**) (**b**)

Figure 1. Plan (**a**) and aerial view (**b**) of the School Complex I.T.C. F. Carrara (Lucca–Italy).

Figure 2. View of the B pavilion (**right**) and C pavilion (**left**).

(**a**)   (**b**)
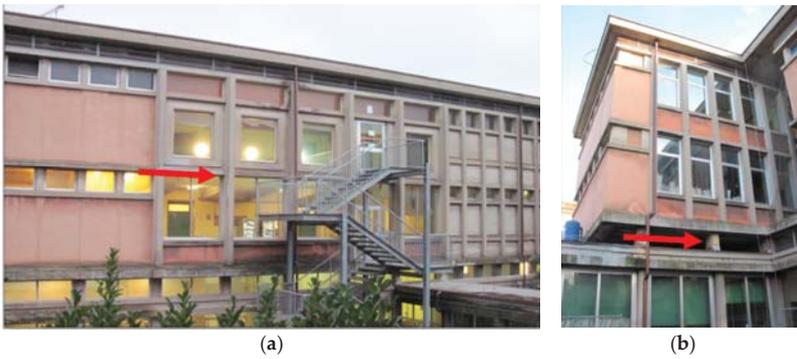
Figure 3. Details of seismic vulnerability: (**a**) slender columns close to a double height spacing; (**b**) squat element (brittle shear force) in r.c. columns.
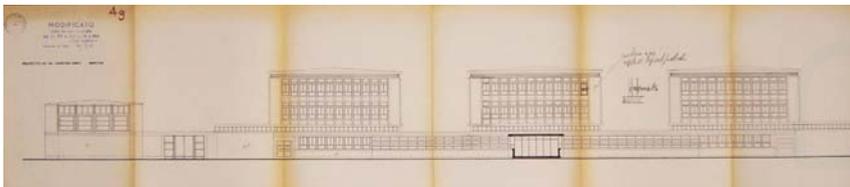
Figure 4. Original drawing of the complex—Frontal view.
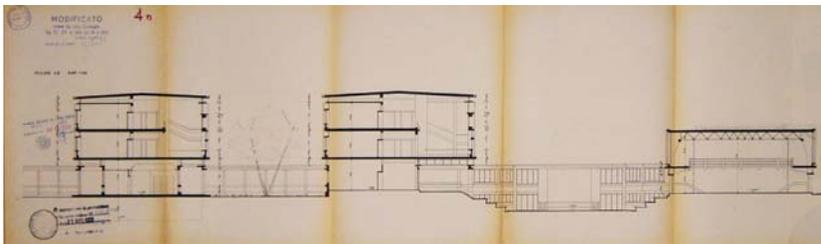
Figure 5. Original drawing of the complex: vertical section.

(**a**)   (**b**)
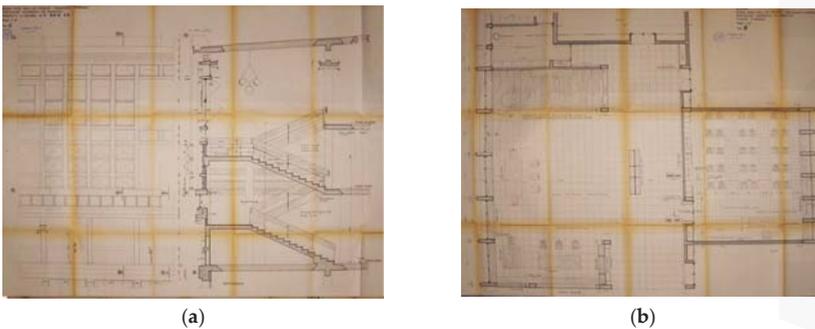
Figure 6. Original drawing of the B pavilion: (**a**) vertical section; (**b**) plan view.

The requirements of economy and short time for intervention (to minimize the interruption of school service), together with conservation of most of the interior parts, forced towards a solution of external r.c. walls. This choice was also induced by the need to reduce the structural effects due to material irregularity of concrete columns.

2. Analysis before Intervention

A typical feature of concrete constructions built in the 1960s and 1970s is the relevant scattering of the concrete compression strength, caused by the reduced level of automation which in that period allowed columns to be put in place with low productivity levels (only a few columns per day). The in-situ production of concrete was then influenced by environmental and episodic or local conditions (Figure 7). A numerical study was carried out on the strength variability of concrete columns, with the aim of evaluating the sensitivity to this phenomenon. In the absence of more accurate assessments, mechanical experiments on concrete columns were performed through 12 cylindrical cores and 60 Schmidt Hammer tests (each of 15 rebound measurements) from the adjacent pavilion, available for experiments. A mean compression strength of 24.8 MPa was determined, with a standard deviation of 9.6 MPa. A conventional upper strength of 34.4 MPa and a lower of 15.2 MPa have then been assumed. The Confidence Factor of the structure was determined according to EC8, by the analysis of geometry, details, and materials of the structure. Geometry was defined starting from original drawings (examples in Figures 4–6), verified by a full structural survey (Figure 8). A satisfactory knowledge of beams and column size was allowed with the help of the calculation report of the time of construction. A set of 20 different column and beam sections was found. One-way r.c. slabs showed 160 or 200 mm thickness without concrete slab. Structural details such as steel bar configurations were obtained by simulating design, joined with a partial availability of original drawings, according to codes and constructive practice of the 1960s. The mechanical characterization of the steel bars was referred to data from [22], verifying it with technical indications on the original calculation report. A yielding strength of 3699 MPa was then assumed. Finally, due to the in situ tests, a Confidence Factor of 1.20 was applied to mechanical proprieties (Table 1) as by Italian code [20].

The model of the B pavilion was implemented with the code SAP2000 v.17.0 (CSI, New York, NY, USA). Only main structural elements were modelled (columns and beams) as elastic mono-dimensional elements (frame), taking into account their actual stiffness and resistance. The model did not consider the node failure. Node failure is affected by variability of the strength of both the concrete and the steel [22], but in the adopted model the non-linearity was assumed to be only caused by the mechanical behavior of columns, neglecting the role of the beam–column nodes. Secondary structural elements such as perimeter and internal non-loadbearing walls were represented in term of mass. Gravity loads acting on slabs were transferred to beams by shell elements by means of influence areas. The foundation was not modelled, with full restrained joints at the base neglecting any structure–foundation interaction.

(**a**)   (**b**)
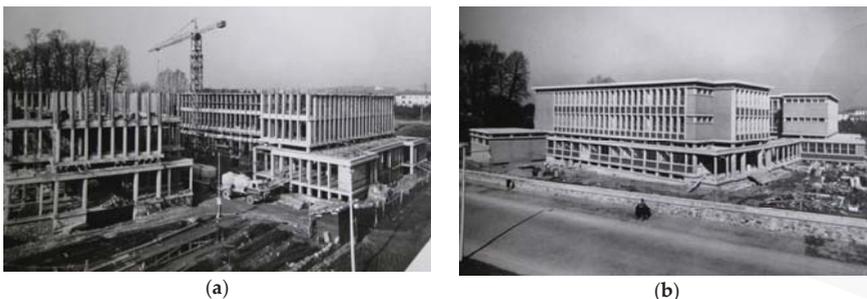
Figure 7. Historical images of the complex during construction.
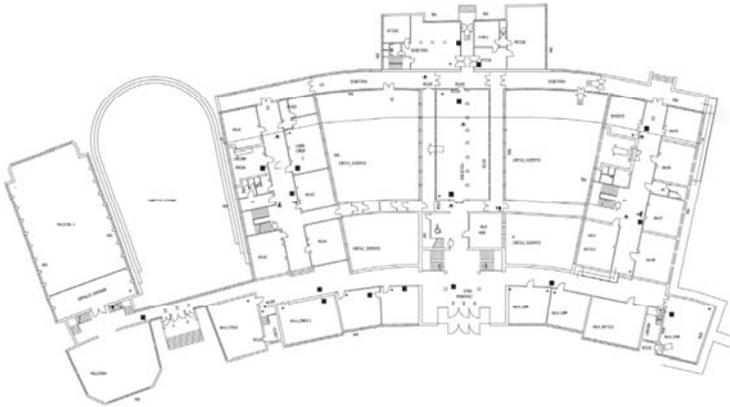
Figure 8. Ground floorplan of the complex.

Table 1. Mechanical characteristics of the reference model.

Material	fc (MPa)	Ec (MPa)	fy (MPa)
Concrete	248	28,904	-
Steel	-	-	3699

Two different schemes were analyzed: the first one with rigid floor diaphragm and the second one with in-plane flexible floors by means of equivalent thickness membrane. In both models, the mean values of material proprieties were initially implemented. Classic modal analysis was firstly performed to evaluate the modal frequencies and the mass participant ratios (Table 2).

Table 2. Modal properties: rigid floor and flexible floor model.

Model	Mode	T (s)	Mx	My
Rigid floor	1	0.450	0.78	-
	2	0.445	-	0.63
Flexible floor	1	0.494	-	0.70
	2	0.445	0.37	0.77

A non-linear static analysis was then performed for both models under gravity and monotonically increasing horizontal loads. According to EC8 and Italian NTC 2008, two load distributions were used: one proportional to the modal shape, and the other proportional to the masses. Participant mass of the first mode for the Y direction was lower than 75%, so the modal distribution has been taken as proportional to the force distribution of a response spectrum analysis.

In the case of rigid floors, seismic forces were applied at the centre of mass of each storey. In the case of flexible floor, seismic forces were distributed through "areas of influence" and unidirectional slabs. Seismic masses were uniformly distributed on the supports of the beams. The non-linearity in frames [23] was defined by considering a lumped plasticity model by means of plastic hinges assigned at the extremities of each column [24]. In SAP2000 plastic hinges, properties can be defined depending on the type of hinge, and thus on the type of load–deformation relationship (moment–rotation), and depending on available form, as forms for only axial, shear, torsion, and moment or for interacting hinges (P-M2, P-M3, M2-M3, and P-M2-M3). The main force–deformation relation for r.c. elements, suggested by FEMA 356, were already implemented; limit values depended on the non-linear behaviour of each structural type and were indicated by FEMA itself or by laboratory

tests. The different strength of the two groups of columns also affect the stiffness according to the relation [20]:

$$E = 22,000 \left(\frac{f_{cm}}{10} \right)^{3/10} \tag{1}$$

From the capacity curve obtained by push-over analysis (Figure 9), the frames appeared sensible to the floor flexibility, particularly along the Y direction.

(**a**)

(**b**)
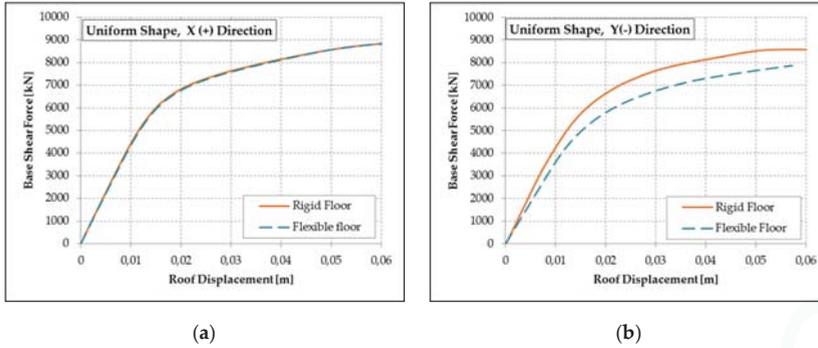
Figure 9. Pushover capacity curves in X (**a**) and Y (**b**) direction, with "uniform" pattern load distribution.

The evaluation of the displacements was performed by referring to the N2-method [25] by comparing seismic demand to capacity. A set of numerical analysis occurred for both rigid and flexible slabs. The structural checks were performed with two types of analyses:

(i)   Evaluation of shear behavior (brittle mechanism).

(ii)   Evaluation of compression-bending behavior (ductile mechanism).

As expected, the brittle mechanisms were more dangerous than the ductile ones, taking place for lower displacements (Figure 10). More in detail, the collapse of the structure started with a shear failure of the squat columns along the building perimeter between first and second floor, followed by a shear failure of the ground floor columns.
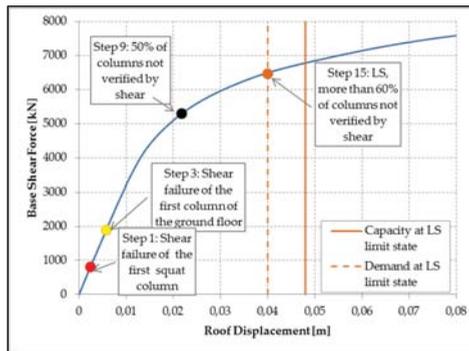
Figure 10. Capacity curve X direction from "modal" pattern of load distribution—rigid slab.

Values of maximum and minimum concrete compression strength, as defined before, were assigned to the structural elements (beams and columns) with two extreme distributions in plan

(Figure 11), considering both models (rigid and flexible slabs). The capacity curves—given by push-over analysis in both *X* and *Y* directions—showed the structure as more sensitive to the variation of the concrete strength in the model with flexible floors—particularly in the *Y* direction (Figures 12 and 13). The mode shape distributions of the equivalent seismic transverse loads systematically furnished a more severe result with respect to the uniformly shaped ones. To compare the different cases, the compression-bending strength of the ground floor pillars was chosen as collapse mechanism.

(**a**)   (**b**)
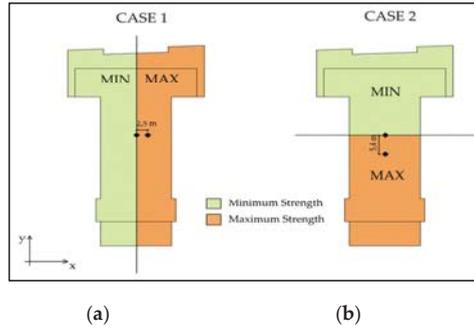
Figure 11. Extreme distributions of material irregularity: (**a**) CASE 1 (*X* direction); (**b**) CASE 2 (*Y* direction).

(**a**)   (**b**)
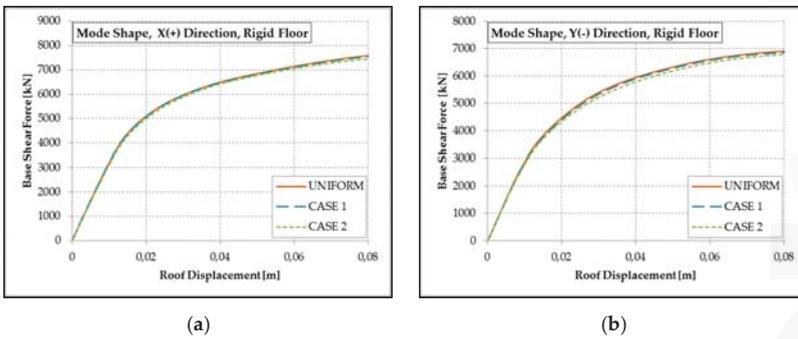
Figure 12. Capacity curves: (**a**)*X* direction; (**b**) *Y* direction with "mode shape" load—rigid floor.

(**a**)   (**b**)
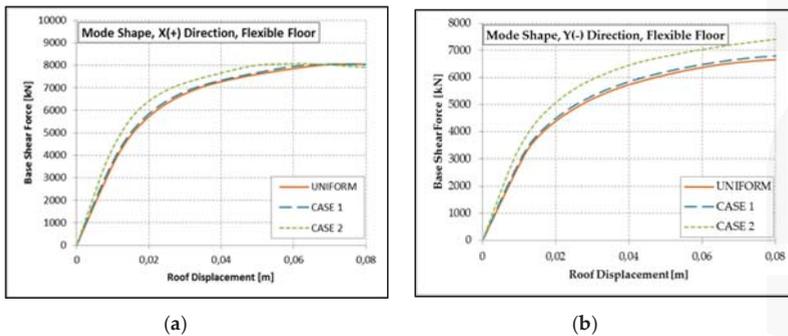
Figure 13. Capacity curves: (**a**) *X* direction; (**b**) *Y* direction with "mode shape" load—flexible floor.

3. Results of analysis

The assumption of rigid slab has made unessential any material asymmetry assumed (Figure 12). It can be noticed that in this case, the displacement of the control point is related to the average value of the assigned concrete strength. The average concrete strength does not differ significantly from the average value assumed for uniform distribution assumed in non-linear static analysis. The capacity curves of Figure 12 are emblematic in this sense. On the contrary, in the model with flexible slabs (Figure 13) sensible differences occurred, mainly for irregular distributions along the Y direction. It was also testified by the higher number of columns allowing the failure limit, compared with the uniform distribution of strength, as in the histograms of Figure 14.

(**a**)   (**b**)
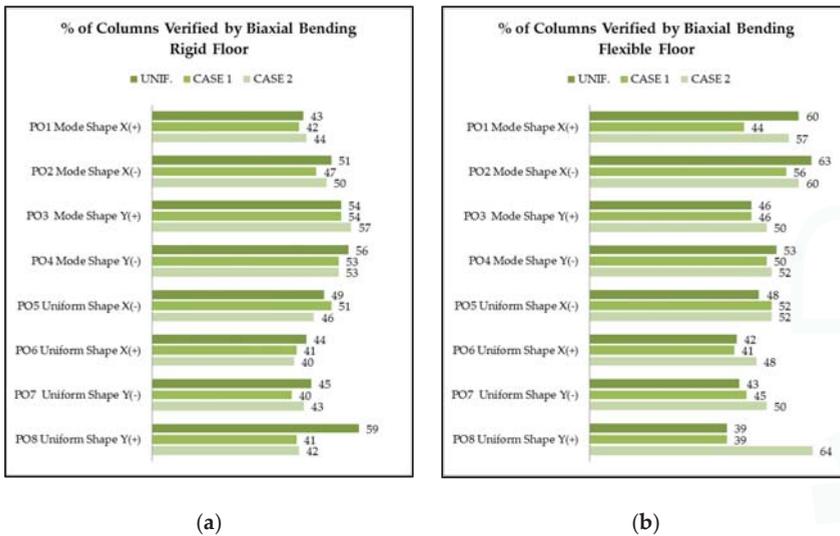
Figure 14. Biaxial bending with axial force verification for (**a**) rigid floor; (**b**) flexible floor.

The results obtained show the role of the rigid slabs in mitigating the effect of irregularity in horizontal force strength of the r.c. columns. Conversely, a flexible slab is more sensible to the variation of stiffness of the elements produced by the variation of the mechanical properties. This does not necessarily mean a worsening in the global behavior of the structure, as evidenced by Case 2. Finally, the Index of Seismic Risk (I_R) of the unreinforced state was estimated, with the following formulas:

$$I_R(PGA) = \left(\frac{PGA_C}{PGA_D} \right)^K \tag{2}$$

where PGA_C refers more specifically to the acceleration to the bedrock that determines severe damage and therefore a loss of structural resistance; PGA_D is the acceleration value with the probability of exceeding 10% in 50 years (return period 712 years);

$$I_R(T_R) = \left(\frac{T_{RC}}{T_{RD}} \right)^\alpha \tag{3}$$

where T_{RC} is the return period of the structure before intervention, and T_{RD} is the return period associated at the ultimate limit state (712 years).

Its variation has been analyzed modifying the slab type (rigid or flexible) and the distribution of the concrete strength (Case 1 and Case 2), depending on both the peak ground acceleration (PGA) and the reference return period (T_R) of the earthquake.

The values of I_R (Figure 15) confirmed the sensitivity of the structure to the variation in distribution of the material, with lower risk for Case 1 and higher risk for Case 2, with respect to uniform distribution of the concrete strength.

(**a**)   (**b**)
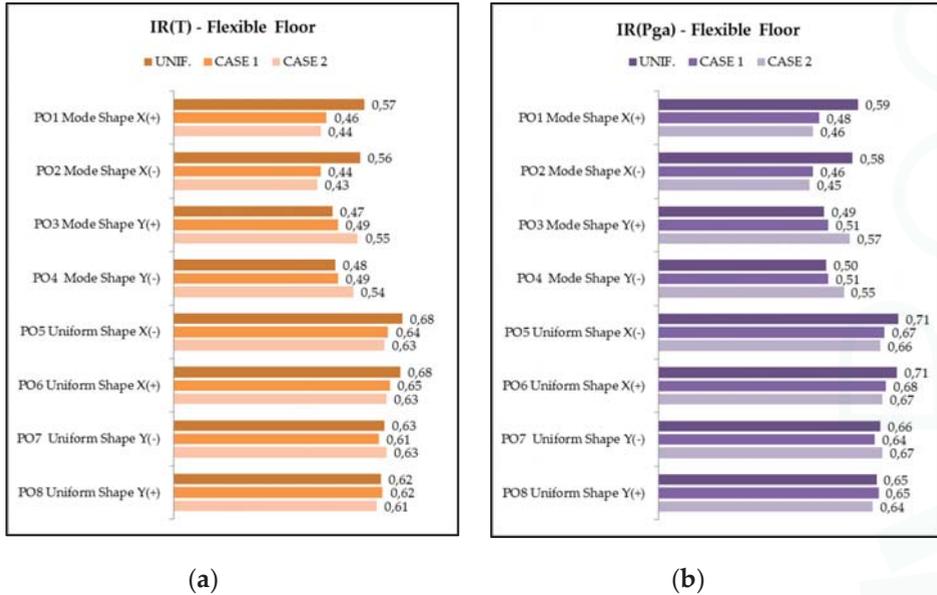
Figure 15. Seismic risks index for (**a**) reference return period and (**b**) peak ground acceleration (PGA).

4. Seismic Retrofitting

The pavilions in this study are under seismic reinforcement. The images provided are of the A pavilion. The intervention consists of the insertion of couple of symmetrical opposed r.c. bracing walls, stiffened by transverse r.c. buttresses, able to absorb the majority (more than 85%) of the design seismic action. Their positions correspond to the inner stairs and the toilets, with the aim of minimizing the impact on classrooms. These bracing systems are appropriately connected to the building: each portion of slab between the opposed walls is demolished and reconstructed through new r.c. plates well connected to walls. The r.c. bracing walls are also supported by a series of micropiles (Figures 16 and 17). The bracings are calculated to absorb the entire amount of the design seismic actions (Figure 18), achieving after retrofitting an index of seismic risk (IR) greater than one. The r.c. walls are also able to perform a stiffness more than ten times the global stiffness of the existing r.c. frames. The quality and uniformity of the concrete used on the new r.c. walls are strongly controlled. In this sense, the effect of material irregularity is then neglected. The geometrical disposition of the bracing system is based on centering of the center of strength, decreasing the eccentricity due to the dispersion of the concrete strength. The architectural effect of the refurbishment is in Figure 19, where the r.c. bracing walls are also aesthetically harmonized with the new façades.

(**a**)   (**b**)
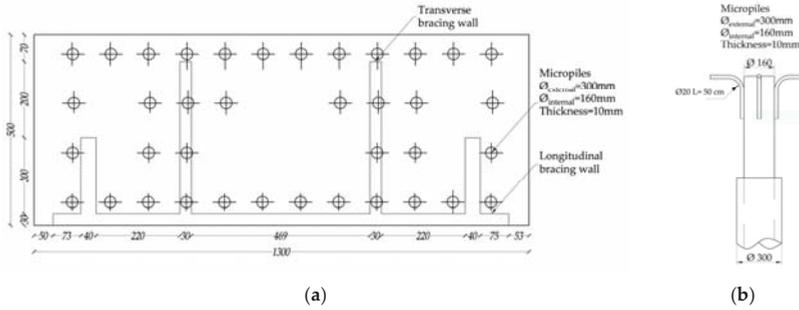
Figure 16. (**a**) Micropiles position; (**b**) Micropile detail.

(**a**)   (**b**)   (**c**)
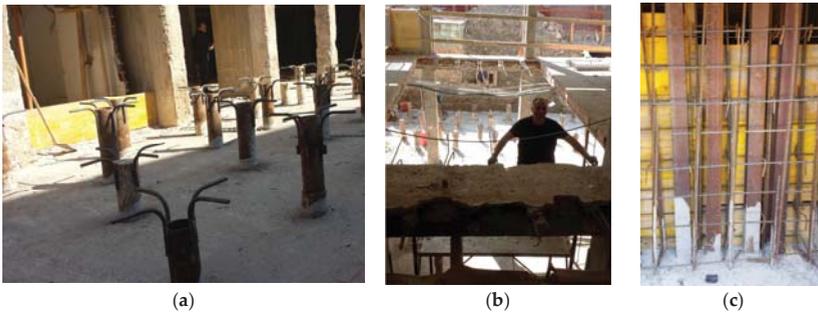
Figure 17. Phases of the intervention in A pavilion: (**a**) Micropiles anchoring, before casting of the concrete foundation; (**b**) Demolition of the slab to ensure the connectivity of the opposing bracing walls; (**c**) Insertion of the steel reinforcing with profiles HEB100.

(**a**)   (**b**)
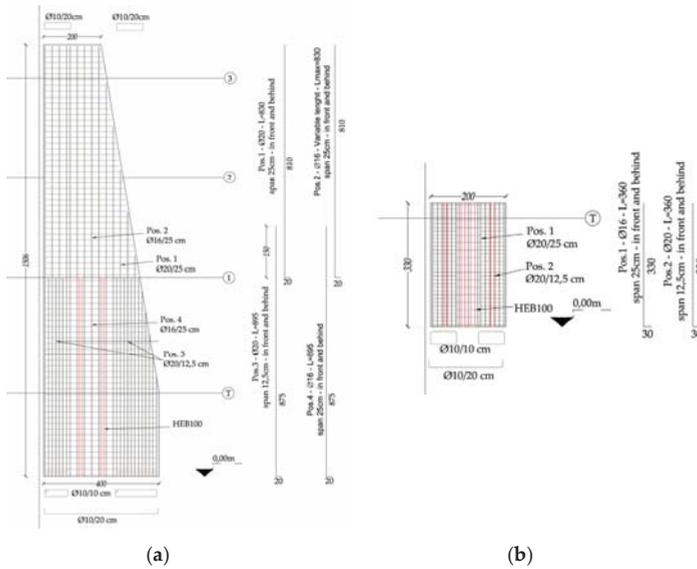
Figure 18. (**a**) Longitudinal r.c. bracing wall; (**b**) Transverse r.c. bracing wall.

(**a**)   (**b**)

Figure 19. Rendering views of the school from (**a**) south-east; (**b**) north-west.

5. Discussion and conclusions

The paper deals with the concept of center of strength and its "material eccentricity" on r.c. framed structures, in order to highlight its influence on the seismic response. It was performed through pushover analyses applied to a real case of r.c. building located in Italy. Two limit scenarios were considered, in order to emphasize the in-plan location of the center of strength. In the case of rigid slabs, the differences resulted less relevant, whereas if the floors were flexible, much greater differences emerged, in terms of global capacity curve, single elements verifications, and local generalized displacements. Concerning global capacity curves, the most important differences with the uniform case were found in the strength distribution orthogonal to the axis of symmetry of the building. The analysis showed how the structure was influenced by variability of the concrete compression strength. Comparison of the extreme distribution with the reference model with uniform distribution was performed both at global level (comparison between push-over curves) and at local level. The maximum differences (about 25%) of columns with respect to the failure limit have been observed in case of flexible slabs. Seismic risk index varied from 0.45 to 0.71. Thus, the "material eccentricity" can be assumed as a geometric factor, in addition to the accidental eccentricity.

Those values obtained neglecting the role of beams and nodes made necessary a structural intervention [26] to increase the strength of the structure. The illustrated strategy of reinforcement was based on additional r.c. shear walls, forced to move the majority of seismic actions from columns to the new walls, joined with a relevant reduction of the eccentric of the center of strength. Further studies should be addressed to evaluate their mechanical behavior in the case of blast loads as in [27] to appreciate the role of external r.c. walls as a practical strategy for the reinforcement of existing r.c. framed structures, together with more effective monitoring strategies for concrete [28].

Author Contributions: M.S. conceived the intervention and the design strategy. M.L.P. managed the engineering structural retrofit of the school complex and improved the structural details. E.M. and M.L.P. performed the numerical analysis. All the authors contributed in the same way to prepare the paper.

Conflicts of Interest: The authors declare no conflict of interest.

References

1. De Stefano, M.; Pintucchi, B. A review of research on seismic behaviour of irregular building structures since 2002. *Bull. Earthq. Eng.* **2008**, 285–308. [CrossRef]
2. Andreini, M.; De Falco, A.; Giresini, L.; Sassu, M. Structural damage in the cities of Reggiolo and Carpi after the earthquake on May 2012 in Emilia Romagna. *Bull. Earthq. Eng.* **2014**. [CrossRef]

3. Rovero, L.; Alecci, V.; Mechelli, J.; Tonietti, U.; De Stefano, M. Masonry walls with irregular texture of L'Aquila (Italy) seismic area: Validation of a method for the evaluation of masonry quality. *Mater. Struct.* **2016**, *49*, 2297–2314. [CrossRef]

4. Augenti, N.; Parisi, F. Learning from Construction Failures due to the 2009 L'Aquila, Italy, Earthquake. *J. Perform. Constr. Facil.* **2010**, *24*, 536–555. [CrossRef]

5. De-la-Colina, J.; Gonzalez-Perez, C.A.; Valdes-Gonzalez, J. Accidental eccentricities, frame shear forces and ductility demands of buildings with uncertainties of stiffness and live load. *Eng. Struct.* **2016**, *124*, 113–127. [CrossRef]

6. Basu, D.; Giri, S. Accidental eccentricity in multistory buildings due to torsional ground motion. *Bull. Earthq. Eng.* **2015**, *13*, 3779–3808. [CrossRef]

7. Parisi, F.; Augenti, N. Seismic capacity of irregular unreinforced masonry walls with openings. *Earthq. Eng. Struct. Dyn.* **2013**, *42*, 101–121. [CrossRef]

8. De Stefano, M.; Tanganelli, M.; Viti, S. Variability in concrete mechanical properties as a source of in-plan irregularity for existing RC framed structures. *Eng. Struct.* **2014**, *59*, 161–172. [CrossRef]

9. Giresini, L.; Sassu, M. Horizontally restrained rocking blocks: Evaluation of the role of boundary conditions with static and dynamic approaches. *Bull. Earthq. Eng.* **2017**, *15*, 385–410. [CrossRef]

10. Giresini, L.; Fragiacomo, M.; Sassu, M. Rocking analysis of masonry walls interacting with roofs. *Eng. Struct.* **2016**, *116*, 107–120. [CrossRef]

11. Giresini, L.; Fragiacomo, M.; Lourenço, P.B. Comparison between rocking analysis and kinematic analysis for the dynamic out-of-plane behavior of masonry walls. *Earthq. Eng. Struct. Dyn.* **2015**, *44*, 2359–2376. [CrossRef]

12. Sassu, M. The Reinforced Cut Wall (RCW): A Low-Cost Base Dissipator for Masonry Buildings. *Earthq. Spectra* **2006**, *22*, 533–554. [CrossRef]

13. Sassu, M. Biaxiality effect on the energy dissipated by elastoplastic base-isolators. *J. Eng. Mech.* **2003**, *129*, 607–612. [CrossRef]

14. Giresini, L. Energy-based method for identifying vulnerable macro-elements in historic masonry churches. *Bull. Earthq. Eng.* **2016**, *14*, 919–942. [CrossRef]

15. Andreini, M.; De Falco, A.; Giresini, L.; Sassu, M. Mechanical characterization of masonry walls with chaotic texture: Procedures and results of in-situ tests. *Int. J. Archit. Herit. Conserv. Anal. Restor.* **2014**, *8*, 376–407. [CrossRef]

16. EC8–3 Eurocode 8: Design of Structures for Earthquake Resistance—Part 3: Assessment and Retrofitting of Buildings 2005. Available online: http://eurocodes.jrc.ec.europa.eu/home.php (accessed on 13 April 2017).

17. Andreini, M.; De Falco, A.; Giresini, L.; Sassu, M. Collapse of the historic city walls of Pistoia (Italy): Causes and possible interventions. *Appl. Mech. Mater.* **2013**, *352*, 1389–1392. [CrossRef]

18. De Falco, A.; Giresini, L.; Sassu, M. Temporary preventive seismic reinforcements on historic churches: Numerical modeling of San Frediano in Pisa. *Appl. Mech. Mater.* **2013**, *352*, 1393–1396. [CrossRef]

19. Hurst, L. *Historic Concrete: Background to Appraisal*; Thomas Telford: London, UK, 2001; pp. 45–67.

20. CMIT Circolare del Ministro delle Infrastrutture e dei Trasporti 2 febbraio 2009, n. 617, contenente le Istruzioni per l'applicazione delle "Nuove norme tecniche per le costruzioni" di cui al DM 14 gennaio 2008. *Suppl. Ord.* **2009**. (Italian). Available online: www.cslp.it/cslp/index.php (accessed on 13 April 2017).

21. Myslimaj, B.; Tso, W.K. Desirable strength distribution for asymmetric structures with strength-stiffness dependent elements. *J. Earthq. Eng.* **2004**, *8*, 231–248. [CrossRef]

22. Casapulla, C.; Jossa, P.; Maione, A. Rocking motion of a masonry rigid block under seismic actions: A new strategy based on the progressive correction of the resonance response | Il moto sotto sisma del blocco murario: Analisi per progressiva correzione della risposta in risonanza. *Ing. Sismica* **2010**, *27*, 35–48.

23. Carta, G.; Stochino, F. Theoretical models to predict the flexural failure of reinforced concrete beams under blast loads. *Eng. Struct.* **2013**, 306–315. [CrossRef]

24. De Luca, F.; Verderame, G.M. A practice-oriented approach for the assessment of brittle failures in existing RC elements. *Eng. Struct.* **2013**, *48*, 373–388. [CrossRef]

25. Fajfar, P. A Nonlinear Analysis Method for Performance-Based Seismic Design. *Earthq. Spectra* **2000**, *16*, 573–592. [CrossRef]

26. De Luca, F.; Verderame, G.M.; Manfredi, G. Eurocode-based seismic assessment of modern heritage RC structures: The case of the Tower of the Nations in Naples (Italy). *Eng. Struct.* **2014**, *74*, 96–110. [CrossRef]

27. Stochino, F. RC beams under blast load: Reliability and sensitivity analysis. *Eng. Fail. Anal.* **2016**, *66*, 544–565. [CrossRef]

28. Mistretta, F.; Piras, M.V.; Fadda, M.L. A reliable visual inspection method for the assessment of r.c. structures through fuzzy logic analysis, Life-Cycle of Structural Systems: Design, Assessment, Maintenance and Management. In Proceedings of the 4th International Symposium on Life-Cycle Civil Engineering IALCCE 2014, Tokoy, Japan, 16–19 November 2014; pp. 1154–1160.

Analysis of Cylindrical Granular Material Silos under Seismic Excitation

Christoph Butenweg [1], Julia Rosin [1,*] and Stefan Holler [2]

[1]   SDA-Engineering GmbH, Kaiserstraße 100, TPH III/B, 52134 Herzogenrath, Germany;
     butenweg@sda-engineering.de

[2]   CH-Ingenieure GbR, Charlottenburger Allee 41, 52078 Aachen, Germany; holler@ch-ing.de

*   Correspondence: rosin@sda-engineering.de; Tel.: +49-2407-56848-16

Abstract: Silos generally work as storage structures between supply and demand for various goods, and their structural safety has long been of interest to the civil engineering profession. This is especially true for dynamically loaded silos, e.g., in case of seismic excitation. Particularly thin-walled cylindrical silos are highly vulnerable to seismic induced pressures, which can cause critical buckling phenomena of the silo shell. The analysis of silos can be carried out in two different ways. In the first, the seismic loading is modeled through statically equivalent loads acting on the shell. Alternatively, a time history analysis might be carried out, in which nonlinear phenomena due to the filling as well as the interaction between the shell and the granular material are taken into account. The paper presents a comparison of these approaches. The model used for the nonlinear time history analysis considers the granular material by means of the intergranular strain approach for hypoplasticity theory. The interaction effects between the granular material and the shell is represented by contact elements. Additionally, soil–structure interaction effects are taken into account.

1. Introduction

Adequate seismic design of silos is especially important in the field of plant engineering since structural damage often leads to consequential damage such as fires, explosions, and the release of toxic substances into the air and soil. Furthermore, silos are important supply structures that serve to store foodstuffs and industrial goods and to compensate for fluctuations between production and consumption. However, past earthquakes have repeatedly caused damage to silos. One of the main causes for damage is buckling on the foot of the wall of the silo as a result of a combination of axial compressive stresses, circumferential tensile stresses and high shear stresses that is also referred to as "elephant's foot buckling" and typically related to steel silos. For silos made of reinforced concrete different failure modes may occur [1–3]. In addition, slender silos are at risk of tipping over due to high seismic inertial forces when the anchoring or the foundation fails. Silos with substructures are especially at risk of tipping over due to the weight of the silo, which causes the structure to be top-heavy. Figure 1 shows the collapse of a slender silo made of steel as a result of a series of earthquakes in the Emilia–Romagna region in Northern Italy in 2012. In addition to the collapsed silo, the other three silos in the group also exhibited clearly visible buckling damage in the highly stressed areas.

Seismically excited silo structures have long been the subject of intensive research, which has always been the goal of understanding the interaction between filling and silo wall and to derive comprehensible calculation and design concepts. Rotter and Hall [1] investigated the problem of compact cylindrical silos, identified the main failure modes, and derived design criteria for steel

silos based on a numerical model. Yokota et al. [4], Shimamato et al. [5], and Sakai et al. [6] carried out vibration tests on cylindrical model silos filled with coal, and derived basic knowledge about the vibration behavior of silos. Younan and Veletsos [7] developed an analytical formulation for describing the seismic response of material-filled silos with rigid walls for constant accelerations, harmonic excitations, and stochastic seismic effects, which were also extended to flexible tank shells [8]. Bauer [9] and Braun [10] dealt with the material behavior of bulk materials and their behavior under dynamic loads. The current version of the Eurocode 8, Part 4 [11], is essentially based on the formulation of Younan and Veletsos [7] and the work of Rotter and Hall [1]. The complex interaction between the filling material and the silo shell is not explicitly taken into account, among other things, by the pressure conditions as well as the soil and wall friction coefficients. Holler and Meskouris [12] showed that the loading rates are too conservative in the case of compact silos, whereas loads on slender silos are well represented. Recent shaking table tests [13] have shown that the approaches in Eurocode 8 [11] are too conservative and the dynamic response is strongly dependent on the wall friction coefficient. Better agreement with the experimental results is obtained with the analytical approach according to Silvestri et al. [14]. The same results are obtained by Pieraccini et al. [15] with an improved approach based on the theory of Silvestri [14].

Figure 1. Total collapse of a slender silo during the earthquake series in Emilia Romagna/Northern Italy in 2012.

In the following, firstly the design by means of a non-linear calculation model for cylindrical silos with granular bulk materials is presented taking into account the non-linearities of the bulk material and the interaction of the bulk material with the silo wall. After that, the static load approach of Eurocode 8, Part 4 [11], is applied to a slender silo. A comparison of the two calculation approaches as well as the approach of Silvestri [14] for a squat silo then follows.

2. Equivalent Load Method

The static replacement loads for silo structures must be determined both for the components due to seismic excitation in the horizontal as well as in the vertical direction. The vertical component is not negligible as is often the case in building construction, since the acceleration of the high concentrated silo masses leads to dynamic stress pressures, which are particularly relevant for the design of the hopper outlet.

2.1. Equivalent Seismic Loads in Horizontal Direction

Due to seismic excitation silo walls are subjected to additional horizontal seismic actions caused by the acceleration of the mass of the granular material. These actions can be represented according to

Eurocode 8, Part 4 [11], through an additional normal pressure on the wall, which for cylindrical silos is given by

$$\Delta_{ph,s} = \Delta_{ph,so} \cdot \cos\theta. \tag{1}$$

The resulting pressure distribution is shown in Figure 2. Herein $\Delta_{ph,so}$ is the reference pressure acting on the silo wall at a distance x from the flat bottom or from the tip of a conical or pyramidal hopper:

$$\text{Silo wall}: \Delta_{ph,so} = \alpha(z) \cdot \gamma \cdot \min\{r_s^*, 3x\} \tag{2}$$

$$\text{Silo hopper}: \ \Delta_{ph,so} = \alpha(z) \cdot \gamma \cdot \min\{r_s^*, 3x\}/\cos\beta. \tag{3}$$

The reference pressure $\Delta_{ph,so}$ depends on the following material and geometrical parameter:

$\alpha(z)$ response acceleration of the silo at a depth z from the equivalent surface of the fill mass in g;
γ characteristic value for the specific weight of the fill mass;
r_s^* $r_s^* = \min\left\{h_b, \frac{d_c}{2}\right\}$;
h_b total height of the silo from a flat floor or a hopper tip to the equivalent surface of the fill mass;
d_c interior diameter in cylindrical silos;
θ angle relative to the direction of the seismic excitation ($0 \leq \theta \leq 360°$);
β slope of the hopper wall relative to a vertical axis or maximum wall slope (relative to the vertical) for pyramidal hoppers.
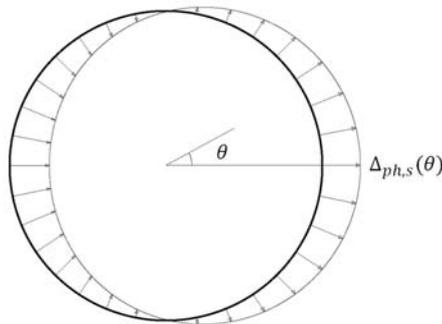
Figure 2. Equivalent static load for cylindrical silos according to Eurocode 8, Part 4 [11].

Generally, combinations of the seismic pressure with those resulting from filling or emptying the silo must be considered in order to ensure that no negative (pointing to the interior) pressures arise and the contact between the fill mass and the silo wall is maintained at all times. When such pressure situations occur in higher sections, the negative pressure is redistributed to the opposed pressure-loaded wall of the silo. The acceleration of the silo is described by a variable distribution according to a function $\alpha(z)$, for which the variation of the acceleration along the height must be determined beforehand. If the latter is not known, $\alpha(z)$ may be substituted by the value of the acceleration acting at the height of the mass center. Figure 3 shows the pressure distributions due to seismic actions and filling and their superposition for a constant and variable acceleration over the silo height. The static load distributions are reduced at the bottom to take into account that for squat silos a large part of the lateral seismic force is taken up by internal friction in the fill mass and does not affect the silo wall. However, it has to keep in mind, that the simplified distributions are just approximations of the real dynamic pressures.

Dynamic pressures	Pressures due to filling	Superposition
Pressure distributions using a constant acceleration over the silo height		
Pressure distributions using a variable acceleration over the silo height		
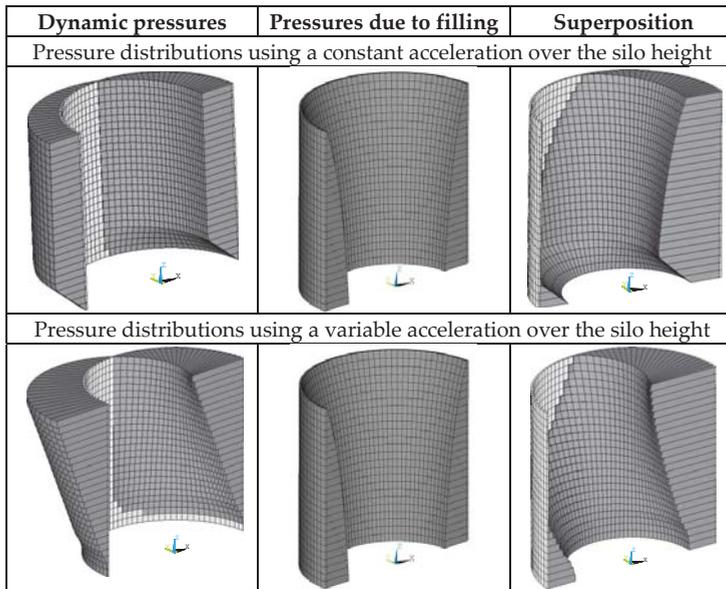
Figure 3. Pressure distributions—dynamic pressures, pressures due to filling and superposition.

2.2. Equivalent Seismic Loads in Vertical Direction

Eurocode 8, Part 4 [11], stipulates that vertical seismic loads must be considered in addition to the lateral seismic loads but does not prescribe how to apply them to the silo walls. A meaningful approach consists in deriving the additional dynamic forces directly from the static forces due to filling. To that effect a scaling factor C_d is determined as the spectral acceleration for the fundamental vertical vibration mode, given in units of g. Measurements and numerical results have shown that the fundamental vertical vibration mode is located in the low-period range of the response spectrum, so that the plateau spectral acceleration value $S_{av,\max}$ can be assumed to be on the safe side. The scaling factor is given by

$$C_d = \frac{S_{av,\max}}{g}. \tag{4}$$

C_d is then used for computing additional friction pressures p_w for walls and vertical pressures p_v for silo floors and hoppers according to Eurocode 1, Part 4 [16], by simply scaling the pressures due to filling. However, it should also be mentioned that additional seismically induced forces may be computed for the loads arising during silo emptying—which load combination is the most unfavorable must be decided on a case-by-case basis. The importance of vertical seismic pressures increases with higher seismic loads, since the additional pressures are no longer covered by the safety factors for the serviceability limit states. The need to take into account vertical seismic effects is also shown by Silvestri et al. [14]. Here, a comparable load approach to increase the vertical and horizontal wall pressures is proposed.

2.3. Combination of Equivalent Seismic Loads in Horizontal and Vertical Directions

Generally, lateral (in two mutually orthogonal directions) and vertical seismic loads applied to silos must be considered to act jointly. This effect may be taken into account approximately through the standard 30% rule according to Eurocode 8, Part 1 [17]. On the other hand, Eurocode 8, Part 4 [11],

stipulates that, for axisymmetric silos, it is sufficient to consider a single lateral component together with the vertical component. Therefore, it is sufficient to consider in total two load combinations.

3. Nonlinear Numerical Simulation Model

The hypoplastic material law is used to describe the behavior of the granular material. Different formulations for hypoplasticity have been investigated: the hypoplasticity based on the formulation of Gudehus [18], two modified versions using time history functions according to Bauer [9] and Braun [10] and the intergranular strain approach developed by Niemunis and Herle [19]. Comparisons of the different approaches with soil mechanic cyclic tests clarifies that the intergranular strain approach according to Niemunis and Herle [19] leads to the most realistic results [12,20]. Therefore, this approach was applied within the overall model.

The set-up of the nonlinear simulation model is presented in Figure 4. The foundation slab is placed on the soil, which is regarded as an elastic half space represented by the well-known cone model according to Wolf [21]. The granular material is modeled by 20-node solid elements incorporating the intergranular strain approach according to Niemunis and Herle [19]. The silo wall is represented by eight node shell elements and connected with contact elements to the granular material. The contact elements transfer compression and friction forces and allow for a separation between the filling and the silo wall. The proposed model was validated by shaking table tests of scaled steel silo models [12].
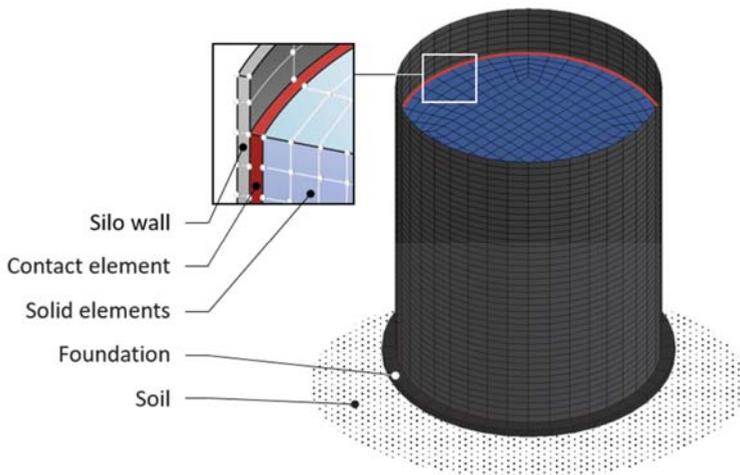
Figure 4. Nonlinear calculation model.

4. Calculation Examples

The design approach of Eurocode 8, Part 4 [11], bases on equivalent static loads representing additional inertial forces due to the acceleration of the material. This assumption leads, in the case of slender silos, to a sufficient correspondence with the actual load-bearing behavior. In the case of squat silos, the internal friction of the granular material near the ground and its load bearing behavior is taken into account only by a short linear increase in the lower region of the silo shell. For this reason, this approach is to be assessed more precisely by a comparison with the non-linear simulation model. For the slender silo, the influence of the use of a constant and variable acceleration profile over the silo height is investigated. The geometry and material parameters for the slender and squat silo are summarized in Table 1.

Table 1. Geometry and material parameter of the slender and squat silo.

Silos			
Height (squat/slender)	h	10.0/30.0	m
Inner diameter (squat/slender)	d_c	10.0/6.0	m
Thickness silo wall (squat/slender)	t	10.0/8.0	mm
Young's modulus	E	210.000	N/mm^2
Poisson's ratio	v	0.3	[-]
Bulk Material			
Bulk unit weight	γ	15.0	kN/m^3
Horizontal load ratio	K	0.45	[-]
Wall friction angle	μ	0.40	[-]
Amplification factor	c_{pf}	1.00	[-]
Amplification factor pressure on the bottom	c_b	1.00	[-]

4.1. Slender Silo

According to Table 1, the slender silo has a height of 30 m, an inner diameter of 6 m, and a constant wall thickness of 8 mm. To determine the acceleration profiles, the silo is simulated as a beam model with 15 lumped masses. These masses consider the dead weight of the silo shell and the granular material (Figure 5). The first eigenfrequency is determined for the multiple mass oscillator at 1.0 Hz. A spectral acceleration of 5 m/s^2 is assigned for a location in New Zealand in accordance with the spectrum [22] set in Figure 6, if the ascending branch in the response spectrum is neglected.
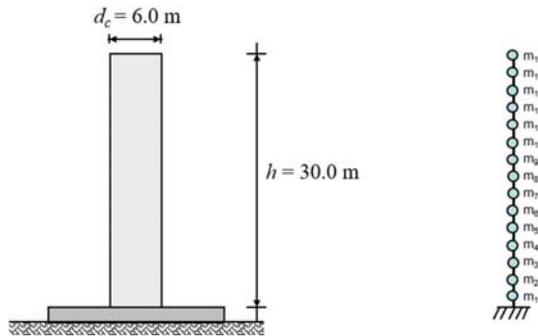
Figure 5. Slender silo and idealization as multiple mass oscillator.
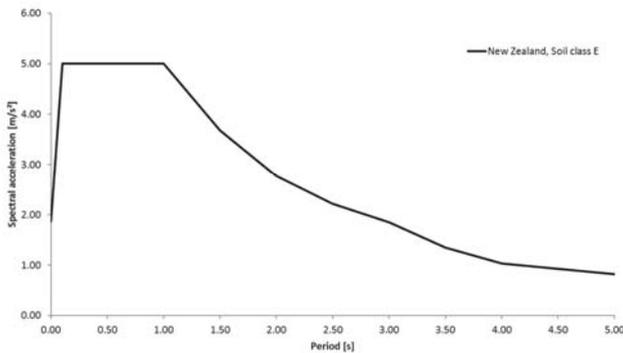
Figure 6. Design response spectrum according to the seismic code of New Zeeland, Soil Class E [22].

With the spectral acceleration of 5 m/s^2 and the total mass of 1756.26 t, the base shear is F$_b$ = 8781.3 kN.   From this, the linear acceleration profile is determined by the height- and mass-proportional distribution of the forces on the heights of the masses. In addition, the multiple mass oscillator is used to perform a calculation using the multimodal response spectra method, taking into account 10 eigenforms. The course of the accelerations from the multimodal calculation in comparison to the linear approach is shown in Figure 7.
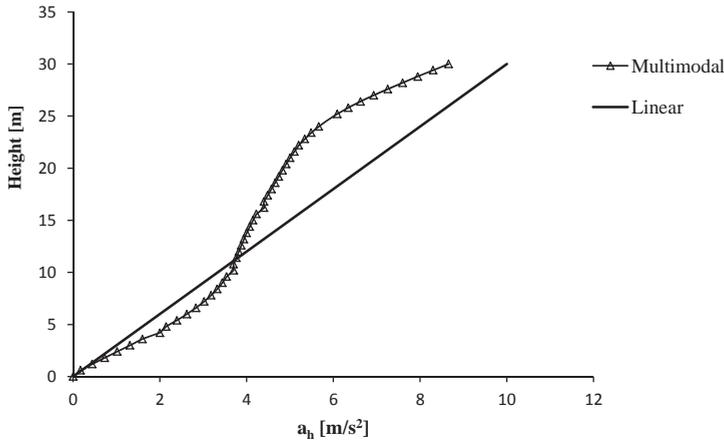
Figure 7. Linear and multimodal acceleration profile.

The horizontal seismic pressures acting on the silo wall are calculated according to Section 2.1 using the variable acceleration profiles (Figure 7). They are applied as static equivalent loads together with the static pressures on a finite element model of shell elements. In addition, the seismic loads due to vertical seismic excitation with a$_v$ = 0.7a$_h$ = 3.5 m/s^2 according to Section 2.2 are taken into account in the model. Figure 8 shows the resulting circumferential and axial stresses for a constant acceleration as well as for the acceleration profiles given in Figure 7.
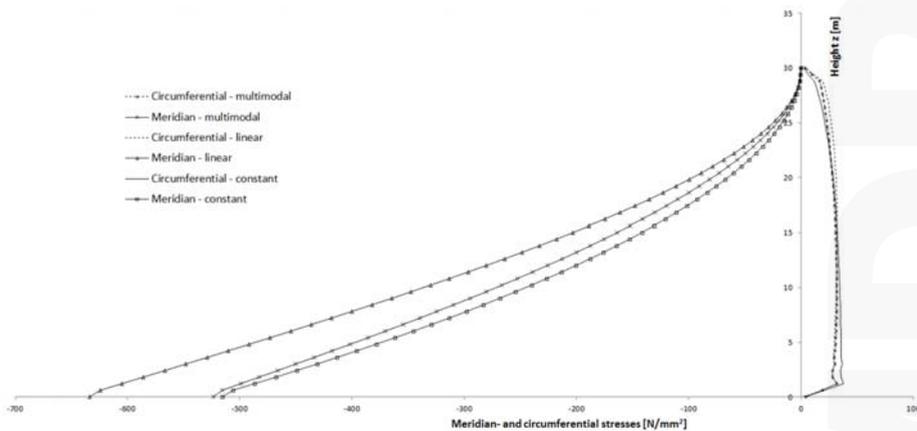
Figure 8. Circumferential and axial stresses as results of the different approaches of the acceleration.

To the regarded silo construction, the results show that the linear approach provides the greatest axial stresses, whereas the constant and multimodal approach results in comparable stresses. This is due to the higher accelerations and the more unfavorable distribution of the horizontal forces over the height. The results of the different approaches also vary over the height in the case of the circumferential stresses, although the differences are not as great as for the axial stresses.

4.2. Squat Silo

According to Table 1, the regarded squat silo ($h/d_c < 1.0$) has a height of 10 m, an inner diameter of 10 m and a constant wall thickness of 8 mm. The connection to the foundation is assumed to be rigid. A simplified model of the foundation as a rigid reinforced concrete block with a density of 25 kN/m^3 is used. The connection to the lower edge of the foundation is represented by a stiffness matrix that models the elastic half space under the foundation for a shear wave velocity of 500 m/s based on the truncated cone model of Wolf [21]. The associated mass fractions and damping ratios are also taken into account in the model.

The silo is located in Istanbul, for which a reference peak ground acceleration a_g of 4.16 m/s^2 must be assumed. The corresponding elastic response spectra in the horizontal and vertical direction according to Eurocode 8, Part 1 [17], for Spectrum Type I and Soil Class B is shown in Figure 9.
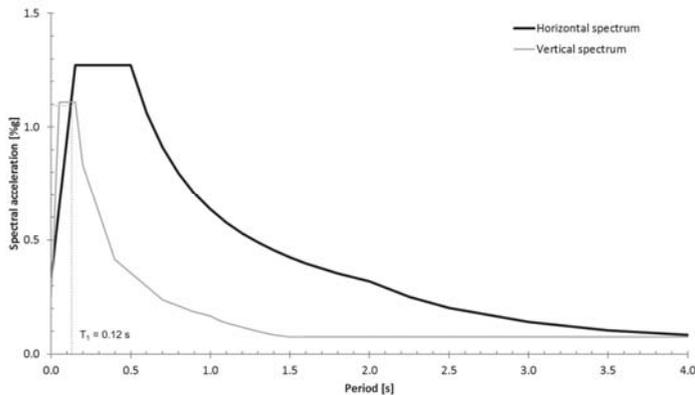
Figure 9. Elastic response spectrum for the location in Istanbul according to [17].

Due to the thin walls of the silo and the associated risk of the shell buckling, a behavior factor will not be used (q = 1.0). A linear-elastic continuum model will be used to determine the first Eigen period. The bulk material is idealized using volume elements, and the silo shell is idealized using shell elements. The contact area between the bulk material and the wall of the silo is assumed to be rigid. This model yields a first Eigen period of $T_1 = 0.12$ s taking the interaction between the soil and the structure into account. This results in spectral accelerations of $S_{ah} = 10.9$ m/s^2 in the horizontal direction and $S_{av} = 11.0$ m/s^2 in the vertical direction. The vertical acceleration results in a scaling factor of $C_d = 1.12$ according to Equation (4). Due to the stockiness of the silo, the horizontal spectral acceleration is assumed to act on the center of mass and is considered to be constant along the height of the silo as an approximation. Using the approaches for the static equivalent loads of Sections 2.1 and 2.2, the circumferential and axial stresses presented in Figures 10 and 11 are obtained as a result of the horizontal and vertical effects of the earthquake. Figure 11 additionally shows the comparison of the resulting meridian and ring stresses using the load approach according to Silvestri et al. [14] at a constant spectral acceleration $S_{av} = 11.0$ m/s^2. It becomes clear here that the approach of Silvestri is more conservative with equal input values. This is because in the proposed

approach, the pressure is scaled exponentially according to the theory of Jansen [23] while that of [14] suggests a linear approach.
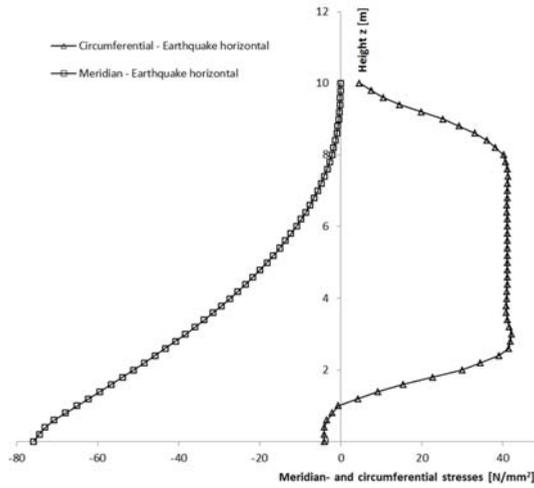
Figure 10. Circumferential and axial stresses due to horizontal seismic excitation.
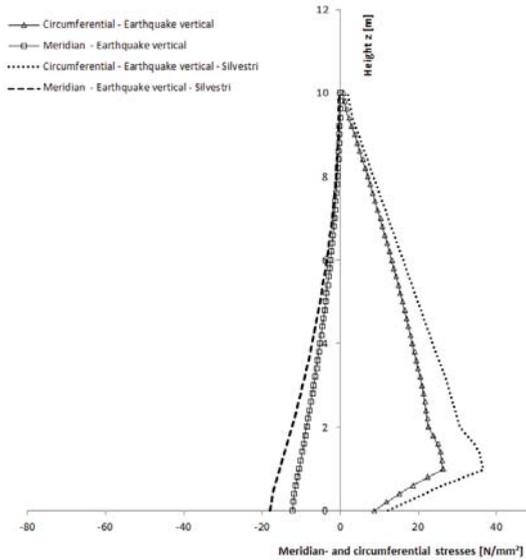
Figure 11. Circumferential and axial stresses due to vertical seismic excitation.

To enable the comparison with transient analyses, synthetically time histories are generated in horizontal and vertical direction (Figure 12) using the elastic response spectra shown in Figure 9.
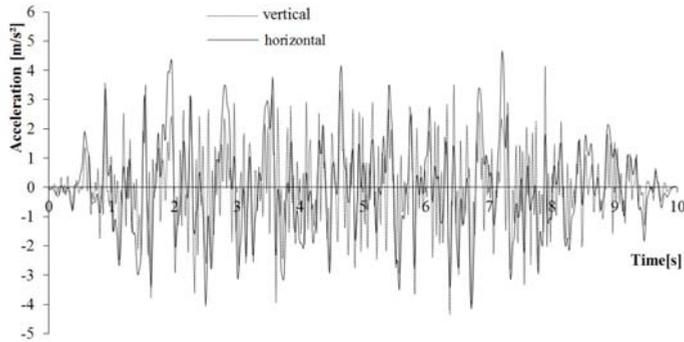
Figure 12. Synthetically generated acceleration time histories.

A comparison between the dynamic stresses between the equivalent load method and the non-linear simulation model is provided in Figure 13. As in the non-linear simulation model, the time history is applied as acting in both a horizontal and a vertical direction, it is necessary to make the comparison with the earthquake combinations in both directions. The combination of the directions is based on the 30% rule. Additionally, the full superposition of both of the directions was applied.
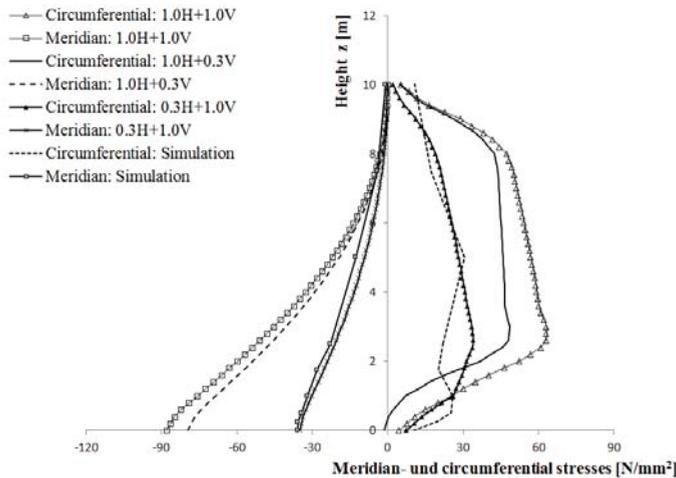
Figure 13. Circumferential and axial stresses due to seismic excitation.

The results show considerable differences. The increase factors that were calculated on the basis of the equivalent load method result in a 2–3 times higher factor when compared with the simulation results on the basis of the 30% rule, whereby the combination of 1.0 times the horizontal loads with 0.3 times the vertical loads is decisive. The full superposition provides results that tend to be more certain when compared with the simulation calculation. This is mainly due to the load assumptions of the Eurocode 8, Part 4 [11], which is based on the loads that are to be applied from the horizontal acceleration of the bulk materials being fundamentally transferred from the silo shell to the foundation soil. Contrary to this, it is discernible in the simulation that a substantial part of the horizontal loads due to the acceleration of the material is transferred directly by friction in the foundation soil (or the foundation itself).

This effect is especially pronounced in the squat silo that is being considered here. Its effect decreases the higher the H/D ratio becomes. With the equivalent load method, an attempt is made to do justice to this effect, by a linear progression of the cosine-shaped earthquake load being assumed to exist from the base of the silo up to a defined height. With this reduction of the load applied to the base of the silo considered here, a comparison made with the non-linear simulation under application of the equivalent load method still produces conservative results.

When applied to slender silos, the differences between the calculation methods become considerably less with the equivalent load method reflecting the dynamic stress distribution well. This has been proven by Holler and Meskouris [12] in advanced experimental and numerical studies.

5. Conclusions

The article presents an approach for the seismic calculation of cylindrical silos made of steel containing granular bulk materials. A simplified calculation approach with static equivalent loads is presented for seismic excitation due to the horizontal and vertical direction. In addition, a non-linear simulation model for calculations in the time domain is introduced. The application of the approach with static equivalent loads to a slender silo shows that it is more realistic and economical to determine the acceleration profile along the height of the silo using multimodal analysis on a simplified beam model and not to use a simplified linear acceleration profile as the latter yields results that are too conservative.

A comparison of the results with static equivalent loads and a non-linear simulation model for a squat silo clearly shows that the approach with static equivalent loads yields results with a more than adequate safety margin. The reason for this is that the load approach does not model with adequate precision the fact that, in the case of a squat silo, a large portion of the stress is removed directly through the friction of the bulk material. This results in very conservative stress curves, which in turn can result in uneconomical designs. Here, the use of the nonlinear numerical model can lead to advantages regarding the economical design of the silo structure.

References

1. Rotter, J.M.; Hull, T.S. Wall loads in squat steel silos during earthquake. *Eng. Struct.* **1989**, *11*, 139–147. [CrossRef]
2. Rotter, J.M. Structures, stability, silos and granular solids: A personal adventure. In *Structures and Granular Solids: From Scientific Principles to Engineering Application*; Chen, J.F., Ooi, J.Y., Teng, J.G., Eds.; Taylor & Francis Group: London, UK, 2008; pp. 1–20.
3. Rotter, J.M. Silos and tanks in research and practice: State of the art and current challenges. In Proceedings of the International Association for Shell and Spatial Structures (IASS) Symposium 2009—Evolution and Trends in Design, Analysis and Construction of Shell and Spatial Structures, Valencia, Spain, 28 September–2 October 2009; Domingo, A., Lazaro, C., Eds.; Universitat Politècnica de València: Valencia, Spain, 2009.
4. Yokota, H.; Sugita, M.; Mita, I. Vibration tests and analyses of coal-silo model. In Proceedings of the 2nd International Conference on the Design of Silos for Strength and Flow, Stratford-upon-Avon, UK, 7–9 November 1983; pp. 107–116.
5. Shimamoto, A.; Kodama, M.; Yamamura, M. Vibration tests for scale model of cylindrical coal storing silo. In Proceedings of the 8th World Conference on Earthquake Engineering, San Francisco, CA, USA, 21–28 July 1984; Volume 5, pp. 287–294.

6.   Sakai, M.; Matsumura, H.; Sasaki, M.; Nakamura, N.; Kobayashi, M.; Kitagawa, Y. Study on the dynamic behavior of coal silos against earthquakes. *Bulk Solids Handl.* **1985**, *5*, 1021.

7.   Younan, A.H.; Veletsos, A.S. Dynamics of solid-containing tanks I: Rigid tanks. *J. Struct. Eng.* **1998**, *124*, 52–61. [CrossRef]

8.   Veletsos, A.S.; Younan, A.H. Dynamics of solid-containing tanks II: Flexible tanks. *J. Struct. Eng.* **1998**, *124*, 62–70. [CrossRef]

9.   Bauer, E. Zum Mechanischen Verhalten Granularer Stoffe unter Vorwiegend ödometrischer Beanspruchungen. Veröffentlichungen des Institutes für Bodenmechanik und Felsmechanik der University Fridericiana in Karlsruhe, No 130. Ph.D. Thesis, Universität Fridericiana zu Karlsruhe, Karlsruhe, Germany, 1992.

10. Braun, A. Schüttgutbeanspruchungen von Silozellen unter Erdbebeneinwirkungen. Institut für Massivbau und Baustofftechnologie. Ph.D. Thesis, Karlsruhe Institute of Technology, Karlsruhe, Germany, 1997.

11. *Eurocode 8: Design of Structures for Earthquake Resistance—Part 4: Silos, Tanks and Pipelines, German Version EN 1998-4:2006*; Deutsches Institut für Normung e.V., Beuth-Verlag GmbH: Berlin, Germany, 2006.

12. Holler, S.; Meskouris, K. Granular Material Silos under dynamic excitation: Numerical simulation and experimental validation. *J. Struct. Eng.* **2006**, *1320*, 1573–1579. [CrossRef]

13. Silvestri, S.; Ivorra, S.; Chiacchio, L.D.; Trombetti, T.; Foti, D.; Gasparini, G.; Taylor, C. Shaking-table tests of flat-bottom circular silos containing grain-like material. *Earthq. Eng. Struct. Dyn.* **2016**, *45*, 69–89. [CrossRef]

14. Silvestri, S.; Gasparini, G.; Trombetti, T.; Foti, D. On the evaluation of the horizontal forces produced by grain-like material inside silos during earthquakes. *Bull. Earthq. Eng.* **2012**, *65*, 69–89. [CrossRef]

15. Pieraccini, L.; Silvestri, S.; Trombetti, T. Refinements to the Silvestri's theory for the evaluation of the seismic actions in flat-bottom silos containing grain-like material. *Bull. Earthq. Eng.* **2015**, *131*, 3493–3525. [CrossRef]

16. *Eurocode 1: Actions on Structures—Part 4: Silos and Tanks. German Version EN 1991-4:2006*; Deutsches Institut für Normung e.V., Beuth-Verlag GmbH: Berlin, Germany, 2006.

17. *Eurocode 8: Design of Structures for Earthquake Resistance—Part 1: General Rules, Seismic Actions and Rules for Buildings, German Version EN 1998-1:2004 + AC: 2009*; Deutsches Institut für Normung e.V., Beuth-Verlag GmbH: Berlin, Germany, 2010.

18. Gudehus, G. A comprehensive equation for granular materials. *Soils Found.* **1996**, *36*, 1–12. [CrossRef]

19. Niemunis, A.; Herle, I. Hypoplastic model for cohesionless soils with elastic strain range. *Mech. Cohesive-Frict. Mater.* **1997**, *2*, 279–299. [CrossRef]

20. Wagner, R. Seismisch Belastete Schüttgutsilos. Ph.D. Thesis, Lehrstuhl für Baustatik und Baudynamik, RWTH Aachen University, Aachen, Germany, 2009.

21. Wolf, J.P. *Foundation Vibration Analysis Using Simple Physical Models*; PTR Prentice Hall Inc.: Upper Saddle River, NJ, USA, 1994; p. 27.

22. *New Zealand Standard 1170.5: Structural Design Actions, Part 5: Earthquake Actions*; Standards New Zealand: Wellington, New Zealand, 2004.

23. Janssen, H.A. Getreidedruck in Silozellen. *Z. Ver. Dt. Ing.* **1895**, *39*, 1045–1049.

Assessment Method for Combined Structural and Energy Retrofitting in Masonry Buildings

Mauro Sassu * [ID], **Flavio Stochino** [ID] **and Fausto Mistretta**

Department of Civil, Environmental Engineering and Architecture, University of Cagliari, 09123 Cagliari, Italy; fstochino@unica.it (F.S.); fmistret@unica.it (F.M.)

* Correspondence: msassu@unica.it; Tel.: +39-070-675-5409

Abstract: The retrofitting of existing masonry buildings is now a crucial problem for Europe. Indeed, structural safety and energy efficiency should represent the target of any renovation. The proposal of a new synthetic performance parameter is presented and discussed. Following this approach, in this paper, after a review of the main studies available in the literature, a proposal of a new performance parameter approach is presented and discussed. It is capable of taking into account both the structural and thermal aspects of masonry retrofitting. An emblematic set of reinforcements and energy improvements for masonry walls is examined. An example, generalized formulas, and a simultaneous evaluation of the role of multiple structural and thermal parameters on masonry buildings are proposed, with a view to optimize several categories of costs related to the intervention.

Keywords: masonry buildings; structural retrofitting; energy retrofitting; combined retrofitting performance; walls refurbishment; generalized performance parameter

1. Introduction

Most of the European traditional buildings are made of masonry. An example of this trend is the graph in Figure 1, representing the impact of masonry constructions built during XX century in Italy. In the past, masonry buildings were often built without structural calculation, only following technical rules or empirical codes. It should be noted that masonry construction has decreased over the years as framed solutions (reinforced concrete (RC) or others) that permit more freedom to the designers have increased. Thus, to assess the structural integrity of such constructions, a thorough review of their current condition has to be perform.
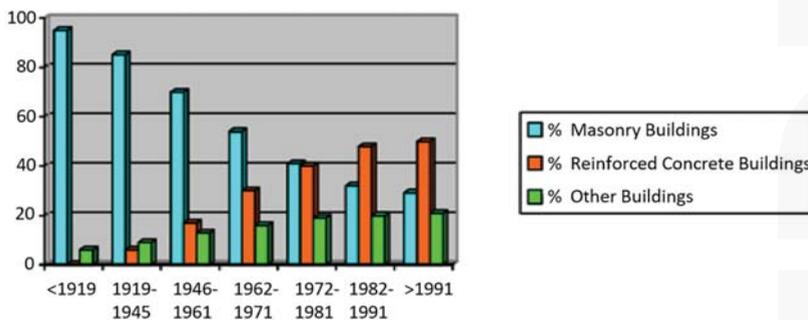
Figure 1. Trend of buildings in Italy during XX century (source ISTAT 2001—Italian Agency of Statistics).

In these cases, to optimize the intervention it is convenient to take into account other aspects, such as thermal and acoustic comfort. Indeed, masonry walls are, at the same time, structural and separating elements.

The CO_2/year emission, joined with the energy spent every year to reach serviceability comfort conditions, represent a primary indicator of the efficiency of the buildings. The most relevant part of energy consumption is commonly represented by the façades. The correct maintenance of their thermal and mechanical properties is crucial: indeed, each construction is subjected to the continuous degradation of structural and energy performance due to environmental actions, anthropic actions, and endogenous ageing (*continuous degradation*). In addition, they can be affected by episodic events like fire [1], explosions [2–4], and seismic actions [5–7] or other phenomena like deliberate attacks or human errors (*discontinuous degradation*). These events can sharply reduce the structural or energy performances of building and their service life. Figure 2 presents a qualitative decrease of performances in the presence of continuous time aging (progressive reduction of performances depending from time) and of traumatic events (discontinuous reduction of performances in case of discrete events). The structural integrity and the energy performance of a building can be described as a monotonic decreasing functions of time with the red lines in Figure 2. After a disruptive event (like fire or impact, earthquake, etc.) there is a sharp transition that modifies these functions and often requires a retrofitting in order to reach the minimum serviceability performance level. In case of an absence of traumatic events, the decay of performances is continuous over time (black lines in Figure 2). After retrofitting, an increase of performance can be achieved (green lines in Figure 2), improving the building condition and lengthening its service life. In this sense it can establish an acceptable level of performances (purple lines in Figure 2) commonly fixed by technical documents, guidelines, or codes.
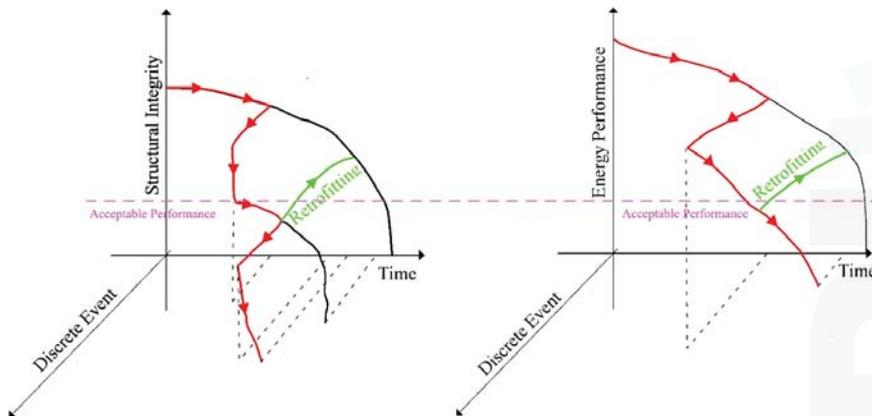
Figure 2. Qualitative evolution of structural and energy performances in the service life of a building.

The opportunity to combine both structural and energy evaluations is relevant to the optimization of resources to address retrofitting strategies. It means the best decision seeks to balance structural and energy improvements. In this sense, structural and energy phenomena are taken into account simultaneously, and the convenience of retrofitting or demolition followed by reconstruction of a building is also assessed.

The cost-benefit analysis, to address an optimum strategy, should be based on a multi-criteria choice: the comfort requirements for a building are of paramount relevance. It should be considered that, in addition, the sustainability awareness of construction life cycles has grown in the last years together with a superior expectation of performance from the buildings. A possible approach could

be based on how much energy will be spent for the direct refurbishment and what is the variation of building energy performance.

An example of multi-criteria decision making is in [8], where the main focus is the seismic risk management of existing structures. A recent work of Calvi et al. [9] introduces the idea of a common indicator for both structural and energy performances presenting a cost/benefit analysis for different retrofitting strategies. However, further aspects can be raised in this field. To better explain the strategy here proposed, a flow-chart scheme of the decision phase is drawn in Figure 3. The flow chart describes the several phases of the life of a building. Each of them computes the energy embodied by the building, together with the decision process on refurbishment/demolition-reconstruction choices. If the construction is below the level of "Acceptable Performance" (dashed line of Figure 3) a choice must be made between demolition or refurbishment. Every cost should be considered, and a balance between structural and energy performance should be found.
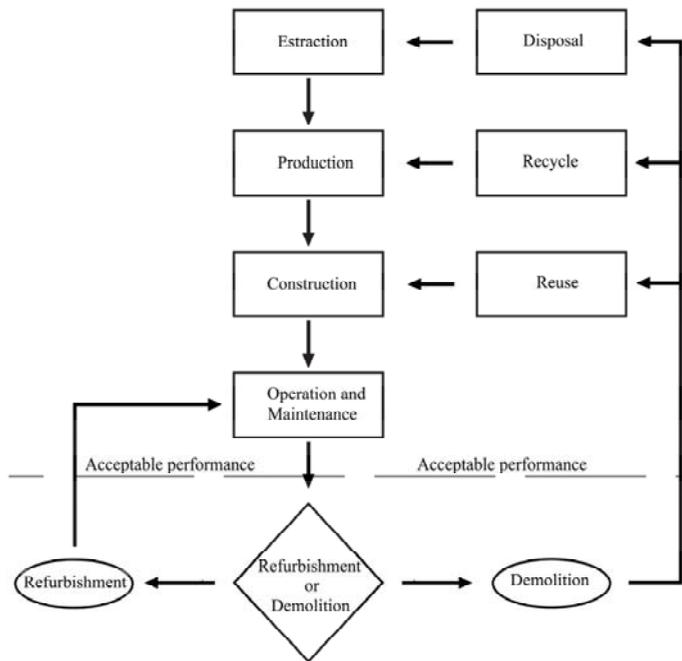
Figure 3. Flow-chart scheme of building assessment decision phase.

After a brief report in Section 2 on the state-of-the-art structural and energy retrofitting techniques for existing masonry constructions, the proposed solution for an integrated approach is discussed in Section 3, based on a simple example of masonry panel. The main idea is to synthesize the decision process throughout a new proposal of dimensionless performance indicators. In Section 4, a generalized approach is presented considering both structural and energy features, proposing a calculation strategy based on the definition of "performance parameter", followed by some conclusive remarks.

2. Retrofitting Techniques

2.1. Structural and Seismic Retrofitting

The problem of structural strengthening in masonry buildings is well known. A synthetic review of the existing methods is reported in [10]. It is possible to group them into surface treatments,

grout and epoxy injections, external reinforcements, confining Reinforced Concrete (RC) frames, post tensioning, center core systems. A brief summary of the most used techniques is explained below.

In the set of surface treatments, we consider the old ferrocement system. This consists of multiple layers of reinforcement mesh embedded in a high strength mortar layer [11]. A similar technique is reinforced plaster where high strength steel reinforcements are applied on the wall surface and covered by a thin layer of cement plaster, see [12]. A valid alternative are the shotcrete overalays directly sprayed on the surface of the masonry wall over a mesh of reinforcements, see [13–15]. Textile Reinforced Mortar (TRM) systems denote an inorganic mortar matrix strengthened by an open fabric made of fiber rovings. They have been used to retrofit tuff masonry in [16] and as a strengthening material for generic masonry subjected to in plane and out of plane cyclic loading [17–20]. To restore the original integrity of the retrofitted wall, filling voids and cracks in existing masonry, grout, and epoxy injections represent an efficient tool [21,22].

External reinforcements are common retrofitting techniques; they involve steel plates, tubes, or grids being directly applied to the masonry, thereby improving the lateral in plane resistance of the wall. In [23], externally bonded grids were applied to unreinforced masonry to increase the load-carrying and deformation capacity under cyclic loading. Recent improvements include the *reticulatus* technique [24] which uses a stainless grid which is able to adapt to the irregular texture of blocks. Other traditional techniques, such as the introduction of horizontal steel rods to anchor masonry walls from out-of-plane displacements, can offer relevant improvement against rocking mechanisms [25,26].

The insertion of confining RC frames inside masonry walls allows for the improvement in the energy dissipation capacity and the ductility of the structure, as in [27,28]. This approach is not applicable in most of existing buildings with historical value as it has a wide impact on the structure. Post tensioning denotes the application of a compressive force to the masonry wall which counteracts the tensile stresses produced by the external load, see [29,30]. The cost of this technique and the technological difficulties are often high, so it is generally restricted to monumental buildings. Center core systems denote a grouted reinforced core inserted in the center of an existing masonry wall.

Recent numerical codes are able to assess the role of several refurbishment techniques on masonry components [31,32] taking into account their dynamical performances near collapse.

In the last few years, the insertion of Fiber Reinforced Polymers (FRP) has been common, mainly with Carbon (CFRP) or Glass (GFRP). FRP are helpful in reducing the impact of the above techniques [33,34]. FRP are used for external surface reinforcements [35] or to create internal frames inside the masonry system [36]. The use of polymers to strengthen masonry subjected to blast loads has been reviewed in [37] with an experimental data set collected from several papers. A special mention is deserved by [38], which refers to the application of a sprayed-on polymer on masonry walls.

Analysis of several types of interventions, in terms of cost-benefits, is in [39] on a set of buildings in the Lisbon area with several fragility curves. A recent approach to join structural retrofitting with energy properties is presented in [40], where the problem of associating a cost-benefit to each different retrofitting procedure is compared with alternative choices in order to optimize the refurbishments.

2.2. Energy Retrofitting

A review of the state-of-the-art energy retrofitting methods to existing buildings is in [41]. After it outlines methods to enhance the energy efficiency from previous studies, it summarizes the following actions:

- improvement of thermal performance of building façades,
- optimization of building insulation,
- modification of indoor temperature set-points,
- improvement of the heating system efficiency,
- installation of energy saving lighting and air ventilation control.

An example of these approaches is in [42], where an historical masonry building in Benevento (Italy) is analyzed. Six retrofitting actions are modelled: modification of the indoor temperatures, reduction of the air draught, increase of the vertical wall thermal insulation, replacement of the boiler with a condensation gas heater, and substitution of the windows. It yields a reduction of the primary energy demand of more than 20%. An important trend is the multi-criteria optimization of the energy performance of buildings. In [43], it is applied to the renovation strategy of some historical masonry buildings in Algeria. In [44] a comparative analysis among different on-site construction systems and materials (wood, steel, and concrete) is presented. It is of interest to compare the energy consumed in the construction process with respect to the total initial embodied energy and greenhouse gas emissions.

Special attention has been devoted to the improvement of thermal insulation and waterproofing properties of masonry walls. A detailed description of the main thermal insulation techniques is in [45,46]. The current systems to build masonry walls with high thermal insulation properties are described in [47]. The technique of Light Weight Concrete (LWC) blocks for thermal insulation is assessed with different arrangements of internal holes or components of the mix design. Recently, the effect of alkaline activation in Compressed Earth Block (CEB) has been studied in [48]. It demonstrates how to reduce the heat transfer coefficient of a wall made of CEB. In [49,50] the effect of titanium dioxide and zinc oxide nano-particulate aqueous façade emulsions on brick walls was tested for water repellent and thermal insulation applications. The results show how this approach can reduce the energy consumption with an important financial saving. The advantageous use of blocks made of hemp fibers or cork grains with NHL (Natural Hydraulic Lime) is another option to improve sustainability by reducing extraction and production energies [51].

A significant application of masonry thermal insulation is reported in [52] where the performance of a refractory masonry glassmaking furnace is studied with a mathematical model. The main thermal insulation is provided by some rigid fiber boards and microporous sandwich boards with positive savings on furnace fuels. In [53], the efficiency of new coatings (realized with silica nano-particles and micro-clay enrichment of alkosiloxane) for brick waterproofing is assessed. In [54,55], different renovation strategies for existing building stock located in Sweden are outlined, depending on each climate zone, in order to furnish parameters for their optimization. Also, an Italian example [56] of analysis of cost-optimal performances shows the possibility to address the design in terms of energy efficiency.

2.3. Combined Seismic and Energy Retrofitting

A large number of papers deal with specific structural or energy retrofitting methods for masonry constructions. Although few researchers have worked on an integrated approach capable of taking into account both issues. A recent paper by Triantafillou et al. [57] discusses the structural and energy performance of a new retrofitting system based on TRM and thermal insulating materials. Medium scale experimental tests were performed on 17 masonry walls subjected to out of plane bending; the combination of TRM jacketing and thermal and fire-resistant insulation proved to be effective. In addition, energy based approaches were recently implemented to assess structural performances in [58], which made a possibly profitable suggestion to use energy as a synthetic parameter to evaluate the vulnerability of a masonry component.

The previously mentioned contribution by Calvi et al. [9] introduces the Green and Resilient Indicator (GRI), after the definition of specialized indicators, the energy expected annual loss, EAL_E, is:

$$EAL_E = \frac{mean\ annual\ energy\ cost}{total\ building\ value},\qquad(1)$$

While the seismic expected annual loss, EAL_s, is:

$$EAL_s = \frac{expected\ annual\ seismic\ lost}{total\ building\ value}. \qquad (2)$$

The annual energy cost is easily calculated from the contributions necessary for the thermal comfort of the building given its location and its thermal characteristics. On the other hand, the expected annual seismic loss is evaluated considering the standard seismic load of its location and its structural characteristics. An example to evaluate seismic damage costs are in [59]. From an energy point of view, the evaluation of the thermal resistance of the building (reciprocal of the thermal transmittance) joined with the thermal performance requested by technical standards, can furnish the corresponding costs. From a structural point of view, a push-over analysis can assess the inter-story drift linked to seismic damage evaluation and performance levels by structural codes or documents (see [60,61]). Then, given the damages, it is easy to calculate the cost of the needed refurbishments. The indicators EAL_E and $EALs$ are cumulative components of the GRI definition and allow for the comparison of several retrofitting strategies. three case studies are in [9], with different reinforced concrete building types characterized by different functions and locations.

3. An Example of an Integrated Approach on Structural and Energy Features

For the sake of simplicity, the focus of this paper is limited to single masonry walls, although the proposed method can be extended to the entire building. With the aim of quantifying the effects of a retrofitting strategy, thermal and structural performances are considered. For each wall panel, it is possible to calculate the relative increment of structural resistance ΔR (in plane or out of plane) and the relative increment in the thermal resistance ΔU (reciprocal of the transmittance) obtained after an assigned retrofitting technique. Thus, they are:

$$\Delta R = (R_1 - R_0)/R_0, \qquad (3)$$

$$\Delta U = (U_1 - U_0)/U_0. \qquad (4)$$

where R_0 and U_0 are structural and thermal parameters before refurbishment, while R_1 and U_1 are after refurbishment. Both properties should be referred to at the specific site in which the building is erected. Considering as an example the Italian peninsula, the seismic events, commonly measured throughout the peak ground acceleration (*PGA*), are mapped in Figure 4. In the meanwhile, the thermal effect, commonly measured throughout the Degree Day (*DD*), is depicted in Figure 5. Thus, both aspects can be measured by the following dimensionless parameters c_R and c_U

$$c_R = \frac{PGA_i}{PGA_{MAX}}. \qquad (5)$$

$$c_U = \frac{DD_i}{DD_{MAX}}. \qquad (6)$$

where PGA_{MAX} represents the maximum peak ground acceleration of the Italian peninsula and PGA_i is the peak ground acceleration for the considered *i*-th location of the building. In the same way, DD_{MAX} is the maximum Degree Day value for the same area and DD_i is the corresponding value for the given *i*-th location.

c_R and c_U parameters are a sort of "weight" of the structural and energy requirements in an assigned area. In the mentioned example, Italy is divided into 107 districts, assigning conventionally to each of them the values of PGA_i and DD_i of the main district town. The ratios in Equations (5) and (6) are determined to rank each district for both phenomena.
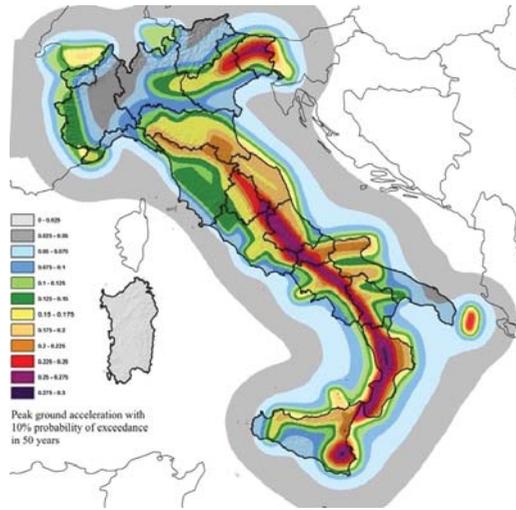
Figure 4. Italian map of seismic *PGA* (peak ground acceleration), taken from [62].
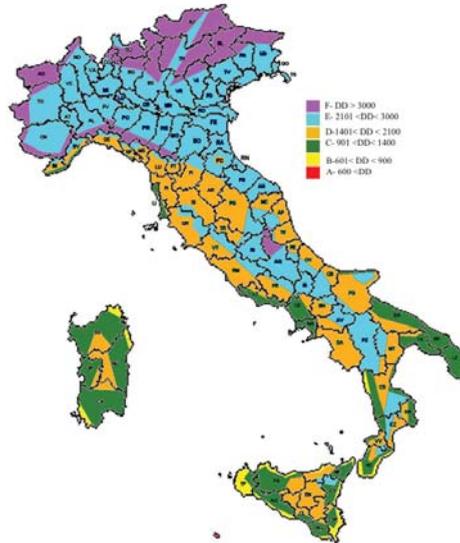
Figure 5. Italian map of heating *DD* (Degree Day), based on Italian technical code [63].

Let us first consider a loadbearing masonry wall of thickness t_m and length b_m, characterized by mechanical parameters f_m (compression strength), t_0 (shear strength), and a thermal parameter $1/\lambda_m$ (thermal resistance). To show the proposed method, it is assumed a building is located in two different emblematic sites in Italy: the first characterized by a low value of *PGA* and a high value of *DD* (i.e., Torino, Italy), the second (i.e., Catania, Italy) by a high value of *PGA* and a low value of *DD*. It also assumes, for the sake of simplicity, that the limit values of the axial force N_0 and of the shear force V_0 are proportional to the section area A_m of the wall:

$$N_0 = f_m \, A_m; \, V_0 = t_0 \, A_m \tag{7}$$

The corresponding thermal resistance is

$$U_{c0} = (1/\lambda_\chi) \, A_m \tag{8}$$

Then, the following set of four possible refurbishment techniques (Figure 6) are examined:
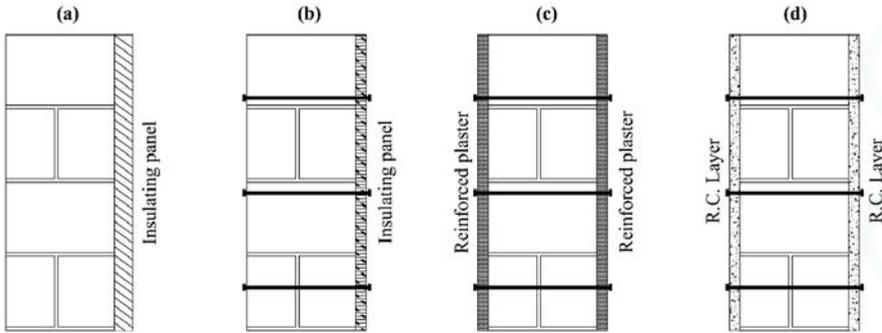
Figure 6. Proposed refurbishment techniques for masonry walls. (**a**) Single insulating panel by natural first choice cork and traditional plaster on both faces; (**b**) single polystyrene panel, transverse connectors and traditional plaster on both faces; (**c**) coupled GFRP (Glass Fiber Reinforced Polymer) plaster and transverse connectors; (**d**) coupled reinforced concrete layer and transverse connectors.

The four intervention techniques are emblematic. Intervention (a) does not appreciably increase the strength, while it enhances the thermal resistance to a new value of U_{A1}. Intervention (b) is aimed to increase the thermal resistance to U_{B1}, but is also able to induce a superior strength of R_{B1}. Intervention (c) is aimed to increase the strength to R_{C1}, but is also able to induce a superior thermal resistance of U_{C1}. Intervention (d) does not appreciably increase the thermal resistance due to the high transmittance of the concrete, while it enhances the strength to a new value R_{D1}.

The scope of the analysis is to individuate the best choice of refurbishment for the two locations: the first site (Torino, low *PGA* or c_R, high *DD* or c_U) will require more thermal improvements with respect to structural enforcement in comparison with those of the second site (Catania, high *PGA* or c_R, low *DD* or c_U). If "performance parameter" *P* is considered the investment cost of refurbishment C_i with respect to the total cost of the building C_{tot}, to compare the several refurbishments, the parameter P can be defined as

$$P = \frac{Ci}{C_{tot}} \tag{9}$$

To compare the effects of each refurbishment with the same *P*, the following rule is assumed:

$$(c_R \Delta \mathbf{R})^\alpha + (c_U \Delta \mathbf{U})^\alpha = P \tag{10}$$

where α is an adaptive coefficient. The following example explains the calculation method of α.

To calculate a numerical result, it is assumed there is a masonry wall of limestone bricks with a thickness of 40 cm. In case (a), simple natural cork 4.0 cm thick ($\lambda = 0.05$ W/mK thermal conductibility) is applied on the external side of the wall, improving the thermal resistance with a negligible contribution to structural resistance. In case (b), a polypropylene panel 3.6 cm thick ($\lambda = 0.06$ W/mK thermal conductibility) is applied with the insertion of structural transverse connectors; it allows an improvement of 50% to the equivalent mechanical characteristics of the masonry f_m, as in Italian code [64] (Appendix A table C8A 2.1.). In case (c), two layers (1.3 cm thick) of premixed lightweight plaster ($\lambda = 0.08$ W/mK thermal conductibility) reinforced by a GFRP net are applied. The improvement in the structural performance of the wall is calculated by homogenization of its cross section A_p. Given

E_p = 1.3 GPa, the plaster Young modulus, and E_m = 1.4 GPa, the corresponding masonry modulus, the homogenized cross section A_i is:

$$A_i = A_m + A_p \times E_p/E_m. \tag{11}$$

Finally, the case (d) presents a structural improvement with two layers of concrete, 20 mm thick, transversally connected to the sides of the wall by steel connectors and reinforced by a micro-steel net. The compressive strength of concrete is f_{ck} = 25 MPa, while its thermal resistance improvement is negligible. The four described techniques are calibrated to have the same investment cost.

The first site is Torino (Italy) with a reference *PGA* value of 0.055 g and a *DD* value of 2617. In the Italian peninsula, the maximum values are in Aosta for *DD* (2850) and Reggio Calabria for *PGA* (0.270). Thus, we can obtain c_R = 0.055/0.270 = 0.767; c_U = 2617/2850 = 0.918. The second site is Catania (Italy) with a reference *PGA* value of 0.207 g and a *DD* value of 833. Compared to the same Italian area, we can obtain c_R = 0.207/0.270 = 0.767; c_U = 833/2850 = 0.292.

The improvements in structural and energy properties were calculated for the four cases and the corresponding points are reported in the diagram of Figure 7. Considering each point belonging to a similar iso-performance curve P = cost, it is then possible to perform a squared interpolation (α = 2.00) for the Catania site (red line in Figure 7) and the Torino site (blue line in Figure 7).
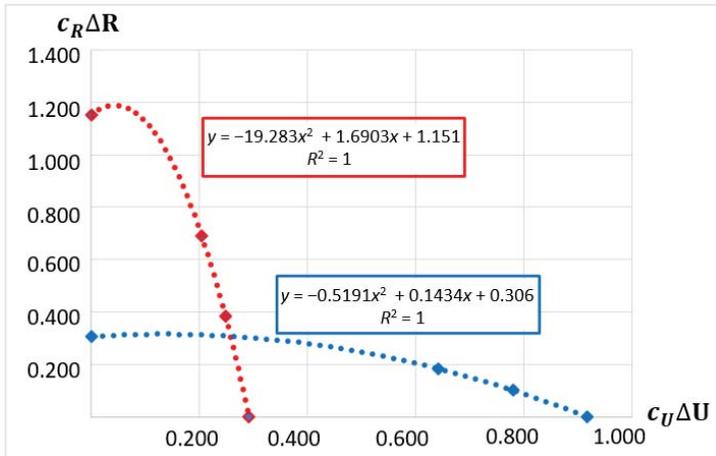
Figure 7. ($c_U\Delta U$, $c_R\Delta R$) diagrams (red: Catania; blue: Torino) interpolating the four techniques.

The performance parameter P identifies the cost of intervention; increasing P increases the budget for refurbishment. It is also possible to plot a series of curves, for each site, with different values of P. Moreover, the intersection of the two curves in Figure 7 identifies the intervention that would generate the same performance in both sites. Finally, each curve permits a comparison of the effects of each technique in the same location with equal investment cost.

4. A Generalized Combined Approach of Structural and Energy Aspects

The Index of seismic risk is typically related to three parameters: *structural vulnerability* (quality of the building), *seismic hazard of the location* (quality of the site), and *exposure of the destination* (relevance of use) [40]. Also, the thermal performance of a construction can be related to a set of three similar parameters: *thermal conductivity* (quality of the building), *thermal characteristics of the location* (quality of the site), and *exposure of the destination* (relevance of use). Thus, the performance parameter P of a wall, related to both aspects (structural and thermal) can be defined as the sum of two products of three components. P can measure the investment cost, but also the maintenance cost or other significant

aspects. Considering the location of the buildings, its structural and thermal properties, and its level of importance, the value of two combination coefficients can be assessed with a single dimensionless performance parameter *P* by:

$$g_R(c_R\Delta\mathbf{R})^{\alpha_R} + g_U(c_U\Delta\mathbf{U})^{\alpha_U} = P \tag{12}$$

where (g_R, α_R) and (g_U, α_U) are dimensionless adaptive coefficients, respectively, of the structural and thermal aspects determined from experimental data. The dimensionless terms (c_R, c_U) can be calculated considering the peak ground acceleration (*PGA*) and the weather characteristics (i.e., the Degree Day or *DD*) of the site as shown in formulas (5) and (6). The dimensionless parameters (g_R, g_U) represent the specific weights that can be assumed for the structural or thermal improvement, depending on the use of the building. In this way, it is possible to compare different retrofitting strategies considering the specific characteristic of each location and of each socio-economical condition (i.e., expected seismic safety, expected thermal comfort, or energy consumption). In this sense, the performance parameter *P* can represent the investment cost of a refurbishment technique, or the maintenance cost, or the environmental cost (i.e., consumption of CO_2), or a social cost (i.e., rate of involved population), to determine thorough management decisions. A series of curves with prescribed *P* in the plane ($\Delta\mathbf{R}$, $\Delta\mathbf{U}$) from equation (12) are qualitatively plotted in Figure 8.
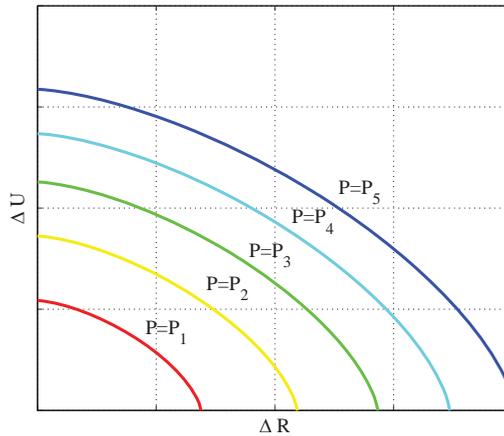
Figure 8. Qualitative curves for a given performance parameter *P* from equation (12).

A more detailed analysis can be done by introducing further quantities to describe the structural and thermal phenomena. It is possible to define another relevant structural parameter that measures the variation of the flexibility (reciprocal of stiffness) of the wall. It consists of the variation of the drift D of the wall (ratio between the transverse displacement and the height) that is strictly linked to the stiffness and flexibility characteristics of the structure. In the meanwhile, a further energy parameter can be adopted to measure the variation of the periodic transmittance, related to the variation of inertial mass M of the wall. Thus defining

$$\Delta D = (D_1 - D_0)/D_0, \tag{13}$$

$$\Delta M = (M_1 - M_0)/M_0, \tag{14}$$

it can obtain a more detailed performance parameter *P* as:

$$g_R(c_R\Delta\mathbf{R})^{\alpha_R} + g_D(c_D\Delta\mathbf{D})^{\alpha_D} + g_U(c_U\Delta\mathbf{U})^{\alpha_U} + g_M(c_M\Delta\mathbf{M})^{\alpha_M} = P \tag{15}$$

Also, in the last formula, the dimensionless adaptive coefficients (g_i, α_i) can give a different "weight" to each structural or energy property that contributes to P.

As previously mentioned, it is possible to consider one of the following set of performance parameters to compare each of the above techniques "before and after" refurbishment:

1. investment cost
2. maintenance cost
3. environmental cost (i.e., consumption of CO_2)
4. social cost (i.e., rate of involved population).

The explained example in Section 3 is based on the first parameter. In fact, it is also possible to change the meaning of the performance parameter P. For example, it can represent the maintenance cost, the environmental cost, or a social cost, and consequently, in order to obtain the iso-performance curves presented in Figure 7 or Figure 8, it is necessary to calibrate the four refurbishment techniques to achieve the same performance parameter P.

5. Conclusions and Perspectives

The constructive management of existing constructions should take into account both the structural safety, the energy cost, and the comfort conditions of the building. In particular, in the case of masonry buildings, structural retrofitting can be matched by the energy cost in the set of possible renovation strategies. The cost-benefit analysis necessary to find the optimum solution needs synthetic performance indicators which, as yet, have not been investigated. Indeed, only a few studies have been developed on integrated solutions based on both structural and energy needs of existing structures. In this work, a brief review of state-of-the-art structural and energy retrofitting techniques for existing masonry buildings was reported. Then, the definition of a new synthetic performance parameter P was presented through an example and a more generalized approach. This new parameter is capable of representing the retrofitting improvement in structural safety and in thermal insulation for each masonry wall.

Further developments of this research are expected with the application to several case studies necessary to determine the best values for the adaptive coefficients (α_i). It would be interesting to enhance the method giving a better definition of the "comfort" inside the building, for example, considering also the hygrometric and acoustic conditions, etc. Finally, an extension of this approach for the complete construction is sought with the aim of obtaining diagrams like the ones presented in Figures 7 and 8 that can be useful for the early design of retrofitting for existing buildings.

Author Contributions: Mauro Sassu conceived the illustrated strategy and the theoretical formulation; Flavio Stochino analyzed the numerical results and contributed to the theoretical formulation; Fausto Mistretta provided the refurbishment solutions. All the authors wrote the paper.

Conflicts of Interest: The authors declare no conflict of interest.

References

1. Stochino, F.; Mistretta, F.; Meloni, P.; Carcangiu, G. Integrated approach for post-fire reinforced concrete structures assessment. *Period. Polytech. Civ.* **2017**. [CrossRef]
2. Acito, M.; Stochino, F.; Tattoni, S. Structural response and reliability analysis of RC beam subjected to explosive loading. *AMM* **2011**, *82*, 434–439. [CrossRef]
3. Stochino, F. RC beams under blast load: Reliability and sensitivity analysis. *Eng. Fail. Anal.* **2016**, *66*, 544–565. [CrossRef]
4. Giovino, G.; Olmati, P.; Garbati, S.; Bontempi, F. Blast resistance assessment of concrete wall panels: Experimental and numerical investigations. *Int. J. Prot. Struct.* **2014**, *5*, 349–366. [CrossRef]
5. Sassu, M. The Reinforced Cut Wall (RCW): A Low-Cost Base Dissipator for Masonry Buildings. *Earthq. Spectra* **2016**, *22*, 533–554. [CrossRef]

6. Sassu, M. Biaxiality effect on the energy dissipated by elastoplastic base-isolators. *J. Eng. Mech. ASCE* **2003**, *22*, 533–554. [CrossRef]

7. Asteris, P.G.; Chronopoulos, M.P.; Chrysostomou, C.Z.; Varum, H.; Plevris, V.; Kyriakides, N.; Silva, V. Seismic vulnerability assessment of historical masonry structural systems. *Eng. Struct.* **2014**, *62*, 118–134. [CrossRef]

8. Tesfamariam, S.; Sadiq, R.; Najjaran, H. Decision making under uncertainty—An example for seismic risk management. *Risk Anal.* **2010**, *30*, 78–94. [CrossRef] [PubMed]

9. Calvi, G.M.; Sousa, L.; Ruggeri, C. Energy Efficiency and Seismic Resilience: A Common Approach. In *Multi-Hazard Approaches to Civil Infrastructure Engineering*; Gardoni, P., La Fave, J.M., Eds.; Springer International Publishing: Basel, Switzerland, 2016; pp. 165–208.

10. El Gawady, M.; Lestuzzi, P.; Badoux, M. A review of conventional seismic retrofitting techniques for URM. In Proceedings of the 13th International Brick and Block Masonry Conference, Amsterdam, The Netherlands, 4–7 July 2004; pp. 1–10.

11. Montes, P.; Fernandez, A. Behaviour of a hemispherical dome subjected to wind loading. *J. Wind Eng. Ind. Aerodyn.* **2001**, *89*, 911–924. [CrossRef]

12. Jabarov, M.; Kozharinov, S.; Lunyov, A. Strengthening of damaged masonry by reinforced mortar layers. In Proceedings of the 7th WCEE, Istanbul, Turkey, 8–13 September 1980; Volume 6, pp. 73–80.

13. Tomazevic, M. *Earthquake-Resistant Design of Masonry Buildings*; World Scientific: Singapore, 1999; Volume 1.

14. Karantoni, F.V.; Fardis, M.N. Effectiveness of seismic strengthening techniques for masonry buildings. *J. Struct. Eng. ASCE* **1992**, *118*, 1884–1902. [CrossRef]

15. Kahn, L. Shotcrete retrofit for unreinforced brick masonry. In Proceedings of the 8th WCEE, San Francisco, CA, USA, 21–28 July 1984; pp. 583–590.

16. Prota, A.; Marcari, G.; Fabbrocino, G.; Manfredi, G.; Aldea, C. Experimental in plane behaviour of tuff masonry strengthened with cementitious matrix-grid composites. *J. Compos. Constr.* **2006**, *10*, 223–233. [CrossRef]

17. Papanicolaou, C.G.; Triantafillou, T.C.; Karlos, K.; Papathanasiou, M. Textile reinforced mortar (TRM) versus FRP as strengthening material of URM walls: In-Plane cyclic loading. *Mater. Struct.* **2007**, *40*, 1081–1097. [CrossRef]

18. Papanicolaou, C.G.; Triantafillou, T.C.; Papathanasiou, M.; Karlos, K. Textile reinforced mortar (TRM) versus FRP as strengthening material of URM walls: Out-of-Plane cyclic loading. *Mater Struct.* **2008**, *41*, 143–157. [CrossRef]

19. Parisi, F.; Lignola, G.P.; Augenti, N.; Prota, A.; Manfredi, G. Nonlinear behaviour of a masonry subassemblage before and after strengthening with inorganic matrix-grid composites. *J. Compos. Constr.* **2011**, *15*, 821–832. [CrossRef]

20. Babaeidarabad, S.; De Caso, F.; Nanni, A. Out-of-plane behavior of URM walls strengthened with fabric-reinforced cementitious matrix composite. *J. Compos. Constr.* **2014**, *18*, 04013057. [CrossRef]

21. Calvi, G.; Magenes, G. Experimental results on unreinforced masonry shear walls damaged and repaired. In Proceedings of the 10th IB2MaC, Calgary, AB, Canada, 5–7 July 1994; pp. 509–518.

22. Schuller, M.; Atkinson, R.; Borgsmiller, J. Injection grouting for repair and retrofit of unreinforced masonry. In Proceedings of the 10th IB2MaC, Calgary, AB, Canada, 5–7 July 1994; pp. 549–558B.

23. Papanicolaou, C.; Triantafillou, T.; Lekka, M. Externally bonded grids as strengthening and seismic retrofitting materials of masonry panels. *Constr. Build Mater.* **2011**, *25*, 504–514. [CrossRef]

24. Borri, A.; Corradi, M.; Speranzini, E.; Giannantoni, A. Consolidation and Reinforcing of stone wall using a reinforced repointing grid. In Proceedings of the 6th International Conference of Structural Analysis of Historical Construction, Bath, UK, 2–4 July 2008.

25. Giresini, L.; Sassu, M. Horizontally restrained rocking blocks: Evaluation of the role of boundary conditions with static and dynamic approaches. *Bull. Earthq. Eng.* **2017**, *15*, 385–410. [CrossRef]

26. Giresini, L.; Fragiacomo, M.; Sassu, M. Rocking analysis of masonry walls interacting with roofs. *Eng. Struct.* **2016**, *116*, 107–120. [CrossRef]

27. Yu, Z.; Zhengyun, W.; Weiping, Z. Experimental research on aseismic strengthening of block masonry buildings using thin structural columns. In Proceedings of the 11th IB2MaC, Shanghai, China, 14–16 October 1997; pp. 626–633.

28. Chuxian, S.; Guiqiu, L.; Wenchao, W. The design of Brick masonry structure with concrete column. In Proceedings of the 11th IB2MaC, Shanghai, China, 14–16 October 1997; pp. 626–633.

29. Lissel, S.; Shrive, N. Construction of diaphragm walls post-tensioned with carbon fiber reinforced polymer tendons. In Proceedings of the 9th NAMC, Clemson, SC, USA, 9 June 2003; pp. 192–203.

30. Rosenboom, O.; Kowalsky, M. Investigation of alternative details for seismic design of post-tensioned clay masonry walls. In Proceedings of the 9th NAMC, Clemson, SC, USA, 9 June 2003; pp. 475–485.

31. Casapulla, C.; Cascini, L.; Portioli, F.; Landolfo, R. 3D macro and micro-block models for limit analysis of out-of-plane loaded masonry walls with non-associative Coulomb friction. *Meccanica* **2014**, *49*, 1653–1678. [CrossRef]

32. Casapulla, C.; Jossa, P.; Maione, A. Rocking motion of a masonry rigid block under seismic actions: A new strategy based on the progressive correction of the resonance response. *Ing. Sismica* **2010**, *27*, 35–48.

33. Ehsani, M.R.; Saadatmanesh, H.; Al-Saidy, A. Shear behavior of URM retrofitted with FRP overlays. *J. Compos. Constr.* **1997**, *1*, 17–25. [CrossRef]

34. Albert, M.L.; Elwi, A.E.; Cheng, J.R. Strengthening of unreinforced masonry walls using FRPs. *J. Compos. Constr.* **2001**, *5*, 76–84. [CrossRef]

35. Gattesco, N.; Boem, I.; Dudine, A. Diagonal compression tests on masonry walls strengthened with a GFRP mesh reinforced mortar coating. *Bull. Earthq. Eng.* **2015**, *13*, 1703–1726. [CrossRef]

36. Priestley, M.J.N.; Seible, F. Design of seismic retrofit measures for concrete and masonry structures. *Constr. Build. Mater.* **1995**, *9*, 365–377. [CrossRef]

37. Buchan, P.A.; Chen, J.F. Blast resistance of FRP composites and polymer strengthened concrete and masonry structures—A state-of-the-art review. *Compos. Eng. Part B* **2007**, *38*, 509–522. [CrossRef]

38. Davidson, J.S.; Porter, J.R.; Dinan, R.J.; Hammons, M.I.; Connell, J.D. Explosive testing of polymer retrofit masonry walls. *J. Perform. Constr. Facil.* **2004**, *18*, 100–106. [CrossRef]

39. Marques, R.; Lamego, P.; Lourenco, P.B.; Sousa, M.L. Efficiency and cost-benefit analysis of seismic strengthening techniques for old residential buildings in Lisbon. *J. Earthq. Eng.* **2017**, 1–36. [CrossRef]

40. Calvi, G.M. Choices and criteria for seismic strengthening. *J. Earthq. Eng.* **2013**, *17*, 769–802. [CrossRef]

41. Ma, Z.; Cooper, P.; Daly, D.; Ledo, L. Existing building retrofits: Methodology and state-of-the-art. *Energy Build.* **2012**, *55*, 889–902. [CrossRef]

42. Ascione, F.; De Rossi, F.; Vanoli, G.P. Energy retrofit of historical buildings: Theoretical and experimental investigations for the modelling of reliable performance scenarios. *Energy Build.* **2011**, *43*, 1925–1936. [CrossRef]

43. Seddiki, M.; Anouche, K.; Bennadji, A.; Boateng, P. A multi-criteria group decision-making method for the thermal renovation of masonry buildings: The case of Algeria. *Energy Build.* **2016**, *129*, 471–483. [CrossRef]

44. Cole, R.J. Energy and greenhouse gas emissions associated with the construction of alternative structural systems. *Build. Environ.* **1998**, *34*, 335–348. [CrossRef]

45. Al-Homoud, M.S. Performance characteristics and practical applications of common building thermal insulation materials. *Build. Environ.* **2005**, *40*, 353–366. [CrossRef]

46. Jelle, B.P. Traditional, state-of-the-art and future thermal building insulation materials and solutions—Properties, requirements and possibilities. *Energy Build.* **2011**, *43*, 2549–2563. [CrossRef]

47. Al-Jabri, K.S.; Hago, A.W.; Al-Nuaimi, A.S.; Al-Saidy, A.H. Concrete blocks for thermal insulation in hot climate. *Cem. Concr. Res.* **2005**, *35*, 1472–1479. [CrossRef]

48. Leitão, D.; Barbosa, J.; Soares, E.; Miranda, T.; Cristelo, N.; Briga-Sá, A. Thermal performance assessment of masonry made of ICEB's stabilised with alkali-activated fly ash. *Energy Build.* **2017**, *139*, 44–52. [CrossRef]

49. Mac Mullen, J.; Zhang, Z.; Radulovic, J.; Herodotou, C.; Totomis, M.; Dhakal, H.N.; Bennett, N. Titanium dioxide and zinc oxide nano-particulate enhanced oil-in-water (O/W) facade emulsions for improved masonry thermal insulation and protection. *Energy Build.* **2012**, *52*, 86–92. [CrossRef]

50. Zhang, Z.; Mac Mullen, J.; Dhakal, H.N.; Radulovic, J.; Herodotou, C.; Totomis, M.; Bennett, N. Enhanced water repellence and thermal insulation of masonry by zinc oxide treatment. *Energy Build.* **2012**, *54*, 40–46. [CrossRef]

51. Sassu, M.; Giresini, L.; Bonannini, E.; Puppio, M.L. On the Use of Vibro-Compressed Units with Bio-Natural Aggregate. *Buildings* **2016**, *6*, 40. [CrossRef]

52. Dzyuzer, V.Y.; Shvydkii, V.S. Thermal Insulation of the Refractory Masonry in Glassmaking Furnaces. *Glass Ceram.* **2015**, *71*, 365–368. [CrossRef]

53. Stefanidou, M.; Karozou, A. Testing the effectiveness of protective coatings on traditional bricks. *Constr. Build. Mater.* **2016**, *111*, 482–487. [CrossRef]

54. Mata, E.; Sasic Kalagasidis, A.; Johnsson, F. Cost-effective retrofitting of Swedish residential buildings: Effects of energy price developments and discount rates. *Energy Effic.* **2015**, *8*, 223–237. [CrossRef]

55. Tronchin, L.; Tommasino, M.C.; Fabberi, K. On the cost-optimal levels of energy-performance requirements for buildings: A case study with economic evaluation in Italy. *Int. J. Sustain. Energy Plan. Manag.* **2014**, *3*, 49–62.

56. Bonakdar, F.; Kalagasidis, A.S.; Mahapatra, K. The Implications of Climate Zones on the Cost-Optimal Level and Cost-Effectiveness of Building Envelope Energy Renovation and Space Heat Demand Reduction. *Buildings* **2017**, *7*, 39. [CrossRef]

57. Triantafillou, T.C.; Karlos, K.; Kefalou, K.; Argyropoulou, E. An innovative structural and energy retrofitting system for URM walls using textile reinforced mortars combined with thermal insulation: Mechanical and fire behavior. *Constr. Build. Mater.* **2017**, *133*, 1–13. [CrossRef]

58. Giresini, L. Energy-based method for identifying vulnerable macro-elements in historic masonry churches. *Bull. Earthq. Eng.* **2016**, *14*, 919–942. [CrossRef]

59. Lamego, P.; Lourenço, P.B.; Sousa, M.L.; Marques, R. Seismic vulnerability and risk analysis of the old building stock at urban scale: Application to a neighbourhood in Lisbon. *Bull. Earthq. Eng.* **2017**, *15*, 2901–2937. [CrossRef]

60. Federal Emergency Management Agency. *Prestandard and Commentary for the Seismic Rehabilitation of Buildings (FEMA Publication No. 356)*; the American Society of Civil Engineers for the Federal Emergency Management Agency: Washington, DC, USA, 2000.

61. Structural Engineers Association of California. *Vision 2000—A Framework for Performance-Based Engineering*; Structural Engineers Association of California: Sacramento, CA, USA, 1995.

62. Italian Institute of Geophysics and Volcanology: Map of seismic hazard. Available online: https.www.ingv.it (accessed on 1 June 2017).

63. Italian Technical Norm on Energy Regulations. Available online: http://www.gazzettaufficiale.it/eli/id/1993/10/14/093G0451/sg (accessed on 1 June 2017).

64. Circ.2009-Instructions for "Technical Norms for Constructions". Available online: http://cslp.mit.gov.it/index.php?option=com_content&task=view&id=79&Itemid=20 (accessed on 1 June 2017).

Article

Rocking and Kinematic Approaches for Rigid Block Analysis of Masonry Walls: State of the Art and Recent Developments

Claudia Casapulla [1], Linda Giresini [2,*] ![ORCID] **and Paulo B. Lourenço [3]**

[1] Department of Structures for Engineering and Architecture, University of Naples Federico II, Via Forno vecchio, 36, 80124 Naples, Italy; casacla@unina.it

[2] Department of Energy Systems, Territory and Constructions Engineering, University of Pisa, Largo Lucio Lazzarino, 1, 56100 Pisa, Italy

[3] ISISE, Department of Civil Engineering, University of Minho, Campus de Azurem, 4800-058 Guimarães, Portugal; pbl@civil.uminho.pt

* Correspondence: linda.giresini@unipi.it; Tel.: +39-0502218204

Abstract: The assessment of the rocking and overturning response of rigid blocks to earthquakes is a complex task, due to its high sensitivity to the input motion, variations in geometry and dissipation issues. This paper presents a literature review dealing with classical and advanced approaches on rocking motion with particular reference to masonry walls characterized by a monolithic behavior. Firstly, the pioneering work of Housner based on the concept of the inverted pendulum is discussed in terms of the most significant parameters, i.e., the size and slenderness of the blocks, the coefficient of restitution and ground motion properties. Free and restrained rocking blocks are considered. Then, static force-based approaches and performance-based techniques, mostly based on limit analysis theory, are presented to highlight the importance of investigating the evolution of the rocking mechanisms by means of pushover curves characterized by negative stiffness. From a dynamic perspective, a review of probabilistic approaches is also presented, evaluating the cumulative probability of exceedance of any response level by considering different earthquake time histories. Some recent simplified approaches based on the critical rocking response and the worst-case scenario are illustrated, as well.

Keywords: rocking; dynamics of rigid blocks; restrained blocks; out-of-plane behavior; force-based approaches; displacement-based approaches

---

1. Introduction

Masonry buildings are constituted of three-dimensional assemblies of walls, where the out-of-plane behavior of each wall is highly influenced by the type and strength of connection with the others. There are traditional (e.g., steel ties or buttresses [1]) and innovative (e.g., composites [2,3]) techniques to ensure a safe seismic behavior at the local level, by considering the typical biaxial stress state that could involve energy dissipation [4–6]. Nevertheless, when a global box-type behavior is not guaranteed, the walls, especially the peripheral ones, are more vulnerable to out-of-plane overturning, which is one of the main causes of damage or collapse induced by earthquakes on existing masonry structures. The main deficiencies are the lack of proper connections between orthogonal walls, the absence of connecting ties, insufficiently rigid floor diaphragms, low strength and deterioration of materials.

However, if a monolithic behavior can be assured for such walls, they can be regarded as rigid blocks, and their out-of-plane seismic response can be treated through two fundamental approaches

on which this paper is mainly focused: rocking dynamics and kinematic analysis. Discrete and finite elements can also be used to assess the response of masonry structures under earthquakes [7], but those involve many uncertainties mainly related to the definition of the constitutive laws of the materials and are more suitable to masonry walls far from monolithic behavior.

On the other hand, the apparent simplicity of the rocking of a single-degree-of-freedom (SDOF) rigid block hides many subtle phenomena, largely investigated in the literature, with more emphasis since the 1980s. The pioneering work of Housner [8] was the basis for the subsequent research in the field of rocking blocks, studied in structural dynamics and particularly in earthquake engineering. After him, the first modern contributions to the rocking issues are due to Aslam and Scalise [9], who considered the motion of a free rocking block subjected to ground motions. They analyzed the transition to the sliding phenomenon, as well. The work of Ishiyama [10] proposed analytical formulations for the transitions between different types of motion (sliding, rotation, translational or rotational jumping).

Despite the numerous studies carried out so far on rigid body rocking (an extensive review work on this subject is reported in [11]), little literature describing the state of the art on masonry walls treated as rigid bodies is available, let alone the rocking of restrained walls. Therefore, this paper proposes an extensive review on kinematic and rocking approaches for monolithic masonry walls, specifically regarded as rigid blocks on rigid foundations, also including recent developments and different models accounting for lateral constraints. These modeling approaches can be used for defining the non-linear static and dynamic response of masonry buildings, especially the historic ones, for which macro-elements and their connections play a crucial role in the seismic vulnerability assessment [12–16].

The kinematic approach includes static force-based and displacement-based approaches based on standard and non-standard limit analysis methods, taking into account the evolution of motion over time through incremental kinematic analysis, while dynamic effects are considered more appropriately by means of the dynamic approach, since it also accounts for the energy dissipation in the motion.

The aim of this work is to illustrate and discuss the issues involved in the classical and non-classical theories and to present the two above-mentioned approaches adapted to masonry structures. In addition, emerging design techniques are illustrated to clarify the direction in which the research is practically oriented. Section 2 describes the basics of the rocking of a free-standing single-degree-of-freedom block, whereas Section 3 introduces the issue of restrained blocks, with an extension to multi-degree-of-freedom (MDOF) systems in Section 4. Section 5 illustrates the static approaches, referring to the static force-based and displacement-based approaches. The last two sections comment on the influence of the input motion parameters on the dynamic response (Section 6) and the deterministic and probabilistic methods of the rocking analysis (Section 7).

2. Rocking of Free-Standing SDOF Block

2.1. The Classical Theoretical Model of Housner and the Main Geometric Parameters Influencing Rocking

Housner's formulation [8], referred to as classical theory in this paper, allows investigating the behavior of a rigid block on a rigid foundation under transient actions such as earthquakes. The considered single-degree-of-freedom (SDOF) block is a rigid prism with a rectangular cross-section, rocking about the two corners O and O' (Figure 1a) and supported by a flat rigid base. Neither bouncing nor sliding are considered in this formulation.

The main geometric parameters influencing the rocking response are two: (i) slenderness ratio α, namely the arctangent of thickness to height $2b/2h$; and (ii) radius vector R, which connects the pivot point to the block center of mass.
Considering the rotation ϑ (>0 if counter-clockwise) as a Lagrangian coordinate, the equation of motion takes the form:

$$I_0\ddot{\vartheta} + sgn(\vartheta)mgR\sin(\alpha - sgn(\vartheta)\vartheta) - m\,g\ddot{u}_g R\cos(\alpha - sgn(\vartheta)\vartheta) = 0 \tag{1}$$

where I_0 is the inertia moment, m the mass and $\ddot{u}_g$ the acceleration time-history (in g) of the mass. Equation (1) can be modified for homogeneous prismatic blocks as follows:

$$\ddot{\vartheta} + sgn(\vartheta)\ p^2 \sin(\alpha - sgn(\vartheta)\vartheta) - p^2\ddot{u}_g \cos(\alpha - sgn(\vartheta)\vartheta) = 0 \qquad (2)$$

where p is the frequency parameter, equal to $\sqrt{\frac{3g}{4R}}$.
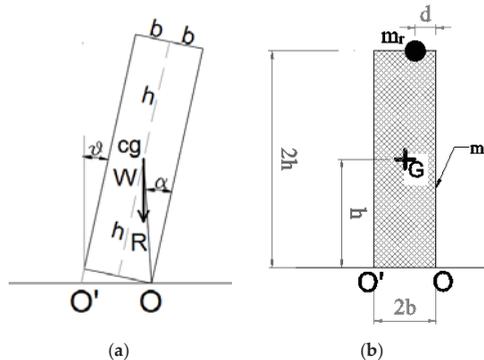
Figure 1. The rectangular free-standing rocking block of Housner's model (**a**) and the centroid G_c of the composed masonry block + the roof mass system with eccentricity d (**b**).

The equation of motion governing the rocking phenomenon of a free-standing rigid block is analogous to that used for investigating the response of a free-standing block with additional mass. A mass placed at the top of the block could simulate a roof mass, whose effect is one of changing the centroid of the composed system block + mass (Figure 1b). Thus, the inertia moment accordingly changes, with multiple values of radius and slenderness, but the equation of motion is basically the same as that of Housner's model (see Section 3) [17].

A relevant finding of the classical theory is that, between two rigid rectangular blocks of the same slenderness, the block with the higher radius vector is more stable. Moreover, between two blocks of the same width, the taller block is more stable than the shorter one [18]. However, the shorter block is related to a smaller amplitude of ground acceleration than that of the taller one. In addition, Kounadis [18] specifies that this behavior is not valid in the case of shocks, when the resisting forces (including inertia) do not have enough time to react, and the taller block results in being less stable than the shorter one (when overturning occurs without impact).

2.2. Geometry Influence and the Formulation of Energy Dissipation

The classical theory considers a rectangular block, but normally, asymmetric blocks or blocks with different shapes are to be modeled. Many authors studied the changes in the equations of motion caused by the modified geometry. These changes affect the following elements:

- moments of inertia and radius vector;
- energy loss at each impact and/or restitution coefficient;
- 3D motion to be considered instead of 2D motion;
- bouncing effect in the case of stocky blocks;
- additional terms in the equation of motion such as those due to damping and springs.

The energy dissipation or damping over rocking motion occurs when the block hits the base and the pivot point suddenly changes from O to O' (Figure 1). In the classical theory, the energy loss is expressed as a reduction of kinetic energy after each impact. By equating the moment of momentum

about O′ immediately before impact to that immediately after impact, Housner found the following expression, valid for slender and rectangular blocks:

$$e_H = 1 - \frac{3}{2}\sin^2\alpha = \frac{2\mu^2 - 1}{2(\mu^2 + 1)} \tag{3}$$

where $\mu = h/b$ is the height to thickness ratio. The so-called "restitution coefficient" e_H depends on the slenderness ratio α: the higher the slenderness, the higher the number of impacts to get the same energy loss for the same input action. A value of $e_H = 0$ means totally inelastic impact, whilst $e_H = 1$ indicates a perfectly elastic impact. Generally, the energy loss during impact is lower in experiments than that predicted by Housner's model. In other words, the experimental value of the restitution coefficient is higher than the theoretical one e_H.

Experimental tests were performed to identify the values of restitution coefficients for different unreinforced masonry (URM) specimens of several construction materials and slenderness ratios. Liberatore et al. [19] tested a marble block rocking on a marble foundation, whereas Aslam et al. [9] tested a concrete block with an aluminum base rocking on a steel foundation. They noticed discrepancies of the restitution coefficients' values between experimental and analytical results. A relevant contribution was also given by Lipscombe and Pellegrino [20], who conducted four free rocking tests on steel blocks with $\mu = 1, 2, 4, 8$, colliding on a steel base. The blocks, initially tilted almost to the point of overturning and then released, exhibited values of restitution coefficients ranging between 0.88 and 0.93, although it was respectively $e_H = 0.25$, 0.70, 0.91, 0.98 (given by Equation (3)) for the mentioned μ values. Peña et al. [21] performed experimental tests on granite stones with the height to thickness ratio varying from 4–8 under free-vibrations, harmonic and random motions. The restitution coefficient was found to be slightly higher than the experimental one, as the real case does not fully comply with the hypotheses of no bouncing or an ideal block. Indeed, the body not being fully rigid, the moment of momentum was not conserved. In this line, also Sorrentino et al. [22] carried out an experimental campaign on URM solid clay brick or tuff specimens for two-sided and one-sided motion, with height to thickness ratios varying between 6.5 and 14.6. The authors found values of the restitution coefficient equal to 95% of the theoretical value. On the other hand, the lower energy loss during impact in most experiments is related to the unevenness of the colliding surfaces, generating consecutive impacts that reduce the energy loss. That aspect was recently analytically modeled with additional pseudo-bumps at any position of the section. These bumps change the evolution of motion as more impacts occur; the modified equations of motion are proposed in [23]. Recent experimental tests observed relevant results on the evaluation of the coefficient of restitution and motion decay [24–27]. It was shown how the interface material strongly influences the dissipation in the free rocking behavior. Blocks tested on rubber were seen to have the fastest energy dissipation followed by concrete and timber bases [24]. An improved estimation of the coefficient of restitution was proposed in [26] to accurately quantify the energy dissipation of free rocking members. In addition, even for symmetric structures with uniaxial shaking, multiple modes and three-dimensional responses are likely to occur [25].

2.3. Bouncing: Sliding Phenomena and the Role of Vertical Ground Motion

In the classical theory, bouncing and sliding are neglected, but these phenomena have to be sometimes necessarily considered. Indeed, for stocky blocks, say $\mu = 1, 3$, bouncing was shown to occur, and the response was seen to be very sensitive to the restitution coefficient value [20]. For these blocks, such as cubes, a two-dimensional or three-dimensional bouncing model is therefore required. In this case, the determination of a restitution coefficient is then crucial to get a reliable response. The impact response of short blocks is therefore complex to predict for these stocky structures. In [20], a probabilistic approach was suggested to solve this issue. As concerns sliding, the absence of it is acceptable when the static coefficient of friction is larger than the ratio b/h [22,28]. Generally, masonry walls have this ratio much lower than the static friction coefficient, usually equal to 0.6–0.7 [28].

As regards the vertical ground acceleration, this was shown to have a marginal effect on the stability of a free-standing rocking column [29]. As the authors highlight, this is due to the fact that the ground acceleration enters the equation of motion after being multiplied with $\sin(\alpha - \vartheta) \ll 1$, whereas the horizontal acceleration enters the equation of motion after being multiplied by $\cos(\alpha - \vartheta) \approx 1$.

3. Restrained Rocking Blocks

In real conditions, rocking blocks such as masonry walls are restrained by flexible diaphragms. Several authors studied the influence of these boundary conditions on the dynamic response through analytical models [30], showing that diaphragm and shear-wall accelerations might increase with the flexibility of the diaphragm.

Housner's equation of motion was modified for considering the effect of single or smeared horizontal restraint [31] following a variational formulation. A single spring (or bed spring) was considered to have axial stiffness K (or K′ per unit of length) simulating an element with a stabilizing effect, such as a strengthening device (tie-rod), transverse walls or flexible diaphragms. The stiffness K or K′ can assume different values depending on the type of the roof and on the type of the roof-wall connection.

Due to the eccentricity of the roof mass, the radius vector changes depending on the rotation sign, $R_{r.cw}$ for clockwise and $R_{r.cc}$ for counterclockwise rotations, respectively (Figure 2, [17]). However, for slender blocks, the difference between $R_{r.cw}$ and $R_{r.cc}$ is negligible, and the radius vector can be assumed as the double of the radius vector R.

If R_r is the current roof radius vector and the block, subjected to a horizontal thrust H_r, is connected to a single horizontal restraint with stiffness K, the equation of motion reads [17]:

$$I_{0c}\ddot{\vartheta} + sgn(\vartheta)mgR \, \sin\hat{} + sgn(\vartheta)KR_r^2 \cos\hat{}_r \left[\sin \alpha_r - \sin \hat{A}_r\right] + \\ + sgn(\vartheta)m_r g R_r \, \sin \hat{A}_r - H_r R_r \, \cos \hat{A}_r - \left(mR\cos\hat{A} + m_r R_r \cos\hat{A}_r\right) \ddot{u}_g g = 0 \tag{4}$$

where the polar moment I_{0c} includes the contribution of the roof mass, $\hat{A} = \alpha - sgn(\vartheta)\vartheta$ and $\hat{A}_r = \alpha_r - sgn(\vartheta)\vartheta$, m is the block mass and $\ddot{u}_g$ is the acceleration time-history (in gravity acceleration g units) of the mass.

The direction and magnitude of the vector H_r may be assumed constant during motion in the hypothesis of small displacements or acting up to a fixed displacement given, for instance, by the Mohr–Coulomb law. A higher centroid position is due to the presence of the roof mass. Indeed, the roof mass is assumed to participate in the rocking motion by rotating together with the masonry block. In the case of no eccentricity ($d = b$, Figure 1b), the distance of the centroid of the composed system G_c from the base is:

$$h_{G_c} = \frac{(m + 2m_r)h}{m + m_r} \tag{5}$$

and the inertia moment of the system is obtained with the following expression:

$$I_{0c} = I_0 + m_r R_r{}^2. \tag{6}$$

where I_0 is the polar inertia moment with respect to the base corner O, $I_0 = \frac{4}{3}mR^2$.

The effect of vertical restrainers with elastic pre-stressed tendons was also investigated [25]. These systems were shown to be effective in improving the response of rocking frames with small columns subjected to long-period excitations. As the size of the columns, the frequency of the excitations or the weight of the cap-beam increases, the vertical tendons do not apply any beneficial effect. Indeed, the resistance of tall rocking frames primarily originates from the mobilization of the rotational inertia of the columns.
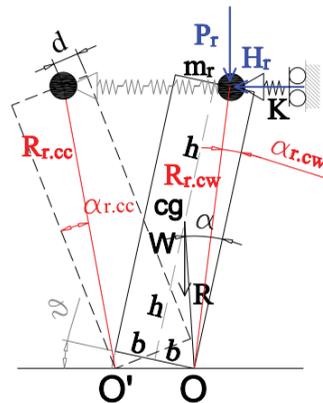
Figure 2. The rocking block with horizontal elastic restraint and roof mass.

4. Extension of SDOF to MDOF Rocking Blocks

Significant equivalence methods allowed extending the results obtained for an SDOF free-standing block to more complex structures, such as rocking frames and masonry arches. Sometimes, flexural bending movements can occur in the out-of-plane failure modes of masonry walls, and the degree of freedom cannot always be assimilated to one. In such cases, the multi rigid body dynamics could be more suitable to represent the structural response [32,33]. In [33], several tests on scale models of masonry 3D assemblies were performed on a shaking table, subjected to sinusoidal input of varying frequency and displacement amplitude, but constant acceleration, and a simplified multi-degree-of-freedom (MDOF) model was presented based on the relative rocking of two portions of walls, each one made of a finite number of bricks. A two-degree-of-freedom (2DOF) model was also presented by Simsir et al. [32] to compute the out-of-plane response of a wall that cracks at the bed joints. This model accounts for the flexibility of the diaphragm, the stiffness of the wall and the possibility for horizontal cracks developing under combined flexural moments and axial forces.

However, in contrast to the single rocking block applied to masonry that has been examined extensively, the dynamic behavior of masonry structures regarded as multi-block structures has not, to date, been exhaustively studied because of its complexity. Therefore, in order to prompt the scientific research in this line, it is here briefly illustrated how the rocking analysis can be applied to MDOF blocks.

When the degree of freedom is one, even with more complex structures, the response is determined by carrying out the same analysis as the free-standing block, but by assuming a modified value of the frequency parameter p. The square of the frequency parameter is the ratio of restoring the moment to the polar moment of inertia $p^2 = mgR/I_0$. For an SDOF rectangular block, the frequency parameter is equal to $\sqrt{\frac{3g}{4R}}$. The dynamic equivalence between a free-standing rocking frame and a free-standing rocking column was first shown by Makris and Vassiliou [34]. It refers to a rocking frame, made by a set of N columns of mass m_c and a cap beam of mass m_b. The frequency ratio of a rocking frame is given by $\hat{p} = p\sqrt{(1+2\gamma)/1+3\gamma}$, where $\gamma = m_b/(Nm_c)$ [34].

The results were extended to the case of an asymmetric rocking frame and the hinging masonry arch, defining proper values of p for each structural system [35]. When the Lagrangian parameter is not only one rotation, namely the system is MDOF, the analysis becomes much more challenging. The pure rocking of two or three-degree-of-freedom systems was investigated in [36]. The number N_u of configuration patterns that may lead to overturning instability for an MDOF with n blocks is:

$$N_u = 3^n - 1 \qquad (7)$$

with corresponding total number of nonlinear differential equations $N \times n$.

Two-DOF systems were first studied in [37]. A relevant contribution to the definition of the dynamics of such systems was given by [38]: in this work, the equations of motion are obtained for each of the four + four modes (Figure 3), and criteria for the initiation of rocking and the transition between them are illustrated. In particular, the discussion of the impact between the lower block and the ground surface, together with the impact with the higher block and the lower one is performed. More recently, other works faced the more complex problem of 3DOF systems, generally solved only with analytical approaches, e.g., in [39], equations of motion are proposed to describe the response of multi-drum ancient Greek columns as 3DOF systems, to which 26 configuration patterns are associated.
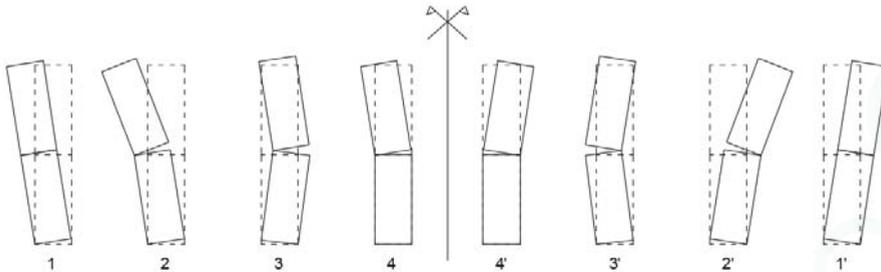
Figure 3. Eight ($N = 8 = 4 + 4$) possible configuration patterns of a two-rigid block ($n = 2$) system (adapted from [39]).

5. Static Approaches

5.1. Static Force-Based Approaches: Standard and Non-Standard Limit Analysis Methods

The static force-based (FB) approach is the most common and the simplest tool to estimate seismic design forces on rocking rigid blocks. It basically consists of the application of the plasticity theory, as first formulated by Kooharian [40] and Heyman [41]. According to this method, recognized as standard limit analysis, the application of the static theorem provides a lower-bound or safe solution of the collapse load factor, based on equilibrium equations, while the application of the kinematic theorem leads to an upper bound multiplier. The solution that satisfies the hypotheses of both theorems, equilibrium, compatibility and material conditions is the correct solution and provides the collapse load multiplier for the specific problem.

The simple mechanical model is based on the following assumptions: blocks with infinite compressive strength (rigid blocks), joints with zero tensile strength and sliding failures not allowed (friction at interfaces is sufficiently high to prevent sliding/twisting).

Based on such assumptions, the maximum horizontal force F_0 that a rigid block can undergo at the onset of rotation can be obtained by imposing equilibrium conditions. For instance, the overturning equilibrium of a cantilever SDOF wall about the pivot point O (Figure 1a) can be used to determine F_0:

$$F_0 h = mgb \tag{8}$$

where m is the block mass. If F_0 is seen as the fraction of the block self-weight $F_0 = \alpha_0 \times mg$, it is possible to calculate the collapse multiplier or the maximum horizontal acceleration (in g) to which the block can be subjected in equilibrium conditions:

$$\alpha_0 = \frac{b}{h} \tag{9}$$

Similar equilibrium conditions can be imposed for blocks with different support conditions. For example, a load-bearing SDOF simply-supported wall (vertical-spanning wall) with a horizontal

hinge at mid-height has a higher F_0 than that of a cantilever non-loadbearing wall. In particular, the force of the load-bearing simply-supported wall is $4(1 + \Psi)$ times the force of the free-standing wall, where Ψ is the ratio of overburden weight and self-weight of the upper-half of the wall above mid-height [42].

In real conditions, rocking blocks such as masonry walls are restrained by horizontal diaphragms and transverse walls, as already mentioned above. In particular, in masonry buildings without a box-type behavior and subjected to seismic loadings, in-plane and out-of-plane failure mechanisms can take place where frictional resistances might play a predominant role. Hence, it is often necessary to consider the more realistic assumptions of the presence of sliding during rocking mechanisms and also to calibrate the role of friction with reference to other systems of resistance in masonry buildings (e.g., insertion of tie-rods, rigid diaphragms, etc.), as addressed in [13].

On the other hand, it is well known that when treating such so-called non-standard materials, the bounding theorems of plastic limit analysis do not generally provide unique solutions for collapse loads, due to the non-associated flow rules imposed by friction.

Drucker [43] was perhaps the first to point out that whilst the exact solution to a problem involving Coulomb friction interfaces could be bounded from above and below, unfortunately, such bounds will often be too wide to be of practical use. In this class of problems, in fact, the lower bound is generally the condition that assumes no friction and cannot obviously be proposed for the analysis of most masonry structures. A novel modeling strategy, based on a simplified macro-block approach, is capable of providing a closer range of solutions for the ultimate load factor [44] and a reliable solution falling within the range [45]. However, for the simple out-of-plane mechanism of a front wall interlocked with sidewalls involving vertical cogged cracks along the corners (laterally-constrained rigid block), the reliable solution can be computed directly by considering the full action of friction on the bed joints along the cracks. In fact, the frictional resistances can be expressed as [13]:

$$F_P = 2 \sum_{1}^{n} S_i = \gamma t h_b l_b \frac{n(n+1)}{2} f \tag{10}$$

where n is the number of rows crossed by the vertical crack line ($H = n \times h_b$), t is the thickness of the sidewalls, f is the friction coefficient, h_b and l_b are the height and length of the single masonry unit, respectively, and S_i is the single limiting shear force due to friction at contact interface i, obeying the cohesionless Coulomb's law and stepwise increasing from the top to the bottom of the wall (Figure 4).
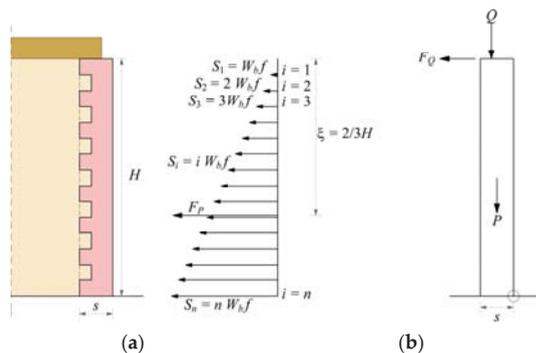
Figure 4. Frictional resistances transmitted to the façade wall by the shear walls (**a**) and the simply-supported horizontal diaphragm (**b**).

On the other hand, the presence of a horizontal diaphragm that is simply supported on the façade wall implies that beams can slip out, acting on the wall with a horizontal friction force, which is (cohesionless Coulomb's law):

$$F_Q = Q f_d \tag{11}$$

where f_d is the beam-wall friction coefficient and Q is the vertical load transmitted to the wall. Thus, by imposing equilibrium, the activation load multiplier α_0 for incipient rotation around the hinge at the base of the façade wall in Figure 4 is given by the expression:

$$\alpha_0 = \frac{P\frac{s}{2} + Q\frac{2}{3}s + F_Q H + F_P \frac{H}{3}}{QH + \frac{PH}{2}} \tag{12}$$

where s is the thickness of the front wall and the vertical resultant of the overload is assumed, e.g., applied at $s/3$ from the internal edge.

In general, the static force-based approach is very useful for the identification of the failure mechanisms, especially when not self-evident, since it is based on minimization routines. However, the evaluation of the static multiplier is only related to the onset of rocking, not to the overturning that may occur under dynamic actions. In fact, the evolution of the dynamic system over time is neglected, and the reserve capacity of the rocking phenomenon is not considered.

5.2. Displacement-Based Approaches

As dynamically-loaded walls can sustain accelerations well in excess of their 'quasi-static' capabilities [46], the displacement-based (DB) approach is revealed to be a more realistic tool to assess the seismic design forces on a rocking wall. A DB approach is based on a force-displacement $F - \Delta$ law, which is different according to whether the model is ideal or has imperfections. The force-displacement function (analogous to a pushover curve) can be obtained by determining the total horizontal reaction (or base shear) F at different displacements by using simple static equilibrium principles or the principle of virtual work. In the latter most adopted case, a non-linear kinematic analysis is applied by considering kinematic varied configurations of the mechanism, in large displacements. The ideal block has a moment-rotation or force-displacement law with negative stiffness (Figure 5a) once the force F_0 at the onset of rotation has been attained.

By contrast, geometrical imperfections cause the force-displacement law to be non-linear. In this case, the block is said to be "semi-rigid". Generally, a tri-linear simplified force-displacement law with a finite initial stiffness is adopted (Figure 5b) [42]. The real block has therefore an initial branch with a finite stiffness, a plateau phase (between Δ_1 and Δ_2) and a third branch with negative stiffness up to an ultimate displacement Δ_u (Figure 5). The ratios Δ_1 / Δ_u and Δ_2 / Δ_u are related to the material properties and the state of degradation of the mortar joints at the points of rotation. Some experimental tests were performed on URM specimens to obtain some values of those ratios [42]. A relevant parameter of the force-displacement law is the secant stiffness, which is amplitude dependent.

One method commonly used is to obtain the secant stiffness from the non-linear force-displacement curve corresponding to the point of maximum (permissible) displacement. For ductile systems, the point of maximum displacement is often associated with a point on the post-peak softening section of the non-linear force-displacement curve where the force has reduced to a fraction (generally 70–80%) of the peak force value.

For non-ductile structures such as masonry, the definition of secant stiffness is difficult due to material strength variability and a lack of yield and or unique softening points. The stiffness corresponding to a line going from the origin to the point of the curve with $\Delta = \Delta_2$ may be considered reasonably consistent [28]. A displacement-based procedure for rocking masonry structures was recently proposed [16]. It is compatible with the PERPETUATE (PERformance-based aPproach to Earthquake proTection of cUlturAlheriTage in European and mediterranean countries) methodology for the seismic performance-based assessment of cultural heritage [47] and is based on the following steps: (1) definition of the rocking mechanism (by considering rigid blocks, constraints, internal and external elasto-plastic links, constructive features and masonry quality); (2) evaluation of the pushover

curve, by the incremental equilibrium limit analysis performed on varied kinematic configurations; (3) definition of performance levels (PLs), in terms of displacement thresholds and related values of the equivalent viscous damping); (4) evaluation of the capacity curve, through the conversion to an equivalent SDOF system; (5) definition of the seismic demand, in terms of an overdamped elastic acceleration-displacement response spectrum (ADRS), modified from the seismic input at the ground level in the case of local mechanisms placed at the higher levels of the structure; (6) evaluation of the values of the intensity measure (IM) that are compatible with the different PLs. It is worth noting that the displacement demand is obtained by the classical capacity spectrum method [48], through the intersection with the overdamped acceleration-displacement spectrum, without the need of defining a proper secant stiffness.

(a)   (b)
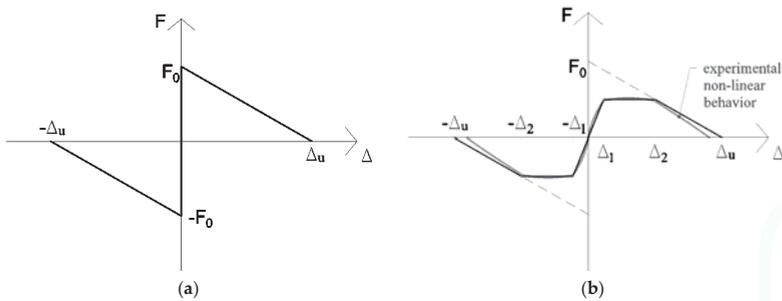
Figure 5. Force-displacement law for the rocking block: ideal model (**a**); model with imperfections (**b**).

Within this framework, some recent developments have highlighted the role of friction stresses, due to interlocking of the rocking rigid block with transverse walls, along the complete cycle of evolution of the mechanism [13,49]. In this case, a greater static multiplier is needed to activate rocking, as described in the previous section, while this effect gradually decreases after a certain displacement, due to the progressive detachment of the façade wall. The variation of the frictional forces acting along the corners can be represented by a stepwise function of the decreasing number of involved rows. In fact, the effectiveness of the frictional forces on the whole height of the corners is guaranteed as long as the first rows at the top of the sidewalls are detached from the rocking wall (first threshold displacement). In Figure 6, two examples of the pushover curve of a façade interlocked with transverse walls are reported together with that of the free wall condition. It is worth noting that the load factor can also be increased by about an order of magnitude for slender units (Figure 6b).

(a)   (b)
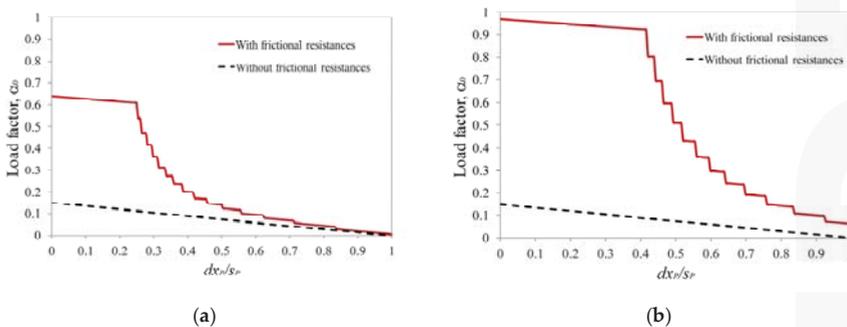
Figure 6. Influence of the frictional resistance due to interlocking between orthogonal walls after the hinge formation [13,49]. Pushover curves with unit aspect ratio $h_b/l_b = 1/3$ (**a**) and $h_b/l_b = 1/5$ (**b**).

6. Influence of Input Motion

6.1. Free-Vibrations, Harmonic Pulses and Real Accelerograms

Small changes in input or geometry (or both) can create large changes in system response for SDOF blocks subjected to random motion, at least for near collapse configurations [8,37]. As introduced in Section 2, the classical theory pointed out the main features of the model highlighting that the restoring mechanism is not elastic, but is governed by gravitational energy; consequently, the frequency of the free motion is amplitude dependent, and it is variable at each half-cycle. In other words, rocking structures do not resonate under a constant frequency, as their effective frequency depends on the response amplitude.

Casapulla and Maione [50,51] recently observed that the free-vibrations of slender rigid blocks can be represented by a succession of uniformly-decelerated motions with decreasing initial rotational velocities at each half-cycle occurring till stopping. Such a formulation was revealed to be in good agreement with Housner's model, not only with reference to the fundamental parameters governing the motion (maximum rotational angle and duration of the cycles of motion), but also with reference to the time histories of the rotational acceleration, velocity and angle.

However, while in the case of free-vibration or harmonic input forces, the response is more controllable, in the case of random motions, such as earthquakes, very large variations are found in the response of similar blocks, both in experimental and in numerical tests [21,24,52–54]. This is due to the combination of different frequency contents, duration and seismic actions parameters. Thus, in order to simplify the analysis, Housner [8] described the base acceleration as a rectangular or a half-sine impulse and derived some expressions for the minimum acceleration required to overturn the block, as a function of the duration of the impulse.

Following this pioneering work, many authors [9,55–57] examined the response of the block using both real or simulated accelerograms and harmonic loadings. These studies showed that, in contrast with the response to a single pulse, the response to more irregular but simplified accelerograms is very sensitive to the geometrical parameters of the block, as well as to the details of ground motions and the coefficient of restitution. These results allowed increased attention to various sorts of impulses or harmonic shaking and to relationships between pulses magnitude and toppling [58–61].

6.2. Critical Impulse Input and Resonance Conditions

As an alternative to standard approaches, increasing attention has been more recently focused on the identification of the worst input conditions that can imply the resonant response of the blocks [50,51,62,63].

Casapulla et al. [62,64,65] introduced an artificial limit accelerogram as a sequence of instantaneous Dirac impulses to represent the most unfavorable effects on the rocking block of the intense phase of an earthquake. A secondary sequence of intermediate impulses was also considered to reduce the resonance effects and to cover a broad range of conditions. The critical response of the block to the proposed accelerogram, represented by the achievement of the overturning, resulted in being mainly affected by the following issues: the effect of the amplitude of the main impulses; the role of the size and slenderness of the rigid block; the opposite role played by the intermediate impulses; the influence of the secondary sequence on the duration of the cycles of motion. The analysis enables, in particular, distinguishing the actions that cause overturning from those that cause the stabilization of the motion in relation with the influencing parameters.

In this line, DeJong [66] defined a theoretical accelerogram with the condition of maximization of the input energy. It deals with a step function with an alternate sign, always opposite the current rotational velocity of the block; he also assumed a constant value for the amplitude of the ground acceleration and an increasing duration of each step of the accelerogram as the half-cycle of the rocking motion increases. This reference seismic input is then transformed in a sinusoidal signal obtaining a decreasing rate of energy input and more oscillations before the overturning of the block.

The attempt to simplify the representation of the seismic signals through mathematical functions based on the selection of a few meaningful parameters has characterized in particular the research on the near-fault ground ([67,68]). Recently, Kojima et al. [69] and Kojima and Takewaki [70] developed a simple approach that schematizes the impulsive component of a near-fault earthquake as a double impulse. This simplification has also been used to represent long duration earthquakes as a multiple impulse input [69]. In order to achieve a good approximation, the amplitude of the impulse was modulated so that its maximum Fourier amplitude coincides with that of the corresponding one-cycle sinusoidal input, and a relation of proportionality between the velocity of the double impulse and the velocity amplitude of the sinusoidal waves was introduced. The proposed approach has firstly been applied to the identification of the resonant condition of elasto-plastic systems and then extended to obtain the closed form overturning limit for rigid blocks [71].

6.3. Input Motion as Pulse Type Earthquakes

Several earthquakes show dominant pulses, for which rocking structures are particularly vulnerable to pulse-type earthquakes. Zhang and Makris [59] observed the detrimental role of long-period pulses inherent in near-fault ground motions. Pulse-like earthquakes can be approximated by instantaneous Dirac impulses, as introduced in Section 6.2, or more classically, by simple trigonometric functions with specific amplitude and circular frequency. In this latter case, they can be properly idealized with cycloidal pulses or through Ricker wavelets [72]. The latter have the advantage of capturing the slight asymmetry inherent in near fault pulses better than cycloidal pulses and are expressed as [73]:

$$\psi(t) = a_p \left(1 - \frac{2\pi^2 t^2}{T_p^2}\right) e^{-\frac{1}{2}\left(\frac{2\pi^2 t^2}{T_p^2}\right)} \tag{13}$$

where a_p is the amplitude of the acceleration pulse. The value of $T_p = \frac{2\pi}{\omega_p}$ is the period that maximizes the Fourier spectrum of the wavelet, ω_p being the circular frequency of the acceleration pulse. A relevant value correlated with those parameters is the characteristic length scale of the ground excitation. This parameter, $L_p = a_p T_p^2$, gives a measure of the persistence of the most energetic pulse to generate inelastic deformation [74,75]. This parameter is more relevant than the simple acceleration amplitude a_p. Indeed, between two pulses with different acceleration amplitudes (say $a_{p1} > a_{p2}$) and different pulse durations (say $T_{p1} < T_{p2}$), the inelastic deformation does not scale with the peak pulse acceleration, but with the strongest length scale L_p [75]. By performing numerical tests on rectangular blocks of several slenderness and size, Apostolou et al. [73] found the parameters having the strongest influence on the overturning potential. Among them, there are not only the dominant frequency, but also the nature and especially the asymmetry of the seismic input. Therefore, also for masonry panels, the practice of estimating ground shaking levels by analyzing the observations of overturned and not overturned slender blocks after an earthquake is not sufficient and needs to be completed by the analysis of the mentioned parameters.

7. Types of Dynamic Analysis for Rocking Structures

7.1. Deterministic Methods Based on the Critical Rocking Response

The rocking response can be easily obtained through the integration of motion (Equations (1) and (2) for the SDOF free-standing block or Equation (3) for the horizontally-restrained block), e.g., with Runge–Kutta methods, by defining the deterministic geometric parameters and the type of excitation [76,77]. This integration allows obtaining the peak value of the normalized amplitude (also called the amplitude ratio ϑ_{max}/α), which defines the stability of the block, if the rotation is (theoretically) lower than $\pi/2$. The maximum rotation generally attained for a stable rocking block is however about 1.0. Makris et al. [78] introduced a useful representation in terms of overturning spectra of blocks, which describe the stability of a given block in terms of the maximum acceleration amplitude

as a function of the block size or the excitation frequency (Section 7.2). These kinds of spectra can also be developed to perform interesting strategies for the seismic protection of monolithic art objects, as the semi-active control proposed by Ceravolo et al. [79,80] or the addition of a tuned pendulum to the rocking block with the aim of controlling the oscillations presented by Collini et al. [81].

This deterministic method is affected by some limitations, mainly related to the need for using significant acceleration time-histories. Indeed, for a set of earthquakes, the block can result in being stable, but for others not. To avoid this situation, a probabilistic approach could be more reliable, by stochastically varying the input motion and the restitution coefficient. In deterministic methods, it can be useful to fix threshold values of amplitude ratios to define limit states, such us incipient rocking ($\frac{\vartheta_{max}}{\alpha} = 0.0$), limited rocking ($\frac{\vartheta_{max}}{\alpha} = 0.2 - 0.4$) or rocking up to collapse ($\frac{\vartheta_{max}}{\alpha} = 1$) [82]. These values are naturally generic and can be modified depending on the importance class of the element.

7.2. Rocking Structures and Elastic Oscillators in Practical Applications

The problem of the stability against overturning of rigid blocks appears still far from finding a general settlement. The rocking behavior is still a mostly unknown issue in the professional practice of civil engineers. Indeed, currently for rocking structures as masonry walls, standard response spectra are used. These demand functions derive from elastic systems, and therefore, they are not suitable for purely rocking structures. The main difficulties are still related to the description of the seismic input and the great sensitivity of the response to small variations in both system parameters and ground motion details. Priestley et al. [83] presented early experimental studies on a model suitable for slender structures and developed a practical methodology to compute displacements of the center of gravity of the structure due to rocking motion by using standard displacement and acceleration response spectra for an elastic SDOF oscillator. This was then adopted by the FEMA 356 document [84]. Makris and Konstantinidis [85] demonstrated that this methodology is oversimplified and does not take into account the fundamental differences in the dynamical structure of the SDOF systems. They showed that the rocking spectrum is a distinct and valuable intensity measure of earthquakes and offers information on the earthquake shaking that is not identifiable by the response spectrum of an elastic SDOF oscillator. Therefore, rocking structures cannot be replaced by 'equivalent' SDOF oscillators. Nevertheless, up to the formation of a plastic hinge, if the system behaves as elastic, the use of response spectra is justified and recommended. Nowadays, in the common practice of the seismic vulnerability assessment of masonry walls, the use of response spectra is predominant. In particular, according to the Italian code procedure [86], the analysis is performed in terms of displacement capacity. The value of the displacement demand is taken from the response spectra corresponding to the secant period obtained from a capacity curve (Section 5.2). The secant (also called "effective") period can also be used to predict the response of bilinear systems and rocking systems with negative stiffness, as proposed by Makris and Kampas [29]. Nevertheless, this procedure, similar to that suggested by Priestley et al. [83], completely neglects the evolution of motion over time and the behavior of a rocking block [85]. For these reasons, a pure rocking analysis is strongly recommended together with a kinematic analysis for practical applications, as well.

7.3. Methods of Analysis Based on Probabilistic Approaches

Rocking models are extremely sensitive to small variations of many parameters, such as the restitution coefficient, boundary conditions and particularly of the input motion, at least for near collapse configurations, as stated before. Aslam et al. (1980) [9] attributed the main reason for these aspects to the dependency of the vibration period upon the displacement amplitude. This influence addressed the research in studying probabilistic approaches capable of widening the results of rocking analyses in a stochastic perspective. Recently, a contribution was oriented toward defining fragility curves for rocking structures [82] by considering near-fault excitations. In particular, it was seen that by considering only peak ground acceleration (PGA) and not also, e.g., the ratio PGV/PGA (where PGV is the peak ground velocity), leads to unconservative results and not reliable results.

This study offers the conclusion that the use of bivariate intensity measures (IMs) can lead to superior fragility curves compared with conventional univariate IMs. This result confirmed previous studies related to the seismic risk [87], where through various statistical techniques, it is shown that the use of more than one IM leads to a better prediction of the damage state of a building than just a single IM. Other authors [88] performed a seismic reliability assessment of classical columns, by using synthetic ground motions that contain a high- and a low-frequency component. Generally, the demand parameter EDP (engineering demand parameter) is the maximum amplitude ratio, whereas among the most significant IMs, the peak ground velocity is one of the most reliable IM [82]. Nevertheless, the other authors proposed as EDP for columns (i) the maximum displacement at the capital normalized by the base diameter and (ii) the relative residual dislocation of adjacent drums normalized by the diameter of the corresponding drums at their interface. These assumptions can be justified by a different structural configuration, analyzed through the discrete element method (DEM). Performance levels can be then assigned to each EDP (Section 7.1), together with the values of the corresponding thresholds, to generate fragility curves. These tools are then more reliable than a simple deterministic analysis, mainly for the extremely high sensitivity of the response to the input motion, as was seen in Section 6. For these reasons, especially when uncertainties of the model are many (geometry, boundary conditions, input motion), a probabilistic analysis is recommended, by considering the univariate IMs most influencing the response, such as velocity-based parameters or bivariate IMs including acceleration and energy-based parameters.

8. Conclusive Remarks

In this paper, a wide literature review on the methods available to analyze the out-of-plane behavior of masonry walls regarded as rigid blocks subjected to seismic excitation was illustrated, mainly considering rocking and kinematic analysis. In addition, insights on recent developments were discussed, by considering the parameters most influencing the overturning potential. The main uncertainties characterizing this kind of analysis are related to the high sensitivity of the rocking blocks to small variations in system parameters and ground motion details, with possible sudden amplifications due to resonance effects. The difficulties in the analysis are increasing when the rigid block model is taken as a basic reference for the seismic analysis of the out-of-plane mechanisms either of isolated masonry blocks and walls or masonry façades poorly connected to orthogonal walls. In these cases, further uncertainties related to specific aspects of the structural behavior of masonry need to be accounted for.

Following the order in which the different methodologies were presented throughout the text, some conclusions concerning the main issues addressed could be pointed out.

As far as the rocking analysis of the free-standing SDOF block is concerned, intense research was carried out since Housner's pioneering work (1963), leading to important achievements. These have been mostly aimed at highlighting the great influence of geometric parameters and dissipation issues on the rocking motion, both analytically and experimentally. Some recent and interesting developments were also presented as more focused on the influence of boundary conditions on the dynamic response, e.g., considering masonry walls horizontally restrained by flexible diaphragms. These approaches have the potential to be extended to more complex rocking elements, e.g., involving not only simple/complex overturning, but also flexural mechanisms, where MDOF systems could be more suitable to represent the structural response.

However, the problem of the stability against overturning of rigid blocks appears still far from finding a general settlement, and the rocking behavior is a mostly unknown issue in the professional practice of civil engineers. In fact, the static force-based approach is still the most common strategy, usually preferred by practitioners Indeed, staying in the static field, while the force-based approach can be used to analyze the onset of the rocking motion, the displacement-based approach can be recognized as a more realistic tool to assess the out-of-plane response of masonry structures under dynamic actions. Therefore, some interesting contributions focused on linear and non-linear kinematic analysis were

here illustrated as considered relevant for explaining the design and assessment techniques of masonry walls in a static perspective. Incremental kinematic approaches based on standard and non-standard limit analysis methods were discussed, including some recent developments highlighting the role of friction resistances, due to interlocking of the rocking rigid block with transverse walls, along the complete cycle of evolution of the rocking mechanism.

Moreover, the influence of the input motion parameters on the dynamic response was shown to be a crucial issue, for which stochastic analyses are recommended to obtain significant results for a wide range of ground motions of different amplitudes and frequency contents. As an alternative to probabilistic approaches, increasing attention has been more recently focused on the identification of the worst input conditions that can imply the resonant response of the blocks. Related modeling approaches have the potential to schematize the effects of the impulsive component of a near-fault earthquake or of the strong phase of an earthquake.

Lastly, a wide literature has shown that the rocking spectrum is a distinct and valuable intensity measure of earthquakes and offers information on the earthquake shaking that is not identifiable by the response spectrum of an elastic SDOF oscillator. Therefore, rocking structures cannot be replaced by 'equivalent' SDOF oscillators. On the other hand, a useful representation was given in terms of overturning spectra of blocks, which describe the stability of a given block in terms of the maximum acceleration amplitude as a function of the excitation frequency. These kinds of spectra can also been developed to perform interesting strategies for the seismic protection of monolithic art objects.

Author Contributions: C.C. and L.G. conceived the field of investigation, designed the structure of the text and wrote the paper; P.B.L. supervised the paper.

Conflicts of Interest: The authors declare no conflicts of interest.

References

1. Andreini, M.; De Falco, A.; Giresini, L.; Sassu, M. Structural analysis and consolidation strategy of the historic Medicео Aqueduct in Pisa (Italy). *Appl. Mech. Mater.* **2013**, *351–352*, 1354–1357. [CrossRef]
2. Alecci, V.; De Stefano, M.; Luciano, R.; Rovero, L.; Stipo, G. Experimental Investigation on Bond Behavior of Cement-Matrix–Based Composites for Strengthening of Masonry Structures. *J. Compos. Constr.* **2015**, *20*. [CrossRef]
3. Alecci, V.; Briccoli Bati, S.; Ranocchiai, G. Study of brickwork columns confined with CFRP composite. *J. Compos. Constr.* **2009**, *13*, 179. [CrossRef]
4. Lucchesi, M.; Sassu, M. Energy dissipation of a thin elastoplastic tube under torsion and compression. *Int. J. Solids Struct.* **1995**, *32*, 2891–2906. [CrossRef]
5. Sassu, M. The Reinforced Cut Wall (RCW): A Low-Cost Base Dissipator for Masonry Buildings. *Earthq. Spectra* **2006**, *22*, 533–554. [CrossRef]
6. Sassu, M. "Biaxiality effect" on the energy dissipated by elastoplastic base-isolators. *J. Eng. Mech.* **2003**, *129*, 607–612. [CrossRef]
7. De Felice, G.; De Santis, S.; Lourenço, P.B.; Mendes, N. Methods and challenges for the seismic assessment of historic masonry structures. *Int. J. Archit. Herit.* **2016**, *11*, 143–160. [CrossRef]
8. Housner, G.W. The behavior of inverted pendulum structures during earthquakes. *Bull. Seismol. Soc. Am.* **1963**, *53*, 403–417.
9. Aslam, M.; Godden, W.G.; Scalise, D.T. Earthquake Rocking Response of Rigid Bodies. *J. Struct. Div.* **1980**, *106*, 377–392.
10. Ishiyama, Y. Motion of rigid bodies and criteria for overturning by earthquake excitations. *Earthq. Eng. Struct. Dyn.* **1982**, *10*, 635–650. [CrossRef]
11. Makris, N. A half-century of rocking isolation. *Earthq. Struct.* **2014**, *7*, 1187–1221. [CrossRef]
12. Andreini, M.; De Falco, A.; Giresini, L.; Sassu, M. Collapse of the historic city walls of Pistoia (Italy): Causes and possible interventions. *Appl. Mech. Mater.* **2013**, *351–352*, 1389–1392. [CrossRef]

13. Casapulla, C.; Argiento, L.U. The comparative role of friction in local out-of-plane mechanisms of masonry buildings. Pushover analysis and experimental investigation. *Eng. Struct.* **2016**, *126*, 158–173. [CrossRef]
14. De Falco, A.; Giresini, L.; Sassu, M. Temporary preventive seismic reinforcements on historic churches: Numerical modeling of San Frediano in Pisa. *Appl. Mech. Mater.* **2013**, *352*, 1393–1396. [CrossRef]
15. Giresini, L. Energy-based method for identifying vulnerable macro-elements in historic masonry churches. *Bull. Earthq. Eng.* **2016**, *14*, 919–942. [CrossRef]
16. Lagomarsino, S. Seismic assessment of rocking masonry structures. *Bull. Earthq. Eng.* **2014**, *13*, 97–128. [CrossRef]
17. Giresini, L.; Fragiacomo, M.; Sassu, M. Rocking analysis of masonry walls interacting with roofs. *Eng. Struct.* **2016**, *116*, 107–120. [CrossRef]
18. Kounadis, A.N. New findings in the rocking instability of one and two rigid block systems under ground motion. *Meccanica* **2015**, *50*, 2219–2238. [CrossRef]
19. Liberatore, D.; Spera, G.; D'Alessandro, G.N.D. Rocking of slender blocks subjected to seismic motion of the base. In Proceedings of the 12th European conference on earthquake engineering, London, UK, 9–13 September 2002; pp. 9–13.
20. Lipscombe, P.R.; Pellegrino, S. Free Rocking of Prismatic Blocks. *J. Eng. Mech.* **1993**, *119*, 1387–1410. [CrossRef]
21. Peña, F.; Prieto, F.; Lourenço, P.B.; Campos Costa, A.; Lemos, J.V. On the dynamics of rocking motion of single rigid-block structures. *Earthq. Eng. Struct. Dyn.* **2007**, *36*, 2383–2399. [CrossRef]
22. Sorrentino, L.; AlShawa, O.; Decanini, L.D. The relevance of energy damping in unreinforced masonry rocking mechanisms. Experimental and analytic investigations. *Bull. Earthq. Eng.* **2011**, *9*, 1617–1642. [CrossRef]
23. Ther, T.; Kollar, L.P. Refinement of Housner's model on rocking blocks. *Bull Earthq. Eng* **2016**, *15*, 2305–2319. [CrossRef]
24. ElGawady, M.A.; Ma, Q.; Butterworth, J.W.; Ingham, J. Effects of interface material on the performance of free rocking blocks. *Earthq. Eng. Struct. Dyn.* **2011**, *40*, 375–392. [CrossRef]
25. Wittich, C.E.; Hutchinson, T.C. Shake table tests of stiff, unattached, asymmetric structures. *Earthq. Eng. Struct. Dyn.* **2015**, *44*, 2425–2443. [CrossRef]
26. Kalliontzis, D.; Sritharan, S.; Schultz, A. Improved coefficient of restitution estimation for free rocking members. *J. Struct. Eng.* **2016**, *142*. [CrossRef]
27. Chatzis, M.N.; García Espinosa, M.; Smyth, A.W. Examining the Energy Loss in the Inverted Pendulum Model for Rocking Bodies. *J. Eng. Mech.* **2017**, *143*. [CrossRef]
28. Rankine, W. *A Manual of Civil Engineering*, 2nd ed.; Griffin Bohn: London, UK, 1863.
29. Makris, N.; Kampas, G. Size Versus Slenderness: Two Competing Parameters in the Seismic Stability of Free-Standing Rocking Columns. *Bull. Seismol. Soc. Am.* **2016**. [CrossRef]
30. Tena-Colunga, A.; Abrams, D. Seismic behavior of structures with flexible diaphragms. *J. Struct. Eng.* **1996**, *122*, 439–445. [CrossRef]
31. Giresini, L.; Sassu, M. Horizontally restrained rocking blocks: Evaluation of the role of boundary conditions with static and dynamic approaches. *Bull. Earthq. Eng.* **2017**, *15*, 385–410. [CrossRef]
32. Simsir, C.C.; Aschheim, M.; Abrams, D. Out-of-plane dynamic response of unreinforced masonry bearing walls attached to flexible diaphragms. In Proceedings of the 13th World Conference on Earthquake Engineering, Vancouver, BC, Canada, 1–6 August 2004; pp. 1–15.
33. D'Ayala, D.; Shi, Y. Modeling masonry historic buildings by multi-body dynamics. *Int. J. Archit. Herit.* **2011**, *5*, 483–512. [CrossRef]
34. Makris, N.; Vassiliou, M.F. Planar rocking response and stability analysis of an array of free-standing columns capped with a freely supported rigid beam. *Earthq. Eng. Struct. Dyn.* **2013**, *42*, 431. [CrossRef]
35. DeJong, M.J.; Dimitrakopoulos, E.G. Dynamically equivalent rocking structures. *Earthq. Eng. Struct. Dyn.* **2014**, *43*, 1543–1563. [CrossRef]
36. Kounadis, A.N. On the rocking complex response of ancient multispondyle columns: A genious and challenging structural system requiring reliable solution. *Meccanica* **2015**, *50*, 261–292. [CrossRef]
37. Allen, R.H.; Oppenheim, I.J.; Parker, A.R.; Bielak, J. On the dynamic response of rigid body assemblies. *Earthq. Eng. Struct. Dyn.* **1986**, *14*, 861–876. [CrossRef]

38. Psycharis, I.N. Dynamic behaviour of rocking two-block assemblies. *Earthq. Eng. Struct. Dyn.* **1990**, *19*, 555–575. [CrossRef]

39. Kounadis, A.N.; Papadopoulos, G.J. On the rocking instability of a three-rigid block system under ground excitation. *Arch. Appl. Mech.* **2016**, *86*, 957–977. [CrossRef]

40. Kooharian, A. Limit analysis of voussoir (segmental) and concrete arches. *Proc. Am. Concr. Inst.* **1953**, 317–328.

41. Heyman, J. The stone skeleton. *Int. J. Solids Struct.* **1966**, *2*, 249–279. [CrossRef]

42. Doherty, K.; Griffith, M.C.; Lam, N.; Wilson, J. Displacement-based seismic analysis for out-of-plane bending of unreinforced masonry walls. *Earthq. Eng. Struct. Dyn.* **2002**, *31*, 833–850. [CrossRef]

43. Drucker, D.C. Coulomb Friction, Plasticity and Limit Loads. *Def. Tech. Inf. Cent.* **1953**, *2902*, 1–16.

44. Casapulla, C.; Cascini, L.; Portioli, F.; Landolfo, R. 3D macro and micro-block models for limit analysis of out-of-plane loaded masonry walls with non-associative Coulomb friction. *Meccanica* **2014**, *49*, 1653–1678. [CrossRef]

45. Casapulla, C.; Argiento, L.U. In-plane frictional resistances in dry block masonry walls and rocking-sliding failure modes revisited and experimentally validated. *Compos. Part B Eng.* **2015**. accepted.

46. Abrams, D.P.; Angel, R.; Uzarski, J. Out-of-plane strength of unreinforced masonry infill panels. *Earthq. Spectra* **1996**, *12*, 825–844. [CrossRef]

47. Lagomarsino, S.; Cattari, S. PERPETUATE guidelines for seismic performance-based assessment of cultural heritage masonry structures. *Bull. Earthq. Eng.* **2015**, *13*, 13–47. [CrossRef]

48. Freeman, S.A. Development and use of capacity spectrum method. In Proceedings of the 6th US NCEE Conference on Earthquake Engineering, Seattle, WA, USA, 31 May–4 June 1998; p. 12.

49. Casapulla, C.; Argiento, L. Non-linear kinematic analysis of masonry walls out-of-plane loaded. The comparative role of friction between interlocked walls. In Proceedings of the COMPDYN 2017 6th ECCOMAS Thematic Conference on Computational Methods in Structural Dynamics and Earthquake Engineering, Rhodes Island, Greece, 15–17 June 2017; pp. 1–11.

50. Casapulla, C.; Maione, A. Free damped vibrations of rocking rigid blocks as uniformly accelerated motions. *Int. J. Struct. Stab. Dyn.* **2016**, *17*, 1–19. [CrossRef]

51. Casapulla, C.; Maione, A. A simplified equation of motion for free rocking rigid blocks. In *Insights and Innovations in Structural Engineering, Mechanics and Computation, Proceedings of the 6th International Conference on Structural Engineering, Mechanics and Computation, SEMC 2016, Cape Town, South Africa, 5–7 September 2016*; CRC Press: Boca Raton, FL, USA, 2016; pp. 120–126.

52. Kafle, B.; Lam, N.T.; Gad, E.F.; Wilson, J. Displacement controlled rocking behaviour of rigid objects. *Earthq. Eng. Struct. Dyn.* **2011**, *40*, 1653–1669. [CrossRef]

53. Acikgoz, S.; Ma, Q.; Palermo, A.; DeJong, M.J. Experimental identification of the dynamic characteristics of a flexible rocking structure. *J. Earthq. Eng.* **2016**, *20*, 1199–1221. [CrossRef]

54. Wittich, C.E.; Hutchinson, T.C. Shake table tests of unattached, asymmetric, dual-body systems. *Earthq. Eng. Struct. Dyn.* **2017**, *46*, 1391–1410. [CrossRef]

55. Yim, C.S.; Chopra, A.K.; Penzien, J. Rocking response of rigid blocks to earthquakes. *Earthq. Eng. Struct. Dyn.* **1980**, *8*, 565–587. [CrossRef]

56. Spanos, P.D.; Koh, A.S. Rocking of Rigid Blocks Due to Harmonic Shaking. *J. Eng. Mech.* **1985**, *110*, 1627–1642. [CrossRef]

57. Hogan, S.J. On the Dynamics of Rigid-Block Motion Under harmonic Forcing. *Proc. R. Soc. A Math. Phys. Eng. Sci.* **1989**, *425*, 441–476. [CrossRef]

58. Anooshehpoor, A.; Heaton, T.H.; Shi, B.; Brune, J.N. Estimates of the ground accelerations at Point Reyes Station during the 1906 San Francisco earthquake. *Bull. Seismol. Soc. Am.* **1999**, *89*, 845–853.

59. Zhang, J.; Makris, N. Rocking Response of Free-Standing Blocks under Cycloidal Pulses. *J. Eng. Mech.* **2001**, *127*, 473. [CrossRef]

60. Dimitrakopoulos, E.G.; DeJong, M.J. Revisiting the rocking block: Closed-form solutions and similarity laws. *Proc. R. Soc. A Math. Phys. Eng. Sci.* **2012**, *468*, 2294–2318. [CrossRef]

61. Voyagaki, E.; Psycharis, I.N.; Mylonakis, G. Rocking response and overturning criteria for free standing rigid blocks to single-lobe pulses. *Soil Dyn. Earthq. Eng.* **2013**, *46*, 85–95. [CrossRef]

62. Casapulla, C.; Jossa, P.; Maione, A. Rocking motion of a masonry rigid block under seismic actions: A new strategy based on the progressive correction of the resonance response [II moto sotto sisma del blocco murario: Analisi per progressiva correzione della risposta in risonanza]. *Ing. Sismica* **2010**, *27*, 35–48.
63. Casapulla, C. On the resonance conditions of rigid rocking blocks. *Int. J. Eng. Technol.* **2015**, *7*, 760–771.
64. Casapulla, C.; Maione, A. Critical Response of Free-Standing Rocking Blocks to the Intense Phase of an Earthquake. *Int. Rev. Civ. Eng.* **2017**, *8*, 1–10. [CrossRef]
65. Casapulla, C.; Maione, A. Rocking resonance conditions of large and slender rigid blocks under the intense phase of an earthquake. In Proceedings of the 6th International Conference on Computational Methods in Structural Dynamics and Earthquake Engineering (COMPDYN 2017), Rhodes Island, Greece, 15–17 June 2017.
66. DeJong, M.J. Amplification of Rocking Due to Horizontal Ground Motion. *Earthq. Spectra* **2012**, *28*, 1405–1421. [CrossRef]
67. Mukhopadhyay, S.; Gupta, V.K. Directivity pulses in near-fault ground motions I: Identification, extraction and modeling. *Soil Dyn. Earthq. Eng.* **2013**, *50*, 1–15. [CrossRef]
68. Mukhopadhyay, S.; Gupta, V.K. Directivity pulses in near-fault ground motions II: Estimation of impulse parameters. *Soil Dyn. Earthq. Eng.* **2013**, *50*, 38–52. [CrossRef]
69. Kojima, K.; Fujita, K.; Takewaki, I. Critical double impulse input and bound of earthquake input energy to building structure. *Front. Built Environ.* **2015**, *1*. [CrossRef]
70. Kojima, K.; Takewaki, I. Critical earthquake response of elastic-plastic structures under near-fault ground motions (part 1: Fling-step input). *Front. Built Environ.* **2015**, *1*. [CrossRef]
71. Nabeshima, K.; Taniguchi, R.; Kojima, K.; Takewaki, I. Closed-form overturning limit of rigid block under critical near-fault ground motions. *Front. Built Environ.* **2016**, *2*, 1–11. [CrossRef]
72. Ricker, N. Wavelet functions and their polynomials. *Geophysics* **1944**, *9*, 314. [CrossRef]
73. Apostolou, M.; Gazetas, G.; Garini, E. Seismic response of slender rigid structures with foundation uplifting. *Soil Dyn. Earthq. Eng.* **2007**, *27*, 642–654. [CrossRef]
74. Black, C.J. Dimensional analysis of rigid-plastic and elastoplastic structures under pulse-type excitations. *J. Eng. Mech.* **2004**, *130*, 1006.
75. Makris, N.; Black, C.J. Dimensional analysis of bilinear oscillators under pulse-type excitations. *J. Eng. Mech.* **2004**, *130*, 1019. [CrossRef]
76. De Felice, G.; Giannini, R. Out-of-plane seismic resistance of masonry walls. *J. Earthq. Eng.* **2001**, *5*, 253–271. [CrossRef]
77. Shawa, O.A.; de Felice, G.; Mauro, A.; Sorrentino, L. Out-of-plane seismic behaviour of rocking masonry walls. *Earthq. Eng. Struct. Dyn.* **2012**, *41*, 949–968. [CrossRef]
78. Makris, N.; Zhang, J. Rocking response of anchored blocks under pulse-type motions. *J. Eng. Mech.* **2001**, *127*, 484–493. [CrossRef]
79. Ceravolo, R.; Pecorelli, M.L.; Zanotti Fragonara, L.Z. Comparison of semi-active control strategies for rocking objects under pulse and harmonic excitations. *Mech. Syst. Signal Process.* **2017**, *90*, 175–188. [CrossRef]
80. Ceravolo, R.; Pecorelli, M.L.; Zanotti Fragonara, L.Z. Semi-active control of the rocking motion of monolithic art objects. *J. Sound Vib.* **2016**, *374*, 1–16. [CrossRef]
81. Collini, L.; Garziera, R.; Riabova, K.; Munitsyna, M.; Tasora, A. Oscillations Control of Rocking-Block-Type Buildings by the Addition of a Tuned Pendulum. *Shock Vib.* **2016**, *2016*, 1–11. [CrossRef]
82. Dimitrakopoulos, E.G.; Paraskeva, T.S. Dimensionless fragility curves for rocking response to near-fault excitations. *Earthq. Eng. Struct. Dyn.* **2015**, *44*, 2015–2033. [CrossRef]
83. Priestley, M.J.N.; Evision, R.J.; Carr, A.J.; Evison, R.J.; Carr, A.J. Seismic response of structures free to rock on their foundations. *Bull. N. Z. Natl. Soc. Earthq. Eng.* **1978**, *11*, 141–150.
84. Federal Emergency Management Agency. *Prestandard and Commentary for the Seismic Rehabilitation of Buildings*; FEMA 356; Federal Emergency Management Agency: Washington, DC, USA, 2000.
85. Makris, N.; Konstantinidis, D. The rocking spectrum and the limitations of practical design methodologies. *Earthq. Eng. Struct. Dyn.* **2003**, *32*, 265–289. [CrossRef]
86. Ministerial Circular of Infrastructure and Transport. *Instructions for the application of the New Technical Rules for Constructions (M.D. 14/01/08)*. M.C. n. 617, published on 02/02/09, Official Gazette of the Italian Republic n. 47. 26 February. Available online: http://www.gazzettaufficiale.it/eli/gu/2009/02/26/47/so/27/sg/pdf (accessed on 4 August 2017).

87. Gehl, P.; Seyedi, D.M.; Douglas, J. Vector-valued fragility functions for seismic risk evaluation. *Bull. Earthq. Eng.* **2013**, *11*, 365–384. [CrossRef]
88. Psycharis, I.N.; Fragiadakis, M.; Stefanou, I. Seismic reliability assessment of classical columns subjected to near-fault ground motions. *Earthq. Eng. Struct. Dyn.* **2013**, *42*, 2061–2079. [CrossRef]

Article

Strengthening Masonry Arches with Lime-Based Mortar Composite

Valerio Alecci [1,*], Mario De Stefano [1], Francesco Focacci [2], Raimondo Luciano [3], Luisa Rovero [1] and Gianfranco Stipo [1]

[1]   Department of Architecture, University of Florence, piazza Brunelleschi 6, 50121 Firenze, Italy;
       mario.destefano@unifi.it (M.D.S.); luisa.rovero@unifi.it (L.R.); gianfranco.stipo@unifi.it (G.S.)
[2]   eCampus University, via Isimbardi 10, Novedrate, 22060 Como, Italy; francesco.focacci@uniecampus.it
[3]   Department of Mechanics, Structures and Environment, University of Cassino, via G. Di Biasio 43,
       03043 Cassino, Italy; luciano@unicas.it
*   Correspondence: valerio.alecci@unifi.it

Abstract: In recent decades, many strengthening interventions on masonry elements were performed by using fiber reinforced polymers (FRPs). These advanced materials proved to be effective to increase the load-carrying capacity of masonry elements and to improve their structural behavior, avoiding the most critical failure modes. Despite the advantages of this technique compared to more traditional methods, FRP systems have disadvantages related to their low resistance to high temperatures, impossibility of application on wet surfaces, low permeability, and poor compatibility with masonry supports. Therefore, composite materials made of a fiber textile embedded in an inorganic matrix were recently proposed as alternatives to FRPs for strengthening historic masonry constructions. These composite materials are easier to install, have higher resistance to high temperatures, and permit higher vapor permeability than FRPs. The inorganic matrix is frequently a cement-based mortar, and the composite materials made of a fiber textile embedded in a cement-based mortar are usually identified as FRCM (fabric reinforced cementitious matrix) composites. More recently, the use of natural lime mortar as an inorganic matrix has been proposed as an alternative to cement-based mortars when historic compatibility with the substrate is strictly required, as in case of restoration of historic buildings. In this paper, the effectiveness of a fabric made of basalt fibers embedded in lime mortar matrix (Basalt-FRLM) for the strengthening of masonry arches is investigated. An experimental investigation was performed on 1:2 scaled brick masonry arches strengthened at the extrados with a layer of Basalt-FRLM and tested under vertical load. The results obtained are compared with previous results obtained by the authors by testing masonry arches strengthened at their extrados with FRCM and FRP composites. This investigation highlights the effectiveness of Basalt-FRLM in increasing load-currying and the displacement capacities of masonry arches. The Basalt-FRLM-strengthened arch exhibited higher displacement capacity when compared to arches strengthened with polymeric and cementitious matrix composites.

Keywords: masonry arch; strengthening; composite material; FRCM; lime mortar

1. Introduction

Masonry constructions are an important part of historical and artistic heritage. Recent seismic events have increased the attention of architects and engineers towards the assessment of the seismic response of historical buildings through more appropriate strategies, based on different approaches such as rocking analyses [1–6], energy-based methods [7], and numerical and experimental procedures [8–11].

Masonry arches and vaults are often present in historical buildings, representing elements of remarkable architectural value, but, at the same time, showing high seismic vulnerability. For this reason, there is an increasing interest in the development of innovative strengthening techniques to improve the structural performances of masonry arches and vaults. Traditional strengthening techniques (i.e., steel profiles or reinforced concrete hoods), which revealed many drawbacks, have been replaced by advanced strengthening solutions, based on the use of polymeric-based composite materials (fiber reinforced polymer, FRP). Innovative composite materials constituted by a fabric embedded in a cement-based matrix (FRCM, fabric reinforced cementitious mortar) are being studied [12–18] as an alternative to FRPs [19–23], mainly to strengthen historic buildings due to their high compatibility with masonry substrate in terms of resistance to high temperature and vapor permeability. Recently, a natural lime mortar matrix has been proposed as alternative to the cement-based matrix [24] when historic compatibility with the substrate is required, as in case of restorations of monumental buildings.

In this paper, the effectiveness of a composite material made of a basalt fiber textile embedded in a natural lime mortar (Basalt-FRLM) for strengthening masonry structures is investigated. In particular, the paper deals with an experimental campaign on brick masonry arches strengthened at the extrados with Basalt-FRLM. The structural behavior of Basalt-FRLM-strengthened arches is analyzed and compared with the structural behavior of un-strengthened arches and arches strengthened with FRP and FRCM composites tested in a previous step of this research [17,18,25]. The purpose of this research is to provide the first experimental evaluation of the structural effectiveness of lime matrix composite materials for strengthening masonry structures, and to compare it with the effectiveness which can be achieved with more traditional composite materials such as FRPs and FRCMs.

2. Experimental Program

An experimental campaign was performed on un-strengthened and extrados-strengthened models of brick masonry arches, in a scale of 1:2, subjected to a vertical force. The mechanical properties of the masonry components, cement-lime mortar, and bricks were obtained according to References [26,27], respectively. The masonry mechanical properties were evaluated with compressive tests on six masonry prisms in a scale of 1:2. Table 1 summarizes the mechanical properties of the masonry and its components.

Table 1. Results of tests performed on bricks, cement-lime mortar, and masonry (standard deviation and coefficient of variation are reported in parentheses). ε_u = failure strain; f_c = compressive strength; E_c = compressive Young modulus; f_{tf} = tensile flexural strength.

Material	ε_u	f_c [MPa]	E_c [MPa]	f_{tf} [MPa]
Cement-lime mortar	/	3.22 (0.31; 9.72)	727.7 (69.82; 9.59)	1.49 (0.025;1.68)
Brick	/	24.08 (2.73; 11.37)	2701.81 (585.05; 21.65)	5.60 (0.58; 10.44)
Masonry	0.0076 (0.002; 17.66)	8.53 (1.29; 13.95)	1753.7 (282.52; 16.11)	/

The Basalt-FRLM strengthening system used in this experimental investigation, produced by KeraKoll S.p.A (Sassuolo, Modena, Italy), is made up of a basalt bidirectional balanced textile (Figure 1a), named GeoSteel Grid 200, embedded in an Natural Hydraulic Limes (NHL) 3.5 lime mortar named GeoCalce® Fino (Sassuolo, Modena, Italy). The basalt fibers are provided with an alkali-resistant protective treatment made of solvent-free water-based resin and AISI 304 stainless steel micro-threads welded together to guarantee a stable sheet. The textile is made of 17-mm spaced rovings. Its equivalent thickness in both fiber directions is equal to 0.032 mm. The matrix has compressive

strength class M15 in agreement with EN 998-2. This mortar contains strictly raw, natural, and recycled minerals, with low CO_2 emissions material and very low emissions of volatile organic compounds. It is recycled as inert at the end of its life. The properties of basalt fibers and natural lime mortar are summarized in Table 2.
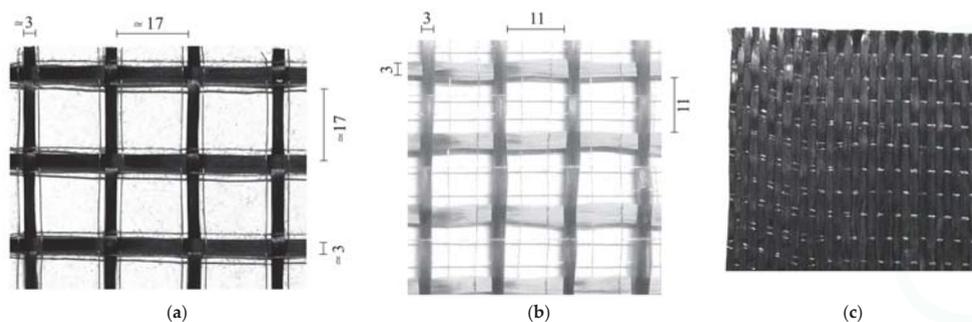
Figure 1. (**a**) Poliparafenilenbenzobisoxazole (PBO) balanced textile; (**b**) basalt balanced textile; (**c**) unidirectional carbon sheet. Dimensions in mm.

Table 2. Properties of the composite materials provided by the manufacturer. t_f = equivalent thickness; f_f = fiber tensile strength; E_f = fiber Young modulus; ε_{fu} = fiber failure strain f_{mc} = compressive strength; E_m = matrix Young modulus; f_{mtf} = tensile flexural strength. [*] Experimentally determined.

Composite Material	Fibers Material	t_f [mm]	f_f [MPa]	E_f [GPa]	ε_{fu} [%]	Matrix Material	f_{mc} [MPa]	E_m [GPa]	f_{mtf} [MPa]
Basalt-FRLM	Basalt	0.032	≥3000	≥87	-	Lime	11.2 [*]	1.3 [*]	3.72 [*]
PBO-FRCM	PBO	0.014	5800	270	2.5	Cement	20 [*]	2.8 [*]	6.15 [*]
CFRP	Carbon	0.17	4800	240	2.00	Epoxy	>50	-	-

An FRCM composite and an FRP composite produced by Ruredil S.p.A Company (San Donato Milanese, Milano, Italy) were also considered in this experimental investigation for comparison purposes. The FRCM composite, Ruregold® (San Donato Milanese, Milano) XR Muratura, is made up of a poliparafenilenbenzobisoxazole (PBO) fiber bidirectional balanced textile (Figure 1b) made of 14-mm spaced rovings (equivalent thickness 0.014 mm) embedded in a pozzolanic cement-based mortar. The FRP composite, Ruredil X Wrap 310, is made up of a unidirectional carbon sheet with an equivalent thickness 0.17 mm (Figure 1c), impregnated and glued to the substrate through a two-component epoxy-based matrix. These composites are denoted as PBO-FRCM and CFRP, respectively. Their properties are summarized in Table 2.

Experimental tests were carried out on five 1:2 scaled masonry arch models. The arch models had a 1500 mm span, 866 mm intrados radius, 961 mm extrados radius, 432.5 mm rise, and 95 mm × 95 mm cross-section (Figure 2). The dimensions of the bricks and the thickness of the mortar layers were scaled according to the scale of the model. Bricks had dimensions of 95 mm × 46 mm × 21 mm and were obtained by cutting standard bricks my means of a circular saw with water. The mortar joints were 5 mm thick. To obtain proper masonry mechanical properties, the compressive tests on masonry prisms, whose results are summarized in Table 1, were performed on specimens made of scaled bricks and thickness of the mortar joints.

The choice to test 1:2 scaled models was decided by the limited dimension of the steel frame employed to perform the tests. It was impossible to scale the dimensions of the strengthening materials in terms of size of the mesh and size of the particles of the matrix, since commercial composites have been adopted in this study. Furthermore, the scaled models can be considered representative of masonry arches strengthened with two layers of textile. Two un-strengthened (specimens 1-US

and 2-US) and three strengthened (specimens B-FRLM, P-FRCM, and CFRP) arches were tested. The adopted strengthening configuration consisted of the application of a layer of composite material on the whole extrados surface of the arches.
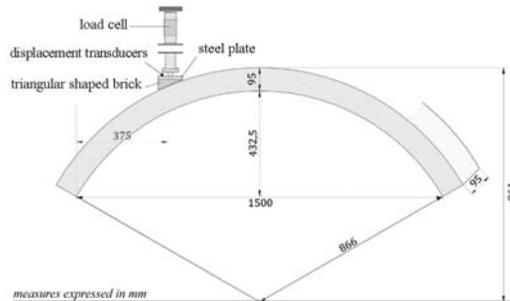
Figure 2. Scheme of the arch model test.

The compatibility between the masonry substrate and lime and cement matrices allowed their application without special treatments. After cleaning and damping the extrados surface, a first 3 mm thick layer of lime or cement matrix was applied. Subsequently, the textile was applied and finally another matrix layer of the same thickness was applied. For the CFRP composite, after cleaning the extrados surface, the classical hand layup procedure was applied; a thin layer of primer was applied prior to the application of the matrix. Subsequently, the epoxy matrix and the carbon sheet were applied. Finally, the composite material was completed with the application of a further layer of epoxy matrix.

Each arch was subjected to a vertical force applied at a quarter of the arch span (375 mm from one abutment, Figure 2). A displacement control device made of a screw jack controlled through a flywheel was used to register the loading history, up to the point of a conventional test-end corresponding to a residual strength equal to 80% of the maximum load. The load was measured through a load cell with a capacity of 100 kN (TCLP-10B tension/compression load cell). Two displacement transducers (type cantilever) were used to measure vertical displacements. The test apparatus and arch dimensions are represented in Figure 2.

3. Test Results

The experimental results are summarized in Table 3 in terms of failure load, tangent stiffness, kinematic ductility, and increase of failure load per unit cross-sectional area of fibers. The tangent stiffness is calculated as the slope of the linear phase of the load–displacement curve. The kinematic ductility is determined as the ratio of the displacement at the failure load to the displacement at the end of the linear phase of the load–displacement curve. The increase of the failure load per unit cross-sectional area of fibers is evaluated as:

$$\Delta f = \frac{F_{max} - F_{max0}}{A_f} \tag{1}$$

where F_{max} and F_{max0} are the failure loads of the strengthened and un-strengthened arches, respectively, and A_f is the cross-sectional area of the fibers in the composite material. Parameter Δf is representative of the strengthening effectiveness of the composite materials in terms of increase of failure load, while kinematic ductility represents the capacity of the specimen to exhibit displacements after the linear elastic range, up to the peak load.

Table 3. Structural parameters identified during tests on arch models.

| Specimen	Failure Load [N]	Tangent Stiffness [N/mm]	Kinematic Ductility	Δf [N/mm^2]
1-US	910	7179	1.85	-
2-US	1066	6197	1.11	-
Basalt-FRLM	5366	7200	36.6	1.37
PBO-FRCM	4968	16,221	20.32	2.84
CFRP	11,345	10,106	10.93	0.61

3.1. Un-Strengthened Arch Models

The un-strengthened arch models collapsed by the four-hinges mechanism, as shown in Figure 3. The first hinge (hinge 1) formed at the arch extrados on the loaded cross-section, while the second hinge (hinge 2) formed at the intrados. The third and fourth hinges (hinges 3 and 4) formed on the left and right abutment, respectively.
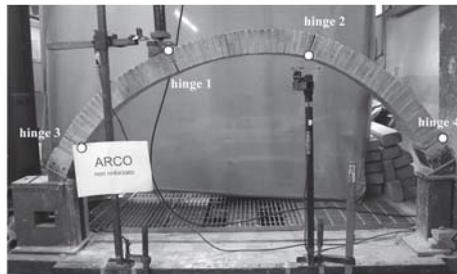
Figure 3. Hinges on the un-strengthened arches.

3.2. Arch Models Strengthened with Basalt-FRLM

The Basalt-FRLM-strengthened arch exhibited a different collapse mechanism, as shown in Figure 4. The first hinge (hinge 1) formed on the loaded cross-section, as it had happened in the un-strengthened arches. The opening of hinges 2 and 3 (Figure 3) was prevented by the composite material. A first crack was noted on the lime matrix, approximately where hinges 2 and 3 formed in the un-strengthened arch models. The onset of hinge 4 (Figure 3) occurred after the onset of hinge 1 and the cracking of the matrix, but it did not open due to the joint sliding at the right abutment of the arch. Before the collapse, additional cracks occurred on the lime mortar matrix near the cross-section where hinge 2 formed on the un-strengthened arches (Figure 5). The opening of these cracks was associated with slip of the fibers with respect to the surrounding matrix, and allowed a displacement capacity much higher than the displacement capacity of the un-strengthened arches. At the failure of the specimen, the lime mortar was still perfectly attached to the extrados of the arch.
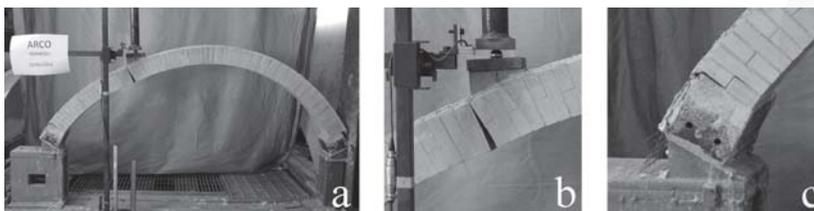

Figure 4. Basalt-FRLM-strengthened arch: (**a**) collapse mechanism; (**b**) opening of hinge 1; (**c**) opening of hinge 4.

Figure 6 shows the load-displacement responses of the un-strengthened and Basalt-FRLM-strengthened arches. The displacement shown in this figure is the vertical displacement of the loaded cross-section. In Table 3, the contribution of Basalt-FRLM composite sheet can be noted in increasing the failure load (about 5 times) and kinematic ductility (about 20 times) with respect to the un-strengthened arches.

Figure 5. Superficial cracks on lime matrix, where hinge 2 formed on the un-strengthened arch.
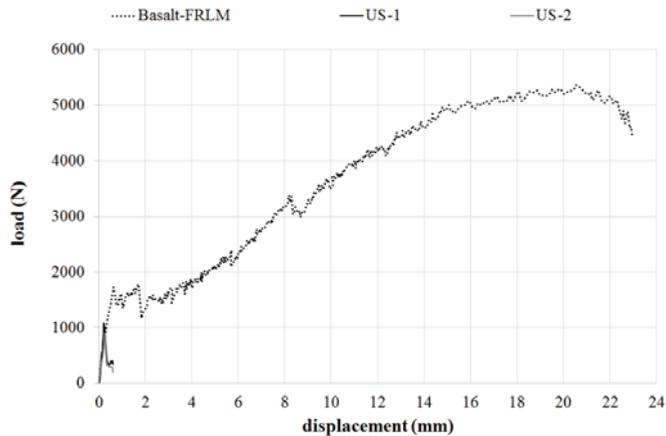

Figure 6. Load-displacement curves of un-strengthened and Basalt-FRLM-strengthened arch.

### 3.3. Comparison with Arches Strengthened with Cementitious and Polymeric Matrix Composites

The experimental results obtained on the arch model strengthened with Basalt-FRLM were compared with the experimental results of similar arch models strengthened with different composite materials (PBO-FRCM, CFRP) obtained in a previous step of this research [21,28]. The different composite materials had the same width, equal to the width of the arch extrados surface. Consequently, the fiber cross-sectional area was 3.2 mm^2, 1.4 mm^2 and 17 mm^2 in the case of Basalt-FRLM, PBO-FRCM, and CFRP composites, respectively. In Figure 7, the load-displacement curves of un-strengthened and Basalt-FRLM-strengthened arches are compared with the load-displacement curves of PBO-FRCM- and CFRP-strengthened arches.

The PBO-FRCM- and the Basalt-FRLM-strengthened arches exhibited a similar structural behavior. After the cracking of the loaded cross-section (Figure 9a), the PBO-FRCM cracked at the extrados of the cross-section where hinge 2 formed on the un-strengthened arch at a higher load than the Basalt-FRLM-strengthened arch (points A in Figure 7). This is probably related to the higher tensile strength of the cementitious matrix used for the PBO-FRCM material with respect to the natural lime mortar used for the Basalt-FRLM material (Table 2). Afterwards, the increase of the applied force is

associated with an increase in the bending moment. Consequently, the thrust line crosses the intrados surface, as schematically shown in Figure 8.
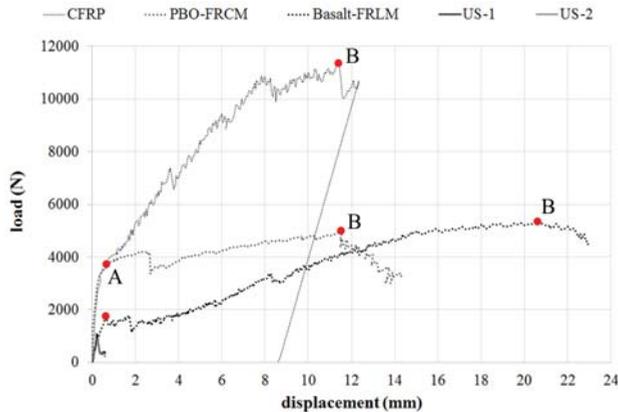

Figure 7. Load-displacement curves of un-strengthened and Basalt-FRLM-, PBO-FRCM-, and CFRP-strengthened arches.
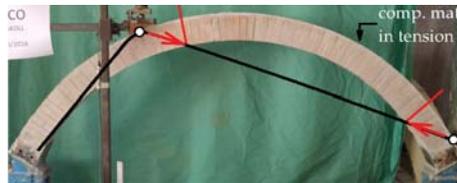
Figure 8. Schematic thrust line of the extrados-strengthened arches.

In this phase, the equilibrium condition requires a tensile force in the fibers (Figure 8). The increase of this tensile force after the cracking of the matrix and before the joint sliding at the right abutment (point B in Figure 7) is associated with a slip at the fiber-matrix interface, as evidenced by the crack pattern shown in Figures 5 and 9b. This allowed a good displacement capacity. It was observed that a greater number of cracks formed in the matrix of the PBO-FRCM composite than in the matrix of the Basalt-FRLM composite (Figures 5 and 9b). This indicates that higher interfacial shear stress acts at the PBO fiber-cement matrix interface than at the basalt fiber-lime mortar interface. The failure loads of the Basalt-FRLM- and PBO-FRCM-strengthened arches were similar, while the displacement capacity of the Basalt-FRLM-strengthened arch was higher than the displacement capacity of the PBO-FRCM-strengthened arch (Table 3). The different slope of the load-displacement responses of the PBO-FRCM- and Basalt-FRLM-strengthened arches is probably associated with different shapes of the bond-slip behavior of these composite materials; from the presented results, it can be argued that the fiber-matrix interface of the PBO-FRCM composite allows higher shear stress than the fiber-matrix interface of the Basalt-FRLM composite. Conversely, a non-zero shear stress is maintained up to larger fiber-matrix slip in the case of the Basalt-FRLM composite than in the case of the PBO-FRCM composite. This statement needs to be confirmed by the results of shear bond tests to be performed on the Basalt-FRLM composite, while the bond behavior of the PBO-FRCM composite has been analyzed in several papers [14,28–32]. In References [16–18,25], it is shown that the failure load of strengthened arches can be analytically evaluated with the approach of the limit analysis. This requires the knowledge of the fiber debonding strain, i.e., the fibers strain associated with debonding at the fiber-matrix interface. The debonding strain of PBO-FRCM composites was experimentally determined

by means of shear bond tests [14,28–32], while the debonding strain of the Basalt-FRLM material is not currently available. Therefore, the next step of this research work will involve the characterization of the Basalt-FRLM material in terms of bond behavior and the use of bond properties within the framework of the limit analysis to evaluate the collapse load of the Basalt-FRLM-strengthened arches.
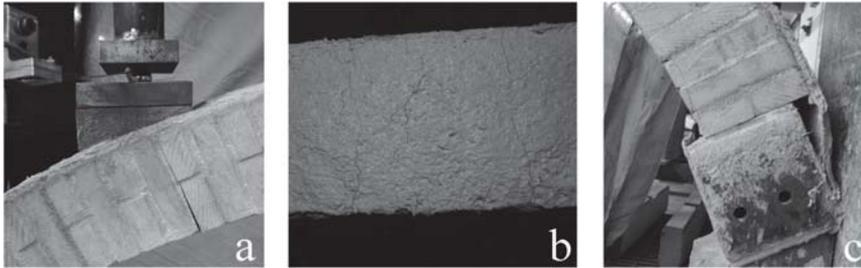
Figure 9. PBO-FRCM-strengthened arch: (**a**) hinge 1; (**b**) cracks in cementitious mortar matrix; (**c**) joint sliding at the right abutment [16].

The CFRP-strengthened arch exhibited brittle behavior. After the formation of the first hinge on the loaded cross-section and the cracking of the masonry where hinge 2 formed on the un-strengthened arch, the force in the fibers increased. This required lower interfacial slip than in the case of the PBO-FRCM and Basalt-FRLM composites, since the debonding phenomenon of FRP-masonry joints is associated with the formation of an interfacial crack within the supporting masonry [33–36]. The collapse was caused by the sudden shear sliding at the right abutment (Figure 10c). The collapse load of the CFRP-strengthened arch was roughly twice the collapse load of the PBO-FRCM- and Basalt-FRLM-strengthened arches. Conversely, the load-displacement response of the CFRP-strengthened arch showed lower displacement capacity than the PBO-FRCM- and Basalt-FRLM-strengthened arches.
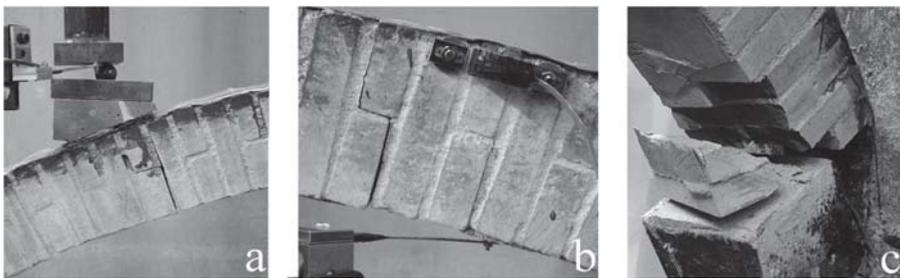
Figure 10. CFRP-strengthened arch: (**a**) hinge 1; (**b**) opening of hinge 2; (**c**) joint sliding at the right abutment.

A comparison of the specific effectiveness of the strengthening of the composite materials considered in this experimental work can be performed considering the parameter Δf defined by Equation (1) (Table 3). Δf is representative of the strengthening effectiveness of the composite materials even though the collapse of the arches was always associated with the shear force, since the composite materials bonded on the surface of an arch produces an increase in both the flexural and shear capacity of the strengthened cross-sections, as observed in References [17,25]. It can be observed that the increase of the collapse load associated with a unit fiber cross-section is higher for the PBO-FRCM and Basalt-FRLM composites with respect to the CFRP composite.

4. Conclusions

This paper concerns a preliminary study on the effectiveness of a composite material made of basalt textile and lime-based mortar matrix (Basalt-FRLM) for strengthening masonry structures. The structural behavior of arches strengthened at the extrados with Basalt-FRLM is experimentally evaluated. The results obtained highlight the effectiveness of the Basalt-FRLM composite; the maximum load and kinematic ductility results highly increased with respect to the un-strengthened arches (about 5 and about 20 times, respectively).

The Basalt-FRLM-strengthened arch exhibited similar failure load to and higher ductility than a similar arch strengthened with a composite material made of PBO fibers embedded in a cement-based matrix (PBO-FRCM). The different displacement capacity of the Basalt-FRLM- and PBO-FRCM-strengthened arches can be associated with the different fiber-matrix bond properties of these composite materials and to the lower elastic modulus of the basalt fibers with respect to carbon fibers. Furthermore, the Basalt-FRLM- and PBO-FRCM-strengthened arches exhibited a lower (roughly half) failure load than a similar arch strengthened with a carbon fiber reinforced polymer (CFRP) composite. This can be associated with the higher cross-sectional area of fibers in the CFRP composite than in the Basalt-FRCM composite (roughly 5 times) and PBO-FRCM composite (roughly 12 times).

The presented preliminary experimental results encourage further research on the use of the Basalt-FRCM composite for strengthening masonry structures, especially in terms of characterization of the basalt fibers-lime mortar bond properties, since the tests highlighted the excellent adhesion at the masonry-lime matrix interface.

The use of this type of composite is of interest to applications aimed at strengthening historical and monumental buildings where the historical compatibility with the substrate is strictly required. Moreover, the tested strengthening system responds to the increasing requirements of sustainable interventions.

Author Contributions: All the Authors contributes in the same way to the research.

Conflicts of Interest: The authors declare no conflict of interest.

References

1. Giresini, L.; Sassu, M. Horizontally restrained rocking blocks: evaluation of the role of boundary conditions with static and dynamic approaches. *Bull. Earthq. Eng.* **2016**, *15*, 385–410. [CrossRef]
2. Giresini, L.; Fragiacomo, M.; Sassu, M. Rocking analysis of masonry walls interacting with roofs. *Eng. Struct.* **2016**, *116*, 107–120. [CrossRef]
3. D'Ambrisi, A.; Feo, L.; Focacci, F. Masonry arches strengthened with composite unbonded tendons. *Compos. Struct.* **2013**, *98*, 323–329. [CrossRef]
4. Foraboschi, P. Resisting system and failure modes of masonry domes. *Eng. Fail. Anal.* **2014**, *44*, 315–337. [CrossRef]
5. Foraboschi, P.; Vanin, A. Non-linear static analysis of masonry buildings based on a strut-and-tie modeling. *Soil Dyn. Earthq. Eng.* **2013**, *55*, 44–58. [CrossRef]
6. Misseri, G.; Rovero, L. Parametric investigation on the dynamic behaviour of masonry pointed arches. *Arch. Appl. Mech.* **2017**, *87*, 385–404. [CrossRef]
7. Giresini, L. Energy-based method for identifying vulnerable macro-elements in historic masonry churches. *Bull. Earthq. Eng.* **2015**, *14*, 919–942. [CrossRef]
8. Andreini, M; De Falco, A.; Giresini, L.; Sassu, M. Structural damage in the cities of Reggiolo and Carpi after the earthquake on May 2012 in Emilia Romagna. *Bull. Earthq. Eng.* **2014**, *12*, 2445–2480. [CrossRef]
9. Andreini, M.; De Falco, A.; Giresini, L.; Sassu, M. Structural analysis and consolidation strategy of the historic Mediceo Aqueduct in Pisa (Italy). *Appl. Mech. Mater.* **2013**, *351–352*, 1354–1357. [CrossRef]
10. De Falco, A.; Giresini, L.; Sassu, M. Temporary preventive seismic reinforcements on historic churches: Numerical modeling of San Frediano in Pisa. *Appl. Mech. Mater.* **2013**, *352*, 1393–1396. [CrossRef]
11. Giresini, L.; Sassu, M. Tests Results and Simple Structural Analysis of the Main Lighthouse in the Harbor of Livorno (Italy). *Adv. Mater. Res.* **2014**, *834*, 1299–1303. [CrossRef]

12. Larrinaga, P.; Chastre, C.; San-José, J.T.; Garmendia, L. Non-linear analytical model of composites based on basalt textile reinforced mortar under uniaxial tension. *Compos. Part B Eng.* **2013**, *55*, 518–527. [CrossRef]
13. Prota, A.; Marcari, G.; Fabbrocino, G.; Manfredi, G.; Aldea, C. Experimental In-Plane Behavior of Tuff Masonry Strengthened with Cementitious Matrix–Grid Composites. *J. Compos. Constr.* **2006**, *10*, 223–233. [CrossRef]
14. Alecci, V.; De Stefano, M.; Luciano, R.; Rovero, L.; Stipo, G. Experimental Investigation on Bond Behavior of Cement-Matrix–Based Composites for Strengthening of Masonry Structures. *J. Compos. Constr.* **2015**, *20*, 04015041. [CrossRef]
15. Garmendia, L.; Larrinaga, P.; San-Mateos, R.; San-José, J.T. Strengthening masonry vaults with organic and inorganic composites: an experimental approach. *Mater. Des.* **2015**, *85*, 102–114. [CrossRef]
16. D'Ambrisi, A.; Focacci, F.; Luciano, R.; Alecci, V.; De Stefano, M. Carbon-FRCM materials for structural upgrade of masonry arch road bridges. *Compos. Part B Eng.* **2015**, *75*, 355–366. [CrossRef]
17. Alecci, V.; Focacci, F.; Rovero, L.; Stipo, G.; De Stefano, M. Extrados strengthening of brick masonry arches with PBO-FRCM composites: Experimental and analytical investigations. *Compos. Struct.* **2016**, *149*, 184–196. [CrossRef]
18. Alecci, V.; Misseri, G.; Rovero, L.; Stipo, G.; De Stefano, M.; Feo, L.; Luciano, R. Experimental investigation on masonry arches strengthened with PBO-FRCM composite. *Compos. Part B Eng.* **2016**, *100*, 228–239. [CrossRef]
19. Rovero, L.; Focacci, F.; Stipo, G. Structural behavior of arch models strengthened using FRP strips of different lengths. *J. Compos. Constr.* **2013**, *17*, 249–258. [CrossRef]
20. Briccoli Bati, S.; Rovero, L.; Tonietti, U. Strengthening of masonry arches with composite materials. *J. Compos. Mater.* **2007**, *11*, 33–42. [CrossRef]
21. Briccoli Bati, S.; Rovero, L. Towards a methodology for estimating strength and collapse mechanism in masonry arches strengthened with fibre reinforced polymer applied on external surfaces. *Mater. Struct.* **2008**, *41*, 1291–1306. [CrossRef]
22. Rotunno, T.; Rovero, L.; Tonietti, U.; Briccoli Bati, S. Experimental study of bond behavior of CFRP-to-brick joints. *J. Compos. Constr.* **2015**, *19*, 04014063. [CrossRef]
23. Alecci, V.; Briccoli Bati, S.; Ranocchiai, G. Study of brickwork columns confined with CFRP composite. *J. Compos. Constr.* **2009**, *13*, 179–187. [CrossRef]
24. De Felice, G.; De Santis, S.; Garmendia, L.; Ghiassi, B.; Larrinaga, P.; Lourenco, P.B.; Oliveira, D.V.; Paolacci, F.; Papanicolaou, C.G. Mortar-based systems for externally bonded strengthening of masonry. *Mater. Struct.* **2014**, *47*, 2021–2037. [CrossRef]
25. Alecci, V.; Focacci, F.; Rovero, L.; Stipo, G.; De Stefano, M. Intrados strengthening of brick masonry arches with different FRCM composites: experimental and analytical investigations. *Compos. Struct.* **2017**, in press. [CrossRef]
26. UNI EN 1015-11. *Methods of Test for Mortar for Masonry—Determination of Flexural and Compressive Strength of Hardened Mortar*; European Standard; BSI: London, UK, 2007.
27. UNI EN 772-1. *Methods of Test for Masonry Units—Determination of Compressive Strength*; European Standard: Milton Keynes, UK, 2011.
28. D'Ambrisi, A.; Feo, L.; Focacci, F. Bond-slip relations for PBO–FRCM materials externally bonded to concrete. *Compos. Part B Eng.* **2012**, *43*, 2938–2949. [CrossRef]
29. Caggegi, C.; Carozzi, F.G.; De Santis, S.; Fabbrocino, F.; Focacci, F.; Hojdys, Ł.; Lanoye, E.; Zuccarino, L. Experimental analysis on tensile and bond properties of PBO and aramid fabric reinforced cementitious matrix for strengthening masonry structures. *Compos Part B Eng.* **2017**, in press. [CrossRef]
30. Carloni, C.; D'Antino, T.; Sneed, L.; Pellegrino, C. Role of the matrix layers in the stress transfer mechanism of FRCM composites bonded to a concrete substrate. *J. Eng. Mech.* **2014**, *141*. [CrossRef]
31. D'Antino, T.; Carloni, C.; Sneed, L.H.; Pellegrino, C. Matrix-fiber bond behavior in PBO FRCM composites: A fracture mechanics approach. *Eng. Fract. Mech.* **2014**, *117*, 94–111. [CrossRef]
32. Focacci, F.; D'Antino, T.; Carloni, C.; Sneed, L.H.; Pellegrino, C. An indirect method to calibrate the interfacial cohesive material law for FRCM-concrete joints. *Mater. Des.* **2017**, *128*, 206–217. [CrossRef]
33. Focacci, F.; Carloni, C. Periodic variation of the transferable load at the FRP-masonry interface. *Compos. Struct.* **2015**, *129*, 90–100. [CrossRef]

34. Carloni, C.; Focacci, F. FRP-masonry interfacial debonding: An energy balance approach to determine the influence of the mortar joints. *Eur. J. Mech.—A/Solids* **2016**, *55*, 122–133. [CrossRef]

35. Malena, M.; Focacci, F.; Carloni, C.; De Felice, G. The effect of the shape of the cohesive material law on the stress transfer at the FRP-masonry interface. *Compos. Part B Eng.* **2017**, *110*, 368–380. [CrossRef]

36. Foraboschi, P. Effectiveness of novel methods to increase the FRP-masonry bond capacity. *Compos. Part B Eng.* **2016**, *107*, 214–232. [CrossRef]

Nonlinear Modelling of Curved Masonry Structures after Seismic Retrofit through FRP Reinforcing

Bartolomeo Pantò [1],*, **Francesco Cannizzaro [1]**, **Salvatore Caddemi [1]**, **Ivo Caliò [1]** [iD],
César Chácara [2] and **Paulo B. Lourenço [2]**

[1]   Department of Civil Engineering and Architecture, University of Catania, 95125 Catania, Italy;
      francesco.cannizzaro@dica.unict.it (F.C.); scaddemi@dica.unict.it (S.C.); icalio@dica.unict.it (I.C.)
[2]   Department of Civil Engineering, Institute for Sustainability and Innovation in Structural
      Engineering (ISISE), University of Minho, Azurem, 4800-058 Guimarães, Portugal;
      c.chacara@pucp.pe (C.C.); pbl@civil.uminho.pt (P.B.L.)
*   Correspondence: bpanto@dica.unict.it; Tel.: +39-095-738-2275

Abstract: A reliable numerical evaluation of the nonlinear behaviour of historical masonry structures, before and after a seismic retrofitting, is a fundamental issue in the design of the structural retrofitting. Many strengthening techniques have been introduced aimed at improving the structural performance of existing structures that, if properly designed and applied, provide an effective contribution to the preservation of their cultural value. Among these strategies, the use of fabric-reinforced polymeric (FRP) materials on masonry surface is being widely adopted for practical engineering purposes. The application of strips or 2D grid composite layers is a low invasive and easy to apply retrofitting strategy, that is able to improve both the in-plane and the out of plane behaviour of masonry elements also in the presence of complex geometries thanks to their flexibility. For this reason, these techniques are frequently employed for reinforcing masonry curved elements, such as arches and vaults. In this paper, taking advantage of an existing general framework based on a discrete element approach previously introduced by the authors, a discrete element conceived for modelling the interaction between masonry and FRP reinforcement is applied to different curved masonry vaults typologies. This model, already used for evaluating the nonlinear behaviour of masonry arches, is here employed for the first time to evaluate the effectiveness of FRP reinforcements on double curvature elements. After a theoretical description of the proposed strategy, two applications relative to an arch and a dome, subjected to seismic loads, with different reinforced conditions, are presented. The benefit provided by the application of FRP strips is also compared with that associated to traditional retrofitting techniques. A sensitivity study is performed with respect to the structure scale factor.

Keywords: macro-model approach; monumental masonry structures; masonry arches and vaults; historical structural analyses; seismic assessment; cultural heritage protection; FRP-reinforcement; HiStrA software

1. Introduction

The numerical simulation of the seismic response of historical masonry structures (HMS) is a key aspect of the cultural heritage preservation, and represents a challenging issue within the structural and earthquake engineering. Historical masonry structures represent a high percentage of existing buildings in several regions of the world, and their value is relevant both from the economic and social-cultural points of view. On the contrary, they suffer from scattered structural degradation, due to static loads, chemical and physic degradation of the materials, previous earthquakes, and wrong alterations of the original structural conception. Normally, they are not able to resist to earthquakes

even if characterized by a low intensity. Recent seismic events occurred in Italy, such as the Central Italy Eartkquakes (2016), the Emilia (2012), and L'Aquila (2009); they produced severe damage patterns or the complete destruction of several historical sites. Such events, well documented in terms of post earthquake technical survey, demonstrated many critical aspects, which make vulnerable the historical structures to the horizontal and vertical seismic actions. One of the most important aspects is the presence of elements with a curved geometry such as arches and vaults, which interact with the vertical elements (walls or columns) during the earthquake motion, producing a significant effect on the seismic response of the entire structure.

Curved structures have been widely adopted in the past for building purposes, since their shape allows an effective transfer of the static vertical action to the walls, and induces compression along their span; for the latter reason curved shapes are still adopted and proposed for modern structures [1,2]. When it comes to single and double curvature masonry structures, their study is still an open problem debated in the literature [3]. Aimed at the reduction of the seismic vulnerability of HMS in presence of curved masonry elements, several retrofitting techniques based on reinforced composite materials, applied by means of polymeric (FRP) or cementitious (FRCM) matrix, have been introduced, and widely investigated by means of experimental tests and numerical simulations during the last years. The use of these techniques is getting more and more frequent in the retrofitting of historical and monumental masonry buildings since they consist of reversible and low invasive interventions; with regard to the design of FRP reinforcements, several proposals have been made [4,5]. On the other hand, there is a lack of fast and reliable numerical tools to assess the effectiveness of such techniques.

In fact, even considering unreinforced masonry structures, the numerical simulation of their actual behaviour is still a very complex task within the computational structural mechanics field. The main issue is related to the difficulty in providing reliable simulations of the high nonlinear degrading cyclic response of masonry. To this regard, a great variability of the mechanical characteristics is encountered, thus making difficult the definition of a general constitutive law that is suitable for all masonry typologies. When it comes to retrofitting techniques, and in particular to fibre-composite strengthened structures, a crucial aspect is related to the correct simulation of the tangential stress transferred from the reinforcement to the masonry substrate, and the relative failure collapse for tensile rupture of the textile or delamination of the reinforcement from the support. On this task, several contributions have been given by different authors and now are available in the literature [6–9], also in presence of curved support [10,11].

Recently, a 3D macro-model has been proposed for the non-linear seismic simulations of masonry structures aiming at a reduced computational effort when compared to the traditional finite element approaches. The main idea of the model was to use a 2D mechanical scheme, governed by unidirectional non-linear links, which, according to different typologies, have to reproduce the main masonry failure modes [12]. Such a model has been successfully employed in the simulation of laboratory tests [13] and in the seismic assessment of ordinary and mixed masonry buildings [14–16]. Subsequently, the model has been extended to catch the out-of-plane behaviour of masonry walls [17,18] and the behaviour of structures with a curved geometry [19–21].

In this paper this discrete macro-modelling approach is used to assess the seismic capacity of some typologies of masonry vaults commonly present in historical structures, before and after a reinforcing retrofit through composite materials. With this aim, a new non-linear model recently proposed in the literature [22], able to simulate the presence of FRP strips or 2D-webs and to grasp the interaction with the masonry support, also in presence of a curved substrate, is here employed. The model is able to simulate the debonding of the reinforcement from the masonry support due to tangential delamination or to normal tensile detachment, which represent the most probable collapse mechanisms of FRP reinforced structures.

Different strips arrangements applied either to the intrados or to the extrados surfaces are considered in the paper. The efficiency of the FRP retrofitting is compared to the traditional technique of adding steel tie-rods in order to investigate the optimal solutions with respect to the retrofit design and

to the use of composite material. The results of the numerical simulations relative to the arches, have been compared with those obtained through limit analysis approach, and applied to simpler models. The analytical results are used to validate the numerical results and are duly discussed providing a contribution towards the understanding of reinforced curved structures subjected to seismic actions. The results show that the composite reinforcements can produce a significant increment of the seismic capacity in terms of both strength and ductility, without increasing the stiffness of the structure. The employed macro-model is able to effectively grasp the behaviour of unreinforced and reinforced (both with traditional and innovative techniques) curved masonry structures, as well as providing reliable results which contribute to the relevant literature towards the optimal design of historical masonry structures retrofit.

2. The Modelling of Historical Masonry Structures

In this work a numerical strategy based on a discrete macro-model, already available in the literature, is employed for the nonlinear numerical simulations of both unreinforced and FRP reinforced masonry structures. According to this approach, the masonry is modelled by an equivalent mechanical scheme, constituted by a hinged quadrilateral endowed with one or two diagonal links to rule the diagonal shear cracking, and interacting with contiguous elements along its four edges by means of nonlinear discrete interfaces which govern the flexional and the sliding behaviour. Each discrete interface is made of a single or multiple (according to the model) rows of transversal links for the flexional behaviour and single or multiple (according to the model) sliding links. The different stages of this discrete element are reported in Figure 1. This approach was originally introduced for modelling the in-plane behaviour of Unreinforced Masonry Structures [12], Figure 1a. This plane element possesses four degrees of freedom, a single row of transversal links and a single in-plane sliding link, and is able to model the main failure mechanisms of the masonry in its own plane, as long as a proper calibration procedure of the links is adopted. Two subsequent upgrades were achieved to expand the potentialities of the approach. First, the out of plane (spatial) behaviour, typical of historical constructions, was added [17,18] by considering additional rows of transversal links, and two additional out-of-plane sliding links (able to govern the out of plane shear behaviour and the torsion), thus enabling the out of plane degrees of freedom, as shown in Figure 1b. Subsequently, a further upgrade was introduced considering a shell macro-element characterized by an irregular geometry, variable thickness along the element, and skew interfaces [19,21] in order to deal with structures with a curved geometry, such as vaults and domes, Figure 1c. The calibration procedures, concerning the mechanical properties of the links, were properly extended in order to account for the more complicated geometry of the element, but keeping the same general philosophy.

Numerical and experimental validations of the proposed approach, with reference to full-scale structures can be found in [23,24]. More recently this approach was also extended to the dynamic context [25].


(a)   (b)   (c)
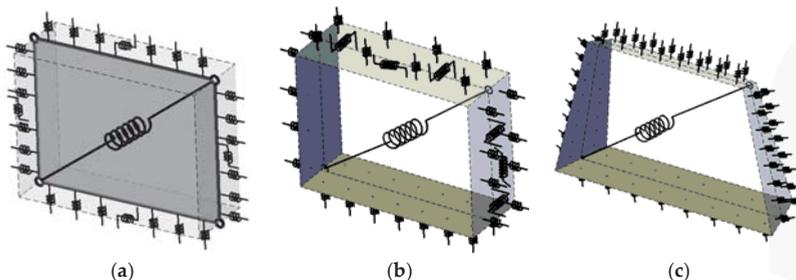
Figure 1. Layout of the macro-element adopted for masonry at its three stages: (**a**) plane element, (**b**) spatial regular element and (**c**) three-dimensional element for curved structures.

3. The Modeling of FRP Reinforcing

The extension of the macro-element approach to account for the presence of FRP-reinforcements was proposed in [22], and is here briefly recalled. The presence of the fibre-reinforced elements is modelled by means of zero thickness rigid flat elements, partially or totally lying on one of the surfaces of the masonry element, as shown in Figure 2. A special zero-thickness non-linear interface, whose kinematics is related to the relative displacements between the masonry and reinforcement macro-elements, was introduced to simulate a proper interaction between the FRP element and the masonry support. In particular, the FRP-masonry interface discretization is here performed according to a discrete distribution of nonlinear links whose nonlinear laws account for the presence of the adhesive, organic, or cementitious, matrix by allowing the mutual reinforcement-masonry normal and tangential stresses. In particular, a layer of transversal links is introduced to model a flexural detachment of the textile, while two longitudinal orthogonal links model the crucial aspect of the delamination phenomenon. The calibration of the transversal links is performed according to a bilinear constitutive law (with different compressive and tensile strengths) with a post-elastic branch calibrated according to the relevant compressive and tensile fracture energies. On the other hand, the sliding links are calibrated with a symmetric bilinear law whose post-elastic branch is associated to proper fracture energy, with a dependency of the current strength on the normal action on the interface.

Discrete interfaces made of a single row of links (calibrated according to a fiber discretization approach) rule the constitutive behaviour of the textile itself. This latter aspect, together with the sliding links of the FRP-masonry interface, leads to a progressive transfer of the tangential forces between masonry and FRP reinforcement; thus, implying a numerical definition of the so called anchorage length. In the applications reported in the following, the mechanical properties for the FRP laminates have been assumed according to a simple elasto-fragile law attributed to a homogenous material, with an equivalent thickness (t_f), characterized by a Young's modulus (E_f) and tensile strength (f_t), incapable to resist to compression loads. A schematic layout of the modelling approach of a masonry element reinforced with a FRP strip is reported in Figure 2.

Despite its simplicity, the model is able to predict the main collapse mechanisms associated to the reinforcement: the rupture in tensile of the fiber, the shear debonding, and/or the peeling of the reinforcement. Furthermore, mixed failure mechanisms in which the masonry is involved, can be predicted.
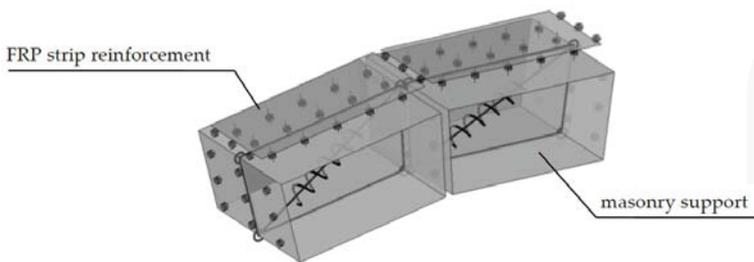
Figure 2. Schematic layout of the interaction between masonry elements and discrete fabric-reinforced polymeric (FRP) reinforcement elements.

4. Retrofitting and Restoration of Curved Masonry Structures by FRP Materials

In this section, the ultimate seismic strength of two typologies of curved structures is numerically simulated before and after a consolidation retrofit. Namely, a circular arch and a spherical dome are considered. A standard technique, that is the application of a tie rod, and an innovative technique, that is the application of FRP strips, are here considered and compared.

4.1. Circular Arch

A simple circular arch with radius R is considered in this section; the other significant geometric parameters are inferred as functions of the radius, that is the half bay ($L = R\sqrt{3}/2$), the rise ($f = R/2$), the thickness ($s = R/10$) which is kept constant, and the width ($b = s$). The basic geometry of the arch is characterized by the value $R_1 = 866$ mm, which corresponds to a prototype tested in the laboratory, subjected to an unsymmetrical vertical static load [26]; then, two additional values of the radius ($R_2 = 1500$ mm and $R_3 = 2500$ mm) are considered in order to investigate the effect of the scale factor on the response of the unreinforced and reinforced systems.

The arch is subjected to the self-weight and to a horizontal mass proportional load distribution (p_0), as represented in Figure 3, increased until the complete collapse of the structure. The results of the push-over analyses are presented both in terms of capacity curves, and collapse mechanisms. The capacity curves report the maximum lateral displacement of the arch vs. the base shear coefficient (base shear normalized by the own weight).
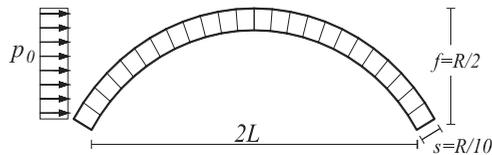
Figure 3. Geometry of the arch with the indication of the seismic load condition (p_0).

In order to calibrate the numerical model, an initial comparison was performed with the results of the experimental campaign reported in [26]. In the mentioned paper two identical arches were subjected to a vertical concentrated load according to the experimental layout reported in Figure 4. The mechanical parameters of the masonry have been estimated by means of experimental tests [26], and are here reported in Table 1. E and G represent the normal and the tangential deformation moduli of masonry, σ_t and σ_c the tensile and compressive strengths, G_t and G_c the corresponding values of fracture energy, c the cohesion, μ the friction factor, and w the specific self-weight of masonry.

The results of the macro-element model are reported in terms of capacity curve (applied force vs. vertical displacement at the loaded section) with the black line, and are compared with the experimental capacity curves or the two specimens (grey lines). In terms of collapse mechanism, the location and the opening sequence of the plastic hinges are in agreement with the experimental evidence as well.
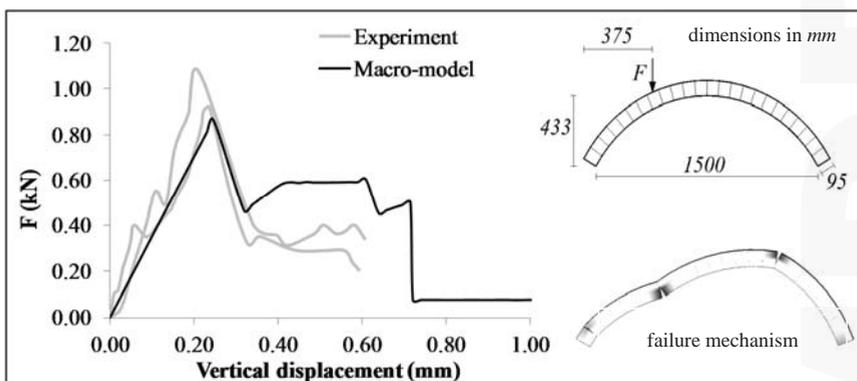

Figure 4. Validation of the numerical model.

Table 1. Mechanical property of the masonry.

E (Mpa)	G (Mpa)	σ_t (Mpa)	σ_c (Mpa)	G_t (N/mm)	G_c (N/mm)	c (Mpa)	μ (-)	W (kN/m^3)
2700	1080	0.30	8.53	0.01	0.30	0.26	0.6	18

Once the proposed model has been validated considering the masonry arch, as described in Figure 3, and subjected to a concentrated vertical load as reported in Figure 4, the load scenario corresponding to a uniform horizontal load is considered in the following (Figure 3). In particular, Figure 5 reports the capacity curves relative to the different geometries in terms of global base shear V_b (Figure 5a) and in terms of base shear coefficient $C_b = V_b/W$ (Figure 5b), being W the total weight of the arch. It can be observed that, as the radius of the arch increases, the global resistance of the arch increases as well (Figure 5a). On the contrary, in terms of the base shear coefficient, as the radius increases, the peak strength reduces, and all the models tend to the same residual strength (Figure 5b).
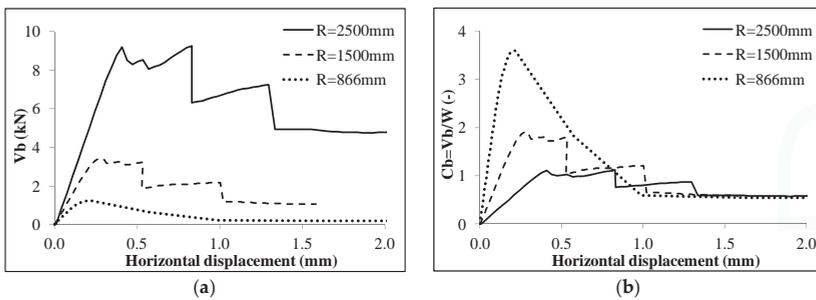
Figure 5. Capacity curves of the unreinforced arches, expressed in terms of (**a**) global base shear, and (**b**) base shear coefficient.

With regard to the assessment of the effectiveness of the structural retrofitting of the arch, three different typologies of reinforcing are considered. The first one consists of the introduction of a tie rod, whose diameter varies proportionally to the radius of the arch, from φ10 mm in the case of $R = 866$ mm, to φ30 mm in the case of $R = 2500$ mm, with Young's modulus $E = 200$ GPa, and an ultimate tensile strength equal to $f_y = 200$ Mpa. The diameters of the tie-rods are empirically chosen among commercial diameters, keeping constant the ratio between the radius of the arch and the diameter of the tie-rod. In the considered models the tie-rods' heights h_r with respect to the base of the arch is about $R/4$ (Figure 6). The yielding stress of the steel has been chosen among widely adopted steel typologies, and large enough to keep the tie-rods in the elastic field. The other two strategies consist of the introduction of FRP strips, at the intrados and at the extrados surfaces respectively (Figure 6). The reinforcement is constituted by strips arranged over the entire width and length of the arch made of glass fiber composite material (GFRP) and organic matrix. The adopted mechanical properties have been set according to [27], and reported in Table 2, in which E_f and f_t are the tensile module and the ultimate tensile strength of the reinforcement, and t_f is the equivalent thickness. The bond-slip behaviour is described by the initial shear stiffness of the matrix k_s, the ultimate debonding stress t_f, the fracture energy G_s, and the friction factor μ_s.

Figure 6. Different reinforcing interventions considered for the arch.

Table 2. Tensile and bond-slip parameters of the FRP reinforcement.

Tensile			Bond-Slip			
E_f (GPa)	f_t (MPa)	t_f (mm)	k_s (N/mm^3)	τ_f (MPa)	G_s (N/mm)	μ_s (-)
450	1473	0.149	20	1.3	2.5	0.75

Figure 7 shows the failure mechanisms of the reinforced arches, respectively with $R = 2500$ mm and $R = 866$ mm. The collapse mechanism observed for the model reinforced with the tie rod is very similar to the failure mechanism of the unreinforced arch, which is not here reported for the sake of conciseness. The latter aspect seems to demonstrate that the presence of the tie rod does not increase the strength of the arch, at least in seismic conditions and neglecting the interaction with the underlying walls. On the contrary, the failure mechanisms of the arches reinforced by means of FRP strips are characterized by a wide spread of the damage. It is worth to note that, due to the transfer of tangential stress between the FRP strip and the arch, the presence of FRP strips delays or prevents the opening of plastic hinges on the surface to which the strips are applied. For all of the investigated cases, the failure mechanism is concentrated in the masonry and in the FRP strips due to the tensile rupture; whereas, no shear no delamination of the reinforcement is encountered. In both cases of strips applied to the intrados and to the extrados, the failure is associated to the activation of an intermediate plastic hinge. The latter is located on the extrados surface of the arch in the case of the intrados reinforcing (point A_1 in Figure 7a and point A_2 in Figure 7b) or at the intrados surface, closer the support of the arch, in the case of the extrados reinforcing (point B_1 in Figure 7a and point B_2 in Figure 7b). It is worth to note that, although the arches reported in Figure 7 are not scaled according to the relevant radius, they refer to different size of the arch, as better specified in the caption.
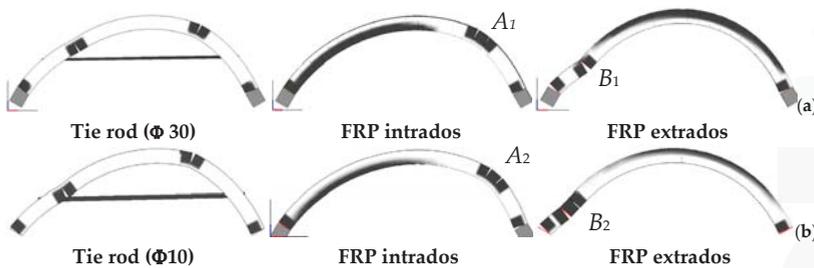

Figure 7. Failure mechanisms of the reinforced (**a**) $R = 2500$ mm and (**b**) $R = 866$ mm arches.

Figure 8 shows the comparison of the considered reinforcing techniques in terms of capacity curves for two of the three radiuses investigated: the smallest (866 mm) and the largest (2500 mm). The capacity curves and the failure mechanisms of the models reinforced with tie rods are very close to the findings relative to the unreinforced model, whereas the capacity curves of the arches reinforced by means of the FRP strips show significant increments, both in terms of strength and ductility. For those models, after the achievement of the peak load a sudden drop in the global strength is encountered; such a drop is associated to the opening of a cylindrical hinge in the arch, associated to the FRP strip tensile rupture. Then, for larger displacements, the FRP strips-masonry interface tends to mobilize the tangential force, progressively transferring stresses to the fibres. The latter aspect implies a higher residual force of the strengthened models with respect to the unstrengthened model. The influence of the arrangement of the FRP reinforcement (at the extrados or at the intrados) on the global resistance is negligible in the case of $R = 866$ mm (Figure 8a), while this effect is important in the case of $R = 2500$ mm (Figure 8b).
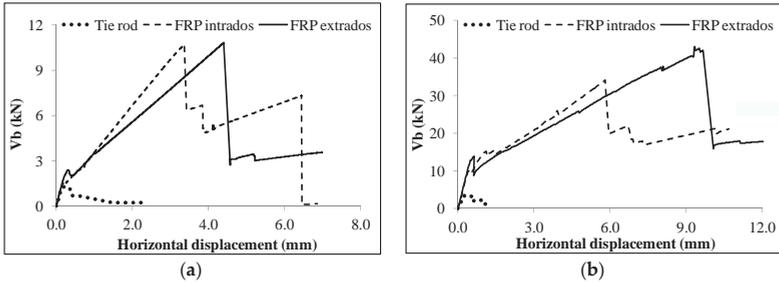
Figure 8. Capacity curves of the reinforced arch: (**a**) R = 866 mm; (**b**) R = 2500 mm.

The presence of the FRP composite strips produces an increment of the ultimate bending moment of the cross section of the arch. In order to highlight the contribution of the reinforcement on the structural response, the eccentricity of the normal action ($e = M/N$), normalized with respect to the height H of the section, along the curvilinear abscissa (s) of the arch, normalized with respect to the arch length Φ, is reported in Figure 9. In particular, the arches with R = 866 mm are considered, both in the configurations with FRP at the extrados (Figure 9a) and at the intrados (Figure 9b). The tensile axial force (N) is considered positive, and the bending moment (M) is considered positive if it stretches the FRP reinforcement fibres. The zero of the abscissa is set at the left abutment, while the unit value corresponds to the right abutment of the arch. The reported eccentricities are associated to the peak-load conditions, which are characterised by the opening of three hinges in both of the considered cases. In the model reinforced at the extrados (Figure 9a), two hinges are located at the intrados (at the normalized abscissa 0.29 and at the right end of the arch) and one hinge corresponding to the tensile rupture of the textile, is opened at the extrados at the left end of the arch. In the model reinforced at the intrados, two hinges are located at the extrados (left end of the arch and at the normalized abscissa 0.67), and one hinge at the intrados, located at the right end of the arch.
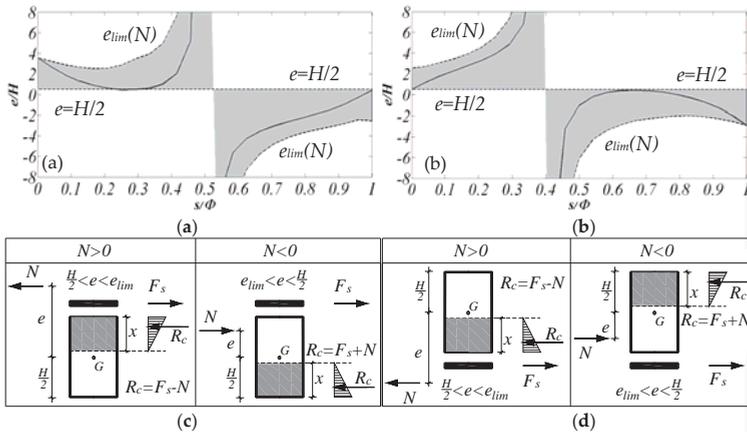

Figure 9. Contribution of the FRP reinforcement at the peak load: normalized abscissa versus eccentricity of the acting force of the models with R = 866 reinforced at the (**a**) extrados and (**b**) intrados. Cross section internal equilibrium for extrados (**c**) and intrados (**d**) reinforcing.

It is important to notice that the distribution of the plastic hinges in correspondence of the peak-load does not correspond to the locations at collapse (Figure 7), since the rupture of the textile,

corresponding to the third plastic hinge, implies an internal force redistribution which induces the opening of hinges in masonry at different locations.

In Figure 9 the theoretical limit values of the eccentricity, as evaluated through the limit analysis approach [26], are reported. The masonry is considered as a no-tension material and linear-elastic in compression, whereas the FRP strips are not capable of transferring compressive force and elastic-brittle in tension. The limit conditions, reported with dashed lines, are associated to the rupture in traction of the FRP strip (curved lines), and to the tensile action on the masonry (straight lines at the dimensionless eccentricity 0.5). The grey areas in the graphs represent the field of the admissible eccentricities. It is worth noting that the left parts of the arches are in tension while the right parts are in compression. This is due to the particular load scenario here considered (i.e., horizontal force distribution proportional to the self-mass of the arch). In proximity of the abscissa associated to the change of sign of the normal force, the eccentricities tend to diverge (see Figure 9a,b). In order to clarify the equilibrium of the reinforced arch cross section, simple schemes are reported in Figure 9c,d, for the case of extrados and intrados reinforcing, respectively. In each figure the two possible scenarios are reported: tensile ($N > 0$) and compressive axial force ($N < 0$). The grey areas (whose height is equal to x) and the white ones (whose height is equal to $H - x$) represent the areas in compression and tension, respectively. The internal forces are represented by the tensile action of the FRP strip (F_s) and the global compression on the masonry (R_c). The ultimate equilibrium of the section is imposed by considering the ultimate value of F_s and evaluating the corresponding value of x under the hypothesis of linear elastic behaviour of the masonry (confirmed by the numerical simulations). Once the internal forces are computed, the ultimate moment (M_u) and the ultimate eccentricity $e_{\lim}(N) = M_u/N$ can be easily inferred.

Figure 10 shows the working rates of the reinforcement at the peak load of the arches with $R = 866$ mm reinforced at the extrados (Figure 10a) and at the intrados (Figure 10b). The working rates are expressed in terms of $\varepsilon_f/\varepsilon_{fu}$, being ε_f and ε_{fu} the current and the ultimate tensile strains of the textile, respectively. These rates are useful to identify the achievement of the tensile rupture of the reinforcement, which is here identified at the left end of the arch for the model reinforced at the extrados, and at the right end of the arch for the model reinforced at the intrados. These ruptures produce the sudden drops of the global resistance, as observed in the global capacity curves.
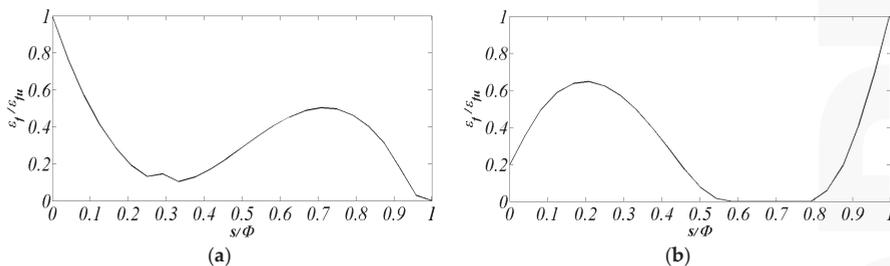
Figure 10. Contribution of the FRP reinforcement at the peak load: normalized abscissa versus working rates of the reinforcement for the models reinforced at the (**a**) extrados and (**b**) intrados.

Aiming at highlighting the shear bond behaviour of the FRP reinforcement, in Figure 11 shows the tangential stress τ at the interface between masonry and FRP reinforcement in correspondence of the peak load (continuous lines), as well as the yielding tangential stress $\tau_y(N)$ at the same step (dashed lines), depending on the current compression force on the interface (N). The figures refer to the arches with $R = 866$ mm reinforced at the extrados (Figure 11a) and at the intrados (Figure 11b). In both cases, the tangential stress is lower than the corresponding yielding value confirming that the debonding mechanism does not occur. The latter results are apparently in contrast with other experimental and numerical results available in the literature, obtained considering similar FRP reinforced prototypes

subjected to a vertical eccentric force [27]. The fact that no delamination phenomenon occurs for the treated cases might be due, in part, to the geometry and in part to the horizontal mass-proportional load distribution considered.

(a)   (b)
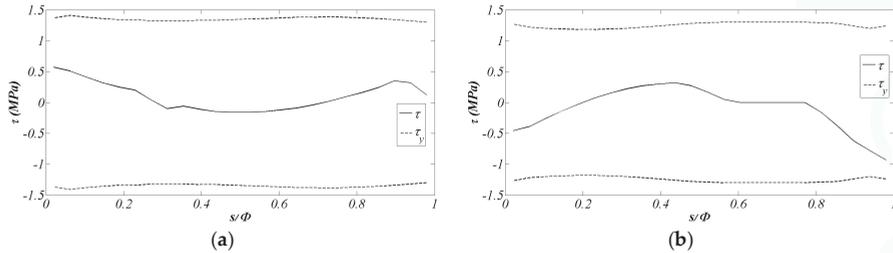
Figure 11. Tangential stress at the interface between masonry and FRP reinforcement in correspondence of the peak load for the models reinforced at the (**a**) extrados; and (**b**) intrados.

A comparison among all the reinforced and unreinforced models, in terms of ultimate load capacity ($V_{b,max}$) and increment of resistance (ΔV_b), is reported in Table 3. The benefits in terms of strength resistance are higher in the models with the lowest radius ($R = 866$ mm) and the beneficial effects decrease as the radius increases. Furthermore, the comparison of the effects of the extrados and intrados arrangements of the FRP strips demonstrates that the scale effect observed in Figure 8 is confirmed for all of the cases investigated: in addition, for small radius models the application of FRP strips to the intrados and to the extrados provides similar effects (see the first column of Table 3), while in the case of large radius models the benefit associated to the extrados FRP reinforcement is significantly higher if compared to the intrados reinforcing.

Table 3. Ultimate strength of the arches and increment of the ultimate load with respect to the unreinforced configuration.

Model	R = 866 mm		R = 1500 mm		R = 2500 mm	
	$V_{b,max}$ (kN)	ΔV_b (%)	$V_{b,max}$ (kN)	ΔV_b (%)	$V_{b,max}$ (kN)	ΔV_b (%)
Unreinforced	1.23	-	3.43	-	9.26	-
Tie rod	1.23	0	3.43	0	9.26	0
Intrados FRP	10.83	780	19.14	458	34.10	268
Extrados FRP	10.72	772	21.93	539	43.00	364

Finally, in order to investigate the influence of the fibre content on the lateral strength of the structure, a further parametric investigation on the arch with $R = 866$ mm reinforced at the intrados is performed. In particular, a model considering a double equivalent thickness of reinforcement ($t_f = 0.298$ mm) is investigated.

In Figure 12, the corresponding capacity curve is reported (Figure 12a) together with the trend of the tangential stress at the interface between masonry and FRP reinforcement (Figure 12b), and the damage pattern in correspondence of the peak load and the collapse of the arch (Figure 12c,d). In Figure 12a,b, the pushover curve and the corresponding tangential stresses of the previously investigated model ($t_f = 0.149$ mm) are reported for comparison. An increment of strength and ductility is associated to the model with $t_f = 0.298$ mm if compared to the standard thickness model. However in this case the ultimate lateral capacity is limited by the activation of the delamination as demonstrated by tangential stress distribution, which overlaps the yielding stress close to the right end of the arch (Figure 12b). At the peak load, the opening of the cylindrical hinges at the intrados is significantly delayed by the presence of FRP reinforcement (Figure 12c), causing a significant delamination in the post-peak branch (Figure 12d).

(a)

(b)

delamination →

← delamination →

(c)

(d)
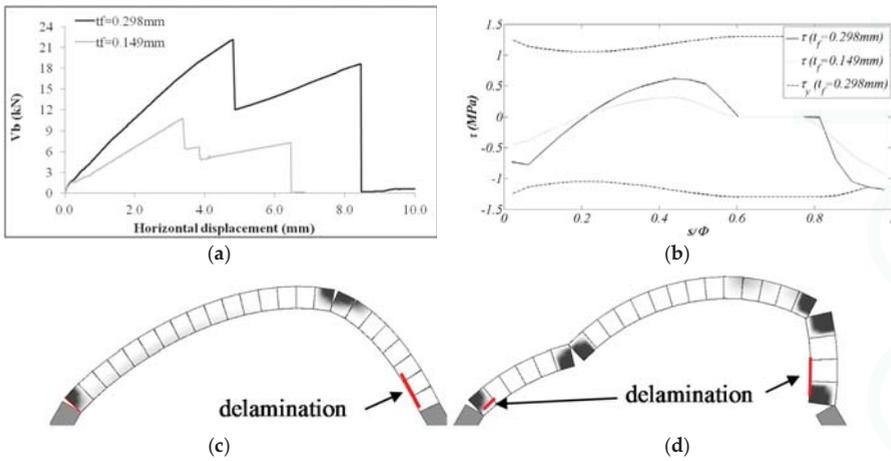
Figure 12. Arch with R = 866 mm reinforced at the intrados with a double thickness of the textile (t_f = 0.298 mm): (**a**) capacity curve; (**b**) tangential stress at the interface between masonry and FRP reinforcement in correspondence of the peak load, damage pattern at (**c**) the peak load; and (**d**) collapse.

4.2. Hemisperical Dome

A further example relative to a double curvature vault is considered in this section. In particular, a masonry hemi-spherical dome, already studied in the elastic field in [28], with a thickness t = 20 cm, and whose geometric layout is reported in Figure 13 is here studied with reference to the nonlinear field. The masonry dome is initially subjected to its own self-weight, and subsequently, a horizontal force distribution proportional to the masses (p_0) is applied until collapse in order to investigate a typical load scenario in seismic conditions.
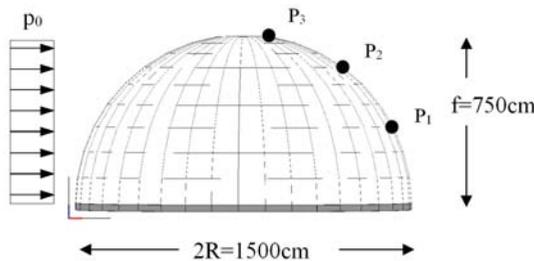

Figure 13. Geometry of the dome and control points.

The displacements of three different nodes has been monitored according to the layout showed in Figure 13. The adopted mechanical properties for the numerical simulations are reported in Table 4. The results are reported in Figure 14 in terms of collapse mechanisms, damage patterns (Figure 14a), and capacity curves with respect to the three monitored nodes (Figure 14b).

Table 4. Mechanical characteristics of the masonry.

E (Mpa)	G (Mpa)	σ_t (Mpa)	σ_c (Mpa)	G_t (N/mm)	G_c (N/mm)	c (Mpa)	μ (-)	w (kN/m^3)
1200	480	0.15	2.50	0.10	0.5	0.15	0.7	25

The collapse mechanism is characterized by a large damaged area along the meridians in the positive direction of the load and two smaller damaged areas at about a latitude of 30° at the two symmetric upper and lower sides orthogonal to the direction of the load distribution. In terms of capacity curves, the structure is characterized by a significant peak load (C_b = 0.6) and by a significant residual resistance as well. It is worth to note that the horizontal displacements of the monitored points decrease as the height of the control point increases.


Normal plastic deformations (%)		
10.0	6.67	3.33
9.16	5.83	2.50
8.33	5.00	1.66
7.50	4.16	0.83
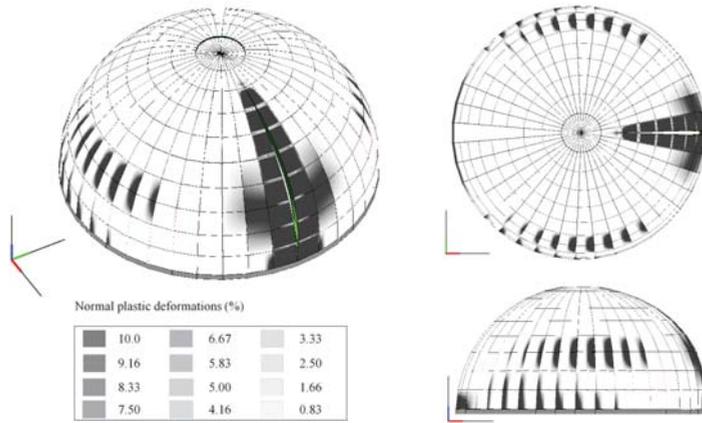
(**a**)
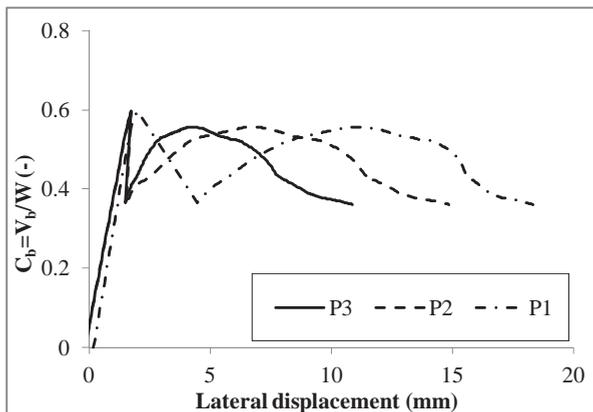
(**b**)

Figure 14. Response of the unreinforced dome in terms of (**a**) failure mechanism; and (**b**) capacity curves.

Regarding the structural retrofitting strategies, the application of FRP strips has been adopted. The strips (which have a width equal to 120 cm) have been arranged along the parallels to prevent the occurrence of damage along the meridians. Two different levels of retrofitting have been considered: a soft one with two strips centred at the latitudes of 22.5° and 49.5° (Figure 15a), and a strong retrofitting with four strips centred, respectively, at the latitudes of 13.5°, 31.5°, 49.5°, and 67.5° (Figure 15b). The same mechanical properties of the reinforcement considered for the circular arches, are adopted (see Table 2).

(**a**)   (**b**)
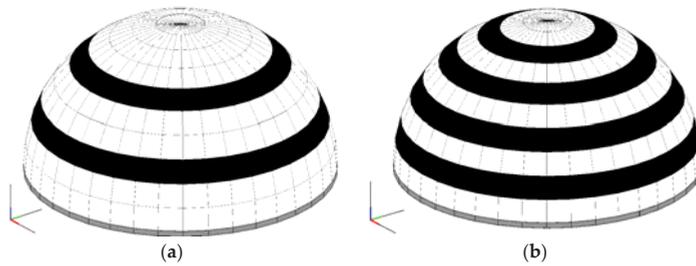
Figure 15. Typologies of reinforcing: (**a**) soft and (**b**) strong retrofitting.

Again, the results are reported in terms of collapse mechanisms (Figure 16), and pushover curves, considering the same three monitored displacements of the unreinforced configuration (Figure 17). As expected, increasing resistances are obtained with both the softly and strongly reinforced models with respect to the unreinforced configuration. In both cases the three monitored nodes show closer displacements to each other. Nevertheless, only in the post peak branches the lowest of the monitored nodes have larger displacements than the other two. The latter aspect is due to the confinement effect of the FRP strips, as demonstrated also by the damage distribution at the collapse, which show how plastic strains develop only along the unreinforced parts of the meridians. The failure mechanism of both reinforced models are characterized by a spread damage at the base section of the dome, below the first FRP strip. In the model reinforced by two strips (soft reinforcing), the damage propagates along the entire height of the dome involving a limited radial portion (Figure 16a). A different failure mode is observed for the model reinforced by four FRP strips (strong reinforcing): in this case the damage propagates above the lowest strip involving a large portion of the dome, the damage doesn't propagate at the top of the dome (Figure 16b).


(**a**)

(**b**)
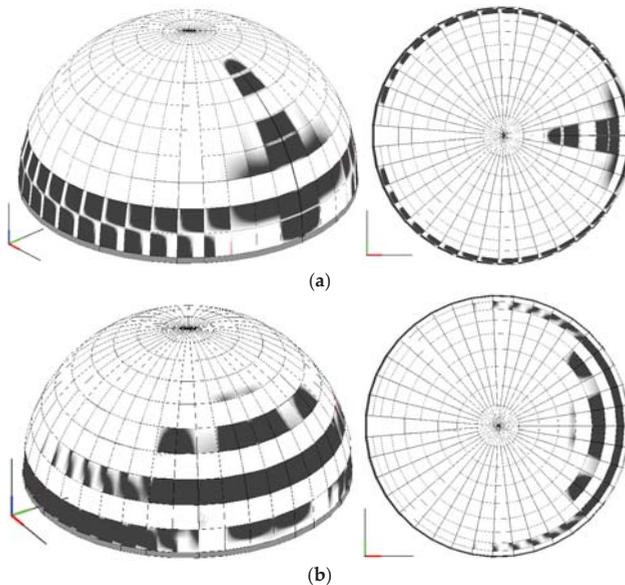
Figure 16. Failure mechanisms of the reinforced models: dome with (**a**) soft; and (**b**) strong reinforcement.
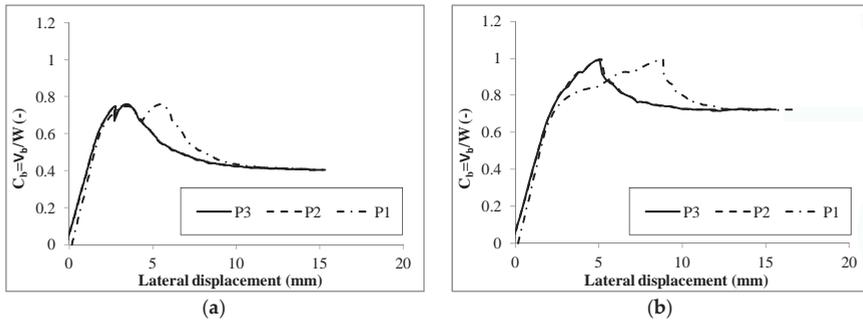
Figure 17. Capacity curves of the reinforced models: (**a**) soft and (**b**) strong retrofitting.

The comparison in terms of pushover curves between the unreinforced configuration and the two retrofitted domes, as reported in Figure 18, considering as monitored displacement P_1, shows the effectiveness of the FRP retrofitting technique, which leads to a significant improvement in terms of resistance without implying any global stiffness alteration, thus guaranteeing that no significant change of the seismic demand for the structure occurs. On the other hand, the presence of FRP strips, not only increases the peak load of the arch, but significantly delays the loss of resistance in the post-peak branch (from around 2.5 mm for the unreinforced dome, to around 10 mm for the case of the strongly retrofitted dome), thus guaranteeing to the dome a larger ductility as well. In Table 5 the ultimate lateral resistance ($C_{b,max}$) and the percentages of strength increment (ΔC_b) are reported, highlighting the enhancement associated to the FRP reinforcement application. The softly retrofitted model presents a residual lateral strength close to that relative to the unreinforced model, whereas the strongly retrofitted model presents a higher value of residual resistance due to a larger spreading of the damage at the ultimate condition, as shown in Figure 18.

It is worth to point out that the numerical investigation reported in this section considers only the load scenario corresponding to a horizontal force distribution proportional to the masses, representative of seismic condition. Nevertheless, structures can be subjected to very different load scenarios (e.g., static conditions, concentrated loads). Further investigations to assess the effectiveness of FRP strengthening technique, under different seismic loads distributions (e.g., proportional to the eigenmodes) or static loads should be investigated in further studies.
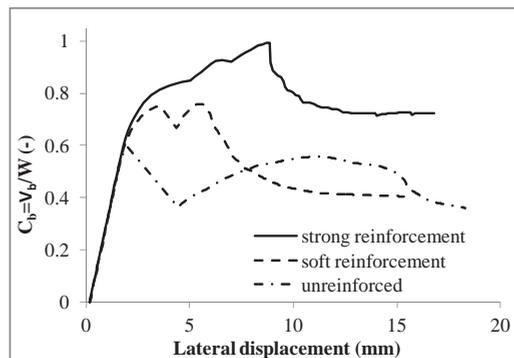
Figure 18. Comparison of the capacity curves of the unreinforced and reinforced models.

Table 5. Ultimate strength of the domes.

Model	$C_{b,max}$ (-)	ΔC_b (%)
Unreinforced	0.60	-
Softly retrofitted	0.75	25
Strongly retrofitted	1.00	67

5. Conclusions

A comprehensive discrete element strategy to simulate the nonlinear behaviour of existing masonry structures is employed here. The adopted model, based on a simple but effective mechanical scheme, was initially conceived for the nonlinear simulation of the in-plane behaviour of the masonry panels, and then upgraded to account for the out-of-plane behaviour and for the presence of curved elements (such as arches and vaults). More recently, the same modelling strategy has been extended with a new discrete element to model FRP strips, able to interact with a masonry support. In this paper, the numerical results obtained with this strategy are shown, aiming at demonstrating its capability to grasp the pre- and post-retrofitting capacities in seismic conditions. The approach has been first validated with a comparison with the results obtained in the nonlinear static context on a unreinforced masonry arch; then, the benefits provided by traditional and innovative retrofitting techniques (namely insertion of tie rods and application of FRP strips) are assessed and discussed. Significant vault typologies with a scheme of both single and double curvature masonry structures are considered. The results relative to the arches are validated by the comparison with analytical results, as obtained through the limit analysis approach in order to demonstrate the effectiveness of the proposed approach to grasp the ultimate behaviour of the reinforced masonry cross sections (activation of the plastic hinges), and the changing of the global collapse of the structure. The proposed approach, being based on a model in which masonry and FRP strips are modelled with separate elements interacting with each other by means of discrete interfaces, is able to clearly identify the actual failure mode of the structure. The seismic load scenario, which, in spite of its high risk is not very debated in the academic literature, is here investigated, and the effectiveness of widely adopted FRP reinforcement arrangements are assessed and discussed. In spite of the relevance of the achieved results, in the future further investigations will be needed to assess different retrofitting techniques, also considering other load scenarios and structural typologies. In addition, with regard to the application of FRP reinforcements, different disposals of the strips have to be investigated with the aim of providing useful guidelines for the optimal retrofitting design.

Author Contributions: B.P. and F.C. conceived the investigation strategy; B.P., C.C. and F.C. developed and calibrated the numerical models, analysed the results and wrote the paper; I.C., S.C and P.B.L. supervised the research, approved the outcome of the numerical investigations and revised the paper.

References

1. Huerta, S. Structural Design in the Work of Gaudi. *J. Archit. Sci. Rev.* **2006**, *49*, 324–339. [CrossRef]
2. Foti, D.; De Tommasi, D. An Innovative Modular System for the Building of Timber Cylindrical Roofs. *Int. J. Mech.* **2013**, *7*, 226–233.
3. Fabbrocino, F.; Farina, I.; Berardi, V.P.; Ferreira, A.J.M.; Fraternali, F. On the thrust surface of unreinforced and FRP-/FRCM-reinforced masonry domes. *Compos. Part B Eng.* **2013**, *83*, 297–305. [CrossRef]
4. Carpentieri, G.; Modano, M.; Fabbrocino, F.; Feo, L.; Fraternali, F. On the minimal mass reinforcement of masonry structures with arbitrary shapes. *Meccanica* **2017**, *1*, 1561–1576. [CrossRef]
5. Fraternali, F.; Carpentieri, G.; Modano, M.; Fabbrocino, F.; Skelton, R.E. A tensegrity approach to the optimal reinforcement of masonry domes and vaults through fiber-reinforced composite materials. *Compos. Struct.* **2015**, *134*, 247–254. [CrossRef]

6. Foti, D. On the numerical and experimental strengthening assessment of tufa masonry with FRP. *Mech. Adv. Mater. Struct.* **2013**, *20*, 163–175. [CrossRef]

7. Capozucca, R. Experimental FRP/SRP-historic masonry delamination. *Compos. Struct.* **2010**, *92*, 891–903. [CrossRef]

8. Valluzzi, M.R.; Oliveira, D.V.; Caratelli, A.; Castori, G.; Corradi, M.; De Felice, G.; Garbin, E.; Garcia, D.; Garmendia, L.; Grande, E.; et al. Round Robin Test for composite-to-brick shear bond characterization. *Mater. Struct.* **2012**, *45*, 1761–1791. [CrossRef]

9. Napoli, A.; de Felice, G.; De Santis, S.; Realfonzo, R. Bond behaviour of Steel Reinforced Polymer strengthening systems. *Compos. Struct.* **2016**, *152*, 499–515. [CrossRef]

10. Bertolesi, E.; Fabbrocino, F.; Formisano, A.; Grande, E.; Milani, G. FRP-Strengthening of Curved Masonry Structures: Local Bond Behavior and Global Response. In Proceedings of the Mechanics of Masonry Structures Strengthened with Composite Materials (MURICO5), Bologna, Italy, 28–30 June 2017.

11. Malena, M.; de Felice, G. Debonding of composites on a curved masonry substrate: Experimental results and analytical formulation. *Compos. Struct.* **2014**, *112*, 194–206. [CrossRef]

12. Caliò, I.; Marletta, M.; Pantò, B. A new discrete element model for the evaluation of the seismic behaviour of unreinforced masonry buildings. *Eng. Struct.* **2012**, *40*, 327–338. [CrossRef]

13. Marques, R.; Lourenço, P.B. Possibilities and comparison of structural component models for the seismic assessment of modern unreinforced masonry buildings. *Comput. Struct.* **2011**, *89*, 2079–2091. [CrossRef]

14. Caliò, I.; Pantò, B. A macro-element modelling approach of Infilled Frame Structures. *Comput. Struct.* **2014**, *143*, 91–107. [CrossRef]

15. Caliò, I.; Cannizzaro, F.; D'Amore, E.; Marletta, M.; Pantò, B. A new discrete-element approach for the assessment of the seismic resistance of composite reinforced concrete-masonry buildings. *Proc. AIP Am. Inst. Phys.* **2008**, *1020*, 832–839.

16. Caddemi, S.; Caliò, I.; Cannizzaro, F.; Pantò, B. A new computational strategy for the seismic assessment of infilled frame structures. In Proceedings of the 2013 Civil-Comp Proceedings, Sardinia, Italy, 3–6 September 2013.

17. Pantò, B.; Cannizzaro, F.; Caliò, I.; Lourenço, P.B. Numerical and experimental validation of a 3D macro-model for the in-plane and out-of-plane behaviour of unreinforced masonry walls. *Int. J. Archit. Herit.* **2017**, 1–19. [CrossRef]

18. Pantò, B. La Modellazione Sismica Degli Edifici in Muratura. Un Approccio Innovativo Basato su un Macro-Elemento spaziale. Ph.D. Thesis, University of Catania, Catania, Italy, April 2007.

19. Caliò, I.; Cannizzaro, F.; Marletta, M. A discrete element for modeling masonry vaults. *Adv. Mater. Res.* **2010**, *133–134*, 447–452. [CrossRef]

20. Caddemi, S.; Caliò, I.; Cannizzaro, F.; Pantò, B. The Seismic Assessment of Historical Masonry Structures. In Proceedings of the 12th International Conference on Computational Structures Technology, Naples, Italy, 2–5 September 2014.

21. Cannizzaro, F. Un Nuovo Approccio di Modellazione Della Risposta Sismica di Edifici Storici. Ph.D. Thesis, University of Catania, Catania, Italy, April 2011.

22. Caddemi, S.; Caliò, I.; Cannizzaro, F.; Lourenço, P.B.; Pantò, B. FRP-reinforced masonry structures: Numerical modelling by means of a new discrete element approach. In Proceedings of the 6th International Conference on Computational Methods in Structural Dynamics and Earthquake Engineering, Rhodes Island, Greece, 15–17 June 2017.

23. Cannizzaro, F.; Lourenço, P.B. Simulation of Shake Table Tests on Out-of-Plane Masonry Buildings. Part (VI): Discrete Element Approach. *Int. J. Archit. Herit.* **2017**, *11*, 125–142. [CrossRef]

24. Pantò, B.; Cannizzaro, F.; Caddemi, S.; Caliò, I. 3D macro-element modelling approach for seismic assessment of historical masonry churches. *Adv. Eng. Softw.* **2016**, *97*, 40–59. [CrossRef]

25. Chácara, C.; Lourenço, P.B.; Pantò, B.; Cannizzaro, F.; Caliò, I. Parametric numerical studies on the dynamic response of unreinforced masonry structures. In *2016 Structural Analysis of Historical Constructions: Anamnesis, Diagnosis, Therapy, Controls: Proceedings of the 10th International Conference on Structural Analysis of Historical Constructions (SAHC, Leuven, Belgium, 13–15 September 2016)*; CRC Press: Boca Raton, FL, USA, 2016; pp. 239–245.

26. Alecci, V.; Focacci, F.; Rovero, L.; Stipo, G.; De Stefano, M. Extrados strengthening of brick masonry arches with PBO–FRCM composites: Experimental and analytical investigations. *Compos. Struct.* **2016**, *149*, 184–196. [CrossRef]

27. Basilio, I. Strenghtening of Arched Masonry Structures with Composite Materials. Ph.D. Thesis, University of Minho, Guimares, Portugal, July 2007.

28. Caddemi, S.; Caliò, I.; Cannizzaro, F.; Occhipinti, G.; Pantò, B. A parsimonious discrete model for the seismic assessment of monumental structures. In *2015 Civil-Comp Proceedings*; Civil-Comp Press: Stirlingshire, UK, 2015.

Multi-Directional Seismic Assessment of Historical Masonry Buildings by Means of Macro-Element Modelling: Application to a Building Damaged during the L'Aquila Earthquake (Italy)

Francesco Cannizzaro [1,*] , **Bartolomeo Pantò** [1] **, Marco Lepidi** [2] **, Salvatore Caddemi** [1] and **Ivo Caliò** [1]

1   Department of Civil Engineering and Architecture, University of Catania, 95125 Catania, Italy; bpanto@dica.unict.it (B.P.); scaddemi@dica.unict.it (S.C.); icalio@dica.unict.it (I.C.)
2   Department of Civil Chemical and Environmental Engineering, University of Genoa, 16145 Genoa, Italy; marco.lepidi@unige.it
*   Correspondence: francesco.cannizzaro@dica.unict.it; Tel.: +39-095-738-2275

Abstract: The experience of the recent earthquakes in Italy caused a shocking impact in terms of loss of human life and damage in buildings. In particular, when it comes to ancient constructions, their cultural and historical value overlaps with the economic and social one. Among the historical structures, churches have been the object of several studies which identified the main characteristics of the seismic response and the most probable collapse mechanisms. More rarely, academic studies have been devoted to ancient palaces, since they often exhibit irregular and complicated arrangement of the resisting elements, which makes their response very difficult to predict. In this paper, a palace located in L'Aquila, severely damaged by the seismic event of 2009 is the object of an accurate study. A historical reconstruction of the past strengthening interventions as well as a detailed geometric relief is performed to implement detailed numerical models of the structure. Both global and local models are considered and static nonlinear analyses are performed considering the influence of the input direction on the seismic vulnerability of the building. The damage pattern predicted by the numerical models is compared with that observed after the earthquake. The seismic vulnerability assessments are performed in terms of ultimate peak ground acceleration (PGA) using capacity curves and the Italian code spectrum. The results are compared in terms of ultimate ductility demand evaluated performing nonlinear dynamic analyses considering the actual registered seismic input of L'Aquila earthquake.

Keywords: macro-model approach; monumental masonry structures; L'Aquila earthquake; historical structural analyses; seismic assessment; cultural heritage protection; irregular structures; 3DMacro software; HiStrA software

1. Introduction

In the last ten years, three destructive earthquakes struck Italy causing severe damage to the cultural heritage of the country. The experiences of L'Aquila (2009), Emilia (2012) and, more recently, Amatrice (2016) demonstrated the vulnerability of the buildings to possible seismic events. In particular, historical constructions cannot be considered as modern structures, since their preservation is crucial to maintain the tourism potential of many sites and to preserve the conservation of the historical memories of communities.

The mentioned seismic events gave a strong impulse towards the understanding and the interpretation of the seismic response of structures with reference to different structural typologies [1–3],

especially if exposed to high seismic hazards or unfavourable soil properties [4]. In particular, a large effort was devoted to the analysis of masonry monumental structures, such as churches [5–9]. However, more rarely, studies were devoted to historical palaces [10–17], which are characterized by a wider spectrum of different typologies and peculiarities, and the large part of these studies is based on the observation on the field of the effects of the earthquakes without a complete numerical counterpart.

With respect to churches, which usually kept the original configuration during the centuries, ancient palaces are often characterized by structural changes made during their life mainly due to functional needs. The latter aspect implies a more difficult interpretation and prediction of the structural response. A further difference with respect to churches and other ancient structures [17] is related to the out-of-plane behaviour of the walls, which usually involves a large part of the building in the case of churches, whereas it is often a local collapse mechanism in the case of palaces.

In this paper, the case of Palazzo Gualtieri is investigated. The building was the object of a preliminary study [18] in the immediate aftermath of the main shock within a larger campaign of investigation of several buildings of the city of L'Aquila. In this paper, a historical and architectural description of the building is provided and a survey of the past strengthening interventions is reported to facilitate the understanding of the main structural features of the building.

Then, taking advantage of some numerical models previously proposed by the authors, a deep numerical investigation on the building was performed. In particular, the adoption of a numerical simplified model proposed for unreinforced masonry structures (URM) [19] and in-filled frame structures (IFS) [20–22], which was implemented in a dedicated software environment allowed implementing a global numerical model of the building on which nonlinear static analyses were performed considering the influence of the direction of the input. Such an approach was also compared in the literature with other numerical strategies on definite structural typologies, such as URM buildings [23] and slender towers [24], showing its reliability with reference to different buildings typologies and it also appeared suitable in the case of ancient masonry palaces. In the numerical applications reported here, the interaction between the in-plane and out-of-plane responses is not considered in the simulations, thus limiting the computational demand. The latter choice was taken in consideration of the fact that the connection of the walls with the slabs and the orthogonal walls appeared solid, and the out-of-plane collapses can be considered in this case as local mechanisms, to be investigated by means of more detailed models of limited portions of structure.

Since the building was subjected to a localized partial collapse of secondary elements (a frescoed mirror vault located in one of the two main halls of the palace), an additional detailed local model of the room was implemented considering a more advanced model accounting for the out-of-plane masonry behaviour [25,26], also in the presence of curved elements [27,28].

The results of both the global and the local models were compared in terms of collapse mechanism with the damage pattern observed in the field. In particular, the detailed local numerical model allowed justifying the partial collapse of the frescoed vault. Finally, a vulnerability assessment of the building in terms of peak ground acceleration (PGA) was performed according to the Eurocode 8 [29,30], as already done with reference to reinforced concrete masonry infilled frames [31]. The procedure was compared with an alternative vulnerability assessment based on nonlinear dynamic analyses conducted on equivalent single degree of freedom systems. Due to the high irregularity of the building an investigation of the direction of the input allowed identifying the main weaknesses of the structure.

The proposed case study not only is a significant example of interpretation of the seismic response of ancient palaces, but the combined use of global simplified and local refined models may represent a more general methodological approach to be pursued in similar circumstances.

2. The Case Study: The Gualtieri Building in L'Aquila

2.1. Historical and Architectural Description

The ancient building presently known as Palazzo Gualtieri (also referred to as Palazzo Ximenes-Bonomo), formerly Palazzo Alfieri (then Alfieri-Ossorio), is located in the inner core of the

historical centre of L'Aquila, dating back to the Middle Ages. The main façade of the building forms the southern front of Piazza Santa Giusta, an L-shaped public square named after the Romanesque Church of Santa Giusta, free-standing in the north-eastern corner. Palazzo Gualtieri is embedded in a rich context of stately historical architectures, including also Palazzo Centi (western front) and Palazzo Dragonetti (northern front). The main part of the building, denoted as "principal body" in the following, is free-standing on the front, right and back sides, while the left side, facing the so-called Via dei Francesi is partially connected with the coeval adjacent building, characterized by strongly similar structural features and denoted as "secondary body" in Figure 1, where the main part is contoured in blue and the secondary body in red. The structural connection bridging the two buildings, hosting two small rooms at the first and second level, is sustained by a masonry arch, which covers the passageway known as Arco dei Francesi.

(**a**)

(**b**)
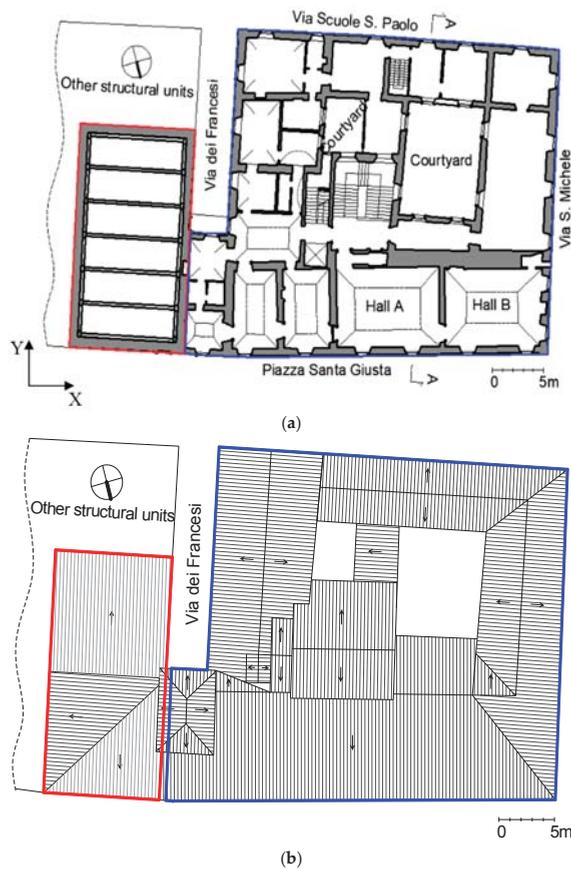
Figure 1. Plans: (**a**) of the first level; and (**b**) of the roof, with indication of the main body of the building (contoured in blue) and of the secondary reinforced concrete body (contoured in red). Reproduced with permission from [18].

The building, presently holding different private apartments for residential use, is traced by local historical tradition to the fifteenth century [32]. However, the architectural elements that, in the absence of more reliable documents, allow an approximate dating, that is, window frames and doorways, tend to delay the construction date to the late sixteenth century. The internal courtyard can be dated

back to the mid-seventeenth century with sufficient confidence, while minor constructional aspects recall late-Renaissance standards. The two monumental lateral fronts, in particular, are strongly featured by a valuable severe regularity, not tormented by the openings of convenience which have altered the original formal order of the principal façade over the years. In any case, the building—in its original layout—is certainly more ancient than it presently appears due to the architectural additions from the sixteenth and seventeenth centuries. The major historical and architectural value can be undoubtedly attributed to the courtyard. Even if not well-maintained, its original, elegant configuration is still correctly recognizable, and some of the original resistant elements can be clearly identified. Indeed, a regular sequence of thick columns, sustaining round arches, is revealed by decorative lesenes, despite the arcades originally surrounding the court are presently infilled.

2.2. Past Strengthening Interventions of Structural Retrofitting

In the early 1990s, the building was interested by an important strengthening intervention of structural retrofitting. However, the ownership fragmentation, together with the recurrent time delay and progressive downsizing of the original plan of structural interventions, caused by continuous reductions of the available financial resources, did not allow an integrated, organic design oriented to the general improvement of the global structural behaviour.

Nonetheless, numerous local interventions allowed the technical solution of the most evident and critical issues, mainly related to, first, the low quality of the rubble masonry, made of an irregular stonework and poor mortar, and, second, deficient connections among orthogonal walls. To this end, large portions of cracked or deteriorated masonry were consolidated with the traditional indenting procedure, many masonry panels were individually strengthened through the jacketing technique, by employing diffuse shotcrete and light steel net reinforcements, while several pairs of weakly-connected orthogonal walls were pinned together with diagonal steel fastening bars. The intervention was drafted according to the recommendations of the Italian national codes in force at the design time [33]. Owing to the historical and architectural importance of the building, the intervention design had to be submitted for preliminary approval to the competent authorities of the Regional board of the Ministry of Cultural Heritage and Environmental Conservation.

In the principal body (Figure 1), the intervention included local demolitions of the masonry walls for the realization of a modern lift shaft (Figure 2a). In particular, a couple of load-bearing walls, adjacent to the ancient staircase, was partially hollowed to host a reinforced concrete box structure. To recover the structural redundancy and simultaneously improve the concrete-masonry cooperation, the new and old structural elements were anchored to each other by means of several stainless steel pins, inserted into holes drilled through the masonry and finally injected with cement grout. To comply with the modified requirements of the new functional distribution, a second staircase was built, with direct access from the courtyard. The reinforced concrete structure sustaining the stairs was built in adjacency to a pair of existing masonry walls (Figure 2a), and properly connected to them through steel fastening pins. Together with these structural modifications, the remaining intervention were driven by the leading idea of improving, as much as possible, the global behaviour of the entire building and all its box-parts. To this purpose, a number of critical issues had to be solved, the most important being a marked loss of verticality of the principal façade, easily recognizable as an out-of-plane deformation of the masonry wall, characterized by an outward arch-shape between the ground and the roof. From a structural viewpoint, this crucial problem was certainly caused by a questionable, non documented, past intervention, during which the original second-level vaulted floor was completely removed to double the internal height of two noble halls at the first level. The consequent absence of any horizontal element able to offer a suitable out-of-plane stiffness was exposing the masonry wall to serious risks of overturning. The pre-existence of the problem is also testified by the consequent adoption of different palliative countermeasures over the years, including the addition of abutments and the thickening of the wall base. To mitigate the problem without heavy functional interferences, a light planar frame was realized in adjacency, and then strongly connected to the external face of the masonry wall (Figure 2b).

Thin steel profiles were employed to hide the entire frame in the thickness of the plaster exterior finish. The wall-frame system was finally anchored to the central spine wall of the building by several steel rods (Figure 2c). The poor quality of the rubble masonry, made of irregular calcareous stones with weak adhesive bond, has been extensively treated using non-shrink cement grout injections at low pressure. Although recognized as highly vulnerable, the vaults covering the two noble halls were not object of intervention, due to limited financial resources. A complete overhaul of the roof structures suggested to maintain the existing structural scheme, made of traditional wooden trusses. Several steel ties were added to collaborate with the tensioned rods. A light reinforced concrete ring-beam was realized at the top of the masonry wall to the purpose of anchoring the steel ties (Figure 2d,e). After careful revision, the large majority of the timbers was maintained in service, with only minor substitutions. The wooden slab sustaining the gable roof was instead entirely replaced, due to its advanced state of deterioration. During the works, an undocumented underground passageway was discovered, running from the building basement toward the Church.

In the secondary body, the structural intervention was generally heavier and affected all the floor levels. In particular, it included the addiction of a new underground level, which required the ground excavation and was founded on a new thick grid of reinforced concrete foundation beams. Reinforced concrete retaining walls were also designed to support the lateral pressure of soil. These retaining walls were orthogonally stiffened by shear walls, and a concrete slab was realized to ensure the structural redundancy. This stiff structural scheme served also as foundation of a self-sustaining three-dimensional reinforced concrete frame, raising up to the roof level, realized in strict adherence to the existing load-bearing masonry walls, and rigidly anchored to them through a system of fastening steel pins at each level. All the columns were abutted to the internal face of the existing masonry walls, and then connected to each other by flat beams at each level, running horizontally at the same height of the keystones of the vaulted floors. At the first level, the barrel vault was consolidated through a typical saddling intervention, consisting in, first, removing of the heavy but incoherent material constituting the original backfill, second, casting a thin curved concrete slab (saddle slab), reinforced by a steel mesh pinned to the vault extrados, third, replacement of the original backfill with light expanded clay aggregate and, finally, covering with a horizontal reinforced concrete slab at the floor level (Figure 2f). At higher levels, some arched and vaulted structures, without significant architectural value, were evaluated as too seismically vulnerable and demolished. The excessive vulnerability was motivated by the evident vertical misalignment of the load-bearing masonry walls, with some arch abutments erected over the vaults of the first floors. Moreover, at the second and third levels, the horizontal thrust forces at the arch and vault springs were poorly confined. Therefore, the vaults were completely substituted with concrete slabs, while the original vaulted shape was formally reconstructed by a plasterboard false ceiling. A ring beam was added at the top of the masonry walls, with the twofold aim of ensuring the structural box behaviour and supporting the new reinforced concrete roof structure. The building has a mean height of about 14 m and is characterized by an almost rectangular plan, with side lengths of about 36 m and 28 m, respectively. The courtyard, which is also approximately rectangular, has side lengths of about 7.5 m and 10 m. A detailed geometric survey is reported in [18].

During the inspections in the aftermath of the seismic main shock, a direct geometric relief of the building has been done, thus allowing the graphic restitutions of plans, prospects and sections, as well as the crack pattern for each prospect, and the most damaged room [18].

Detailed graphical reconstructions of the northern and western prospects after the main shock are reported in [18], with the corresponding crack patterns; in Figure 1 the plan of the first level and of the roof are reported. Since it was not possible to get access to all the private flats, in case of lack of data, the plans have been reported based on the acquired documents. In Figure 3, the transversal section A-A is reported, and the vaults and structure typologies of the roof are highlighted.
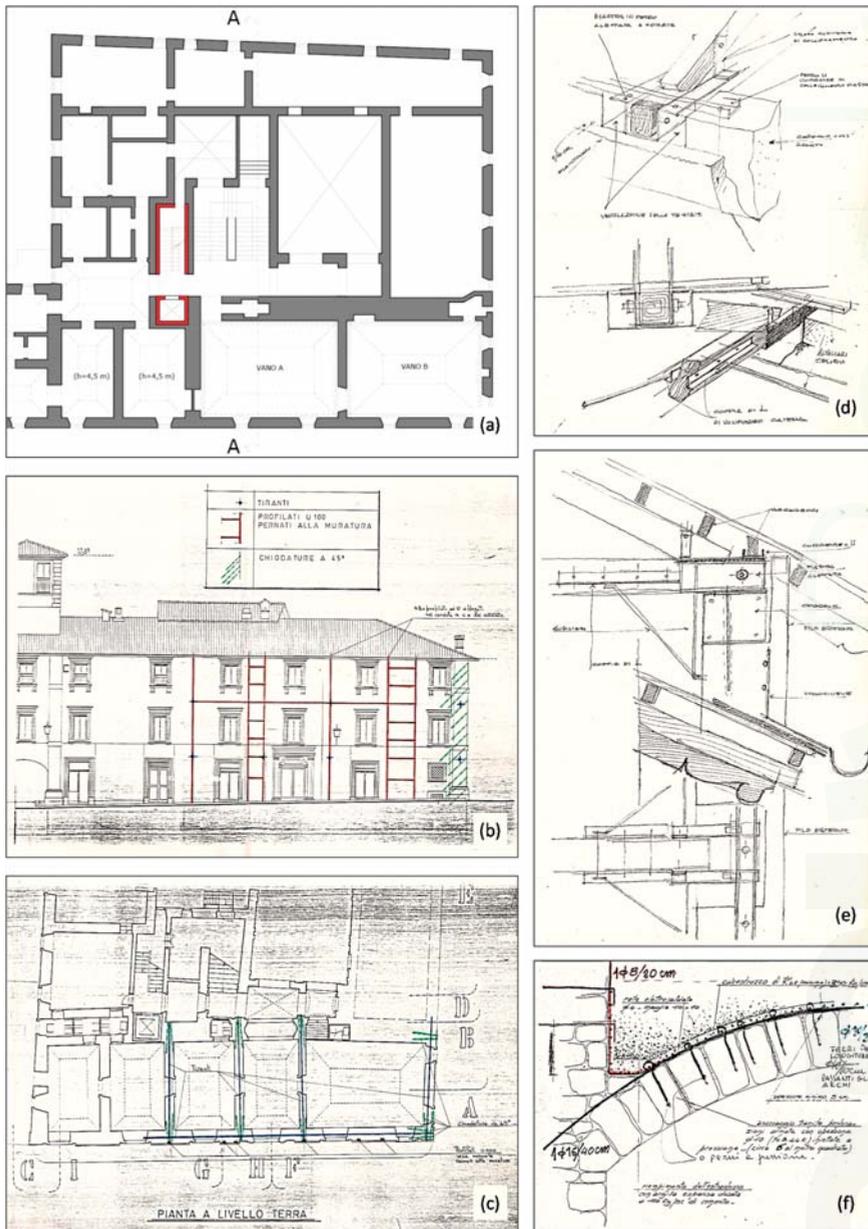
Figure 2. Past strengthening interventions of structural retrofitting (graphical reconstruction and original working drawings): (**a**) reinforced concrete walls and box structure (red) supporting the new staircase and the lift shaft; (**b**) light steel frame (red) built in adjacency to the main building façade; (**c**) steel rods (blue) connecting the light steel frame to the central spine wall and fastening bars (green) connecting some orthogonal walls; (**d**) technical details of the reinforced concrete ring beam; (**e**) technical details of the reinforced steel connections between the reinforced concrete ring beam and the wooden trusses supporting the roof; and (**f**) technical details of the saddling intervention consolidating the barrel vaults.
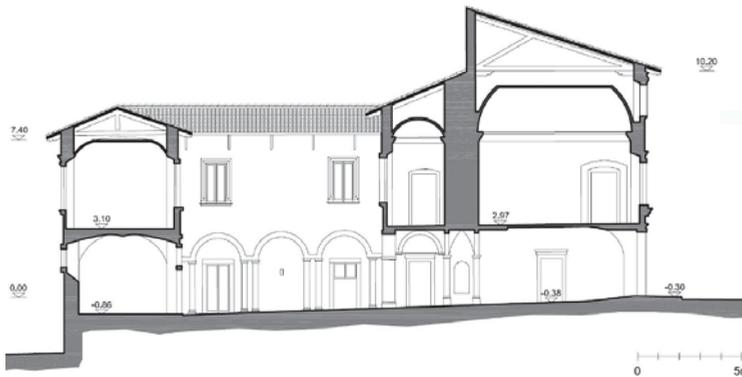
Figure 3. Transversal section (A-A in Figure 1) of the building. Reproduced with permission from [18].

With reference to the large hall at the second level (here called hall B), a high concentration of damage has been observed, both in the perimeter walls, and above all in the surmounting vault, which has partially collapsed (Figure 4). The collapse of the vault represents the main damage of the building, above all for the artistic quality of its frescoes. The wall on S. Michele Street shows severe damage and partial collapse of the masonry medium as well as the loss of the perfect verticality close to the passage of the flue. This hall has been object of specific numerical simulations, the results of which will be described in the following paragraphs.
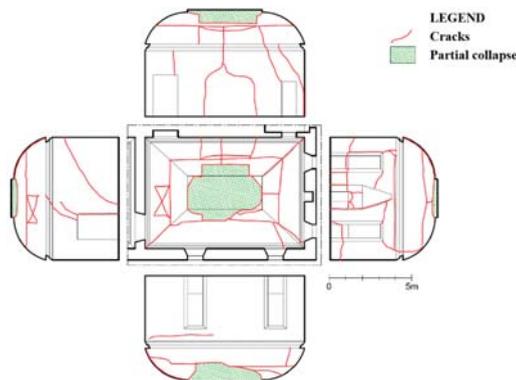

Figure 4. Crack pattern of damaged hall B. Reproduced with permission from [18].

Concerning the masonry media, a visual investigation has lead to the observation of the following characteristics:

- plastered masonry on the northern and western prospects, and on Via dei Francesi, made of calcareous ashlars with some bricks; on the southern front two different masonry typologies with visible leaf can be observed: the first is partially plastered and made of irregular calcareous ashlars, while the second has also some levelings with bricks (Figure 5);
- corner with ashlars (visible and not perfectly smoothed), with lime mortar (Figure 5);
- widest doors at the first level are surmounted by monolithic lintels, the smallest ones and the windows of the upper levels are surmounted by lintels made of several ashlars and brick arches (Figure 5); and

-   vaults of the two halls A and B are made of bricks ordered according to a knife arrangement, with some wooden ribs.

**Figure 5.** Some details of the masonry typologies. Reproduced with permission from [18].

3. The Numerical Modelling Approach

In the following sections, the nonlinear behaviour of the building, until the conventional collapse, is assessed by performing static push-over analyses. To this aim, an innovative discrete element, introduced by Caliò et al. [19], is used. This model, in the original formulation, was conceived for the simulation of the nonlinear in-plane behaviour of unreinforced masonry walls suitable for building with "box behaviour" and then upgraded for modelling infilled frame structures [20–23] and monumental masonry buildings [25–28] in which a complex interaction between in-plane and out-of-plane behaviour is observed.

3.1. The In-Plane Macro Model

The in-plane macro model [19] is characterised by a simple mechanical scheme (Figure 6), constituted by an articulated quadrilateral with rigid edges connected by four hinges and two nonlinear diagonal nonlinear links (NLinks). Each side of the quadrilateral can interact with other elements or supports by means of a discrete distribution of the NLinks, denoted as interface. More in detail, each interface is constituted by *n* orthogonal NLinks, and an additional longitudinal NLink, parallel to the panel edge.

Despite its great simplicity, such a basic mechanical scheme is able to simulate the main in-plane failures of a portion of the masonry wall subjected to in-plane horizontal and vertical loads. These well-known collapse mechanisms, namely the flexural failure, the diagonal shear failure and sliding shear failure, are approximately represented in Figure 7, where the typical crack patterns, together with the qualitative kinematics of the masonry portion, are also sketched. Figure 8 shows how the proposed macro-element allows a simple and realistic mechanical simulation of the corresponding failure mechanisms of a masonry wall in its own plane.
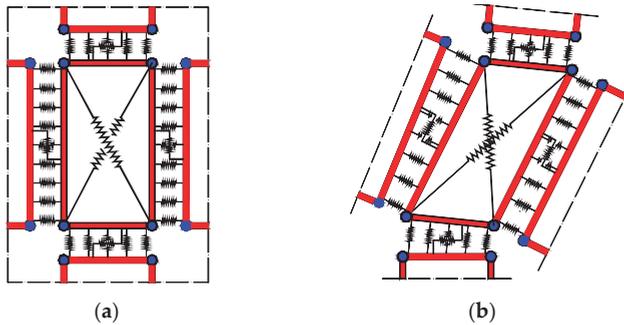
Figure 6. The basic macro-element for the masonry infill: (**a**) undeformed configuration; and (**b**) deformed configuration.
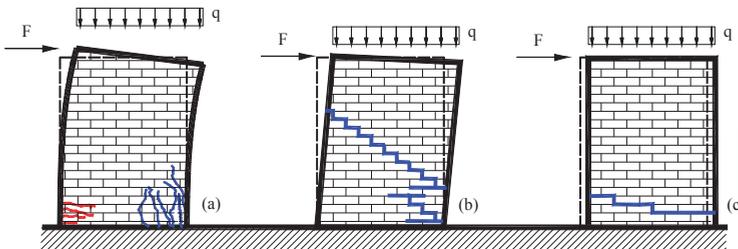
Figure 7. Main in-plane masonry failure mechanisms: (**a**) flexural; (**b**) shear-diagonal; and (**c**) shear-sliding.
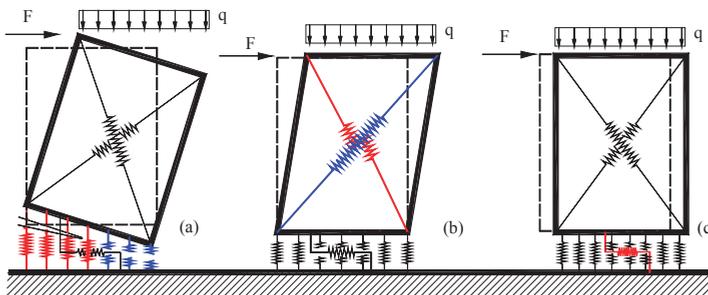


Figure 8. Simulation of a masonry portion collapse mechanisms by means of the macro-element of the in-plane mechanisms: (**a**) flexural; (**b**) shear-diagonal; and (**c**) shear sliding.

Each discrete element is endowed with three degrees of freedom, associated to the in-plane rigid-body motion, and a further degree of freedom, needed for the description of the shear deformability. The deformations of the interfaces are associated to the relative motion between adjacent panels, therefore no further Lagrangian parameter has to be introduced in order to describe their kinematics. Figure 9 shows how a simple masonry wall can be modelled by means of the proposed modelling approach.

The effectiveness of the simulation of the nonlinear behaviour relies on a suitable choice of the mechanical parameters of the model inferred by enforcing an equivalence between the masonry media and a reference continuous model characterised by simple but reliable constitutive laws. This equivalence is based on a straightforward fibre calibration procedure, and is based only on the

main mechanical parameters that characterise the masonry according to an orthotropic homogeneous medium [19]. It is worth noting that each macro-element inherits the plane geometric properties of the corresponding modelled masonry portion; consequently, different from the simplified models based on equivalent strut element approaches, the definition of an effective dimension of the element is not needed. For mixed masonry-reinforced concrete structures, beam-column lumped plasticity elements are included in the model. Frame elements interact with the adjacent masonry, along the entire contact length, by means of the interfaces.
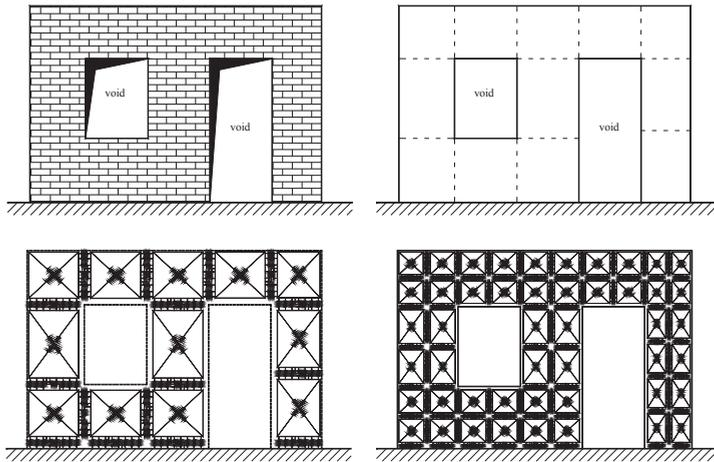

Figure 9. An example of a plane masonry wall and corresponding macro-element discretizations with different mesh resolutions.

Each element of the frame interacts with the masonry infill by means of the Nlinks distribution along the macro-element interfaces. For each interface, a general layout discretization, of *n* orthogonal and single longitudinal NLinks, has been considered. The nonlinear behaviour of the frame element is modelled by rigid-plastic hinges occurring along the beam span at different cross sections. The inelastic behaviour of the element, concentrated at the rigid-plastic hinges, is governed by the interaction of the axial force and two bending moments consistent with yielding surfaces of the concrete cross sections. Once the constitutive laws have been defined, both force and displacement controlled static processes can be performed according to the procedures currently used in finite element analyses. The model here briefly described is implemented in the dedicated software environment 3DMacro.

3.2. The Model for Curved Masonry Structures

The macro-element for curved masonry structures is an extension, to the case of shell structures, of a three-dimensional rectangular macro-element proposed for the simulation of the seismic response of masonry buildings [25] (Figure 10b), able to model the out-of-plane behaviour of masonry walls, which, in turn, is an extension of the previously described plane model (Figure 10a). The rectangular element reported in Figure 10b has been conceived to simulate the mechanical behaviour of masonry walls when subjected both to in-plane and to out-of-plane loadings. It is represented by a simple mechanical scheme consisting in a rectangular quadrilateral with rigid edges and hinged vertices connected by diagonal NLinks which simulate the in-plane shear deformability of the corresponding masonry macro-portion. The quadrilateral can interact with other elements along each rigid layer edge by means of a discrete distribution of NLinks with limited tensile strength. Each interface includes NLinks orthogonal to the rigid edges, which govern the in-plane and out-of-plane flexural behaviour of the element, and NLinks parallel to the edges able to simulate the in-plane and out-of-plane sliding

and torsional behaviour. In particular, the stiffness of these out-of-plane sliding links are calibrated according to the out-of-plane shear stiffness of the panel, their yielding dominia are associated to friction phenomena, and the relative distance is set in order to guarantee an elastic torsion equivalence with the corresponding continuum [25]. As a consequence, the ultimate strength dominium which governs the interaction between torsion and out-of-plane shear response, results linear as shown in [25]; however, more effective models with regard to torsion–shear interaction and its influence in the out-of-plane mechanisms can be found in the literature [34–36]. The kinematics of the element is governed by seven degrees of freedom able to describe both the rigid body motion and the shear deformability of the base element.

(**a**)   (**b**)   (**c**)
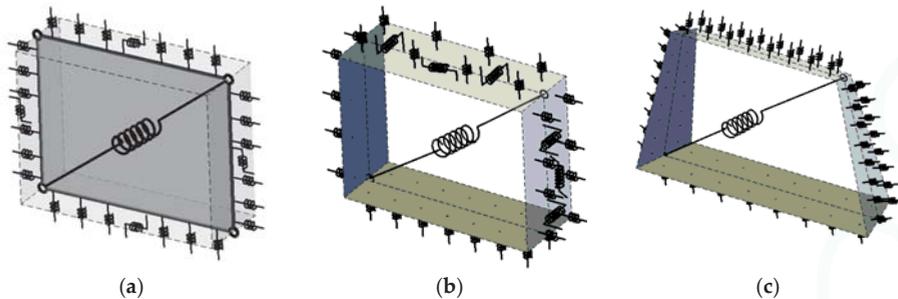
Figure 10. Layout of the macro-element at its three stages: (**a**) plane element; (**b**) spatial regular element; and (**c**) three-dimensional element for curved structures.

The discrete element conceived to model shell masonry elements [27,28,37] represents an extension of the rectangular element and is constituted by an articulated quadrilateral whose geometry is not regular in order to allow the meshing of a generic curved surface with macro-elements (Figure 10c). Each macro-element is still characterized by four rigid edges whose orientation and dimension are associated to the shape of the element and to the thickness of the portion of modelled masonry that is represented. A diagonal NLink simulates the shear deformation of the quadrilateral in its own average plane, while spatial interfaces govern the interaction with the adjacent elements or with the external supports. These interfaces are in general skew with respect to the average plane of the element, and their motions are ruled by a discrete number of NLinks. Each quadrilateral is defined by the geometric coordinates of his vertexes, the four normal unit vectors to the surface and the thicknesses in correspondence of these points.

If the geometric data and the mechanical characteristics of the masonry media are known, the properties of the equivalent macro-element, corresponding to the part of the masonry portion modelled, can be established through a fibre calibration procedure.

4. The Numerical Simulations

In order to assess the global response of the building, a three-dimensional numerical model of the entire structural complex has been developed in the software environment 3DMacro in which the 2D macro-model previously described is implemented; in Figure 11, two axonometric views of the global building are reported. In the numerical model the structural transformations and the recent seismic retrofits provided to the building have been considered. The main aim of the retrofitting interventions made in the 1990s was to prevent the major causes of collapse in masonry buildings, that is the out-of-plane failures. In particular, the insertion of the light reinforced concrete beams and of tie rods (to eliminate the thrusts of the sloping roof and of the vaults), the demolition and reconstruction of numerous slabs and the improvement of the connection of orthogonal walls, guaranteed a global box behaviour of the building, as demonstrated by the overall response exhibited during the earthquake

of 2009. For the latter reason, in the global modelling the plane model described in Section 3.1 was employed, assuming the hypothesis of box behaviour of the building. In addition, in the secondary body of the building, beyond the "Arco dei Francesi", the recent reinforced concrete frame, as well as the stiffening effect of the new slabs, have been modelled.
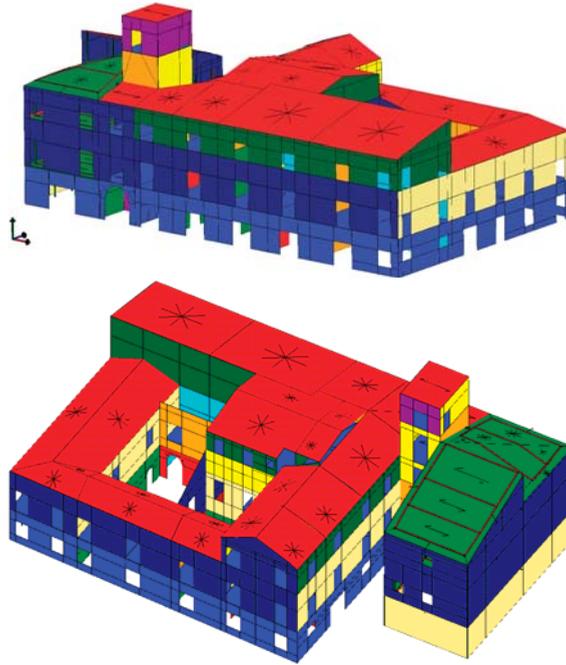
Figure 11. Computational model: axonometric views.

The building is characterized by a wide variety of masonry typologies as well as different masonry thicknesses according to the level of the walls and their age of construction. Furthermore, since the building has been growing in the last 400 years, a significant geometry complexity can be encountered. In particular, in Figure 11, the colours are associated to the thickness of the walls directly observed on the field (which ranges from 25 cm at the top of the tower to 100 cm at the first level).

Since no "ad hoc" in situ investigation has been possible to characterize the mechanical properties, they have been calculated according to the Italian Code [38], based on the masonry typologies detected during the relief. In particular the rubble masonry was considered for all the vertical elements since this masonry typology seemed to be the most appropriate and close to all the typologies present in the building. The localized interventions on the masonry walls, made in the occasion of the recent structural retrofit of the building, aimed at reinforcing the weakest parts of the structure in order to make uniform the structural strengths within the building. This reason has led the authors to consider a single set of mechanical properties for all the walls. On the other hand, the frescoed vaults of the two noble halls were not object of any structural improvement and, as demonstrated by the partial collapse of one of them, they turned out to be the most vulnerable parts of the building, involving the in-plane and out-of-plane behaviour of the masonry elements. For the detailed model of the hall, a different set of mechanical properties was assumed for the vault, since it was made of bricks; to this purpose, the relevant masonry typology of the Italian Code [38] was considered. In all the considered cases, the strengths have been divided by the confidence penalty factor indicated in [38] and associated to the lowest level of knowledge of the structure (LC1). In Table 1, the mechanical properties of both the

considered masonry typologies are reported. The mechanical properties of recent parts of the building (reinforced concrete frames) have been assigned according to the strengthening design. In particular, the concrete typology belongs to the Rck25 class, whereas the bar steels are of FeB44k type.

Table 1. Mechanical properties of the masonry adopted in the numerical model.

Masonry Typology	E (MPa)	G (MPa)	τ_0 (MPa)	σ_c (MPa)	G_c (N/mm)	σ_t (MPa)	G_t (N/mm)	w (kN/m³)
Masonry walls	690	230	0.02	1.0	0.1	0.05	0.02	19
Vault	1200	480	0.04	3.0	0.3	0.1	0.05	19

The area loads on the slabs have been calculated considering as own weight that obtained according to the slab typologies detected in situ, while the overload has been calculated according to the Italian Code [38], considering the use destination of each room. A reinforced concrete slab typology was observed, with a thickness of 20 cm (green in Figure 12 with a self weight of 2.77 kN/m²), slabs characterized by surmounting masonry vaults (blue in Figure 12 characterized by a self weight equal to 5 kN/m²) and the wooden roof (red in Figure 12, self weight equal to 5 kN/m²). The vaults are modelled according to a deformable isotropic plate whose thickness is equal to the vault thickness, and whose Young's modulus corresponds to the one adopted for the masonry vaults (that is 1200 MPa). The seismic weight of the building has been estimated in about 58.580 kN.
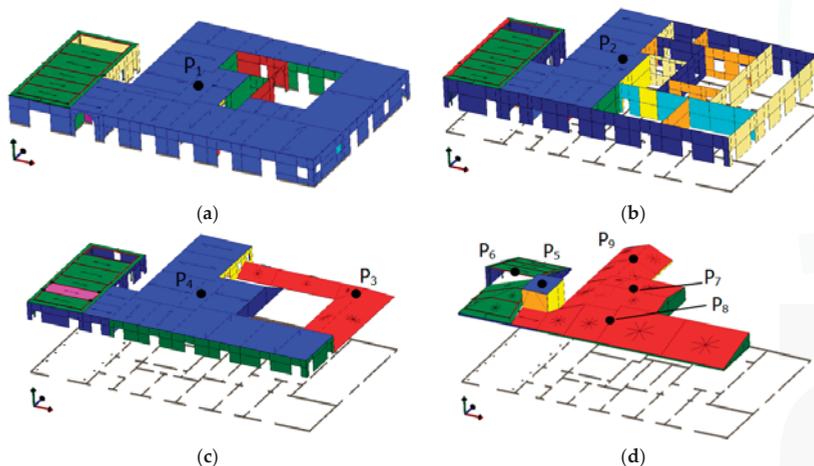
Figure 12. Control points scheme; (**a**) First level: 3.50 m; (**b**) Second level: 7.50 m; (**c**) Third level: 10.20 m; (**d**) Fourth level: 14.45 m.

To assess the seismic capacity of the building nonlinear static analyses have been considered according to a mass proportional force distribution. The structural masses and the additional masses due to the gravity loads are considered distributed in the model in the actual positions. A set of ten control points has been chosen according to Table 2, where the relevant identifiers Id are riported as well, and summarized in the scheme reported in Figure 12. The displacement of each control point is monitored during the push-over analyses.

The vulnerability assessment process has been performed according to the N2 [39] method. A mass is assigned to each control point considering a volume of influence of the structure (see Table 2); the entire structure is simplified considering a nonlinear single degree of freedom system obtained from the capacity curves and the corresponding mass distribution of the adopted control points. A further simplification is then performed, thus allowing to consider an equivalent elastic perfectly plastic system, which is calibrated according to the Italian code [38] for the vulnerability assessment.

Table 2. Control points of the building.

Id	Level (m)	Description	Mass (t)
P1	3.50	First Level	2541.9
P2	7.50	Second Level	1410.5
P3	10.20	Pitched roof	1070.9
P4		Plan floor	
P5	14.45	Tower	689.4
P6		Reinforced concrete part	
P7		Central pitched roof	
P8		Frontal pitched roof	
P9		Rearward pitched roof	
P10	17.75	Tower	31.7

The set of control points was chosen in order to be representative of the mass distribution within the building and to grasp effectively the collapse mechanisms and torsion effects that can occur during the analysis. The choice of the control points is a crucial aspect when nonlinear static analyses are employed and a simplified vulnerability assessment procedure is adopted, as done on this study. On the contrary, nonlinear dynamic analyses do not require the definition of any specific control point, but they still seem to be too numerically cumbersome for such complex structures, especially with reference to practical engineering purposes.

All floors have been considered deformable in the model according to an orthotropic elastic plate (except those corresponding to the vaults which are considered isotropic), and the corresponding mechanical properties were computed according to their actual geometry. Only the recently introduced reinforced concrete slab has been considered rigid. During the analysis, the current displacement of each control point is obtained as the average value of the displacements of all the points of the pertinent area associated to the control point (Figure 12).

4.1. Global Behaviour of the Building

Since the building is highly irregular, its actual response may be significantly influenced by the input direction. With the aim of investigating the influence of the input direction on the seismic response of the building, 12 nonlinear static analyses were performed varying the input direction according to an angular step of 30°. The orientations of the analyses are referred to the main direction of the building (x direction in Figure 13), while the direction 90° is referred to the Y direction. The conventional collapse occurs, for each analysis, with the achievement of a reduction of the base shear of the 20% with respect to the maximum base shear. The maximum base shear coefficients in the analyses range between 0.13 and 0.20, while the maximum displacements range between 5 cm and 7 cm (Figure 13).

In terms of collapse mechanisms they seem to be quite global; however, along the longitudinal direction the damage pattern at collapse mainly involves the spandrels at each level with a base rotation of the piers (which is consistent with the observed crack pattern observed in the field), while in the transversal direction the collapse occurs with the shear failure of the piers at the base level (Figure 14).

The pushover curves obtained for the different loading directions can be synthetically represented by means of the three-dimensional capacity dominium, plotted in a reference system XYZ, in which X and Y identify the two main directions of the building. In such a 3D plot (Figure 15), each push-over curve is represented along the input direction, in a plane perpendicular to the XY plane, so that the base shear coefficient (computed as global base shear divided by the weight of the building) is reported in the Z axis. Such a representation allows easily identifying the overall resistance and ductility of the building along all the investigated directions in a unified representation and it has the great advantage of favouring a quick and easy identification of the strongest and weakest directions of the

building as well as the most brittle and ductile. The level of resistance is represented in a colour scale. For those intermediate directions that have not been specifically investigated, they have been linearly interpolated. The ductility of the structure in all the investigated directions is also readable in the graph. The presence of the central hole in Figure 15 represents a measure of the fragility of the system along each load direction. In the considered applications, the origins of all the pushover curves are set at a distance equal to $1.2 \times u_{max}$, being u_{max} the maximum achieved displacement among all the performed analyses. This way, the more a certain curve approaches the centre of the hole, the highest displacement capacity the structures possesses in that direction.
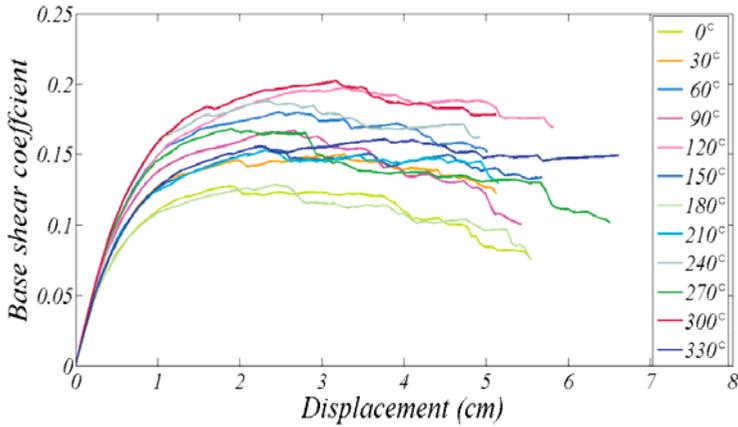
Figure 13. Capacity curves summary.

(a)

(b)
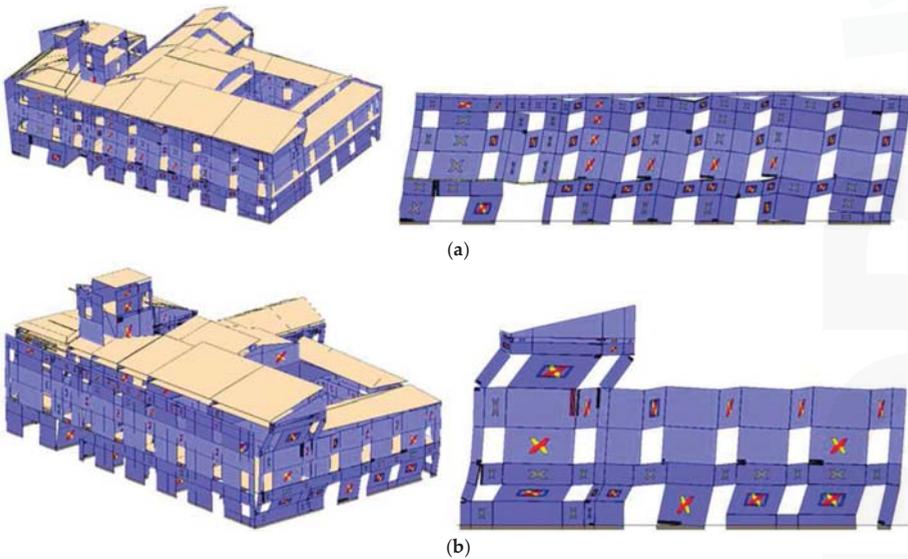
**Figure 14.** Collapse mechanisms: (**a**) longitudinal; and (**b**) transversal directions.
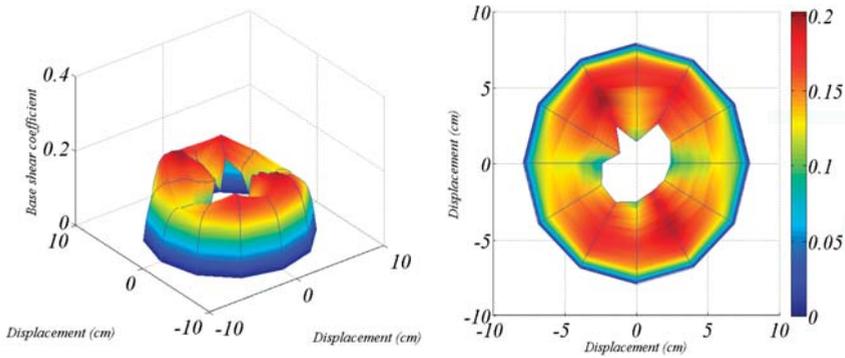
Figure 15. Capacity dominium.

4.2. The Local Response of the Noble Hall

The most significant damage occurred at the two halls at the second level of the building, surmounted by two mirror vaults, whose horizontal parts are frescoed. Both the vaults have suffered heavy damage, and the central frescoed part of the vault in hall B (according to the plan in Figure 1a) has fallen because of the earthquake, as shown in the pictures in Figure 16. To reproduce by means of numerical simulations the crack pattern observed, a numerical model of the hall has been implemented considering the perimeter walls and the surmounting vault, Figure 17.

**Figure 16.** Pictures of the partially fallen vault.
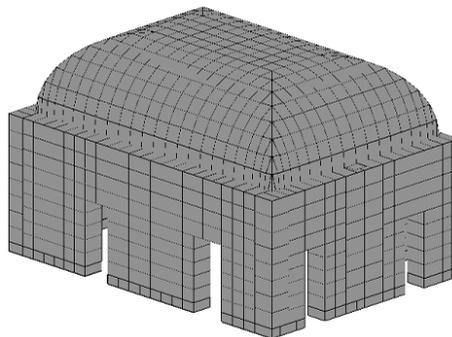
Figure 17. Axonometric view of the numerical model.

In particular, three different load directions have been considered, namely the vertical one (push down) and the two horizontal directions, applying a mass proportional load distribution. For the horizontal load distributions, the two main directions according to the plan of the room have been considered.

The results of the analyses have been reported in terms of collapse mechanisms and capacity curves. The capacity curves report the total base reaction, normalized by the total weight (estimated in 2230 kN), versus the top displacement of the vault. The mechanical properties of the masonry assumed in the numerical simulation are reported in Table 1. It is worth to note that the nonlinear static analyses do not aim at providing a complete vulnerability assessment of the vault, but rather to better understand and justify the collapse of the vault. In fact, a proper vulnerability assessment could not neglect the interaction of the considered structure with the contouring structural elements; in addition, the hall is located at the second level of the building and the filter effect of the first level of the palace should be considered for a reliable vulnerability assessment.

For all the considered load directions, a mass proportional force distribution has been considered. In Figure 18, the collapse mechanisms for all the considered analyses are reported. In particular, in Figure 18a, the collapse mode associated to the vertical mass distribution is reported; as expected the intrados of vaults suffers in the central part, whereas at the extrados the damage is concentrated on a wall of the hall, that surmounts a chimney, where the thickness of the wall is locally much lower (200 mm against 700 mm of the rest of the wall). In Figure 18b,c, the collapse mechanisms associated to the horizontal load distributions are reported; for these load distributions, the base of the vault tends to suffer the heaviest damage, but the chimney represents a weak part of the hall for these load conditions as well, demonstrating that the cause of the partial collapse of the vault must be probably associated to this element. This hypothesis is also supported by the fact that the twin hall (in which no chimney is present) did not suffer the collapse of the vault.

| (**a**) | (**b**) | (**c**) |
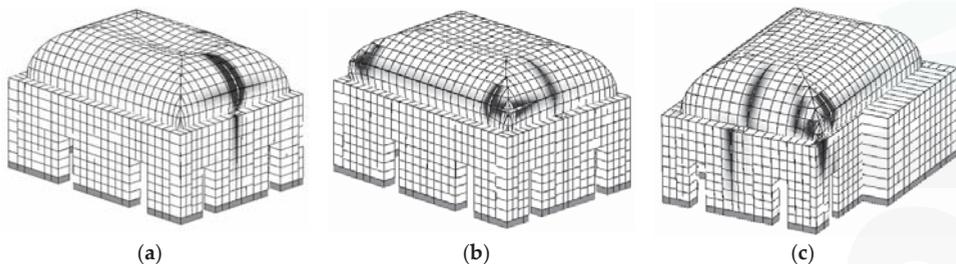
Figure 18. Collapse mechanisms of the mirror vault corresponding to the application of: vertical actions (push down analysis) (**a**); and horizontal actions (push over analyses, along the: longitudinal (**b**); and transversal direction (**c**).

In terms of capacity curves, the results are shown in Figure 19. In each analysis, the maximum displacement along the direction of the loads is considered as monitored displacement. As generalized force parameter, the global vertical base reaction normalized by the weight of the considered portion of the structure is considered for the push-down and the base shear coefficient is considered for the two horizontal push-over analyses.

With regard to the vertical load distribution, the salon exhibits an overstrength with respect to the static condition equal to 2.03, but the global behaviour is brittle, thus making the hall very vulnerable to the vertical component of the earthquake. The capacity curves associated to the horizontal directions have a very low level of displacement capacity (less than 4 mm); the transversal direction has a lower level of strength (maximum base shear coefficient 0.25) and a more pronounced softening branch with respect to the longitudinal direction (maximum base shear coefficient 0.35).
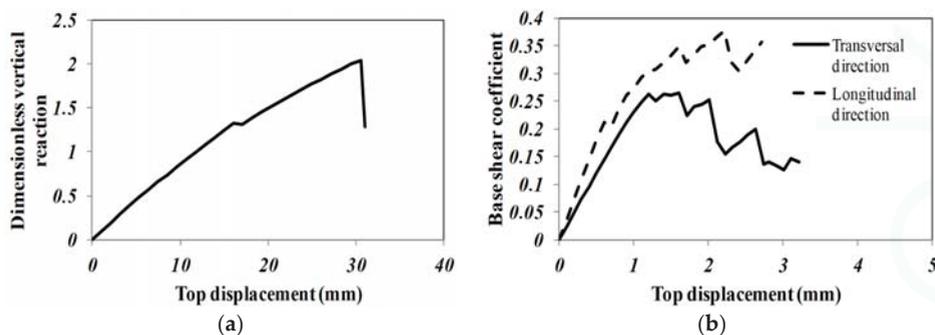
Figure 19. Capacity: (**a**) vertical; and (**b**) horizontal directions.

5. Global Seismic Assessment

In order to assess the seismic safety of the building, in this section two alternative procedures for the evaluation of the seismic performance of the building are presented. In both cases, the role of the direction of seismic input is investigated highlighting the high variability of the seismic performance of irregular structures.

The first procedure is based on the nonlinear static analyses reported in Section 3. The pushover curves, previously obtained, relative to the control points located at the height of 14.45 m (P5, P6, P7, P8 and P9) are combined considering the average value at each step of the analysis. They are used to perform the seismic assessment according to the N2 method [39] and the prescriptions reported in the EC8 [29,30].

With this aim, the ultimate limit state (NC), associated to a global base shear reduction equal to 20% of the peak load, is considered. The equivalent single-degree-of-freedom (SDOF) system is defined by following the steps described in Section 4. The building is assimilated to a nonlinear single degree of freedom by dividing the base shear force (V_b) and the displacement of the target point (D) of a reference control point (in this case the average displacement at level 14.45 m) by the modal participation factor (Γ), according to the procedure described in [38].

In the space of the acceleration spectra (S_a) and displacement spectra (S_d), the coordinates of the SDOF system can be computed as $S_d = D/\Gamma$ and $S_a = V_b/(\Gamma m^* g)$, where m^* is the mass associated to the SDOF system. Since the investigated directions involve not only the main directions, but also intermediate ones, and considering that it is not easy to identify the fundamental vibration modes along those directions from a modal analysis, here the fundamental mode shape along all the directions is approximately assessed consistently with the Italian code [38]; in particular, the mode shape in correspondence of the control points has been approximately estimated proportionally to the mass and height associated to each control point, thus inferring a unique modal participating factor for all the considered directions. From the simplified assumptions here adopted, the Γ factor assumed in the vulnerability assessment has been estimated in 1.57, and the effective mass of the SDOF system has been assumed equal to 3650.9 t. Then, the bi-linear SDOF system is computed according to the procedure proposed in the Italian Code [38]. The main parameters of the equivalent SDOF systems, plotted in terms of acceleration and displacement format (A–D), are reported in Table 3, in which T^* is the equivalent period, S_{Ay} and S_{Dy} are the spectral values associated to the elastic limit of pseudo-acceleration and displacement, respectively. The capacity ductility of the SDOF system turns out to be $\mu = S_{Du}/S_{Dy} = D_u/D_y$.

Table 3. Assessment of the admissible peak ground acceleration (PGA).

Direction (°)	Azimuth (°)	F^*_y (kN)	k^* (kN/cm)	T^* (s)	S_{Ay} (g)	S_{Dy} (cm)	μ_u (-)	PGA Capacity (g)	PGA Demand (g)
0	300	4559	10044	0.33	0.16	0.45	6.29	0.29	0.60
30	270	5370	12517	0.30	0.19	0.43	4.82	0.24	0.66
60	240	6451	13360	0.29	0.23	0.48	4.20	0.24	0.60
90	210	5975	12311	0.30	0.22	0.49	3.64	0.20	0.48
120	180	7066	12878	0.29	0.25	0.55	4.28	0.27	0.55
150	150	5496	11449	0.31	0.20	0.48	4.78	0.25	0.48
180	120	4599	10543	0.33	0.17	0.44	4.21	0.19	0.60
210	90	5471	14312	0.28	0.20	0.38	5.43	0.25	0.66
240	60	6407	13364	0.29	0.23	0.48	1.54	0.09	0.60
270	30	6041	17596	0.25	0.18	0.34	2.24	0.10	0.48
300	0	6591	19184	0.24	0.24	0.34	2.14	0.10	0.55
330	330	5751	10567	0.33	0.21	0.54	7.72	0.44	0.48

Note: * makes reference to the equivalent bilinear SDOF system.

Considering the ductility demand equal to the ductility capacity of the system ($\mu = \mu_u$), the reduction factor $R(\mu)$, defined as the ratio between the elastic spectral acceleration demand and the maximum spectral acceleration of the nonlinear system (S_{Ay}), is computed by using the equal displacement rule ($R = \mu$). The PGA admissible for each limit state (a_g) of the system is computed by equating the acceleration of the system S_{Ay} and the inelastic spectra acceleration $S_A(a_g, T^*, R)$, both associated to the fundamental period of the system. Figure 20 shows a schematic layout of how the procedure for the assessment of the PGA capacity works.
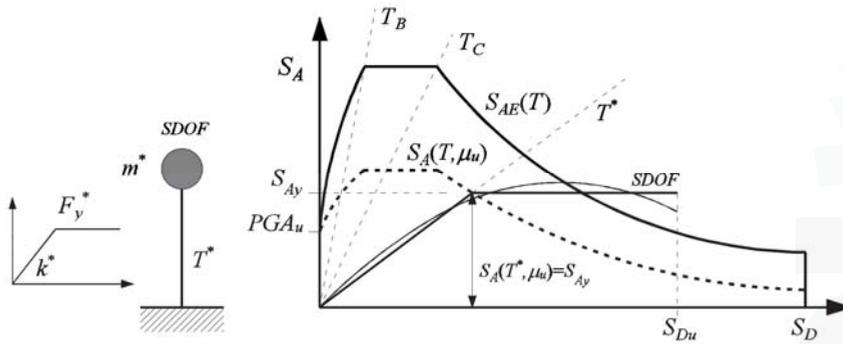
Figure 20. Procedure for the assessment of the admissible PGA.

In the same Table 3, in view of the actual orientation of the building, for each direction with respect to the principal axes of the building, the corresponding azimuth is reported. The accelerometric signal along a specific direction is obtained by composing the ground motion components of the ground motion occurred in L'Aquila on 6 April 2009 along the considered direction; then, the corresponding PGA is computed, as reported in the last column of Table 3. It is worth noting that the actual direction of the seismic input here considered hit the building in direction 300° with respect to its main axes.

Figure 21 shows the admissible PGA at the Near Collapse limit state for each direction of the seismic action; the weakest directions of the building range from 240° to 300° with respect to the principal axes of the building. Besides, in Figure 23, the ratio between capacity and demand in terms of PGA is reported with the dashed line. The safety factor is lower than one for all the considered directions and ranges between 0.145 and 0.919. The safety factor, in this case, represents the ratio between the capacity of the structure in terms of PGA (or ductility as shown later) and the corresponding demand associated to the actual seismic input occurred during the main shock of L'Aquila earthquake.
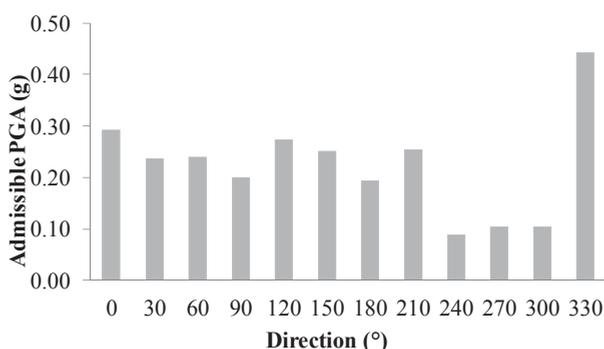
Figure 21. Assessment of the admissible PGA along all the investigated directions.

The second procedure for the assessment of the seismic performance of the building is based on the nonlinear dynamic analyses on the SDOF systems reported in Table 3 (one for each of the considered directions). An elastic-perfectly plastic constitutive scheme was adopted considering the unloading stiffness equal to the initial stiffness. The input was evaluated combining the components of the ground motion occurred in L'Aquila on 6 April 2009 along the considered directions and the ductility demand was assessed as the ratio between the maximum displacement obtained by the nonlinear dynamic analyses conducted on the SDOF systems and the yielding displacement of the bilinear curve. In Table 4, the ductility demand μ_d observed by the numerical simulations is compared with the ductility capacity μ_u associated to the pushover curves, already given in Table 3.

Table 4. Assessment of the ductility capacity.

| Direction (°)	Azimuth (°)	μ_d (-)
0	300	13.97
30	270	16.83
60	240	7.89
90	210	11.06
120	180	5.60
150	150	9.69
180	120	14.86
210	90	17.63
240	60	7.97
270	30	13.57
300	0	10.86
330	330	8.23

Figure 22 shows the admissible ductility demand inferred by the nonlinear dynamic analyses for each direction of the seismic action; the weakest directions of the building correspond to 120° and 240° with respect to the principal axes of the building. Besides, in Figure 23, the ratio between capacity and demand in terms of ductility is reported with the continuous line. The safety factor is lower than one for all the considered directions and ranges between 0.165 and 0.938.

The two considered procedures seem to lead to very similar results, as shown in the comparison reported in Figure 23, for all considered directions and exhibit a high variability of the safety factor with the direction of the seismic input. In both cases, the safety factors are lower than the unit value, which indicates the safety of the structure with respect to the achievement of the Near Collapse Limit State, with reference to the actual seismic event to which the building was subjected. This results is in contrast with the evidence that the building actually did not reach that Limit State during the

event. The latter aspect might be justified by the adopted mechanical properties which were estimated without a proper in-situ investigation campaign and considering a further penalty factor with respect to the mechanical properties suggested by the Italian code [38]. However, the proposed approach led to a conservative estimation of the capacity of the building. Further improvements in the simplified vulnerability assessment procedure could involve an improved definition of the SDOF system, which is defined just like for isolated buildings, although, in this case, it would be more appropriate to see the structure as an assemblage of several structural units interacting with each other.
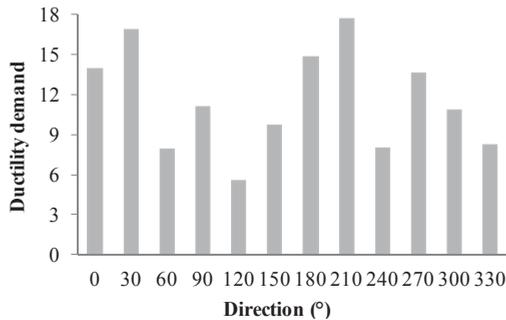
Figure 22. Assessment of the admissible ductility along all the investigated directions.
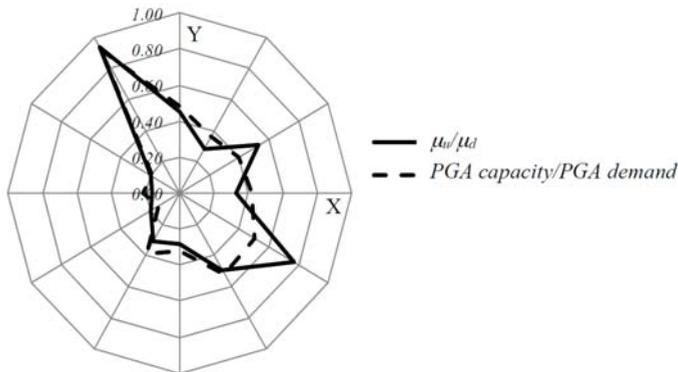
Figure 23. Comparison between the two proposed seismic vulnerability procedures all the investigated directions: ratio between capacity and demand in terms of ductility and peak ground acceleration (PGA).

6. Conclusions

In this paper, the seismic vulnerability of an ancient palace located in L'Aquila (Italy) and subjected to the earthquake occurred in 2009 is investigated. A historical survey of the building, oriented to the reconstruction of the past strengthening interventions, was made. A complete structural assessment of the palace was performed, considering a global model to investigate the overall response and a local model of one of the noble hall, in which the frescoed surmounting vault partially collapsed. The two numerical models were implemented, aiming at grasping both the global seismic response of the building and assessing the so-called "secondary elements". The models were implemented making use of a discrete element approach recently introduced by some of the authors; in particular, the global model was analysed by considering a plane model, since the building globally showed a box behaviour, whereas the hall was investigated with a more sophisticated three-dimensional discrete macro-element,

able to model curved elements as well. The assumptions made in the numerical models descend on a critical study of the available documents which date back to the structural retrofit made in the 1990s. The performed numerical analyses allowed justifying the crack pattern of the building observed in the field and the partial collapse of the mirror vault in the noble hall. In addition, an investigation on the global model was performed by varying the load direction; an original comprehensive representation of the pushover curves is proposed. Finally, a global vulnerability assessment of the building was performed in terms of PGA and ductility; in the first case the results were compared with the Peak Ground Acceleration associated to the main seismic event occurred in L'Aquila in 2009, in the second case the ductility demand of an equivalent SDOF system was compared with the capacity obtained by the pushover curves. The proposed procedures are in good agreement and allowed identifying the weakest directions for the building.

Author Contributions: All the authors conceived the idea, developed the content of the paper, wrote the paper and revised it.

Conflicts of Interest: The authors declare no conflict of interest.

References

1. Chioccarelli, E.; Iervolino, I. Near-source seismic demand and pulse-like records: A discussion for L'Aquila earthquake. *Earthq. Eng. Struct. Dyn.* **2010**, *39*, 1039–1062. [CrossRef]
2. Indirli, M.; Kouris, L.A.S.; Formisano, A.; Borg, R.P.; Mazzolani, F.M. Seismic damage assessment of unreinforced masonry structures after the Abruzzo 2009 earthquake: The case study of the historical centers of L'Aquila and Castelvecchio Subequo. *Int. J. Archit. Herit.* **2013**, *7*, 536–578. [CrossRef]
3. Carocci, C.F. Small centres damaged by 2009 L'Aquila earthquake: On site analyses of historical masonry aggregates. *Bull. Earthq. Eng.* **2012**, *10*, 45–71. [CrossRef]
4. Santucci de Magistris, F.; D'onofrio, A.; Evangelista, L.; Foti, S.; Maraschini, M.; Monaco, P.; Amoroso, S.; Totani, G.; Lanzo, G.; Pagliaroli, A.; et al. Geotechnical characterization of the Aterno Valley for site response analysis. *Riv. Ital. Geotec.* **2013**, *47*, 23–43.
5. Brandonisio, G.; Lucibello, G.; Mele, E.; Luca, A.D. Damage and performance evaluation of masonry churches in the 2009 L'Aquila earthquake. *Eng. Fail. Anal.* **2013**, *34*, 693–714. [CrossRef]
6. Lagomarsino, S. Damage assessment of churches after L'Aquila earthquake (2009). *Bull. Earthq. Eng.* **2012**, *10*, 73–92. [CrossRef]
7. Boscato, G.; Pizzolato, M.; Russo, S.; Tralli, A. Seismic behavior of a complex historical church in L'Aquila. *Int. J. Archit. Herit.* **2014**, *8*, 718–757. [CrossRef]
8. Gattulli, V.; Antonacci, E.; Vestroni, F. Field observations and failure analysis of the Basilica S. Maria di Collemaggio after the 2009 L'Aquila earthquake. *Eng. Fail. Anal.* **2013**, *34*, 715–734. [CrossRef]
9. Pantò, B.; Cannizzaro, F.; Caddemi, S.; Caliò, I. 3D macro-element modelling approach for seismic assessment of historical masonry churches. *Adv. Eng. Softw.* **2016**, *97*, 40–59. [CrossRef]
10. Cimellaro, G.P.; Piantà, S.; De Stefano, A. Output-only modal identification of ancient L'Aquila city hall and civic tower. *J. Struct. Eng.* **2012**, *138*, 481–491. [CrossRef]
11. Ceci, A.M.; Contento, A.; Fanale, L.; Galeota, D.; Gattulli, V.; Lepidi, M.; Potenza, F. Structural performance of the historic and modern buildings of the University of L'Aquila during the seismic events of April 2009. *Eng. Struct.* **2010**, *32*, 1899–1924. [CrossRef]
12. Cardoso, R.; Lopes, M.; Bento, R. Seismic evaluation of old masonry buildings. Part I: Method description and application to a case-study. *Eng. Struct.* **2005**, *27*, 2024–2035. [CrossRef]
13. Mallardo, V.; Malvezzi, R.; Milani, E.; Milani, G. Seismic vulnerability of historical masonry buildings: A case study in Ferrara. *Eng. Struct.* **2008**, *30*, 2223–2241. [CrossRef]

14. Betti, M.; Bartoli, G.; Orlando, M. Evaluation study on structural fault of a Renaissance Italian palace. *Eng. Struct.* **2010**, *32*, 1801–1813. [CrossRef]

15. Castellazzi, G.; D'Altri, A.M.; De Miranda, S.; Ubertini, S. An innovative numerical modeling strategy for the structural analysis of historical monumental buildings. *Eng. Struct.* **2017**, *132*, 229–248. [CrossRef]

16. Castori, G.; Borri, A.; De Maria, A.; Corradi, M.; Sisti, R. Seismic vulnerability assessment of a monumental masonry building. *Eng. Struct.* **2017**, *136*, 454–465. [CrossRef]

17. Andreini, M.; De Falco, A.; Giresini, L.; Sassu, M. Structural analysis and consolidation strategy of the historic Mediceo Aqueduct in Pisa (Italy). *Appl. Mech. Mater.* **2013**, *351–352*, 1354–1357. [CrossRef]

18. Caliò, I.; Cannizzaro, F.; Marletta, M.; Intelisano, M.; Pantò, B.; Caponetto, R.; Margani, G.; Lepidi, M. *L'università e la Ricerca per l'Abruzzo: Il Patrimonio Culturale Dopo il Terremoto del 6 Aprile 2009 (In Italian)*; Milano, L., Morisi, C., Calderini, C., Donatelli, A., Eds.; TEXTUS EDIZIONI: L'Aquila, Italy, 2009.

19. Caliò, I.; Marletta, M.; Pantò, B. A new discrete element model for the evaluation of the seismic behaviour of unreinforced masonry buildings. *Eng. Struct.* **2012**, *40*, 327–338. [CrossRef]

20. Caliò, I.; Pantò, B. A macro-element modelling approach of Infilled Frame Structures. *Comput. Struct.* **2014**, *143*, 91–107. [CrossRef]

21. Caliò, I.; Cannizzaro, F.; D'Amore, E.; Marletta, M.; Pantò, B. A new discrete-element approach for the assessment of the seismic resistance of composite reinforced concrete-masonry buildings. In Proceedings of the Seismic Engineering International Conference Commemorating the 1908 Messina and Reggio Calabria Earthquake, Reggio Calabria, Italy, 8–11 July 2008; Volume 1020, pp. 832–839.

22. Caddemi, S.; Caliò, I.; Cannizzaro, F.; Pantò, B. A new computational strategy for the seismic assessment of infilled frame structures. In Proceedings of the 2013 Civil-Comp, Sardinia, Italy, 3–6 September 2013.

23. Marques, R.; Lourenço, P.B. Possibilities and comparison of structural component models for the seismic assessment of modern unreinforced masonry buildings. *Comput. Struct.* **2011**, *89*, 2079–2091. [CrossRef]

24. Bartoli, G.; Betti, M.; Biagini, P.; Borghini, A. Epistemic Uncertainties in Structural Modeling: A Blind Benchmark for Seismic Assessment of Slender Masonry Towers. *J. Perform. Constr. Facil.* **2017**, *31*, 04017067. [CrossRef]

25. Pantò, B.; Cannizzaro, F.; Caliò, I.; Lourenço, P.B. Numerical and experimental validation of a 3D macro-model for the in-plane and out-of-plane behaviour of unreinforced masonry walls. *Int. J. Archit. Herit.* **2017**, *11*, 1–19.

26. Cannizzaro, F.; Lourenço, P.B. Simulation of Shake Table Tests on Out-of-Plane Masonry Buildings. Part (VI): Discrete Element Approach. *Int. J. Archit. Herit.* **2017**, *11*, 125–142. [CrossRef]

27. Caliò, I.; Cannizzaro, F.; Marletta, M. A discrete element for modeling masonry vaults. *Adv. Mater. Res.* **2010**, *133–134*, 447–452. [CrossRef]

28. Caddemi, S.; Caliò, I.; Cannizzaro, F.; Pantò, B. The Seismic Assessment of Historical Masonry Structures. In Proceedings of the 12th International Conference on Computational Structures Technology, Naples, Italy, 2–5 September 2014.

29. European Committee for Standardization. *EN 1998-3: 2005 Part 3 of the Eurocode 8—Design of Structures for Earthquake Resistance. Section 2: Performance Requirements and Compliance Criteria. Sub-Section 2.2: Compliance Criteria*; European Committee for Standardization: Brussels, Belgium, 2005.

30. European Committee for Standardization. *EN 1998-3: 2005 Eurocode 8: Design of Structures for Earthquake Resistance, Part 3: Assessment and Retrofitting of Buildings*; European Committee for Standardization: Brussels, Belgium, 2005.

31. Pantò, B.; Caliò, I.; Lourenço, P.B. Seismic safety evaluation of reinforced concrete masonry infilled frames using macro modelling approach. *Bull. Earthq. Eng.* **2017**, *15*, 3871–3895. [CrossRef]

32. Dander, M.; Moretti, M. *Architettura Civile Aquilana—Dal XIV al XIX Secolo*; L.U. Japadre 735 Editore: L'Aquila, Italy, 1974. (In Italian)

33. Decreto Ministeriale 20/11/1987: Norme tecniche per la progettazione, esecuzione e collaudo degli edifici in muratura e per il loro consolidamento. Available online: http://www.dist.unina.it/doc/norme/04/04% 2020-11-87.pdf (accessed on 1 September 2017). (In Italian)

34. Casapulla, C.; Portioli, F. Experimental tests on the limit states of dry-jointed tuff blocks. *Mater. Struct.* **2016**, *49*, 751–767. [CrossRef]

35. Casapulla, C.; Maione, A. Formulating the Torsion Strength of Dry-Stacked Stone Blocks by Comparing Convex and Concave Contact Formulations and Experimental Results. *Indian J. Sci. Technol.* **2016**, *9*, 1–7. [CrossRef]

36. Casapulla, C.; Argiento, L.U. The comparative role of friction in local out-of-plane mechanisms of masonry buildings. Pushover analysis and experimental investigation. *Eng. Struct.* **2016**, *126*, 158–173. [CrossRef]

37. Caddemi, S.; Caliò, I.; Cannizzaro, F.; Occhipinti, G.; Pantò, B. A parsimonious discrete model for the seismic assessment of monumental structures. In Proceedings of the 2015 Fifteenth International Conference on Civil, Structural and Environmental Engineering Computing, Prague, Czech, 1–4 September 2015.

38. NTC (2008): Approvazione delle nuove norme tecniche per le costruzioni, Gazzetta Ufficiale della Repubblica Italiana, n. 29 del 4 febbraio 2008—Suppl. Ordinario n. 30. Available online: http://www.cslp.it/cslp/index.php?option=com_docman&task=doc_download&gid=3269&Itemid=10 (accessed on 1 September 2017). (In Italian)

39. Fajfar, P.; Gašperšič, P. The N2 method for the seismic damage analysis of RC buildings. *Earthq. Eng. Struct. Dyn.* **1996**, *25*, 31–46. [CrossRef]